Monte Carlo Simulations and Analyses of Backgrounds in the Sudbury Neutrino Observatory

Xin Chen
Balliol College, Oxford

Thesis submitted in partial fulfillment of the requirements
for the degree of Doctor of Philosophy
at the University of Oxford

Trinity Term 1997

To my parents

Acknowledgement

Thanks are due to all members of the SNO group in Oxford for their support and interest in this work. I am particularly indebted to my supervisor, Dave Wark, who has provided me with considerable encouragement and guidance consistently through out three years. I am impressed by his encyclopedic knowledge of things beyond physics, which makes him a pleasure to work with, and grateful to him for tireless proof-reading of this thesis. I would also like to thank Nick West for his patience in helping me solving problems about computer programming and his good humor. Steve Brice has provided some very useful advises on the pattern recognition technique, as has Martin Moorhead, whose paper stimulated this work. Thanks also go to Nick Jelley who also kindly provided proof-reading of this thesis. I am also grateful to workshop staff who helped me to build the calibration sources and Norm Taplin for his patient explanation of magical chemistry and background counting system. Thanks are especially to Balliol college which gave financial support to my PhD study.

Finally, and perhaps most importantly, I like to thank my parents for their unwaivering understanding and encouragement during the period to complete this thesis.

Abstract

The solar neutrino problem has troubled physicists for almost 30 years since the first solar neutrino experiment, the chlorine experiment, reported a deficiency of the observed neutrino flux relative to the theoretical prediction. This deficiency has been confirmed by 4 other solar neutrino experiments: Kamiokande, GALLEX, SAGE and Super-Kamiokande. As the detection of solar neutrinos has involved two different techniques (electron scattering and radiochemical) and two of the experiments (GALLEX and SAGE) have been carefully calibrated using artificial neutrino sources, it is highly likely that the theoretical predictions rather than the experimental results are wrong. Modifications of the standard theories involve physics beyond the standard solar models or physics beyond the standard electroweak interaction model. The question is which one is the correct solution to the solar neutrino problem. As the suppression of the observed neutrino fluxes is energy-dependent, many physicists prefer the second kind of theories (e.g. neutrino oscillations) to be the correct solution.

The Sudbury Neutrino Observatory (SNO) is a large Čerenkov light detector currently under construction in Canada. Use of 1000 tons of heavy water enables the SNO experiment to detect not only electron neutrinos (by charged current reactions) but also the possible muon and tau neutrinos (by neutral current reactions). The ratio between the numbers of NC and CC events may provide a clear judgement of which theory is the correct solution to the solar neutrino problem.

As is well known, background is often the most serious problem for a neutrino experiment. For SNO, major backgrounds come from radioactive decays of the ^{208}Tl and the ^{214}Bi nuclei in various parts of the detector. Detailed Monte Carlo simulations of these backgrounds have been carried out and affects of backgrounds on the neutrino-induced signals have been analyzed. The reasons behind mis-reconstructions of radioactive decays in the $\approx$ 10000 photomultipliers, which are dirtiest parts in the detector in terms of radioactive impurities, have been studied. Several software background vetoes and a new vertex fitter have been developed, which may be able to reduce the contamination level of PMT background to neutrino events by one order of magnitude.

It is very difficult to get rid of all backgrounds in a neutrino experiment. The problem is more serious for SNO as the signal of a NC background event is almost identical to a neutral current event. Thus it is critical to determine the background levels in the detector

accurately so that we can estimate their contributions to the data and make a correct measurement of the NC/CC ratio. A pattern recognition technique has been developed to provide an in situ and real time determination of the background levels with 5% accuracy. This technique has been checked to be fairly robust against plausible systematic errors of the detector.

As all studies are based on the MC simulations, the reliability of the MC code should be checked. A simple background calibration source has been designed and is being built, which should provide the ultimate verification of the code.

Contents

Chapter 1

The Standard Model and the SNO experiment

The present package of theories (QCD and electroweak interaction theory) dealing with all known interactions among elementary particles is known as the Standard Model. In the Standard Model matter is made up of 3 generations of quarks and leptons, both of which are fermions (with spin 1/2). In addition, there are also various types of vector bosons (listed in order of increasing strength of the interaction they carry): the $W^{\pm}$ and Z^0, which carry the weak force; the photon, which carries the electromagnetic force, and eight gluons, which carry the strong force. These are the only three known and well-established interactions among particles (except for gravity, which is too weak to be seen in interactions between individual particles). There are 61 elementary particles (Both quarks and leptons are structureless at the smallest distances currently probed by highest-energy accelerators.) in the Standard Model: 12 leptons (and anti-leptons), 36 quarks, 12 mediator bosons and one Higgs particle (coupling to which explains the masses of all these particles in the Standard Model). These elementary particles then form our world (for example, a quark and an anti-quark from a meson, three quarks form a baryon like the proton and neutron, protons and neutrons form nuclei and the nuclei and the electron form atoms.) The Standard Model consists of the two gauge theories (a gauge theory is a type of quantum field theory whereby interactions arise when the Lagrangian is assumed to be invariant under a local gauge transformation) mentioned above. The first, QCD or quantum chromodynamics, where the gauge group is $SU(3)_C$ (color), is the model of the strong interaction. As its name implies, the second, electroweak theory, combines the electromagnetic and weak forces into a single theory using the gauge groups

$SU(2)_L$ (weak isospin, L means it only involves left handed fermions or right handed anti-fermions) $\times$ $U(1)_{em}$ (weak hypercharge). In the Standard Model there is as of yet no connection between QCD and the electroweak theory.

Up to now, the Standard Model has been able to explain almost all of experiment data. However there have already been some hints of physics beyond the Standard Model. The so-called solar neutrino problem, which is the discrepancy between the observed electron neutrino flux from the sun and theoretical predictions, is such a example. In the Standard Model, neutrinos are normally assumed to be massless (there does not exist any sound foundation for this assumption). In the Standard Model particle masses arise from couplings to the Higgs boson, and there is no obvious reason why neutrinos should have no such coupling while all other fermions, including the charged leptons, do. If neutrinos do have mass it could lead to mixing in their electroweak eigenstates in a manner similar to the mixing that happens in the quark sector (see Chapter 2). If such neutrino mixings do occur, it is possible that an electron neutrino could turn into other types of neutrinos after travelling a certain distance. At the moment an elaboration of this model, whereby the different interactions between the different types of neutrino and the matter in the Sun lead to a resonant enhancement in the mixing in an effect known as the Mikheyev, Smirnov, Wolfenstein (or MSW) effect, seems the most likely solution to the solar neutrino problem. If data from the SNO experiment confirm this hypothesis, it will be the first solid evidence of physics beyond the Standard Model. Details of the solar neutrino problem and the SNO experiment are presented in the next two chapters.

Chapter 2

The Solar Neutrino Problem

2.1 Overview

The motivation for studying solar neutrinos was originally to provide an experimental answer to the question: How does the sun shine ? This question goes back to the 19th century struggle to reconcile the age of the sun inferred from the theory of gravitational contraction with the much longer time scales required by geological arguments. In the first half of the 20th century, this problem was solved in principle by the recognition that the amount of mass by which four hydrogen nuclei are heavier than a helium nucleus corresponds to a large amount of energy [1]. Since then, 50 years of effort by thousands of scientists has created mathematical models which are able to simulate the complicate physical phenomena inside the sun and reproduce its detailed character. Models which take the most reliable observational values as inputs and use a certain set of widely-accepted physical assumptions in the calculation are called standard solar models(SSM). Section 2.2 is a brief discussion of these models.

A good and correct theory must give accurate predictions which could be checked by different kinds of experiments. This is just where the solar neutrino problem (SNP) arises. Although the standard solar model (SSM) correctly reproduces many solar observables such as age and luminosity, the neutrino fluxes predicted by the model are consistently higher than the values observed by all of the five current operating solar neutrino experiments. The discrepancy between the experimental and theoretical values constitutes the Solar Neutrino Problem. The detailed information about these experiments is presented in section 2.3.

Many theories have been proposed to solve the solar neutrino problem. Almost all of them fall into two categories: non-standard solar models that modify the astrophysical description of the sun and non-standard theories of electroweak interactions that hypothesize new properties of neutrinos. Most of the non-standard solar model solutions are in conflict with something we think we understand, whereas some suggestions of new physics beyond the standard electroweak theory do not suffer from this defect. For example, some solutions based on the non-standard electroweak theory require massive neutrinos, which appear naturally in the framework of Grand Unified Theories. Section 2.4 summarizes some of these solutions.

More data or new experiments are needed to find out the correct answer to the solar neutrino problem. Section 2.5 gives a preview to several important next generation experiments.

2.2 Standard Solar Model

The sun is an astronomical laboratory. Because of its proximity to the earth, we are able to obtain information about the sun that is not accessible from other stars. Solar models attempt to simulate the reactions and the transport phenomena of the sun and thus produce a coherent picture of its internal workings. Based on a realistic set of initial conditions and evolution equations, such models must be able to reproduce or predict the observable features of the sun. A standard solar model is one which uses widely accepted physics and initial conditions, as distinct from the non-standard models where the physical assumptions are adjusted to fit certain kind of data (usually to produce a diminished solar neutrino flux). At present, the most widely quoted SSM is the model calculated by Bahcall and Pinsonneault [2]. Table 2.1 lists some of the most important physical characteristics of the sun either measured by experiments or predicted by Bahcall's SSM.

Section 2.2.1 describe the main input parameters and the principal approximations used in constructing the Standard Solar Model while the mathematical method used in calculations is outlined in section 2.2.2. Section 2.2.3 gives some important SSM's predictions about the solar neutrino. Finally, section 2.2.4 discusses helioseismology, emphasizing the complementary between the studies of p-mode oscillations and the solar neutrino experiments.

[1] The value of Z/X is determined from study of meteorites: Z/X=0.0245 [4].

Table 2.1: **Some important solar quantities. The measured parameters are: photon luminosity, mass, radius, oblateness, and age. All other quantities are calculated by Bahcall's SSM [2, 3].**

Parameter	Value
Photon Luminosity($L_\odot$)	$3.844(1 \pm 0.004) \times 10^{33}\, erg\, s^{-1}$
Neutrino Luminosity	$0.023 L_\odot$
Mass($M_\odot$)	$1.99 \times 10^{33}\, g$
Radius($R_\odot$)	$6.96 \times 10^{10}\, cm$
Oblateness	$\leq 2 \times 10^{-5}$
Effective(surface) temperature	$5.78 \times 10^{3}\, K$
Age	$\approx (4.57 \pm 0.02) \times 10^{9}\, yr$
Initial helium abundance by mass	0.27753
Initial heavy element abundance by mass	0.02 [1]
Depth of convective zone	$0.712 R_\odot (0.024 M_\odot)$
Central density	$156.2\, g\, cm^{-3}$
Central temperature	$1.5843 \times 10^{7}\, K$
Central hydrogen abundance by mass	0.3333
Neutrino flux from pp reaction	$5.91 \times 10^{10}\, cm^{-2}\, s^{-1}$
Neutrino flux from ^{8}B decay	$6.62 \times 10^{6}\, cm^{-2}\, s^{-1}$
Fraction of energy from pp chain	0.984
Fraction of energy from CNO cycle	0.016

2.2.1 The Principal Approximations and The Main Input Parameters

According to the standard stellar structure and evolution theories, the sun is a middle-aged main sequence star, which is calmly burning hydrogen without violent or rapid evolution. Thus it is expected that we should be able to calculate the behavior of the sun more accurately and easily than many other stars.

Some of the principle approximations used in constructing the standard solar model deserve special emphasis because of their fundamental role in the calculations:

- The sun is a spherically symmetric body undergoing no significant rotations. The effects of mass loss and magnetic fields are also neglected.

- The sun is assumed to be in hydrostatic equilibrium, which means the radiative and thermal pressures exactly balance gravity:

$$\frac{\partial P(r)}{\partial r} = -\frac{GM(r)\rho(r)}{r^2} \tag{2.1}$$

  where P(r) and $\rho(r)$ are the pressure and density at a radius r respectively, and M(r) is the solar mass enclosed by this radius. This is known to be an excellent approximation since a small departure from hydrostatic equilibrium would cause the sun to collapse(or expand) in less than an hour.

- Energy is transported by photons or by convective motions. The temperature gradient between the interior and the surface gives rise to a net flux of energy emitted from the central regions of the sun. The equation governing the energy transportation is:

$$L_r = -4\pi r^2 \frac{ac}{3}\frac{1}{\kappa\rho}\frac{\partial T^4}{\partial r} \tag{2.2}$$

  where L_r is the amount of energy passing through a sphere of radius r per unit time and T is the temperature. The total opacity κ is the combination of the radiative and conductive opacities: $\kappa^{-1} = \kappa_{rad}^{-1} + \kappa_{cond}^{-1}$. For solar interior conditions, the radiative opacity is the dominant one. The Stefan-Boltzmann constant a is equal to $\frac{8\pi^5 k^4}{15c^3h^3}$(see [5] for a discussion of the equation of a stellar plasma).

- The primary energy source in the sun is nuclear fusion, including the proton-proton(p-p) chain and carbon-nitrogen-oxygen(CNO) cycle reactions, with minor contributions from gravitational expansion or contraction. The SSM predicts that CNO

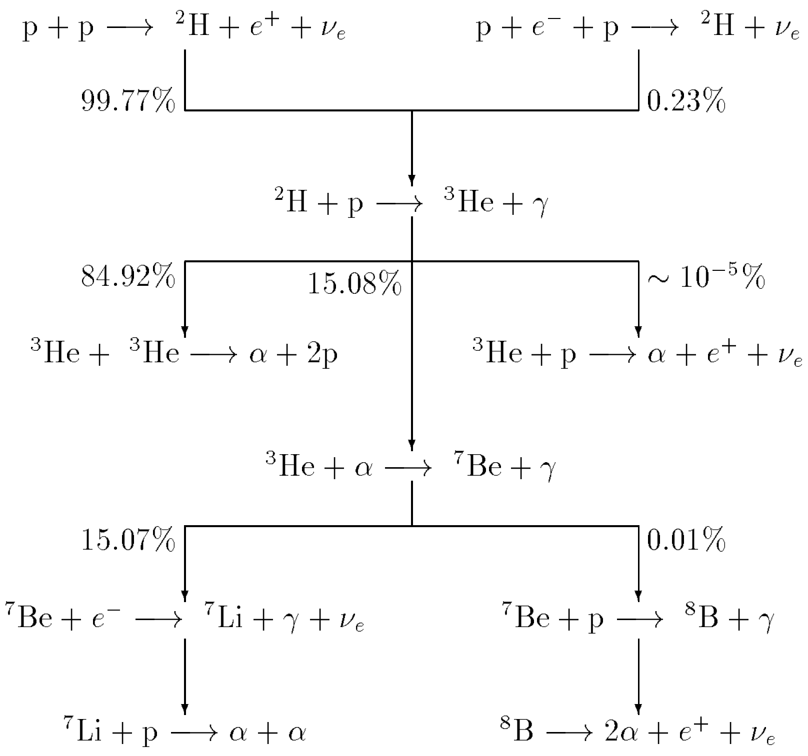

Figure 2.1: **Schematic diagram of the pp chain [3].**

cycle reactions(shown in figure 2.2) play a less important role ($\approx 1.6\%$ of the energy generation) while the pp chain reactions, as shown in figure 2.1, supply most of the solar energy through the following net reaction:

$$4p + 2e^- \rightarrow^4 He + 2\nu_e + 26.731 MeV \tag{2.3}$$

- Changes of the element abundances are caused mainly by nuclear reactions. Recently the diffusion of heavy elements is included in Bahcall's latest solar model [2] which did not make big changes to the calculated neutrino fluxes. The initial solar interior is presumed to have been chemically homogeneous. In regions of the sun that are stable to matter convection, changes in the local abundances of individual isotopes occur solely because of the nuclear reactions and the diffusions of heavy elements.

- The outer layer of the sun is strongly influenced by convection and turbulence which are not well understood in the context of stellar structure theory. However, because the outer boundary conditions do not matter much for processes that occur in the

Table 2.2: **The CNO cycle.** The main reactions are shown for the carbon-nitrogen-oxygen cycle in the sun, taken from [3].

Reaction	ν energy(MeV)
$^{12}C + p \rightarrow ^{13} N + \gamma$	
$^{13}N \rightarrow ^{13} C + e^{+} + \nu_e$	≤ 1.199
$^{13}C + p \rightarrow ^{14} N + \gamma$	
$^{14}N + p \rightarrow ^{15} O + \gamma$	
$^{15}O \rightarrow ^{15} N + e^{+} + \nu_e$	≤ 1.732
$^{15}N + p \rightarrow ^{12} C + \alpha$	

deep interior such as neutrino generation, it is sufficient in practice to assume that the solar outer regions are in convective equilibrium and to apply the well known approximate relations between the pressure and the temperature. Great care must be taken in helioseismology where the comparisons are made between the theory and the observations of the photons emitted from the surface layers.

The major input parameters used in the calculation of the SSMs are:

- **Nuclear parameters.** Table 2.3 lists the nuclear parameters for some important reactions in the p-p chain. The thermal energy release(Q value) is just the mass difference between the initial and the final nuclei. The typical thermal energies of the particles in the sun are only a few keV whereas the Coulomb barriers are in the MeV range, which makes the reaction rates too low to be measured in laboratory experiments. Some form of extrapolation is needed to deduce the low energy cross sections. The usual way of parameterization is:

$$\sigma(E) = \frac{S(E)}{E} exp(-2\pi\eta) \tag{2.4}$$

where $\eta(E) = \frac{\alpha z Z}{v/c}$ for two ions of charges ze and Ze which collide with relative velocity v giving a kinetic energy E in the center of mass frame. S(E) is a slowly varying function expressing the small energy dependence of the matrix element. Values of S(E) can be measured at MeV energy ranges and then extrapolated to the zero energy values used in solar models. Two reactions in the p-p chain do not involve nuclear fusion. They are electron-capture reactions: $^{1}H(pe^{-}, \nu_e)^{2}H$ and

Reaction	ν Label	Q (MeV)	$S(0)$ (keV b)	dS/dE (b)
p(p,e$^+\nu_e$)^{2}H	pp	1.442	4.07×10^{-22}	4.52×10^{-24}
p(pe$^-$,ν_e)^{2}H	pep	1.442	-	-
^{2}H(p,γ)^{3}He	-	5.494	2.5×10^{-4}	7.9×10^{-6}
^{3}He(p,e$^+\nu_e$)^{4}He	hep	19.795	8×10^{-20}	-
^{3}He(^{3}He,2p)^{4}He	-	12.860	$5.15 \times 10^{+3}$	-9×10^{-1}
^{3}He(^{4}He,γ)^{7}Be	-	1.586	5.4×10^{-1}	-3.1×10^{-4}
^{7}Be(p,γ)^{8}B	-	0.137	2.43×10^{-2}	-3×10^{-5}
^{7}Be(e$^-$,ν_e)^{7}Li	^{7}Be	0.862	-	-
	^{7}Be	0.384	-	-
^{8}B(e$^+\nu_e$)^{8}Be	^{8}B	17.980	-	-

Table 2.3: **Values of the cross-section parameters for some reactions of the p-p chain (taken from [6]).**

$^7Be(e^-,\nu_e)^7Li$. These reaction rates can be calculated by standard electroweak interaction theory, taking into account the local physical conditions of the solar plasma [3]:

$$R_{p+e^{-1}+p} \cong 1.102 \times 10^{-4}(\frac{\rho}{\mu_e})T_6^{-0.5}(1+0.02T_6)R_{pp} \quad (2.5)$$

$$R_{^7Be+e^{-1}} \cong 5.54 \times 10^{-9}(\frac{\rho}{\mu_e})T_6^{-0.5}(1+0.004(T_6-16))s^{-1} \quad (2.6)$$

where $\mu_e \approx \frac{2}{1+X}$ is the mean molecular weight per electron.

Of all the solar nuclear fusion reactions, the least well known and the most crucial for solar neutrinos is the ^7Be+p reaction with a quoted uncertainty of $22\%(3\sigma)$([6]).

- **Chemical abundances and radiative opacity.** Photon radiation is thought to be the major method of energy transportation in the inner sun where most of the solar neutrinos are produced. Thus the radiative opacity, which depends on the chemical abundances and the modelling of complex atomic processes in the sun, plays an important role in the solar model. As stated before, the sun is assumed to have been chemically homogeneous when it arrived on the main sequence and the composition of the present solar surface is thought to reflect the initial abundances of all elements that are at least as heavy as carbon. Recently, diffusion of helium and heavy elements is included in Bahcall's latest solar model [2] which changes the element abundances at the solar surface, thus the initial element abundances of the sun can only be taken from meteorite data with minor modifications. The most important input parameter of element abundances is the initial ratio by mass of isotopes heavier than helium relative to hydrogen, $\frac{Z}{X}$, which is 0.0245 in Bahcall's SSM [2] . The typical systematic uncertainty of $\frac{Z}{X}$ is about $6.1\%(1\sigma)$. Two different opacity codes(Los Alamos and Livermore) have been used to calculate the neutrino fluxes, and the computed results agree to better than 16% for all sources of solar neutrinos [3].

- **Solar luminosity and age.** These solar data are measured by experiments, the data have not changed significantly in the last few decades.

- **The equation of state.** Contrary to what some physicists intuitively believe, the equation of state of stellar material(i.e. the relation between the pressure and the density) is thought to be well known under the conditions that apply to the solar interior. The difference among the neutrino fluxes calculated by different physicists with various equations of state is less than or at the order 1.5% [14].

2.2.2 Calculation Procedures

A satisfactory solar model is a solution of the evolutionary equations, which are derived from the major assumptions described above, while taking the current best-estimated values as inputs. The model begins with a main sequence star which is chemically homogeneous. Hydrogen burns in the interior of the sun to balance the force of gravity. Thus the element abundances are changed as the sun evolves, as are the other parameters such as the opacity. The model is iterated forward in discrete time steps until the present age of the sun is reached. This evolution then produces the predictions which can be compared with the observations of the current sun(such as the solar luminosity and radius). Finally, the input parameters (such as helium abundance)are adjusted to fit the data of $M_\odot$, $L_\odot$ and $R_\odot$ from the experiments. This final model predicts the present complete set of physical variables within the sun including the neutrino fluxes and the spectra of acoustic oscillation frequencies observed on the solar surface.

Figure 2.2: **Energy spectrum of solar neutrinos produced in the pp chain reactions [3].**

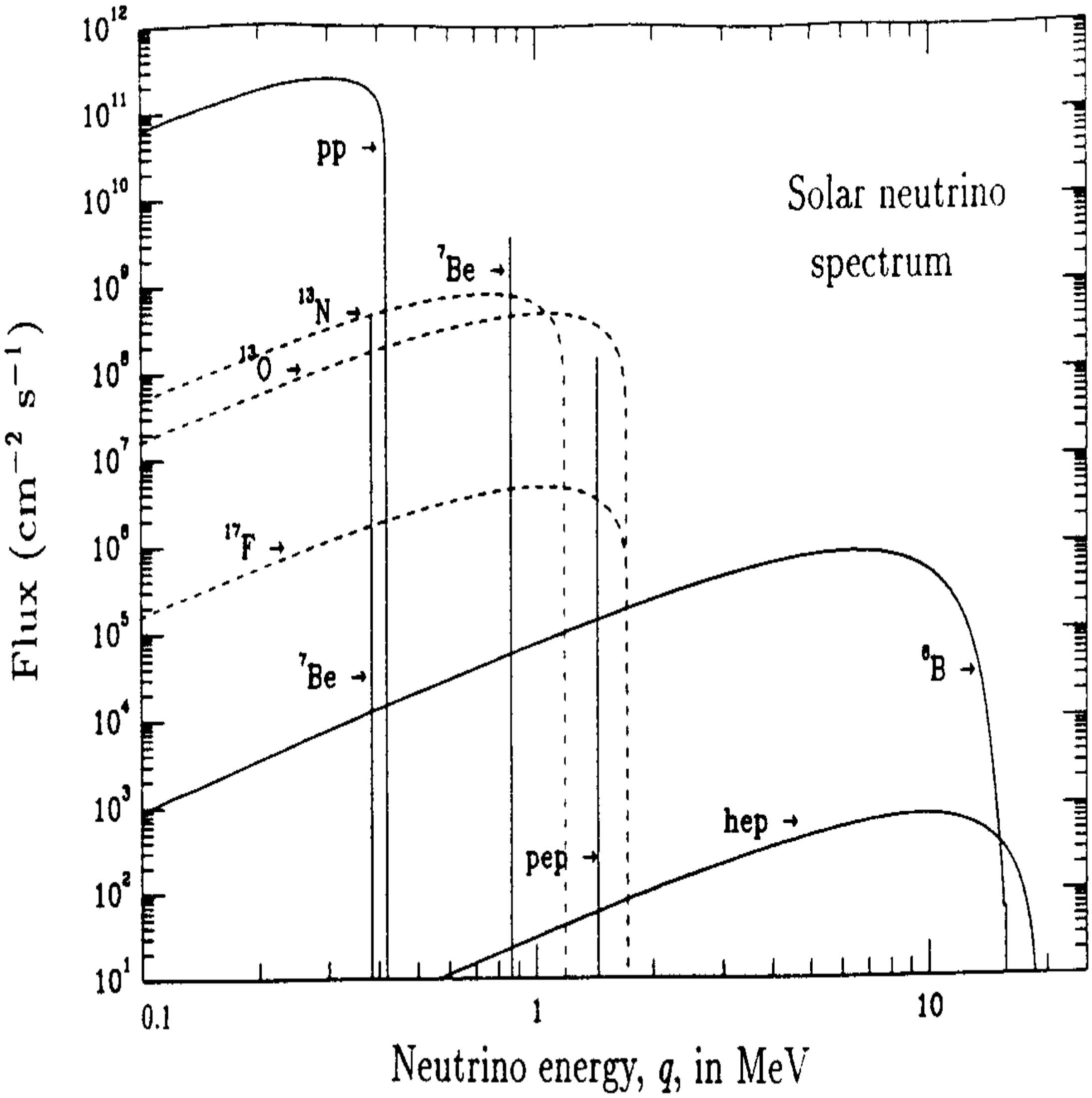

2.2.3 Some predictions of solar neutrinos by the SSM

As shown in figure 2.2, there are five separate neutrino sources within the p-p chain, three of them produce continuous energy spectra: namely pp, ^{8}B and hep neutrinos; the other 2 produce discrete energies: ^{7}Be and pep neutrinos. The shape of the energy spectrum is critical in distinguishing among different solutions to the solar neutrino problem. The spectrum for a particular neutrino source is fixed solely by the nuclear physics so any changes to the astrophysics are not able to appreciably alter its shape, a distortion of the spectrum would therefore be a clear sign of the new physics beyond the standard electroweak interaction theory.

Table 2.4: **Calculated solar neutrino fluxes [2]**

Source	Flux($10^{10} cm^{-2} s^{-1}$)
pp	$5.91(1 \pm 0.01)$
pep	$0.014(1.00^{+0.01}_{-0.02})$
hep	1.21×10^{-7}
^{7}Be	$0.515(1^{+0.06}_{-0.07})$
^{8}B	$6.62 \times 10^{-4}(1^{+0.14}_{-0.17})$
^{13}N	$0.0618(1^{+0.17}_{0.20})$
^{15}O	$0.0545(1^{+0.19}_{0.22})$
^{17}F	$6.48 \times 10^{-4}(1^{+0.15}_{0.19})$

Most of the solar neutrinos are produced in the interior of the sun, thus the measurement of them gives us information about otherwise inaccessible regions where photons, the traditional messengers of astronomy, are trapped. For example, the solar neutrino fluxes are extremely sensitive to the core temperature, the empirical power law relations between them derived by Bahcall[8] are :

$$\phi(pp) \sim T_c^{-0.9}, \quad \phi(^7Be) \sim T_c^{11}, \quad \phi(^8B) \sim T_c^{25} \tag{2.7}$$

The calculated solar neutrino fluxes by Bahcall's SSM are presented in table 2.4. The predicted pp neutrino flux has the smallest uncertainty because of the stringent luminosity constraint(the energy of the sun is almost solely supplied by the p-p chain reactions) while the largest uncertainty in the p-p chain is associated with the ^{8}B neutrinos because the calculated cross section for the $^7Be(p,\gamma)^8B$ reaction is fairly sensitive to conditions in the solar interior which are not fully understood.

2.2.4 Helioseismology

The sun is an oscillating star whose motion can be revealed by Doppler shifts in spectral lines that are formed in the solar atmosphere [9]. Helioseismology, like terrestrial seismology, provides information about the interior of the sun by analyzing observations of these oscillations, which basically divide into two classes: sound waves(also known as p-modes or pressure modes) and gravity waves(also known as g-modes). Sound waves are largely trapped within one spherical shell with the solar surface as the upper boundary and the bottom of the convection zone as the lower boundary. Information about the conditions in this spherical shell is contained in the observed frequency spectrum since the rate of propagation depends on the physical conditions of the medium in which sound waves travel. Thus the accurate measurement of the frequence of the p-mode is an important compliment to the observation of solar neutrinos. The measurement of the g-modes would be more useful since they are expected to probe deeper into the sun than the p-modes. However, they are difficult to detect because their amplitudes decrease rapidly through the convection zone and their periods are long.

The interpretation of the observed results is complex for three reasons:

- There exists a periodicity introduced by the observation cycle. Any single observatory on the earth is only able to take the data for 12 hours in the day time, which may not be long enough to cover the periods of some oscillation modes (especially g-mode). A observatory network known as GONG[2], which constitutes at least six observatories around the world, is intended to carry out continuous measurement of solar oscillations[10].

- The complicated convection and turbulence in the area near to the solar surface are not fully understood and are difficult to simulate.

- It is hard to eliminate the effects of the terrestrial atmosphere for a ground-based observatory. Several helioseismology instruments in a satellite called SOHO[3] provided uninterrupted observations of solar oscillation modes (especially g-modes) [11].

Nevertheless, the calculations using the standard solar model represent well the quantitative features of the measured frequency spectrum. For example, the calculated depth of the solar convection zone by the latest Bahcall's SSM [2] is R = 0.712 $R_\odot$, which agrees with the observed value determined from p-mode oscillation data of R = 0.713 $\pm$ 0.003 $R_\odot$ [12].

[2] Global Oscillation Network Group

[3] Solar and Heliospheric Observatory

2.3 Solar Neutrino Experiments

In the last twenty years, five experiments have been carried out to detect solar neutrinos: three radiochemical experiments (Homestake, GALLEX and SAGE) and two water Čerenkov experiments (Kamiokande II and Super Kamiokande). The following sections present an overview of these experiments in chronological order.

2.3.1 The ^{37}Cl experiment

The ^{37}Cl experiment [13] which began to take data on 1970 [14] is the first and longest-serving solar neutrino experiment in the world. The ^{37}Cl detector is located 4850 feet underground in the Homestake mine, in Lead, South Dakota. Placing the detector deep underground, which is common to all solar neutrino experiments, is needed to reduce the background due to cosmic rays. The reaction that is used to detect solar neutrinos is the inverse beta decay of ^{37}Ar:

$$\nu_e +^{37} Cl \rightarrow e^- +^{37} Ar \tag{2.8}$$

This rection has a low threshold of 0.814 MeV which makes the detector sensitive to all types of solar neutrinos except pp neutrinos. The detector itself is a tank containing $2.2 * 10^{30}$ atoms(133 tons) of ^{37}Cl in the form of $3.8 * 10^5$ liters(615 tons) of C_2Cl_4. The following procedures are carried out to collect the data:

1. At the beginning of every run, a small amount of pure ^{36}Ar (or ^{38}Ar) carrier gas is dissolved in the liquid C_2Cl_4. Since the extraction and counting methods used in this experiment are not able to distinguish between different isotopes of argon, the extraction efficiency can be checked at the end of the run by comparing the amount of ^{36}Ar (or ^{38}Ar) measured with the amount dissolved.

2. The liquid C_2Cl_4 is left in the tank to be exposed to solar neutrinos for some time, usually on the order from one to three months.

3. At the end of the exposure time, about $4 * 10^5$ liters of helium gas are circulated through the whole tank to remove the argon atoms. Then the recovered helium gas passes sequentially through a condenser at $-32^o C$, a molecular sieve at room temperature and finally a charcoal trap cooled to the temperature of liquid nitrogen, where the argon atoms are absorbed.

4. The charcoal trap is heated to release the trapped argon atoms, which are then loaded into a small proportional chamber (counter) along with tritium-free methane serving as a counting gas.

5. The counter is left for approximately eight months or longer to measure the amount of recovered ^{37}Ar by observing the characteristic 2.82keV Auger electrons from the electron capture decay of ^{37}Ar.

The major background for the ^{37}Cl experiment is from penetrating cosmic ray muons whose cascade products ultimately generate ^{37}Ar via (p,n) reactions on ^{37}Cl. This background level has been estimated in two independent ways:

- by exposing 600 gallons of C_2Cl_4 at a higher level in the mine and then extrapolating the observed production rate of ^{37}Ar to the lower level where the chlorine detector is located.
- by multiplying an in-situ measurement of the vertically penetrating muon flux by a theoretical estimate of the ^{37}Ar yield per muon at the average muon energy at the depth of the detector.

The two estimates are in good agreement and yield:

$$Background\ \ rate = 0.4 \pm 0.16\ \ SNU^4 \tag{2.9}$$

A couple of calibration tests have been carried out to check the performance of the detector:

- A measured number of ^{37}Ar atoms (500) are introduced into the detector and then extracted by using the same procedure described before. The overall recovery and counting efficiency is checked to be nearly 100%.
- A special test is performed in order to ensure that ^{37}Ar, which is produced in the form of a recoil ion, becomes a neutral argon atom instead of binding to the C_2Cl_4 molecule (note test 1 only calibrates the recovering efficiency of ^{37}Ar atoms instead of ^{37}Ar ions). A certain amount of $C_2Cl_3^{36}Cl$ is introduced into the detector tank. The following reaction takes place:

$$C_2Cl_3^{36}Cl \rightarrow C_2Cl_3 +^{36} Ar^+ + e^- + \overline{\nu_e} \tag{2.10}$$

[4] SNU(Solar Neutrino Unit) is a unit widely used in solar neutrino experiments, 1 SNU = 10^{-36} captures per second per target atom.

This process is essentially equivalent to the one used in solar neutrino detection. The energy spectrum of ^{36}Ar decay is similar to that of ^{37}Ar decay, therefore full recovery of ^{36}Ar would imply that the argon ions are not trapped in the remnant of C_2Cl_4 molecules. The number of recovered ^{36}Ar atoms is measured to be consistent with the number of $^{36}Ar^+$ ions predicted.

The ^{37}Cl experiment has been running continuously for 26 years except for a break in 1985 due to the failure of two gas pumps. The combined data is analyzed using a maximum-likelihood method to reflect characters of signals with a component decaying with the half life of ^{37}Ar (50.5 days) superimposed on a constant background. The latest result [15] is:

$$Capture\ \ Rate(exp.) = 2.54 \pm 0.14(statistical) \pm 0.14(systematic) SNU \tag{2.11}$$

. This value is much lower than the theoretical value predicted by the standard solar model [16]:

$$Capture\ \ Rate(theory) = 9.3^{+1.2}_{-1.4}\ SNU \tag{2.12}$$

The ^{37}Cl experiment was the first experiment which reported the Solar Neutrino Problem: the discrepancy between the observed rate and the theoretical prediction (figure 2.3 shows the ^{37}Ar production rate in the last two decades). However, the result of this experiment confirms that the p-p chain reaction is the main supplier of solar energy since Bahcall [17] pointed out that the capture rate would be 28 SNU if the CNO cycle was the dominant reaction mechanism in the sun and there was no incredibly large neutrino conversion in this energy region.

The other thing worth mentioning is the possible correlation between the capture rate of the chlorine experiment and the inverse of the sunspot number. There seemed to be a weak correlation in the late 80's. However, with the taking of more data, this correlation diminished.

2.3.2 The Kamiokande II Experiment

The Kamiokande II Experiment [18] is a water Čerenkov detector located in Kamioka mine in the Gifu prefecture of Japan. As shown in figure 2.4, the detector consists of a cylindrical inner tank containing 2140 tons of water, which is viewed by 948 20-inch photomultiplier tubes (PMT), giving approximately 20% coverage of the detector's

Figure 2.3: **Time-averaged ^{37}Ar production rate in the chlorine detector [13].**

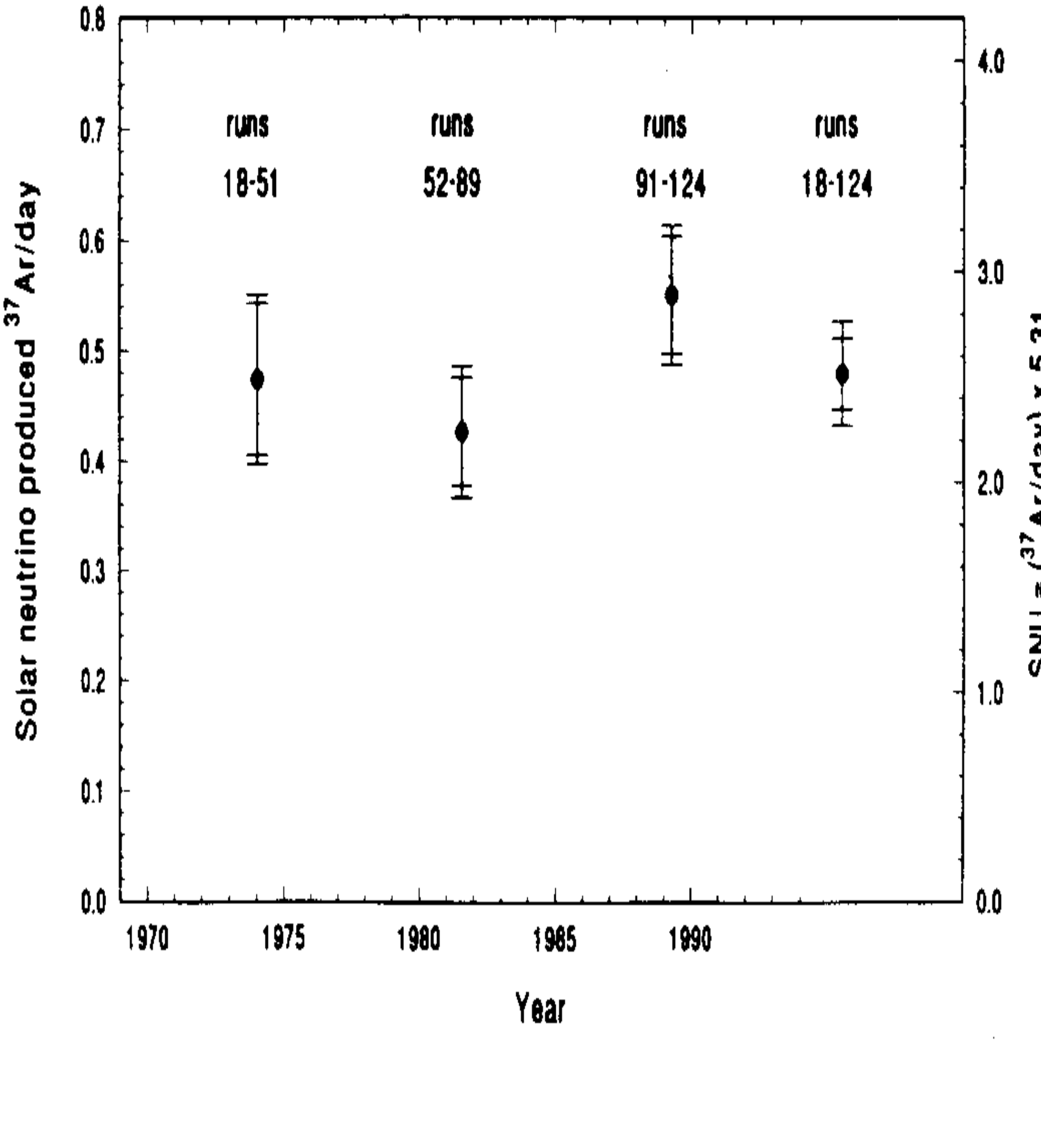

Figure 2.4: **Schematic of the layout of the Kamiokande II experiment [18].**

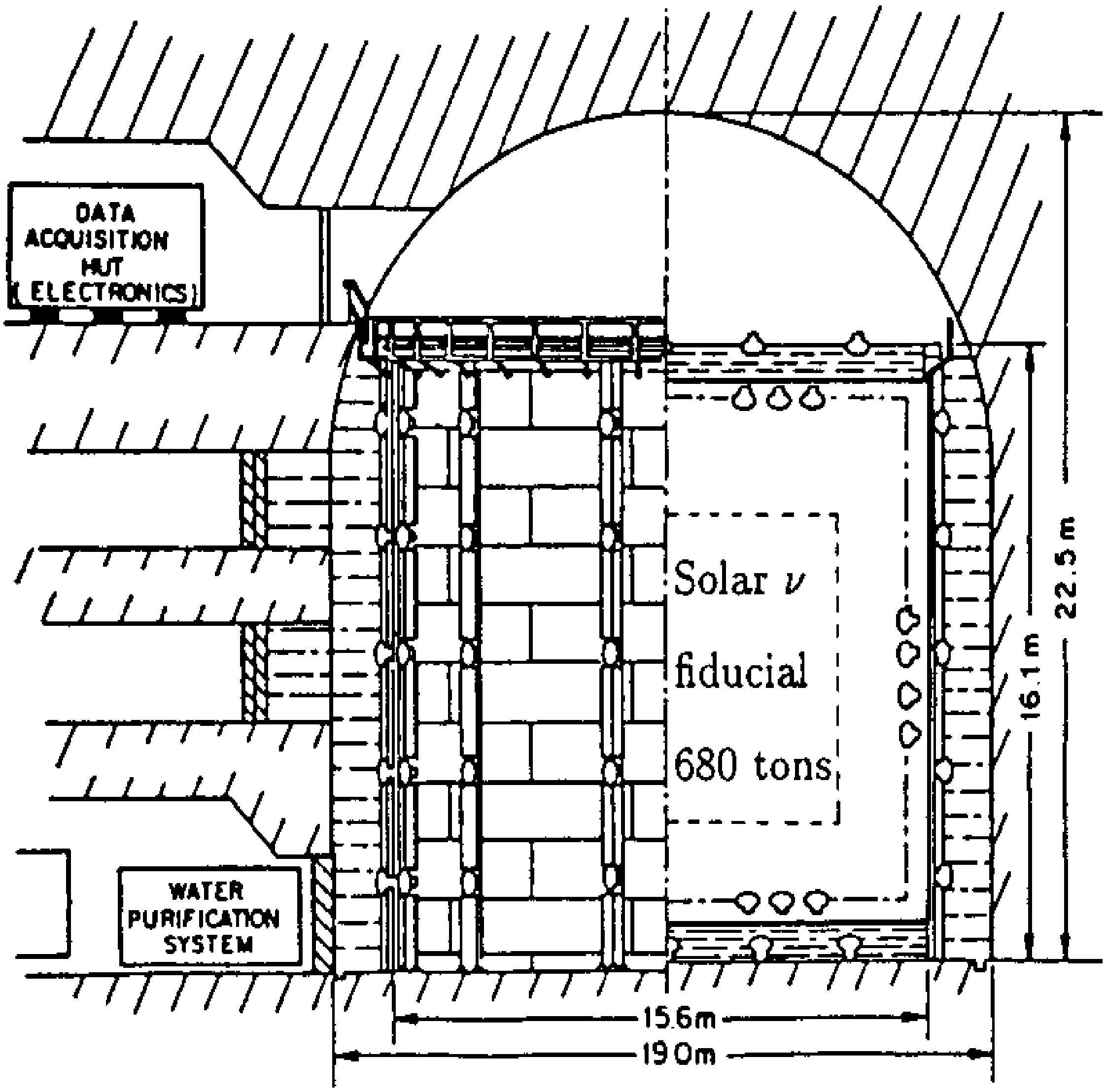

surface. This inner volume, of which the central 680 tons of water is chosen as the fiducial volume, is further surrounded by a second volume of water of total mass 2800 tons, which is viewed by 123 PMTs to serve as a 4π solid angle anti-counter to veto cosmic ray muons. Some important parameters of the detector are presented in table 2.5

The electron elastic-scattering interaction is used to detect solar neutrinos:

$$\nu_x + e^- \rightarrow \nu_x + e^- \quad (x = e, u, \tau) \tag{2.13}$$

The scattered electron emits Čerenkov photons which are detected by the PMT arrays surrounding the detector. There are some advantages in using a ring imaging water Čerenkov detector:

- Neutrinos are detected in real-time, which is important in the case of supernova

Table 2.5: **Some important detector parameters of the Kamiokande II detector [18].**

Fiducial Volume	680 tons
Trigger efficiency	50% at 5.2MeV
	90% at 7.5MeV
Energy resolution	$19/(T_e/10MeV)$%
vertex resolution	1.5m at 10MeV
Direction resolution	28^o at 10MeV

neutrinos where all events occur within seconds. Temporal information also plays a important role in observing (or disproving) the correlation between the solar neutrino flux and some time-dependent solar phenomena such as sun spots.

- The direction and energy of the scattered electron can be deduced from the pattern and the number of the detected Čerenkov photons. The angular distribution of the scattered electrons is peaked in the same direction as the incoming neutrinos, which enables us to experimentally determine the direction of these neutrinos. The accurate measurement of the electron's energy spectrum provides useful information in determining the energy spectrum of solar neutrinos, which may be useful in distinguishing between different solutions to the solar neutrino problem.
- Reaction 2.13 is sensitive to all three types of neutrinos. However, it may be difficult to extract information from this because the cross section for ν_e scattering (involving both neutral and charged interactions) is roughly 6 times larger than for ν_u or ν_τ scatterings.

The disadvantage of a water Čerenkov detector is that, unlike radiochemical detectors, any charged particles with velocities larger than the speed of light in water are able to produce Čerenkov light. Normally the energy threshold of this sort of detector has to be set very high in order to eliminate spurious signals from radioactive backgrounds. For the Kamiokande II Experiment, the threshold was initially set at 9.3MeV and then later reduced to 7.5MeV, which meant that only ^{8}B and hep neutrinos were detected.

The major backgrounds in Kamiokande II Experiment fall into three categories:

1. The dominant background comes from the β-decay of ^{214}Bi , which is a daughter nuclei of ^{222}Rn ($\tau_{1/2} = 3.8days$). Although the end point of the β spectrum from

this decay is only 3.26MeV, it is still a big problem since a 3MeV electron is able to produce the same amount of detected photons as a 7MeV electron by statistical fluctuations and the number of ^{214}Bi decays inside the detector is extremely high. The following procedures have been carried out to remove this kind of background:

- Radioactivity impurities (such as uranium) in the water of the detector were removed by water purification system.
- The water tank was sealed and made air-tight by circulating radon-free gases throughout the whole tank to balance the pressure of the outside air so that radon gas was not able to leak into the detector.
- A degasification system was installed to remove air (containing radon gas) dissolved in the water.

The above efforts reduced the trigger rates due to the β-decay of ^{214}Bi by a factor of 100.

2. γ rays from the surrounding rocks penetrate through the outer water shield to produce electrons inside the inner volume. The level of this kind of background is reduced by applying a fiducial volume cut, which limits events to the inner 680 tons of water, and a γ-ray cut which is based on the fact that γ rays from the surrounding rocks usually travel in the direction perpendicular to the wall (cut: $cos\theta_{wall} > 0.67$ where θ_{wall} is the angle between the direction of γ-ray and the normal to the nearest wall.).

3. Cosmic ray muons produce radioactive nuclei in the detector water, which ultimately lead to β decays. Spatial and temporal correlations between the β signals and the muon signals are used to reject this kind of background.

The experiment is calibrated in three ways:

1. The reaction $Ni(n, \gamma)Ni$, which produce 9MeV γ-rays, can be used as an energy calibration. The γ-rays were also collimated to provide directional information.

2. The spectrum of Michel electrons, the decay products of stopped muons, can be measured and compared with the well-known theoretical prediction.

3. The characteristic signals from the decay of short lived isotopes produced by spallation from cosmic ray muons can be modelled and compared with the data.

The ratio between the measured flux of ^{8}B neutrinos by the Kamiokande II experiment, taken from the combined samples of 450 days at electron energy threshold $E_e \geq 9.3MeV$ and 590 days at $E_e \geq 7.5MeV$, and the value predicted by the standard solar model [19] is [20]:

$$\frac{Data}{SSM} = 0.51 \pm 0.04(statistics) \pm 0.06(system) \tag{2.14}$$

which confirms the result of the chlorine experiment: there is a deficit in at least one of the solar neutrino fluxes. Figure 2.5 is a neutrino image of the sun, where the data density is highest at the center of the figure (the position of the sun). Figure 2.6 also shows a similar characteristic: the angular distribution of the detected electrons is peaked in the direction of the vector from the sun to the earth (although the number of events in the peak is only half of the value predicted by the SSM). The Kamiokande II detector is the first experiment to confirm that the detected neutrinos really come from the sun, or at least the direction of the sun. As mentioned before, the Kamiokande II experiment is able to measure the energy of the recoil electrons, which can be compared with the prediction based on the known neutrino spectrum from reaction $^8B \rightarrow^7 Be^* + e + \nu_e$. Figure 2.7 shows the ratio of the spectrum to the SSM prediction as a function of energy. The shape of the recoil electron energy agrees with the prediction although the overall number of events is down by a factor of two. The other thing worth mentioning is that within the statistical error there is no evidence from the Kamiokande II experiment that the solar neutrino signals have a significant time variation.

1036 days of data collected by the Kamiokande III experiment [21] confirms the result of the Kamiokande II experiment. The combination of results from two experiments is:

$$\frac{Data}{SSM_{BP95}} = 0.424 \pm 0.029 \pm 0.05 \tag{2.15}$$

$$\frac{Data}{SSM_{BP92}} = 0.492 \pm 0.033 \pm 0.06 \tag{2.16}$$

2.3.3 The ^{71}Ga experiments

Two ^{71}Ga experiments have been carried out to measure the flux of solar neutrinos: the SAGE (Soviet-American Gallium Experiment) and the GALLEX experiments. Both experiments use the following reaction to detect solar neutrinos:

$$\nu_e +^{71} Ga \rightarrow e^- +^{71} Ge, \quad E_{th} = 0.2332MeV \tag{2.17}$$

Figure 2.5: **The neutrino image of the sun seen by the Kamiokande II experiment.** The figure is plotted by means of neutrinos in a celestial coordinate of which the sun always sits at the center of the coordinate. The data are divided into 4deg by 4deg bins and a box is plotted, of which the size is weighted by the number of events in each bin [20].

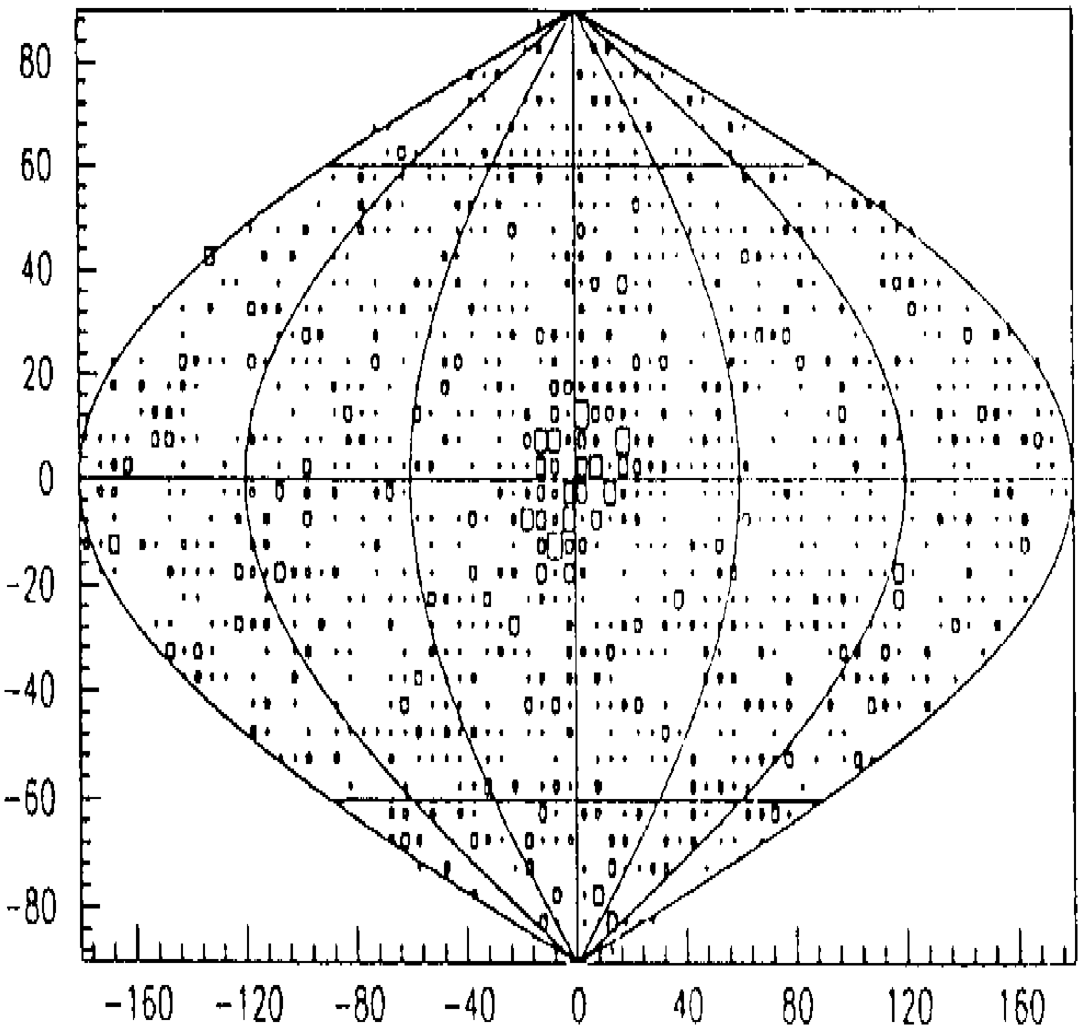

Figure 2.6: **The angular distribution of the events towards the sun. [20]. Also shown is the distribution predicted by the standard solar model.**

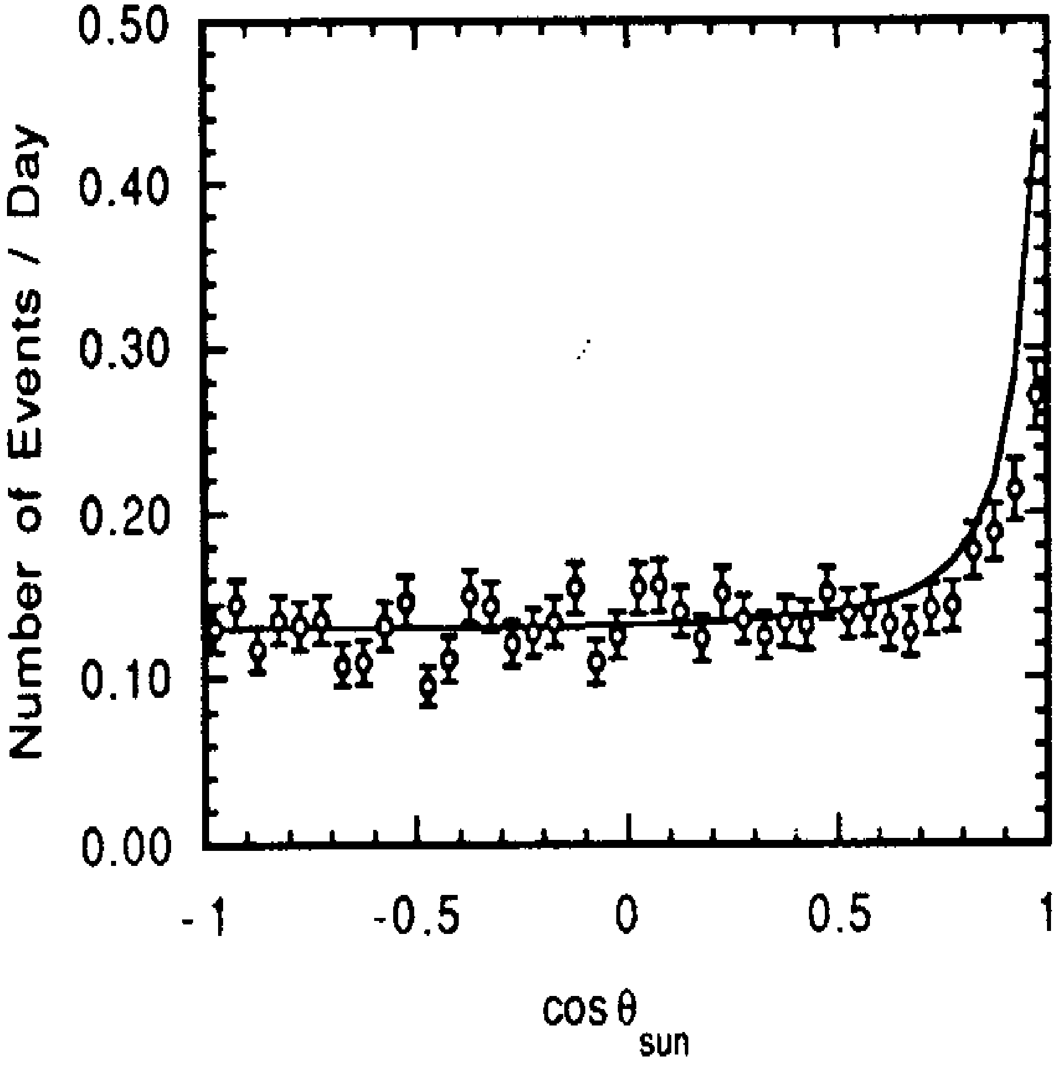

Figure 2.7: **The energy spectrum of the recoil electron detected in the Kamiokande II experiment divided by the spectrum predicted by the SSM. [20].**

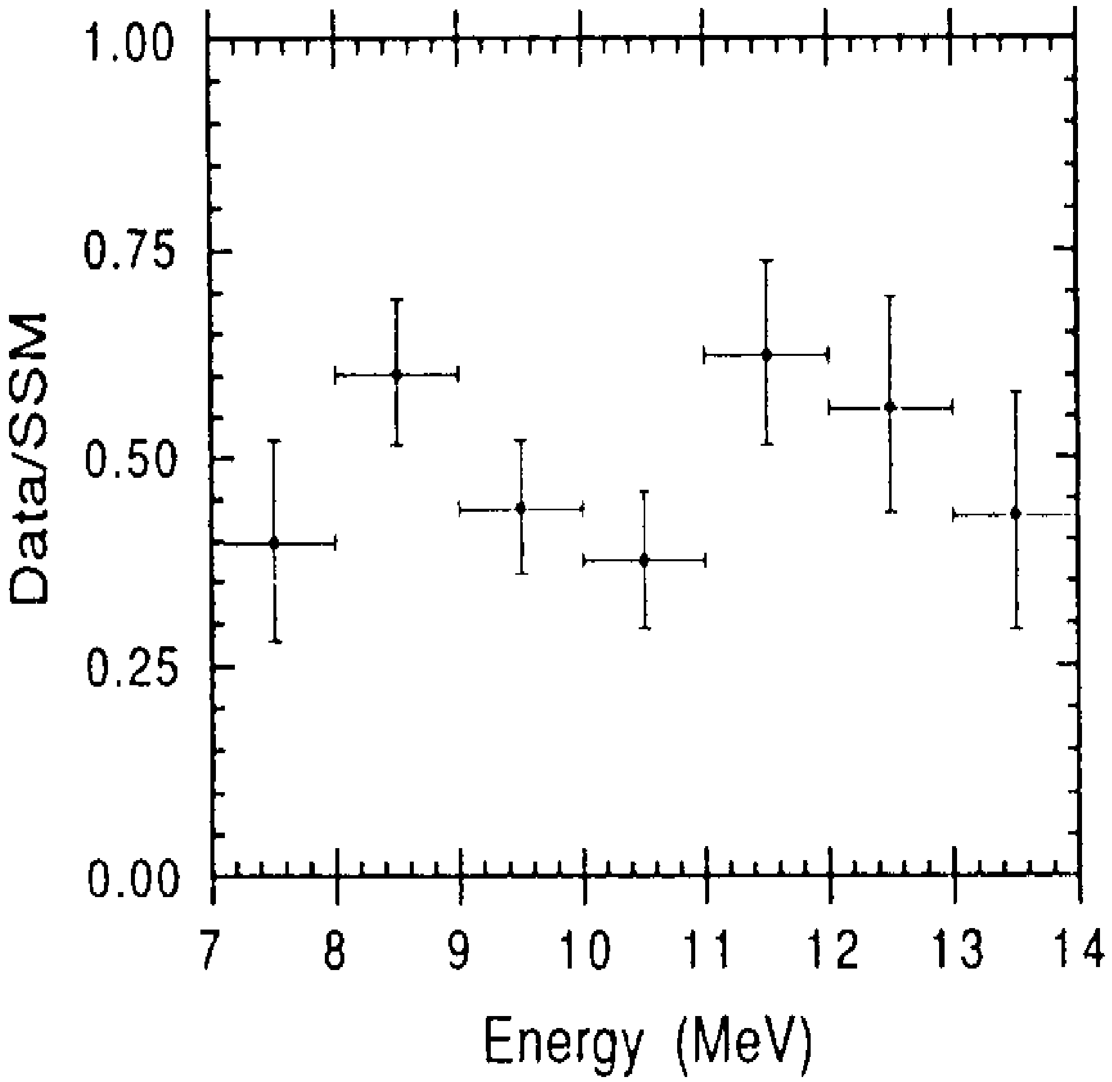

The low energy threshold enables the gallium experiments to detect all branches of solar neutrinos including the dominant pp neutrinos whose highest energy is 0.42 MeV.

Many of the techniques used by the GALLEX and SAGE experiments are similar to those used by Davis and his collaborators in the ^{37}Cl experiment. The GALLEX detector, which is placed in the Gran Sasso Underground Laboratory, consists of 30 tons of gallium in the form of a concentrated $GaCl_3 - HCl$ solution. The procedures of the experiment are:

1. At the beginning of a new run, a measured amount of stable germanium carrier ($\approx$ 1mg) is added to the detector.

2. The detector is then left for a period of usually 3 weeks. The high concentration of chloride and the acidity of the $GaCl_3 - HCl$ solution ensure that the neutrino-induced ^{71}Ge is in the form of tetrachloride ($GeCl_4$).

3. At the end of the exposure time, the volatile $GeCl_4$ is extracted by purging the solution with $1900m^3$ nitrogen gas at 20^o over 20 hours.

4. The N_2 gas stream is passed through two gas srcubbers where $GeCl_4$ gas is absorbed. After further volume reduction, the $GeCl_4$ is absorbed in tritium-free water, where $NaBH_4$ is added to produce GeH_4.

5. The GeH_4 gas, together with xenon, is introduced into small proportional counters. These counters operate within a large shielded tank inside a Faraday cage for more than 6 months, a period much longer than the half decay life of ^{71}Ge (11.43 days). The electron-capture decay of ^{71}Ge is detected by looking for the characteristic L peak (1.2 keV) and K peak (10.4 KeV) Auger electrons following the ^{71}Ge electron capture decay.

6. The overall extraction efficiency is determined by comparing the amount of germanium carrier extracted with the amount added at the beginning of the run.

The energy calibration for the proportional counters is carried out by using X-rays from cerium, which has a three line spectrum at energies of 1.03, 5.09 and 9.75keV. Possible "hot atom" effects are checked by producing ^{71}Ge in situ through the electron-capture decay of ^{71}As, which approximately reproduces the kinematics of neutrino interactions in ^{71}Ga. The result from counting the extracted ^{71}Ge atoms shows that these atoms behave in the same chemical way as the inactive germanium carrier that is added to the detector at the beginning of each run.

^{71}Ge production from non-neutrino sources is dominated by the reaction: $^{71}Ga(p,n)^{71}Ge$. The protons may be secondaries induced by cosmic-ray muons, fast neutrons, or radioactive impurities inside the detector through (α,n) followed by (n,p) reactions. The background rate due to penetrating cosmic muons is estimated to be 3.7 ± 1.1 SNU given the measured muon flux at the underground site and the relevant ^{71}Ge production cross section in the $GaCl_3$ solution determined at the CERN muon beam [22]. The contribution from spontaneous fission of internal radioactive impurities (such as U and Th) is limited to be less than 0.2 SNU by purifying the $GaCl_3 - HCl$ solution. The environmental fast neutron flux is measured and the relevant background rate is estimated to be 0.15 ± 0.10 SNU. The rate of these side reactions can be deduced by measuring the number of ^{68}Ge atoms which are produced from ^{69}Ga by (p,n) reactions and not produced by solar neutrinos in any significant level. The major background in the proportional counters comes from ^{222}Rn (with a 3.82 days half decay life), which is a ubiquitous contaminant of the air in underground laboratories. The pulse-shape analysis technique used to reject this kind of background is based on the fact that the most characteristic signature for the decay of Rn and its daughters is the delayed coincidence (164 ns) between the β decay of ^{214}Bi and the α decay of ^{214}Po.

The SAGE experiment is located in the Baksan Neutrino Observatory underneath the Mt. Andyrchi of the North Caucus region. They use 30 tons (later 57 tons) metallic gallium, instead of $GaCl_3$ solution, as the target. The advantage of the metal target is that it is less sensitive to the backgrounds induced by the radioactive impurities because of it's much larger density, smaller volume and absence of free protons. The main disadvantage is that the metal target needs a more complex extraction procedure to recover the ^{71}Ge atoms than the liquid solutions.

Both experiments have carried out the data analysis with a maximum likelihood method assuming a component decaying with a mean life of 16.49 days superimposed on a constant background (for the GALLEX experiment, a background component decaying with a 288-day half life is taken into account because of possible ^{68}Ge produced by cosmic rays when the solutions were above ground). The results for each extraction and the combined result for SAGE and GALLEX experiments are shown in figure 2.8. The results of the two experiments can be compared with the SSM prediction:

$$SAGE \quad = 74^{+13}_{-12}(stat)^{+5}_{-7}(syst)\ SNU(1\sigma)[23] \tag{2.18}$$

$$GALLEX \quad = 77.1 \pm 8.5(stat)^{+4.4}_{-5.4}(syst)\ SNU(1\sigma)[24] \tag{2.19}$$

$$Theoretical\ \ prediction \ = 137^{+8}_{-7} SNU(3\sigma) \tag{2.20}$$

Once again there is a clear deficit in the measured solar neutrino flux.

Chromium calibration sources have been used by both the SAGE and the GALLEX collaborations to check the overall values of ^{71}Ge extraction efficiency and the neutrino interaction cross section. Neutrinos with similar energies (751 keV (90%) and 426 kev (10%)) to the pp and ^{7}Be neutrinos are produced by electron-capture decay of ^{51}Cr:

$$^{51}Cr + e^- \rightarrow ^{51} V + \nu_e \tag{2.21}$$

By exposing the gallium target to this source and measuring the actual radioactivity of the source, the expected number of ^{71}Ge atoms can be deduced, given the theoretical extraction efficiency and detecting efficiency, and compared with the measured value. Both experiments express the results of this cross check as the ratio R of the measured to the expected value:

$$GALLEX \quad R = 0.92 \pm 0.08(1\sigma\ stat.\&syst.)[25] \tag{2.22}$$

$$SAGE \quad R = 0.95\underline{+}0.11 + 0.05/-0.08(1\sigma\ stat.\&syst.)[26] \tag{2.23}$$

The agreement between the predicted and the observed value gives great confidence to the gallium experiments that their results are correct and accurate.

The Superkamiokande Experiment

The Superkamiokande experiment [28], as its name suggests, is a improved version of the Kamiokande II experiment. The total mass of this detector is 50 kilotons with a fiducial mass for solar neutrinos of 22 kilotons, viewed by 11,200 50cm-diameter PMTs. The fraction of the surface covered by photosensitive material is 40%, which provides a very efficient collection of Čerenkov light and therefore sensitivity to low energy deposited in the detector. The improved PMT timing resolution enables a better rejection of cosmic ray muon spallation backgrounds relative to the Kamiokande II experiment. The hope for decrease in the energy threshold (from 7MeV to 5MeV) due to the reduced radioactive

Figure 2.8: **The solar neutrino capture rate inferred from each extraction in the SAGE [23] and GALLEX [24] experiments. Also shown is the combined result for each experiment.**

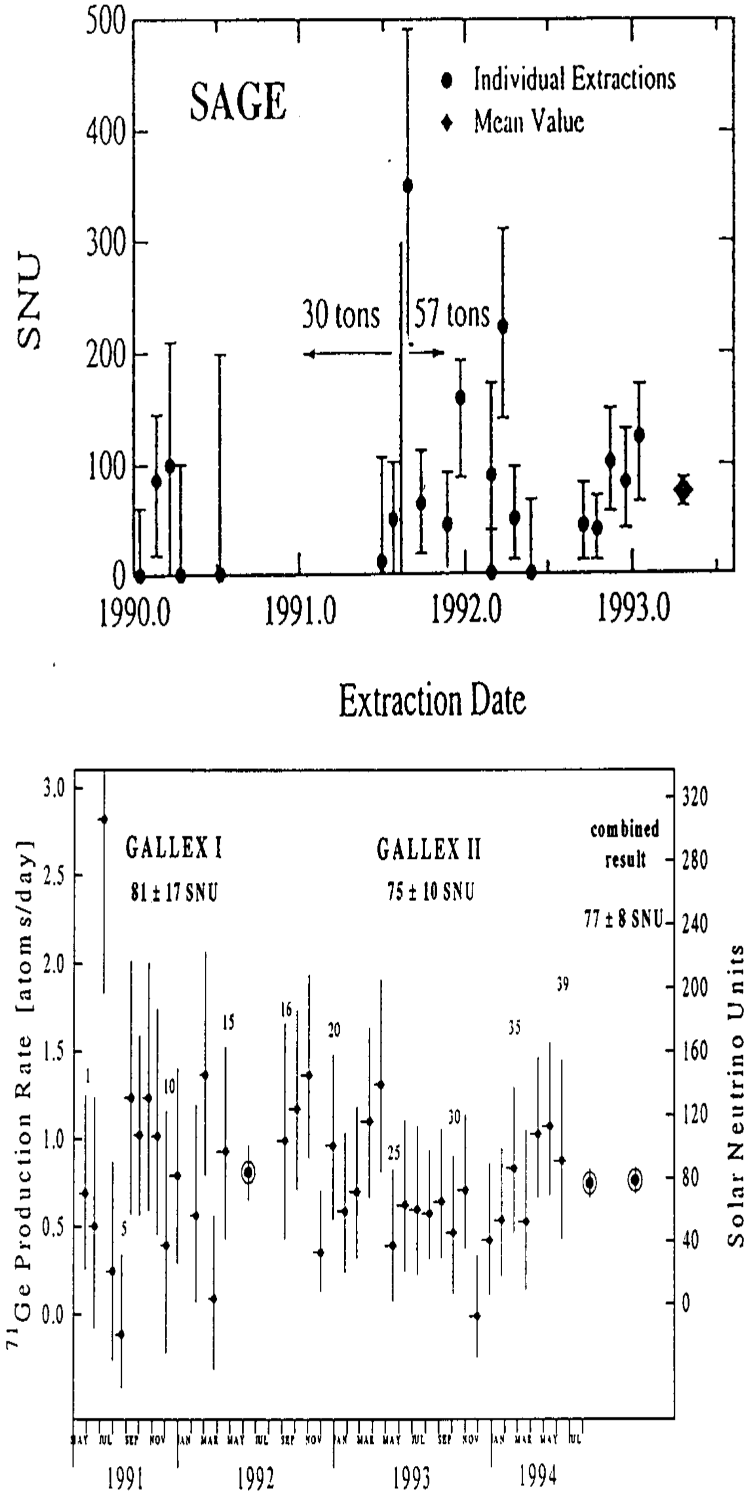

impurities in the construction materials, together with much larger fiducial volume, guarantees much higher event rates than the Kamiokande II detector. Thus a more accurate measurement of the solar neutrino spectrum is expected.

The rate of radon-induced background in the detector is reduced by a factor of 20 compared to the Kamiokande II experiment due to the introduction of low radon air to the volume above the detector tank, better sealing of the tank, and improved processing of the water entering and circulating in the tank. The muon-induced background is removed by rejecting any event occurring in a cylindrical volume (several meters in diameter) around the muon track within a certain period. A new method has been carried out to calibrate the energy response of the detector. An electron linear accelerator (LINAC) has been installed, which is able to deliver monoenergetic electrons into the detector volume at a matrix of positions. The use of this instrument reduces the uncertainties of the electron vertex and the finite width of energy spectrum coming from using other radioactive sources. The calibration data agreed with the Monte Carlo simulations within an accuracy of 1.4% in energy and the beam position and direction were in accord with the MC expectations.

The experiment has taken data since April, 1996. The first 102 days of data have been analysed and preliminary results on solar neutrinos were obtained [29]. Based on the data with energy threshold of 7 MeV, the measured ^{8}B neutrino flux was $(2.51^{+0.14}_{-0.13} \pm 0.18) \times 10^6/cm^2/sec$ [29], which was consistent with the previous result of the Kamiokande II experiment. This result can be compared with the prediction of the SSM[19]:

$$Data/SSM = 0.441^{+0.024}_{-0.023} \pm 0.032 \tag{2.24}$$

With the 102 days of data, the daytime and nighttime flux agree within statistical uncertainties. Figure 2.9 shows the detected flux of solar neutrinos as a function of the angle of the scattered electron relative to the direction of the sun. Similar to the figure from the old Kamiokande II experiment, the distribution peaks at the direction of the incoming solar neutrons and the number of events in the peak is less than half of the theoretical prediction.

The Superkamiokande experiment is taking solar neutron data at a rate of 30 times higher than that of the Kamiokande II experiment. They claimed to be able to measure the ^{8}B neutrino spectrum accurately enough to distinguish various solutions to the Solar Neutrino Problem in two years.

Figure 2.9: **Solar neutrino flux measured by the Superkamiokande experiment as a function of the angle between the direction of the scattered electron and the direction of the sun(taken from [29]).** Also shown is the prediction of the SSM (solid line) and broken line is a fit of the data.

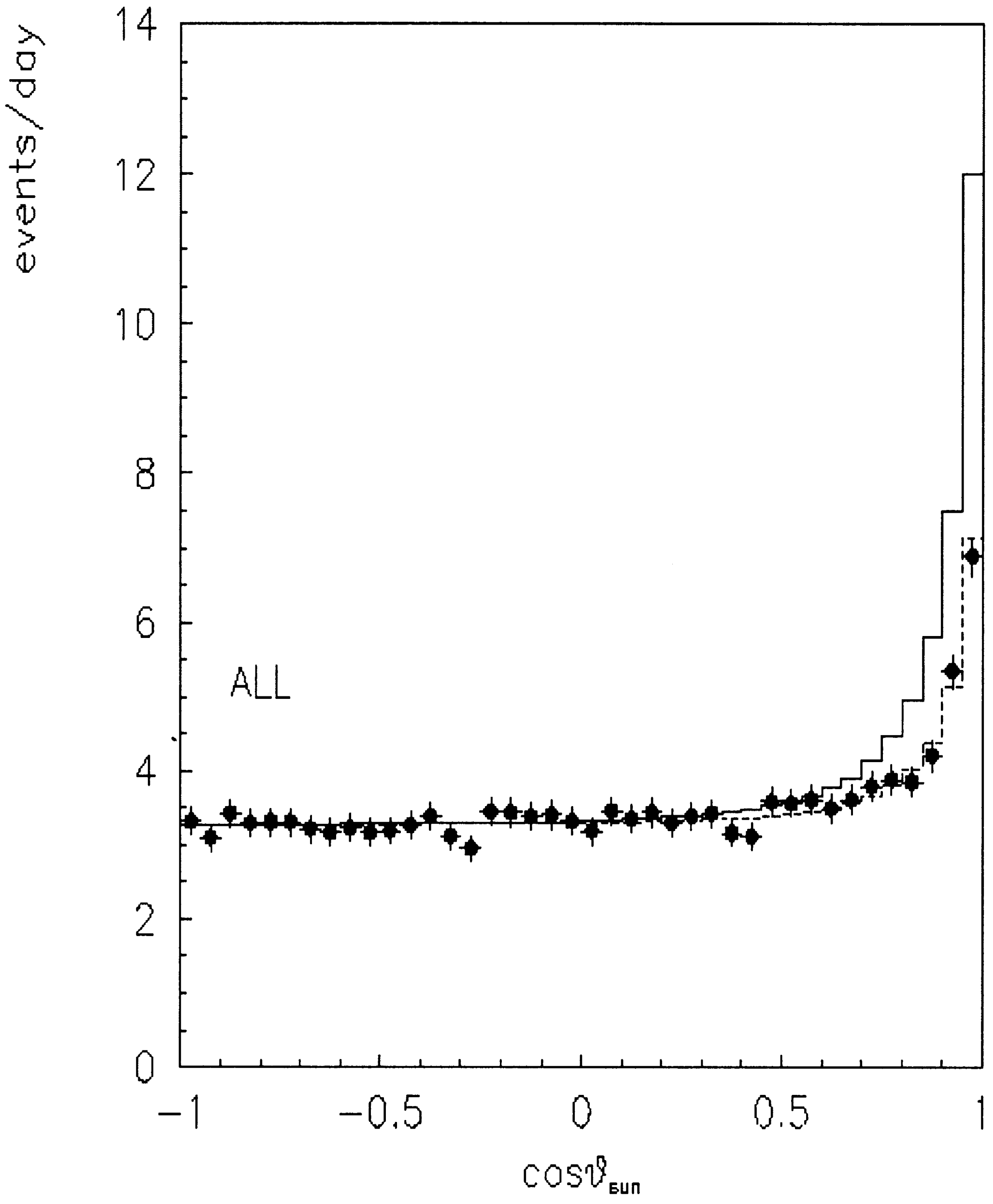

Table 2.6: **The results for four solar neutrino experiments and the corresponding ratios of the measured values to the theoretical predictions.** The experimental results are given in SNU for all of the experiments except Kamiokande, for which the result is expressed by the measured ^{8}B flux above 5 MeV in units of $cm^{-2}s^{-1}$ at the earth. The result cited for the Kamiokande experiment assumes that the shape of the ^{8}B neutrino spectrum is not affected by physics beyond the standard electroweak model. The theoretical predictions by the Standard Solar Model are taken from [19, 2]

Experiment	Result (1σ)	Expt. result/th. calculation	Refs.
Homestake	$2.55 \pm 0.17(stat.) \pm 0.18(syst.)$	0.27 ± 0.03	[13]
GALLEX	$77.1 \pm 8.5(stat.)^{+4.4}_{-5.4}(syst.)$	0.56 ± 0.07	[24]
SAGE	$69 \pm 11(stat.)^{+5}_{-7}(syst.)$	0.50 ± 0.09	[30]
Kamiokande	$(2.89^{+0.22}_{-0.21}(stat.) \pm 0.35(syst.)) \times 10^6$	0.44 ± 0.06	[20]

2.3.4 The Solar Neutrino Problem

The discrepancies between the observed rates of the four solar neutrino experiments and the values predicted by the standard solar model constitute the Solar Neutrino Problem. As shown in table 2.6, these discrepancies cannot be explained by pure statistical fluctuations.

Based on the luminosity constraint, Parke [31] presented a more powerful and clear statement of the solar neutrino problem. This argument makes the following assumptions about the sun, neutrino properties and neutrino interaction cross sections:

- The p-p solar cycle is the dominant energy source of the sun.
- The sun is in quasi-static-equilibrium, i.e., the solar luminosity a few millions years from now will be approximately the same as today.
- The neutrinos are unaffected during their propagation from production at the solar core to their destination in the terrestrial detectors.
- The neutrino interaction cross sections for the three types of experiments are correct.

Results from 3 solar neutrino experiments (data from the GALLEX and the SAGE experiments were combined together) were used to fit the two parameters , $\psi^{^8B}$ and $\psi^{^7Be}$ which are ratios between true neutrino fluxes and fluxes predicted by [2], under

Table 2.7: **Minima of χ^2 for $\psi^{^7Be} \geq 0$ and the value of $\psi^{^8B}$ at the minimum in Parke's analysis [31].** All four minima occur along $\psi^{^7Be} = 0$.

Experiments taken into account	χ^2_{min}, $\psi^{^7Be} \geq 0$	$\psi^{^8B}$
Cl + H_2O + Ga	2.5	0.43
Cl + H_2O	1.4	0.44
Cl + Ga	1.0	0.41
H_2O + Ga	1.3	0.50

the hypothesis mentioned above. The χ^2 values are calculated for four cases: all three experimental results taken into account together and the three ways of choosing two out of three results. Since value of $\psi^{^7Be}$ at the minimum value of χ^2 is negative for all four cases, the additional constraint $\psi^{^7Be} \geq 0$ is imposed. Table 2.7 contains the minimum value of χ^2 with this constraint, which all occur along $\psi^{^7Be} = 0$, as well as the value of $\psi^{^8B}$. Even at the minimum, χ^2 value is larger than the number of degrees of freedom (For the fitting with 3 experimental results, the degree of freedom = 3 data - 2 parameters = 1: while for fittings with 2 experimental results, the degree of freedom = 2 data - 2 parameters =0).

Figure 2.10 shows the iso-contour plots of χ^2 as a function of $\psi^{^7Be}$ and $\psi^{^8B}$ for the four cases, also shown are the predictions by three different solar models: Bahcall-Pinsonneault's SSM, Turck-Chiéze-Lopes's SSM and a *ad hoc* solar model with a decreased solar core temperature. The standard models of Bahcall-Pinsonneault and Turck-Chiéze-Lopes are excluded by at least 5σ independent of which set of experimental data are used in the analysis, even the *ad hoc* solar model is excluded by around 2σ. Again the discrepancies between the observed rates and the theoretical predictions are significant.

Bahcall presents a similar argument in [16], where both pep and CNO neutrinos are taken into account. The result of the chlorine experiment is:

$$Rate\ \ Cl\ \ (observed) = (2.55 \pm 0.17(stat.) \pm 0.18(syst.))\ \ SNU[13] \tag{2.25}$$

The observed rate due to ^{8}B neutrinos can be deduced from the Kamiokande data (assuming the energy spectrum of these neutrinos is not distorted) :

$$Rate\ \ Cl(^8B) = (3.2 \pm 0.23(stat.) \pm 0.39(syst.))\ \ SNU \tag{2.26}$$

Subtracting equation 2.26 from equation 2.25, one finds that the best estimate for the

Figure 2.10: **The results of fitting the ^{7}Be and ^{8}B neutrino fluxes using (Top Left) all three experimental results, (Top Right) only the chlorine and water results, (Bottom Left) only the chlorine and gallium results, and (Bottom Right) only the water and gallium results. See the text for details (taken from [31]).**

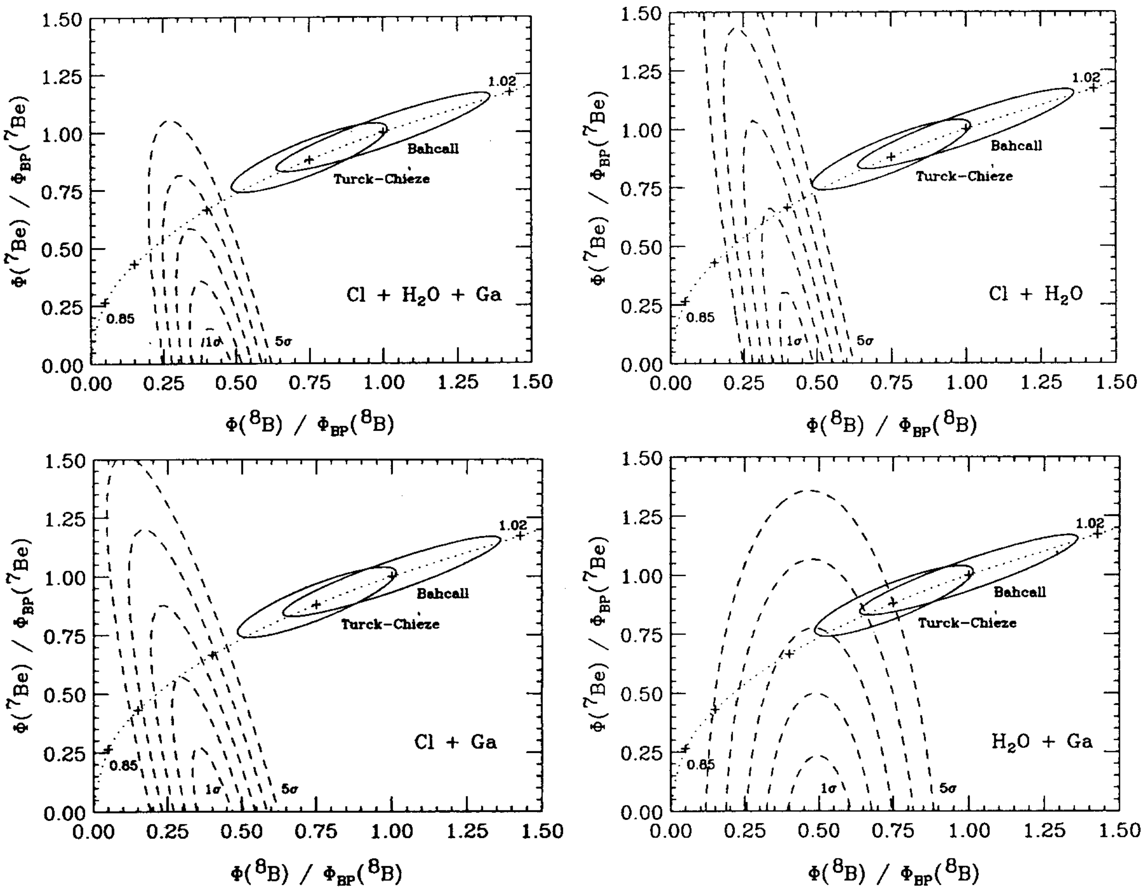

capture rate in the chlorine experiment from all source except ^{8}B neutrinos is:

$$Rate\ \ Cl\ \ Obs.(pep +^7 Be + CNO) = (-0.66 \pm 0.52)\ \ SNU \tag{2.27}$$

$$Rate\ \ Cl\ \ Obs.(pep +^7 Be + CNO) \leq 0.68\ \ SNU\ (at\ \ 95\%\ \ C.f.) \tag{2.28}$$

which is much smaller than the theoretical prediction by the SSM for contributions solely from ^{7}Be neutrinos:

$$Rate\ \ Cl\ \ Theo.(^7Be) = (1.1 \pm 0.1)\ \ SNU\ (3\sigma\ error) \tag{2.29}$$

The results of the Kamiokande and the gallium experiments are compared in the similar way to get the capture rate in the gallium detector due to ^{7}Be solar neutrinos:

$$Rate\ \ Ga\ \ Obs.(^7Be) \leq 19\ \ SNU\ (at\ 95\%\ confidence\ level) \tag{2.30}$$

while the predicted rate by the SSM is:

$$Rate\ \ Ga\ \ Theo.(^7Be) = (34 \pm 4)\ \ SNU\ (3\sigma\ error) \tag{2.31}$$

The incompatibility between equation 2.30 and 2.31 is another quantitative expression of the solar neutrino problem.

2.4 Possible Solutions to the Solar Neutrino Problem

The discrepancies between the experimental results and the theoretical predictions as described in the previous section lead to at least one of the following hypotheses:

1. The standard solar model is wrong: the sun in fact produces many fewer neutrinos than predicted.

2. At least three out of the five existing solar neutrino experiments are wrong.

3. Something happens to solar neutrinos on the way from the solar core to the terrestrial detectors.

Possible solutions to the solar neutrino problem are based on these 3 hypotheses.

Table 2.8: **Neutrino Rates predicted by 10 recent standard solar models.** The entries are in SNU. The two entries from Bahcall and Pinsonneault 1992 refer to models computed with and without helium diffusion respectively [16].

Source	Cl		Ga	
	pep	^{7}Be	pp + pep	^{7}Be
Bahcall and Ulrich 1988	0.22	1.13	74	34
Sackman et al. 1990	0.21	1.02	74	31
Bahcall and Pinsonneault 1992	0.23	1.11	74	34
Bahcall and Pinsonneault 1992	0.23	1.17	74	36
Bahcall and Pinsonneault 1995	0.22	1.24	74	36
Castellani et al. 1994	0.22	1.10	75	36
Turck Chiéze and Lopes 1993	0.22	1.02	74	31
Berthomieu et al. 1993	0.22	1.07	73	33
Castellani et al. 1994	0.22	1.18	74	36
Kovetz and Shaviv 1994	0.22	1.18	74	36
Proffitt 1994	0.22	1.24	73	38
Christensen-Dalsgaard 1994	0.23	1.12	74	34

2.4.1 Astrophysical Solution

The standard solar model reproduces every measurable solar quantity, except the neutrino fluxes, to a considerable accuracy. Most notable is the solar oscillation frequencies, for which the latest SSM [2] predicts values that are in exceptional agreement with the helioseismology data [32]. Table 2.8 gives the theoretical capture rate in the chlorine and gallium experiments predicted by 10 recently-published solar models. All of these calculations lie within a range of $\pm 10\%$ of the average value. Since these models are constructed by different physicists independently, the agreement between the results give us confidence that there are not any significant computational errors in the standard solar model.

An alternative way in which standard solar models may be flawed is that the physical assumptions used in these models may be wrong. This would lead to so called non-standard solar models. Almost all of these non-standard solar models rely on non-standard physics to decrease the solar core temperature since lower temperature makes the penetration of the Coulomb barrier in the p-p chain fusion reactions (especially ${}^7Be(p,\gamma)^8B$) more difficult and thus decreases the reaction rates and solar neutrino fluxes. Thus low Z or low opacity models smooth the temperature distribution inside the sun; strong magnetic field or rapid rotation models alter the equation of hydrostatic equilibrium, inducing turbulent diffusion and thermal instabilities in the solar core; WIMPs (Weakly Interacting Massive Particles) models use a new type of particles to remove energy from the center of the sun. The unfamiliar physical assumptions used in constructing these non-standard solar models alone make these models unfavorable. However, the fatal weakness of these non-standard models is that almost all of them predict a greater reduction of the ^{8}B neutrino flux than the ^{7}Be neutrino flux since the decay of ^{8}B follows the reaction $p +^7 Be \rightarrow^8 B + \gamma$. Any reduction of the ^{7}Be production rate affects both the ^{7}Be and ^{8}B neutrino fluxes equally. As described in the previous section, the solar neutrino problem is not only the deficit of total solar neutrino flux but also the larger suppression of ^{8}B neutrino flux relative to the suppression of ^{7}Be neutrino flux. Figure 2.11 is a clear demonstration of the incompatibility between non-standard solar models and solar neutrino data. The first hypothesis mentioned in page 34, which implies doubt about the validity of the standard solar model, is at least not convincing. The Problem of ${}^7Li$ depletion in SSMs (the abundance of ${}^7Li$ on the solar surface predicted by SSMs is 100 times higher than the observed value) seems to be solved by introducing element segregation and rotation-induced mixing to the solar models [33].

Recently a new nonstandard solar model circumvented the above T_c argument by allowing large ${}^3He$ mixing in the sun [35]. In this model, a large quantity of ${}^3He$ is transported from large radius region into small radius region where the equilibrium of the pp chain is broken. The rate of ${}^3He({}^3He,2p)\alpha$ reaction is quadratically dependent on the abundance of ${}^3He$ while the rate of ${}^3He(\alpha,\gamma)^7Be$ reaction is only linearly dependent on it. Thus the rate of pp chain terminations which produce 2 pp neutrinos relative to terminations which produce ^{7}Be and ^{8}B neutrinos is increased in direct proportional to the ${}^3He$ excess. This leads to a suppression of both ^{7}Be and ^{8}B neutrinos relative to the pp neutrinos. However, short-lived ^{7}Be is produced in the small r region, where the ambient temperature is higher than the value in SSMs. This leads to a suppressed value of $\phi({}^7Be)/\phi({}^8B)$. T_c (the average solar core temperature) in this model is lower than that of the SSM in order to meet the luminosity constraint. The validity of this model is not proved and strange phenomena it described (such as special geometry required to

Figure 2.11: **The experimental data compared with the predictions by nonstandard solar models [34]** The allowed region from the combined fit of the Kamiokande, Homestake, and gallium experimental results at 90, 95, and 99% C.L. allowing (unphysical) negative values for $\phi(Be)$. For $\phi(Be) \geq 0$, $\chi^2 = 4.8$ for the best fit, and the standard model is excluded at 97% C.L. for 1 degree of freedom. Also shown are various nonstandard solar models and the power laws of the central temperature (T_c) and the pp cross section (S_{11}) obtained from Bahcall-Ulrich's SSM [3], and extrapolated from the SSM region. All nonstandard models other than WIMP's can be approximately parameterized by T_c or S_{11}. The error bars show the uncertainty of $\phi(B)$ due to the $p+^7Be$ cross section [19]

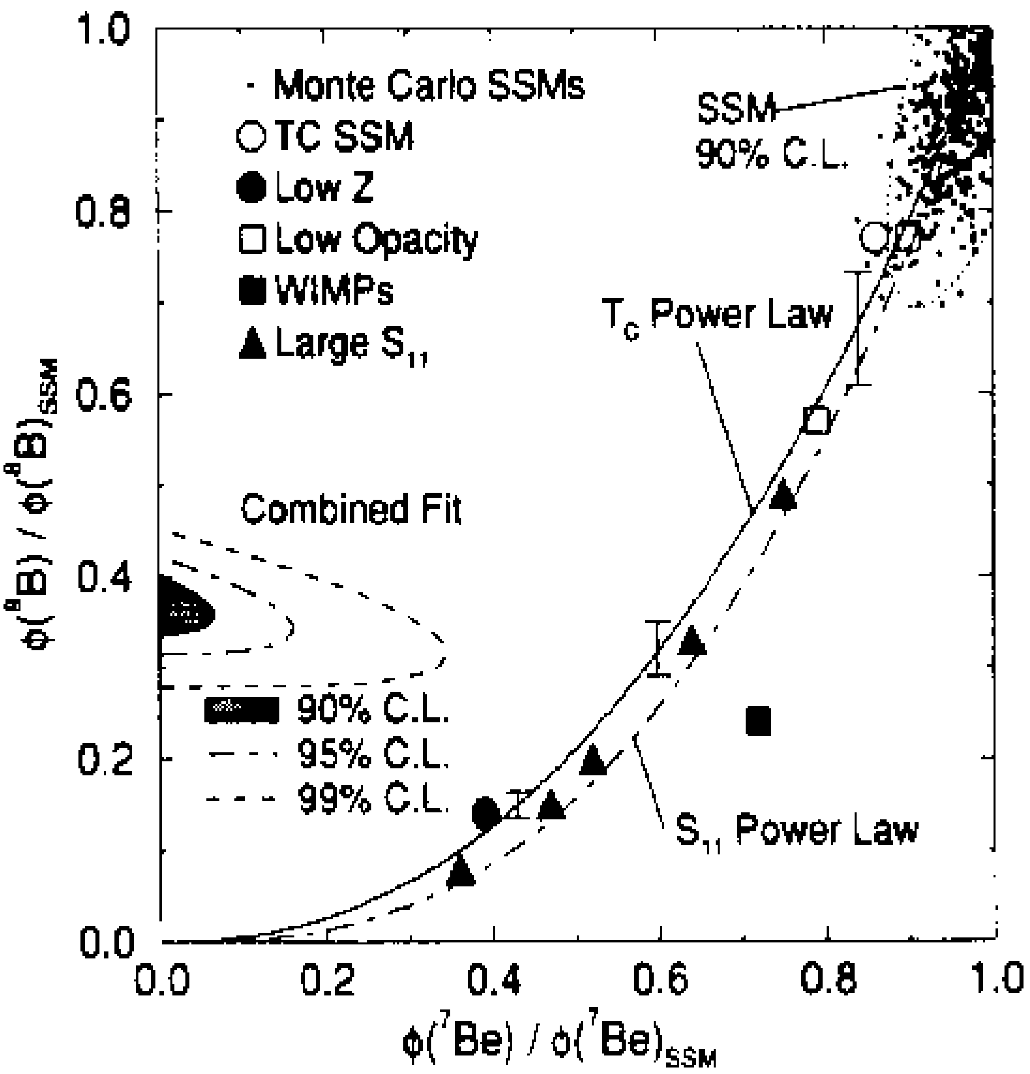

Figure 2.12: **The combined fit when the Homestake experimental error is tripled [34].**

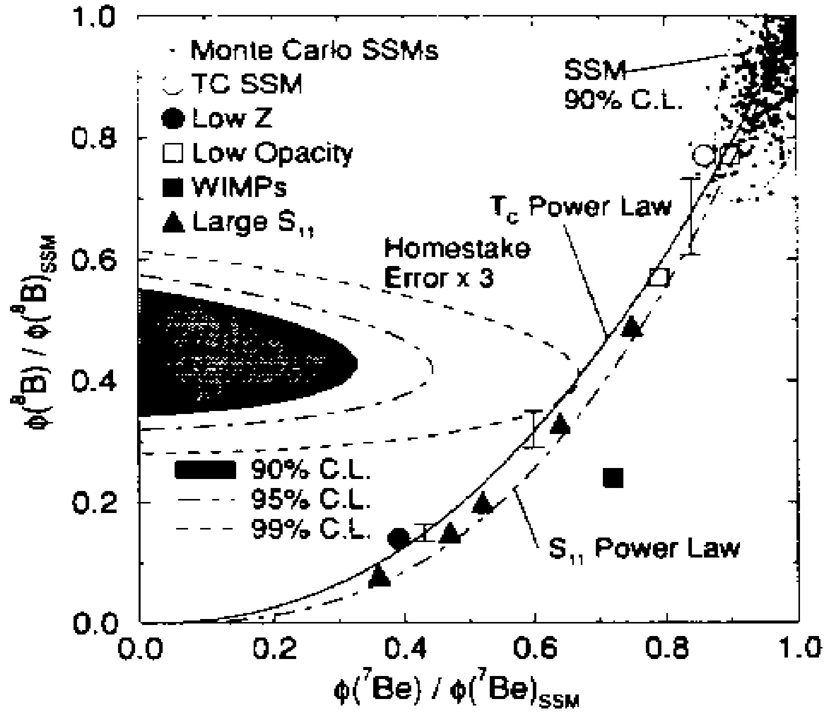

transport ^3He) seemed not to be consistent with the standard model of stellar evolution and the data from helioseismology. In any case the predicted fluxes are still ruled out by the data at $> 2\sigma$ level.

The second hypothesis requires that at least three out of five existing solar neutrino experiments are wrong. Although all five experiments are ground breaking and exceptionally difficult, they have been subject to exhaustive cross checks (such as calibration sources) and it is unlikely that three out of five experiments give wrong results. Even if some experiments underestimate their errors, the data still strongly disfavor both standard and non-standard solar models, as shown in figure 2.12 and 2.13 where the experimental errors are enlarged.

If the data strongly disfavor the first two hypotheses mentioned on page 34, we must look at the third hypothesis seriously for solutions to the solar neutrino problem. A number of mechanisms have been proposed to fulfill this hypothesis. If neutrinos decay, then this could lead to a deficit in the observed rate [27]. However, this mechanism requires new particles and/or new interactions which are not familiar and is ruled out by the data of SN1987a. If neutrinos had a large magnetic moment, then left-handed neutrinos produced in the solar core could be flipped into right-handed neutrinos by the solar magnetic field

Figure 2.13: **The combined fit when the detector cross section uncertainties are tripled from 3.3% (Homestake) and 4% (gallium) [34].**

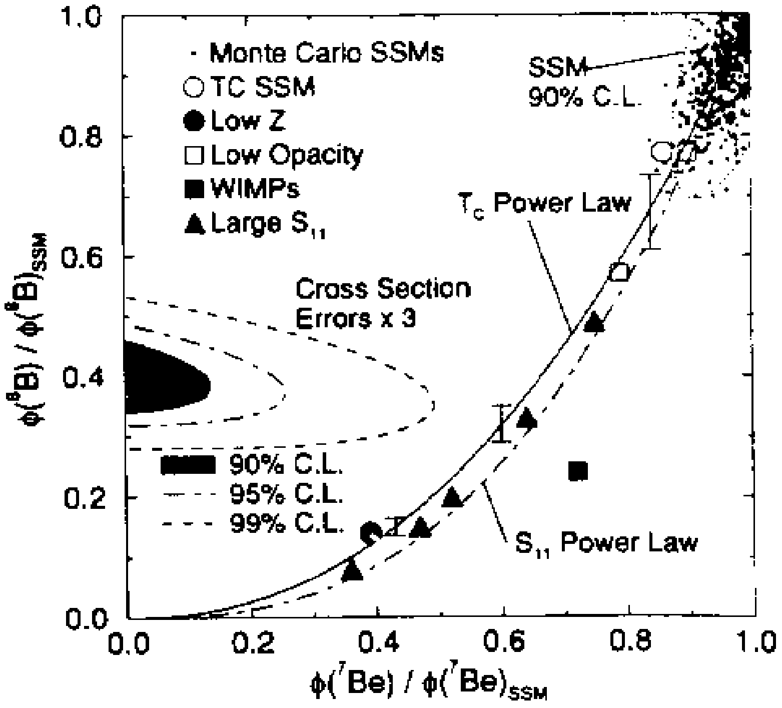

and so become invisible to terrestrial detectors. This mechanism requires a neutrino magnetic moment ($(0.3-1)\times 10^{-10}$ μ_B), which is much larger than the value predicted by conventional models and just under the experimental limit: 2×10^{-10} μ_B, as well as a large solar magnetic field.

A plausible solution to the solar neutrino problem involves neutrino oscillations, where electron neutrinos produced in the solar core oscillate into other flavors of neutrinos which are not detectable in the existing experiments (the Kamiokande experiment is able to detect the electron scatterings of muon or tau neutrinos, but can not distinguish them from ν_e scatterings). The next section describes neutrino oscillations in vacuum. Although it is unlikely to be a solution to the problem itself, the description of this mechanism is needed in order to understand the physics behind matter-enhanced neutrino oscillations, which are now widely accepted as the most favored solution to the solar neutrino problem.

2.4.2 Vacuum Oscillations

In the standard model of electroweak interaction, neutrinos are assumed to be purely left-handed and massless. However, there is no underlying reason for this assumption.

The standard model, with its numerous arbitrary parameters, is considered by many physicists as the low energy limit of a more complete theory. In many such theories, neutrinos have mass. If neutrinos are massive, then their weak interaction eigenstates, which are coupled to charged leptons, may not be same as their mass eigenstates, which are propagation eigenstates and diagonalize the free Hamiltonian. The wave function of a certain electroweak interaction eigenstate could be expanded in terms of wave functions of mass eigenstates. Different mass eigenstates move with different speeds (it is assumed here for clarity that all mass eigenstates have the same momentum, physical results are not changed when this assumption is not included[36].), thus the relative phases of the expansion coefficients vary with time. Depending upon the time of observation, the original electroweak interaction eigenstate has more or less probability of being detected as a different electroweak interaction eigenstate. A extensive review of vacuum oscillation theory can be found in [37].

The basic physics of vacuum oscillations can be understood by studying only two flavors of neutrinos: ν_e and ν_x (ν_x could be ν_μ or ν_τ). As mentioned before, the flavor eigenstates can be expressed in terms of the mass eigenstates. For two flavors, this requires a two-dimension orthogonal matrix U_v:

$$\begin{pmatrix} |\nu_e\rangle \\ |\nu_x\rangle \end{pmatrix} = U_v \begin{pmatrix} |\nu_1\rangle \\ |\nu_2\rangle \end{pmatrix} = \begin{pmatrix} cos\theta_v & sin\theta_v \\ -sin\theta_v & cos\theta_v \end{pmatrix} \begin{pmatrix} |\nu_1\rangle \\ |\nu_2\rangle \end{pmatrix} \tag{2.32}$$

where θ_v is called the vacuum mixing angle, $|\nu_e\rangle$ and $|\nu_x\rangle$ are wave functions for neutrino electroweak interaction eigenstates while $|\nu_1\rangle$ and $|\nu_2\rangle$ are wave functions for neutrino mass eigenstates. The Schrödinger equation describes the propagation of the neutrino mass eigenstate in vacuum:

$$E\,|\nu\rangle = H\,|\nu\rangle = i\frac{d\,|\nu\rangle}{dt} \tag{2.33}$$

The solution to this equation can be written as:

$$\begin{pmatrix} |\nu_1(t)\rangle \\ |\nu_2(t)\rangle \end{pmatrix} = \begin{pmatrix} e^{-iE_1 t} & 0 \\ 0 & e^{-iE_2 t} \end{pmatrix} \begin{pmatrix} |\nu_1(0)\rangle \\ |\nu_2(0)\rangle \end{pmatrix} \tag{2.34}$$

where E_1 and E_2 are the eigenvalues for two mass eigenstates respectively. The probability for an electron neutrino to remain as an electron neutrino after propagating through vacuum for a period time of t, $(\langle\nu_e(t)|\nu_e(0)\rangle)^2$, is:

$$\begin{aligned}&\left((1\ \ 0)\ U_v^{+}\begin{pmatrix} e^{-iE_1t} & 0 \\ 0 & e^{-iE_2t}\end{pmatrix} U_v \begin{pmatrix}1\\0\end{pmatrix}\right)^2 \\ &= 1 - \overset{2}{sin}2\theta_v \overset{2}{sin}[(\ E_2 - E_1)t/2]\end{aligned} \tag{2.35}$$

In the ultrarelativistic approximation,

$$E_2 - E_1 = \frac{m_2^2 - m_1^2}{2E} = \frac{\triangle m^2}{2E} \tag{2.36}$$

where m_1 and m_2 are rest masses of the states ν_1 and ν_2. Equation 2.35 may be rewritten in the following form that appears frequently in the literature:

$$|\,\langle\nu_e|\nu_e\rangle_t\,|^2 = 1 - \overset{2}{sin}2\theta_v \overset{2}{sin}(\frac{\pi R}{L_v}) \tag{2.37}$$

where R is the distance travelled by neutrino in a time t, and $L_v = 4\pi E/\triangle m^2$, which is called the vacuum oscillation length. Because the distance between the sun and the earth is large, solar neutrino experiments are sensitive to small mass differences for which the argument $\frac{\pi R}{L_v}$ can significantly affect the probability of observing an electron neutrino in terrestrial detectors. The minimum mass difference squared, $\triangle m^2_{solar}$, that can be studied with solar neutrinos is:

$$\triangle\, m^2_{solar} = 1.6 \times 10^{-12}(\frac{E}{1MeV})\ ev^2\ \ (assuming\ \ \frac{\pi R}{L_v} = 0.3) \tag{2.38}$$

which is many orders of magnitude smaller than the value probed in terrestrial experiments.

The extension of vacuum oscillations from 2 flavor states to 3 or more flavor states is straightforward. The relation between the electroweak interaction eigenstate $|\nu_\alpha\rangle$ and the mass eigenstate $|\nu_j\rangle$ can be written as:

$$|\nu_\alpha\rangle = \sum_j U_{\alpha j}\,|\nu_j\rangle \tag{2.39}$$

where $U_{\alpha j}$ is the element of a transformation matrix similar to the Cabibbo-Kobayashi-Maskawa matrix in the quark sector. The probability for $|\nu_\alpha\rangle$ to oscillate into $|\nu_\beta\rangle$ after a certain time of t can be deduced as follows:

$$|\nu_\beta(t)\rangle = \sum_j U_{\beta j} exp(-iE_j t)\,|\nu_j\rangle \tag{2.40}$$

$$\langle\nu_\beta(t)|\nu_\alpha(0)\rangle = \sum_j U_{\alpha j}U^*_{\beta j} exp(iE_j t) \tag{2.41}$$

$$|\langle\nu_\beta(t)|\nu_\alpha(0)\rangle|^2 = \sum_{j,k} U_{\alpha j}U^*_{\beta j}U^*_{\alpha k}U_{\beta k}exp(-i(E_k - E_j)t) \tag{2.42}$$

In order to calculate capture rates for experiments, the survival probability of a solar neutrino must be averaged over the neutrino energy spectrum, the region of emission in the sun, and the region of absorption in the earth (the distance from the sun to the earth depends upon the time of year). For typical solar neutrino applications, these averages cause the oscillating terms in equation 2.42 to cancel out for $j \neq k$ [38]. Thus the survive probability for a certain flavor of neutrino is:

$$|\langle\nu_\alpha(t)|\nu_\alpha(0)\rangle|^2_{average} = \sum_i |U_{\alpha i}|^4 = \sum_i X_i^2 \quad (X_i = |U_{\alpha i}|^2) \tag{2.43}$$

The condition that the total probability is conserved is enforced by introducing a Lagrangian multiplier, λ. With the total probability conserved, the minimum probability for a ν_α to remain as a ν_α is found by minimizing the function F, where

$$F = \sum_i X_i^2 + \lambda(\sum_i X_i - 1) \tag{2.44}$$

The function is minimized when all of X_i are equal:

$$X_i = \frac{\lambda}{2} = \frac{1}{N}, \quad F_{min} = \frac{1}{N} \tag{2.45}$$

where N is the total number of neutrino flavors. Since only 3 flavors of neutrinos have been observed, normally

$$|\langle\nu_e(t)|\nu_e(0)\rangle|^2_t \geq \frac{1}{N} = \frac{1}{3} \tag{2.46}$$

Thus in the case of vacuum oscillation, the maximum suppression of solar neutrino flux is a factor of 3. This is sufficient, but only barely, to explain the observed rate in the chlorine experiment if the mixing angle is large, which is not seen in the CKM matrix. Meanwhile, in order to achieve the energy-dependent suppression of solar neutrino fluxes observed by experiments, $\triangle m^2$ must be carefully chosen ($2 \times 10^{-12} eV^2 < \triangle m^2 < 4 \times 10^{-10} eV^2$)so that L_v is at the same magnitude of R (distance from the sun to the earth). The fine tuning of $\triangle m^2$ and the large value of θ_v disfavor vacuum oscillations as a solution to the solar neutrino problem.

2.4.3 Matter Enhanced Oscillations

In 1986, based on the previous work of Wolfenstein [39], Mikheyev and Smirnov ([40, 41]) pointed out that the oscillations between different flavors of neutrinos can be maximal in matter even when the vacuum mixing angle is small. As in vacuum oscillations, the physics of matter enhanced oscillations(or the MSW affect, named after its founders) is easily understood in the case of only two flavors of neutrinos (assumed to be ν_e and ν_x).

Assuming the speed of a neutrino is constant, equation 2.33, which governs the propagation of neutrino mass eigenstates in vacuum, can be rewritten as:

$$i\frac{d}{dx}\begin{pmatrix} |\nu_1\rangle \\ |\nu_2\rangle \end{pmatrix} = \begin{pmatrix} E_1 & 0 \\ 0 & E_2 \end{pmatrix}\begin{pmatrix} |\nu_1\rangle \\ |\nu_2\rangle \end{pmatrix} \tag{2.47}$$

where ν_1 and ν_2 are two mass eigenstates respectively and x is the distance travelled by the neutrino. In the ultra-relativistic case, $E_1 \approx p + \frac{m_1^2}{2p}$, $E_2 \approx p + \frac{m_2^2}{2p}$, where p is the neutrino's momentum. By leaving out a unit matrix times p, which only changes the overall state vector by a phase and does not affect the probability amplitude, we can change equation 2.47 to:

$$i\frac{d}{dx}\begin{pmatrix} |\nu_1\rangle \\ |\nu_2\rangle \end{pmatrix} = \frac{1}{2E}\begin{pmatrix} m_1^2 & 0 \\ 0 & m_2^2 \end{pmatrix}\begin{pmatrix} |\nu_1\rangle \\ |\nu_2\rangle \end{pmatrix} \tag{2.48}$$

Using equation 2.32, equation 2.48 can be expressed on the basis of electroweak interaction eigenstates :

$$i\frac{d}{dx}\begin{pmatrix} |\nu_e\rangle \\ |\nu_x\rangle \end{pmatrix} = \frac{1}{2E}\left[U_v\begin{pmatrix} m_1^2 & 0 \\ 0 & m_2^2 \end{pmatrix}U_v^+\right]\begin{pmatrix} |\nu_e\rangle \\ |\nu_x\rangle \end{pmatrix} \tag{2.49}$$

where U_v is the vacuum transformation matrix between mass and electroweak interaction eigenstates.

Analogous to equation 2.49, the equation governing neutrino propagation in matter can be written as:

$$\begin{aligned} i\tfrac{d}{dx}\begin{pmatrix} \nu_e \\ \nu_x \end{pmatrix} &= \tfrac{1}{2E}\left[U_v\begin{pmatrix} m_1^2 & 0 \\ 0 & m_2^2 \end{pmatrix}U_v^+ + \begin{pmatrix} A & 0 \\ 0 & 0 \end{pmatrix}\right]\begin{pmatrix} \nu_e \\ \nu_x \end{pmatrix} \\ &= \tfrac{1}{2E}M^2\begin{pmatrix} \nu_e \\ \nu_x \end{pmatrix} \end{aligned} \tag{2.50}$$

The new term $\begin{pmatrix} A & 0 \\ 0 & 0 \end{pmatrix}$ in the right side of equation 2.50 is due to the unique charged current (CC) interaction between the electron neutrino and ambient electrons (the muon density in the sun is much smaller than the electron density, so the CC interaction between ν_μ and μ can be ignored.). The form of this new term was first derived by Wolfenstein as:

$$A = 2\sqrt{2}G_F N_e E = 2\sqrt{2}G_F(Y_e/m_n)\rho E \tag{2.51}$$

where G_F is the Fermi constant, ρ is the matter density, Y_e is the number of electrons per nucleon and m_n is the nucleon mass. The matrix M^2 can be explicitly calculated as [42]:

$$M^2 = \frac{1}{2}\left[(\sum + A) + \begin{pmatrix} A - \triangle C_{2\theta} & \triangle S_{2\theta} \\ \triangle S_{2\theta} & -A + \triangle C_{2\theta} \end{pmatrix}\right] \tag{2.52}$$

where $\sum = m_1^2 + m_2^2$, $\triangle = m_2^2 - m_1^2$, $C_{2\theta} = cos(2\theta)$, and $S_{2\theta} = sin(2\theta)$ (θ is neutrino's vacuum mixing angle). The part of the mass matrix M^2 that is proportional to the unit matrix has been pulled out. M^2 can be diagonalized to find the instantaneous mass eigenvalues (the reason that they are not called mass eigenvalues is discussed later.):

$$U_m^+ M^2 U_m = \begin{pmatrix} M_1^2 & 0 \\ 0 & M_2^2 \end{pmatrix} \tag{2.53}$$

where

$$M_{2,1}^2 = \left[(\sum + A) \pm \left[(A - \triangle C_{2\theta})^2 + (\triangle S_{2\theta})^2\right]^{1/2}\right]/2$$

The neutrino mixing matrix in matter, U_m, can be parameterized analogously to the corresponding mixing matrix in vacuum given in equation 2.32:

$$\begin{pmatrix} |\nu_e\rangle \\ |\nu_x\rangle \end{pmatrix} = U_m \begin{pmatrix} |\nu_1^m\rangle \\ |\nu_2^m\rangle \end{pmatrix} = \begin{pmatrix} cos\theta_m & sin\theta_m \\ -sin\theta_m & cos\theta_m \end{pmatrix} \begin{pmatrix} |\nu_1^m\rangle \\ |\nu_2^m\rangle \end{pmatrix} \tag{2.54}$$

where ν_1^m and ν_2^m are two instantaneous mass eigenstates in matter, θ_m is the neutrino mixing angle in matter and is given by:

$$tan2\theta_m = \triangle sin2\theta_v/(-A + \triangle cos2\theta_v) \tag{2.55}$$

or:

$$\overset{2}{sin}2\theta_m = (\triangle sin2\theta_v)^2/[(A - \triangle cos2\theta_v)^2 + (\triangle sin2\theta)^2] \tag{2.56}$$

The most important feature of matter enhanced oscillation is shown in equation 2.56: when $A \to 0$, then $\theta_m \to \theta_v$ and the mixing matrix is just the vacuum expression; when $A \gg \triangle$, then $\theta_m \to \frac{\pi}{2}$; when $A = \triangle cos2\theta_v$, then $sin2\theta_m = 1$ and neutrino mixing is maximized regardless of the value of θ_v.

For a constant-density medium, U_m is a constant matrix independent of x. Thus equation 2.50 can be expressed on the basis of electroweak interaction eigenstates:

$$i\frac{d}{dx}\begin{pmatrix} |\nu_1^m\rangle \\ |\nu_2^m\rangle \end{pmatrix} = \frac{1}{2E}\begin{pmatrix} M_1^2 & 0 \\ 0 & M_2^2 \end{pmatrix}\begin{pmatrix} |\nu_1^m\rangle \\ |\nu_2^m\rangle \end{pmatrix} \tag{2.57}$$

Replacing M_1^2 and M_2^2 with m_1^2 and m_2^2 respectively, equation 2.57 is identical to equation 2.48 which governs neutrino propagation in vacuum. Thus in the case of the constant-density medium, matter enhanced oscillations are identical to vacuum oscillations if we replace the mixing angle. Analogous to equation 2.37, the survival probability for a electron neutrino travelling in a constant-density medium is:

$$|\langle \nu_e|\nu_e\rangle_t|^2 = 1 - sin^2 2\theta_m sin^2(\frac{\pi R}{L_m}) \tag{2.58}$$

where $L_m = 4\pi E/(M_2^2 - M_1^2)$, which is called the neutrino oscillation length in matter.

Obviously the density along the path from the solar core to terrestrial detectors is not constant: it changes from the solar density to 0 in vacuum (the earth effect is ignored here for simplicity.). For a medium with varying density, the mixing matrix U_m is no longer independent of the travelling distance x. Instead of equation 2.57, the propagation equation for neutrinos in a medium with the varying density is:

$$i\frac{d}{dx}\begin{pmatrix} |\nu_1^m\rangle \\ |\nu_2^m\rangle \end{pmatrix} = [\frac{1}{2E}\begin{pmatrix} M_1^2 & 0 \\ 0 & M_2^2 \end{pmatrix} - U_m^+ i\frac{d}{dx}U_m]\begin{pmatrix} |\nu_1^m\rangle \\ |\nu_2^m\rangle \end{pmatrix} \tag{2.59}$$

or:

$$i\frac{d}{dx}\begin{pmatrix} |\nu_1^m\rangle \\ |\nu_2^m\rangle \end{pmatrix} = \begin{pmatrix} \frac{M_1^2}{2E} & -i\frac{d\theta_m}{dx} \\ i\frac{d\theta_m}{dx} & \frac{M_2^2}{2E} \end{pmatrix}\begin{pmatrix} |\nu_1^m\rangle \\ |\nu_2^m\rangle \end{pmatrix} \tag{2.60}$$

Equation 2.60 follows directly from the explicit substitution of the mixing matrix U_m, as defined in equation 2.54, into the second term in the right side of equation 2.59. In this case, $|\nu_1^m\rangle$ and $|\nu_2^m\rangle$ are not mass eigenstates that diagonalize the Hamiltonian matrix. By pulling out a unit matrix times $(M_2^2 - M_1^2)/4E$, which only produces an un-observable phase, equation 2.60 can be re-written as:

$$i\frac{d}{dx}\begin{pmatrix} |\nu_1^m\rangle \\ |\nu_2^m\rangle \end{pmatrix} = \begin{pmatrix} -\frac{M_2^2-M_1^2}{4E} & -i\frac{d\theta_m}{dx} \\ i\frac{d\theta_m}{dx} & \frac{M_2^2-M_1^2}{4E} \end{pmatrix}\begin{pmatrix} |\nu_1^m\rangle \\ |\nu_2^m\rangle \end{pmatrix} \tag{2.61}$$

If the non-diagonal elements in equation 2.61 are much smaller than the diagonal elements and thus can be ignored, the matrix becomes diagonalized and $|\nu_1^m\rangle$ and $|\nu_2^m\rangle$ become the mass eigenstates. This is called the adiabatical approximation which meets the condition:

$$|\frac{d\theta_m}{dx}| \ll |M_2^2 - M_1^2|/4E = \pi/\lambda_m \tag{2.62}$$

Neutrino adiabatic propagation through a medium with varying density can have profound effects. For example, let us consider an electron neutrino produced in the center of the sun.

Figure 2.14 presents a simple picture how the neutrino flavor changes with the density. At the production area, where electron density is high enough to satisfy $A \gg \triangle cos2\theta_v$, $\theta_m = \pi/2$ and the electron neutrino is almost a pure mass eigenstate $|\nu_2^m\rangle$ independent of θ_v. As this neutrino moves outwards through the sun, A decreases with the density and so does θ_m. If the electron density changes slowly enough to satisfy the adiabatic condition, the neutrino always remains as the same mass eigenstate $|\nu_2^m\rangle$. But the electron neutrino is no longer a pure mass eigenstate, it becomes a linear combination of two mass eigenstates:

$$|\nu_e\rangle = cos\theta_m\, |\nu_1^m\rangle - sin\theta_m\, |\nu_2^m\rangle \tag{2.63}$$

This neutrino eventually goes through the resonance position, where $A = \triangle cos2\theta_v$, and proceeds out into the vacuum, where $A = 0$ and $\theta_m = \theta_v$. Since the vacuum mixing angle θ_v is small, in vacuum it is the muon neutrino instead of the electron neutrino which dominantly couples to the heavier mass eigenstate $|\nu_2^m\rangle$. Thus an electron neutrino produced in the solar core oscillate into a muon neutrino. As in vacuum oscillations, the phase information is often lost because the distance the solar neutrino travels is much longer than the neutrino oscillation length in the media. In this case, the survival probability of a electron neutrino is just the classical probability:

$$\begin{aligned} P(\nu_e \to \nu_e) &= \textstyle\sum_i P_m(\nu_e \to \nu_i) P_v(\nu_i \to \nu_e) \\ &= (1 \;\; 0) \begin{pmatrix} cos^2\theta_m & sin^2\theta_m \\ sin^2\theta_m & cos^2\theta_m \end{pmatrix} \begin{pmatrix} 1 & 0 \\ 0 & 1 \end{pmatrix} \begin{pmatrix} cos^2\theta_v & sin^2\theta_v \\ sin^2\theta_v & cos^2\theta_v \end{pmatrix} \begin{pmatrix} 1 \\ 0 \end{pmatrix} \\ &= \tfrac{1}{2}(1 + cos2\theta_v cos2\theta_m) \end{aligned} \tag{2.64}$$

If the electron density does not change slowly and the off diagonal elements $\frac{d\theta_m}{dx}$ in equation 2.61 cannot be ignored, we have to use the non-adiabatic MSW theory. The most likely position for the adiabatic approximation to break down is at resonance, where λ_m is maximized and equation 2.62 is most stringent. As shown in figure 2.14, the gap between two mass eigenstates is smallest at resonance and the neutrino is able to jump from one mass eigenstate to the other mass eigenstate, analogous to the quantum tunneling effect. If we denote P_c as the crossing probability between two mass eigenstates, the classical survival probability for a electron neutrino under the non-adiabatic approximation can

Figure 2.14: **Flavor change for a electron neutrino travelling in a varying-density medium [6].**

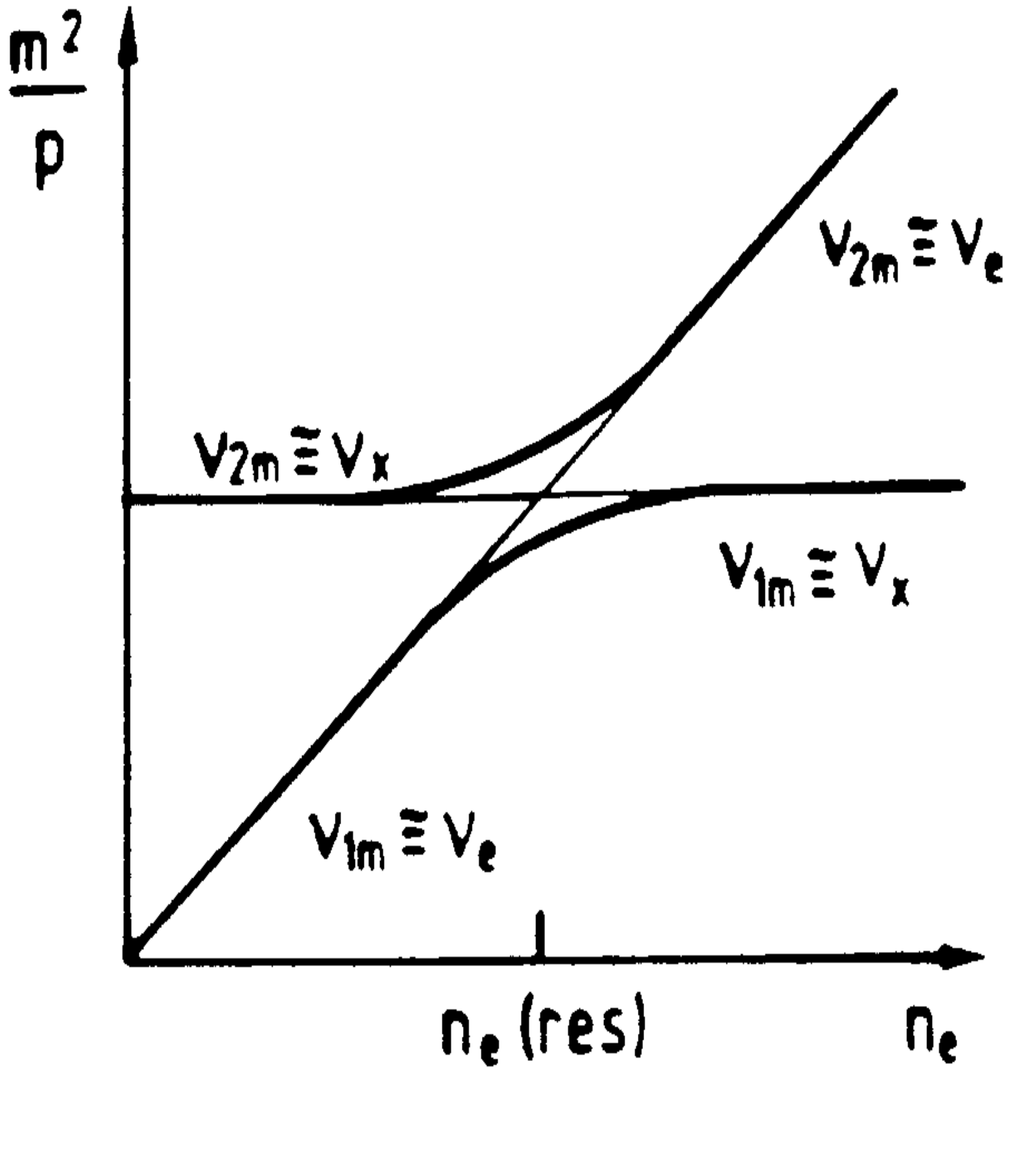

be written as:

$$\begin{aligned} P(\nu_e \to \nu_e) &= \sum_i P_m(\nu_e \to \nu_i) P(crossing) P_v(\nu_i \to \nu_e) \\ &= (1 \;\; 0) \begin{pmatrix} cos^2\theta_m & sin^2\theta_m \\ sin^2\theta_m & cos^2\theta_m \end{pmatrix} \begin{pmatrix} 1-P_c & P_c \\ P_c & 1-P_c \end{pmatrix} \begin{pmatrix} cos^2\theta_v & sin^2\theta_v \\ sin^2\theta_v & cos^2\theta_v \end{pmatrix} \begin{pmatrix} 1 \\ 0 \end{pmatrix} \\ &= \tfrac{1}{2} + (\tfrac{1}{2} - P_c) cos2\theta_v cos2\theta_m \end{aligned} \tag{2.65}$$

Thus the difference between the adiabatic and the non-adiabatic approximation is totally embodied in the function P_c, which is not easy to calculate. The simplest case is for a medium with linear density change, which is also the natural first choice since it corresponds to the first term of a Taylor series expansion of any density function. In this case, Parke [43] calculated P_c as:

$$P_c = e^{-\frac{\pi}{2}\gamma} \tag{2.66}$$

where

$$\gamma = \frac{\triangle m^2 \, sin^2 2\theta_v}{2p cos2\theta_v |\frac{1}{N_e}\frac{dN_e}{dx}|_{res}} \tag{2.67}$$

The probability of a solar neutrino to be detected as a electron neutrino in terrestial detectors is plotted against its energy in figure 2.15. Some global features of this plot can be easily understood. The resonance for neutrino oscillations occurs when $A/\triangle m^2 = cos2\theta_v$ and varies linearly with the neutrino energy. If $E/\triangle m^2$ is small enough so that $A_p/\triangle m^2 < cos2\theta_v$, where A_p is evaluated at the neutrino production point, the electron neutrino does not pass through the resonance and it always remains dominantly as the lower mass eigenstate $|\nu_1\rangle$. In this case, only vacuum oscillations occur , where

$$P(\nu_e \to \nu_e) = \frac{1}{2} + \frac{1}{2} \, cos^2 2\theta_v \tag{2.68}$$

and $P(\nu_e \to \nu_e) \approx 1$ if θ_v is small. For $E/\triangle m^2 > cos2\theta_v$, the neutrino does go through the resonance and the MSW effect can occur, where

$$P(\nu_e \to \nu_e) = \frac{1}{2} + \frac{1}{2} cos2\theta_v cos2\theta_m \tag{2.69}$$

As discussed before in the adiabatic approximation, θ_m can be maximized to be $\frac{\pi}{2}$ independent of θ_v. Thus

$$P(\nu_e \to \nu_e) = sin^2\theta_v \tag{2.70}$$

and the electron neutrino is converted into other flavor neutrino if θ_v is small. If $E/\triangle m^2$ increases continually, according to equation 2.62, at some point the adiabatic approximation is broken. In this case, the crossing probability between two mass eigenstates has

Figure 2.15: **The survive probability for a electron neutrino created at the center of the sun is plotted as a function of $P/\triangle^2$ [42].**

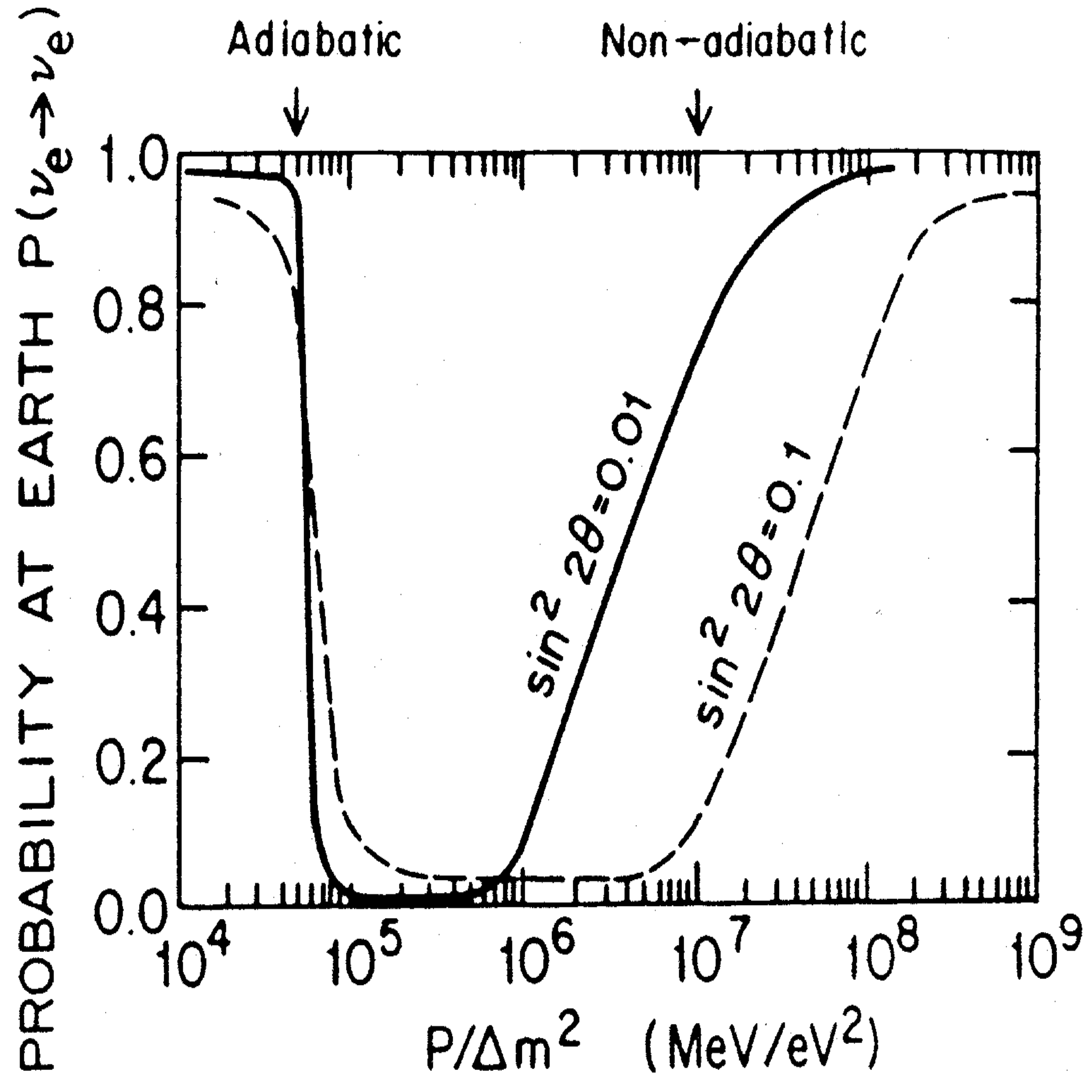

to be taken into account. Thus equation 2.65 is valid, where the non-adiabatic term P_c counteracts the effect of the adiabatic term and the neutrino's survival probability rises. If $E/\triangle m^2$ is so large ($P_c \to 1$) that the non-adiabatic term becomes dominant, then the survival probability returns to the unity when $\theta_m \to \pi/2$ and $\theta_v \to 0$. The effect of increasing $sin^2 2\theta_v$ is to delay the breakdown of the adiabatic condition and so widens the suppression trough.

As far as matter enhanced oscillations are concerned, there are three distinct solutions to the solar neutrino problem: adiabatic, non-adiabatic and large angle solutions, each of which corresponds to different parts of the survival probability plot in figure 2.15. For a fixed $\triangle m^2$, the energy spectrum of solar neutrinos occupies a band in the $P/\triangle m^2$ axis.

By changing $\triangle m^2$, this band can be moved along the abscissa. If this band happens to sit on the adiabatic threshold shown in figure 2.15, the flux of neutrinos with energy larger than the threshold is severely suppressed while the flux of neutrinos with lower energy remains almost unchanged. A similar situation occurs while this band sits on the non-adiabatic threshold, the difference is that here the flux of neutrinos with lower energy is suppressed. Both the adiabatic and the non-adiabatic solutions are able to induce an energy-dependent suppression of solar neutrino fluxes. If the band sits totally inside the valley of the survival probability curve, a large vacuum mixing angle is needed to match the data from experiments.

Given the experimental data, the value of θ_v and $\triangle m^2$ could be determined as two free parameters in the MSW solution to the solar neutrino problem. Normally, the fitting results are illustrated in the so-called $\triangle m^2$-$\overset{2}{sin}2\theta_v$ diagram, as shown in figure 2.4.3. The confidence level contours shown in this figure are more or less in the shape of a triangle, with each side representing one particular MSW solution. The upper horizontal side is the adiabatic solution, where the survival probability of an electron neutrino solely depends on the position of the adiabatic threshold which is almost independent of θ_v. The vertical line represents the large angle solution, where the survive probability solely depends on the mixing angle θ_v, as shown in equation 2.70. The diagonal side of the triangle represents the non-adiabatic solution, where the survive probability depends on the crossing probability P_c. To the first order approximation, $P_c \sim \triangle m^2\ \overset{2}{sin}2\theta_v$. For a fixed P_c, it is a straight line in a log-log plot with $\triangle m^2$ and $\overset{2}{sin}2\theta_v$ as ordinate and abscissa respectively.

The two black regions shown in figure 2.4.3 are the areas where the data of four existing solar neutrino experiments can be explained simultaneously. The non-adiabatic solution with

$$\triangle\, m^2 \sim 6 \times 10^{-6} eV^2 \quad and \quad \overset{2}{sin}2\theta_v = 7 \times 10^{-3} \tag{2.71}$$

gives an excellent description of the experimental observations, while the second region (the large angle solution) with

$$\triangle\, m^2 \sim 9 \times 10^{-6} eV^2 \quad and \quad \overset{2}{sin}2\theta_v = 0.6 \tag{2.72}$$

is marginally allowed at 90% confidence level. Also shown is the parameter space excluded by the fact that the Kamiokande II experiment does not see a day-night effect which would be caused by the MSW oscillations of solar neutrinos as they pass through the earth.

Figure 2.16: The $\triangle m^2$-$sin^2 2\theta_v$ plot, showing the areas of $\triangle m^2 - sin^2 2\theta_v$ space allowed by three different types of experimental data and the area allowed by the combined result. Also shown is the area excluded by the non-observation of a day-night effect in Kamiokande experiment. (taken from [44])

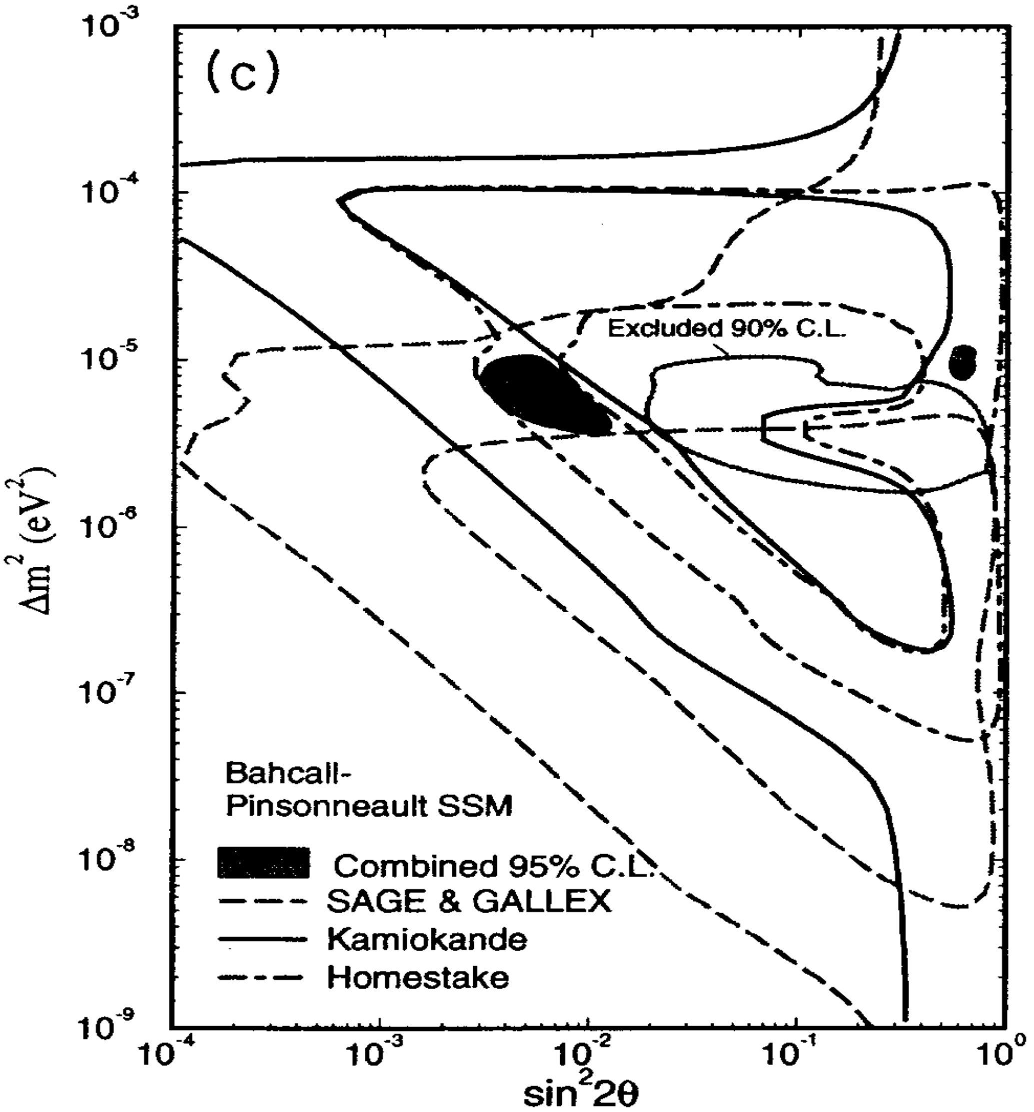

2.5 Future Solar Neutrino Experiments

All four existing solar neutrino experiments observe solar neutrino fluxes which are substantially lower than those predicted by the standard solar model. Basically two types of solutions have been proposed to solve the solar neutrino problem: astrophysics or particle physics solutions. In order to answer this problem unambiguously, new experiments are needed to provide higher count rates, more accurate measurements of the neutrino's energy spectrum and a sensitivity to all types of neutrinos.

The Borexino experiment [45] is designed to provide a clear measurement of the ^{7}Be neutrino flux, which is able to fill the gap in the current observations of solar neutrinos. The detector consists of 300 tons of liquid scintillator surrounded by 4.5 meters of water shielding and viewed by 1700 20cm-diameter PMTs. The ^{7}Be solar neutrinos are detected in real time, via their scattering off electrons. The use of a scintillating target is necessary in order to produce enough light, and therefore provide good energy and spatial resolution for such low energy electrons. The detection of solar neutrinos with low energies (0.862 and 0.384 MeV) requires a extremely low radioactive contamination level in the detector. Many laboratory tests have been carried out with encouraging results. As an example, the deionized water that will be used as the shielding has a content of Uranium and Thorium less than 5×10^{-14} g/g and of ^{40}K less than 5×10^{-11} g/g [46]. The event rate is expected to be 50/day above the threshold of 0.25MeV.

The Sudbury Neutrino Observatory (SNO) [47] is a 1000 tons heavy water detector, which is viewed by $\sim$ 10000 20cm-diameter Hamamatsu PMTs and shielded by 8000 tons light water. The use of D_2O as the target provides a neutral current interaction which is sensitive to all 3 types of neutrinos (ν_e, ν_μ, and ν_τ). The observation of neutrinos of non-electron flavors would be a clear signature for flavour changing neutrino oscillation. In addition, the charged current interaction enables SNO to measure the ^{8}B neutrino spectrum more accurately than existing solar neutrino experiments. The SNO experiment is fully discussed in the next chapter.

Chapter 3

Sudbury Neutrino Observatory

3.1 Overview

Arguably the Sudbury Neutrino Observatory (SNO) will be the best solar neutrino experiment so far in the sense that it is able to provide an unambiguous answer to the question: is the MSW theory, the currently most favored theory, the right solution to the solar neutrino problem? One thousand tons of heavy water is the target used in SNO to detect solar neutrinos. The advantage of using D_2O as the target is that solar neutrinos can be detected not only by charged current interactions (sensitive only to ν_e) but also by neutral current interactions (sensitive to all three electroweak flavors: ν_e, ν_μ and ν_τ). Observation of more neutral current events than charged current events in SNO (after taking into account the difference between the cross sections of two interactions and efficiencies for detecting) would be a clear signature for the flavor-changing neutrino oscillations, clear evidence for the physics beyond the standard model , since the sun produces only electron neutrinos in any significant quantity.

3.2 The Detector Structure

The Sudbury Neutrino Observatory [48] is a large heavy water Čerenkov light detector located in a nickel mine near Sudbury in Ontario, Canada. The chosen site is deep underground(6800 feet), which is common to all solar neutrino experiments in order to shield from cosmic rays. The wall rock in the mine is composed of norite which has a low uranium and thorium content and is suited to the construction of a large enough cavity. The structure of the detector is shown in figure 3.1. The main target for solar neutrinos is 1000 tons of heavy water contained in a spherical vessel of 6 meter radius and 5.5 cm thickness. The vessel is made of 122 acrylic tiles which are bound together using the so called "solvent welded" technique. Thick plates are attached at the equator of the vessel with "U" shape grooves to accommodate ropes which hang from the support deck and lift the whole vessel (30 tons). The acrylic used to construct these tiles has two important properties [49]:

1. Low levels of uranium and thorium contamination, which stems from the fact that the polymethylmethacrylate monomer is kept free from contamination until polymerisation.

2. It is UV-transparent since no stabilizer chemicals or other additives which attenuate UV light are added.

Eight thousand tons of light water acts as the shield between the acrylic vessel and the cavity wall and the PMTs.

The detector is viewed by $\approx$ 9600 photomultipliers (PMTs) placed in a concentric structure (PSUP) built of stainless steel located 2.5 meters away from the acrylic vessel. The photomultipliers are R1408 8-inch diameter bialkali photocathode tubes produced by the Hamamatsu company. There were several reasons to select this kind of tube:

1. The tube is made of materials with low uranium and thorium content, which is required for the SNO experiment.

2. Although the charge resolution of the tube is relatively poor, it has a small spread (1ns) [50] in the transit time of the photoelectrons. Good time resolution leads to accurate reconstructions of the event vertices, which are essential in rejecting backgrounds outside the acrylic vessel (AV).

3. Maybe most importantly, this kind of tube is cheaper than other types.

Each of the photomultipliers has a non-imaging light concentrator [51] attached to it. The concentrators are made from strips of highly polished aluminium used as a substrate for several layers of dielectrics to achieve high durability and reflectivity. The strips are mounted in a plastic holder to ensure that they conform to the desired shape. The addition of the concentrators improves the effective area of light sensitivity by a factor of 1.6, while adding only 4% to the channel cost. The opening angle of the concentrator is carefully chosen so that the detection efficiency of the photomultiplier is largest for photons coming from the volume including the whole D_2O region and the surrounding 1 meter H_2O while the neighboring photomultipliers are optically shielded from each other, which significantly decreases the chance of a radioactive decay event in the front glass of one photomultiplier being detected by the surrounding PMTs. Approximate 9600 PMTs with concentrators provide a 65% photosensitive material coverage of the whole detector, which is much higher than the coverage of the Kamiokande II experiment (20%) and thus provides a better photon detection efficiency. The voltage on each PMT is tuned to produce a charge gain of 10^7. The deposited charge in every PMT is processed by a dual range ADC attached to the tube. The discriminator threshold will be set to be $\frac{1}{4}$ of a photoelectron and the trigger time is referenced to a 50MHz clock. Signals from all the ADCs are processed in a custom data acquisition system situated on the deck above the detector. A global trigger is imposed and the event is written to tape when the number of triggered PMTs (Nhits) within a fixed time window (currently set at 100 ns in the Monte Carlo code) exceeds a preset hardware threshold (This will be the most often used trigger in the SNO experiment although there are other types of triggers.). The level of the threshold will be decided by the speed of writing events to the tape. The time of the global trigger (universal time) is referenced to a 10MHz clock. This 100ns time precision ensures that SNO is able to record the event time very accurately in the case of a supernova.

The 1000 tons of heavy water is on loan from AECL (Atomic Energy of Canada Ltd.) until 2002 and has a isotopic purity of 99.92%, which is essential for detecting the NC events. Having low levels of radioactive contamination in the water is the top priority of the SNO experiment. Radioactive impurities are removed from the heavy and light water by a special water system. A slight overpressure of light water will be held on the inside of the PSUP (PMT supporting structure) in order to carry any radioactive leakages from the PMTs outwards and away from the D_2O.

3.3 Physics in the SNO detector

3.3.1 Čerenkov light

Any charged particle travelling at a speed higher than the speed of light in the ambient medium will cause the emission of Čerenkov light [52]. For electrons in water, the Čerenkov

Figure 3.1: **The outline of the SNO detector.**

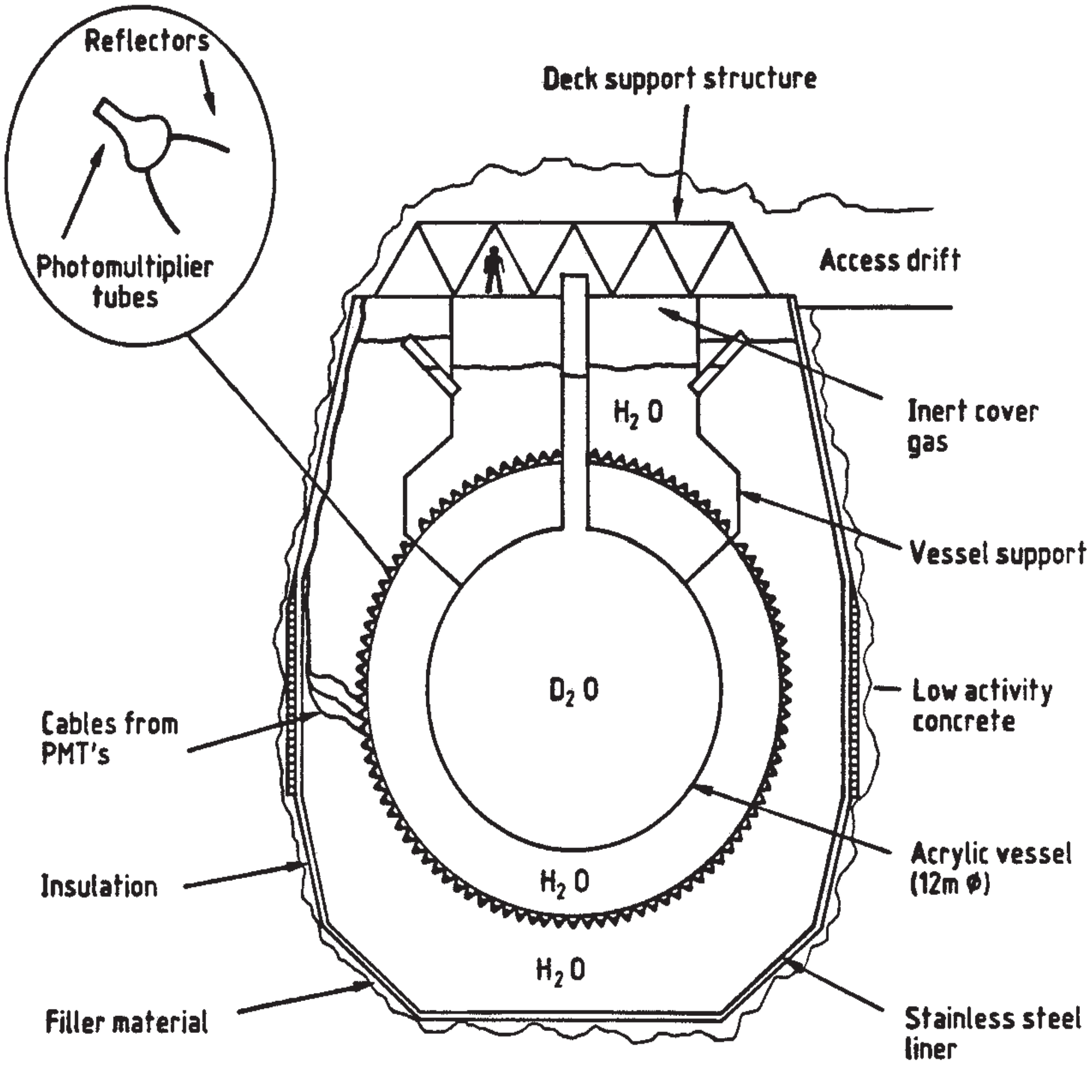

threshold corresponds to a kinetic energy of $\sim 262keV$. The number of Čerenkov photons produced per unit track length by an electron is given by:

$$\frac{dN}{dx} = \frac{\alpha}{c}\int_{\omega_1}^{\omega_2}(1 - \frac{1}{\beta^2\, n(\omega)^2})d\omega \tag{3.1}$$

where $n(\omega)$ is the refractive index evaluated at a frequency ω, $\beta = \frac{v}{c}$ is the relativistic factor, c is the light speed, and α is the fine structure constant. For materials such as water, $n(\omega)$ increases as ω increases. ω_2 is the high frequency cut off when $\beta n(\omega)$ equals 1. Below low frequency cut off ω_1, the radiation is cut off as the medium becomes strongly absorbing. Figure 3.2 shows a Monte Carlo result of the number of photons produced by a 5MeV electron in the D_2O. The angle between the direction of the emitted photons and the instantaneous direction of the electron is given by:

$$cos\theta_c = \frac{1}{\beta^2\, n(\omega)^2} \tag{3.2}$$

For a 5MeV electron travelling in the water, $\theta_c \approx 42^o$. Since the direction and the energy of the electron changes every time it is scattered in the surrounding environment, the angular distribution of the emitted Čerenkov photons is distorted from a perfect cone, as shown in figure 3.3.

3.3.2 Detection of Solar Neutrinos

All fermions are affected by the weak interaction, although strangely in the Standard Model it is only the left-handed part of a fermion's wave-function (or the right-handed part of an anti-fermion's) which couples to the $W^{\pm}$ and Z^0. The photon couples to a particle's electric charge, so only the charged fermions (i.e., all those except the neutrinos) feel the electromagnetic interaction. Amongst the fermions only the quarks feel the strong force, although unlike the other interactions gluons couple to themselves and thus also feel the strong force. The weak interactions mediated by massive bosons $W^{\pm}$ are called CC reactions while interactions mediated by Z^0 or photons are called NC reactions (the relative weakness of the interactions mediated by the $W^{\pm}$ and the Z^0 when compared to those mediated by photons being due to the large masses of the $W^{\pm}$ and the Z^0 bosons). Feynman diagrams of CC and NC reactions in SNO are shown in figure 3.4. For neutrino energies relevant to the solar neutrino problem clearly the CC reaction are only sensitive to electron neutrino (because there is not enough energy to produce the muons or taus

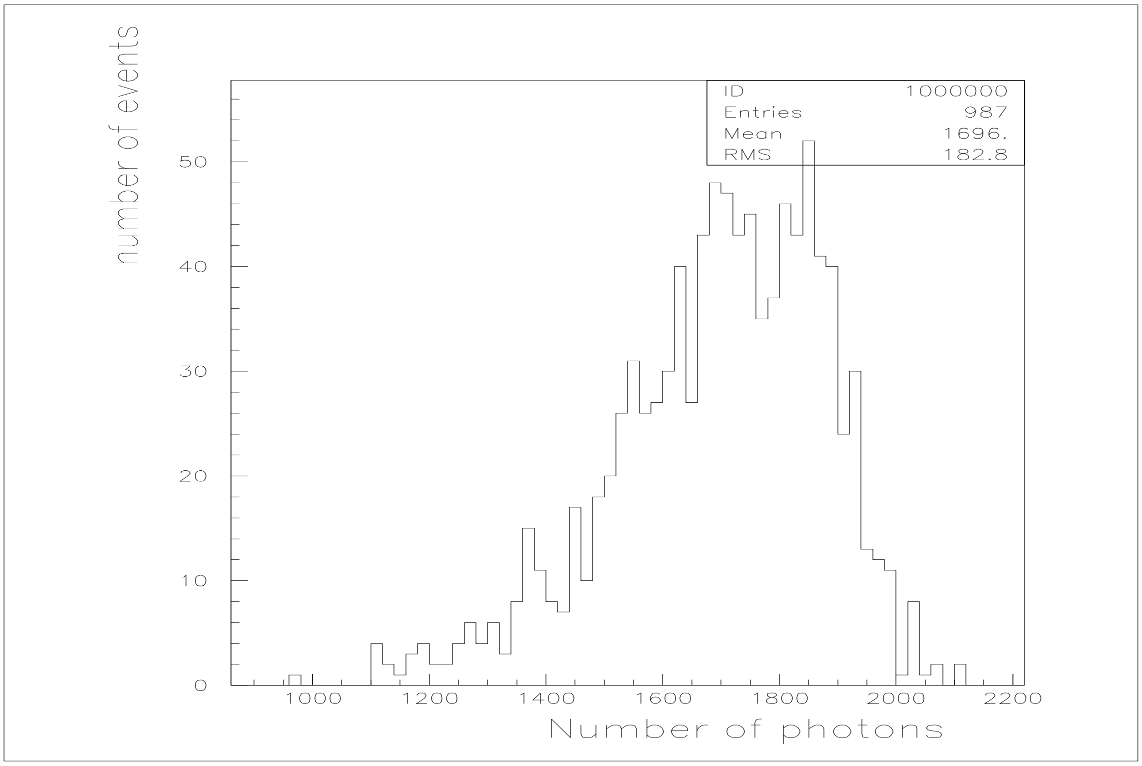

Figure 3.2: **Number of čerenkov photons produced by a 5MeV electron moving in the D_2O.**

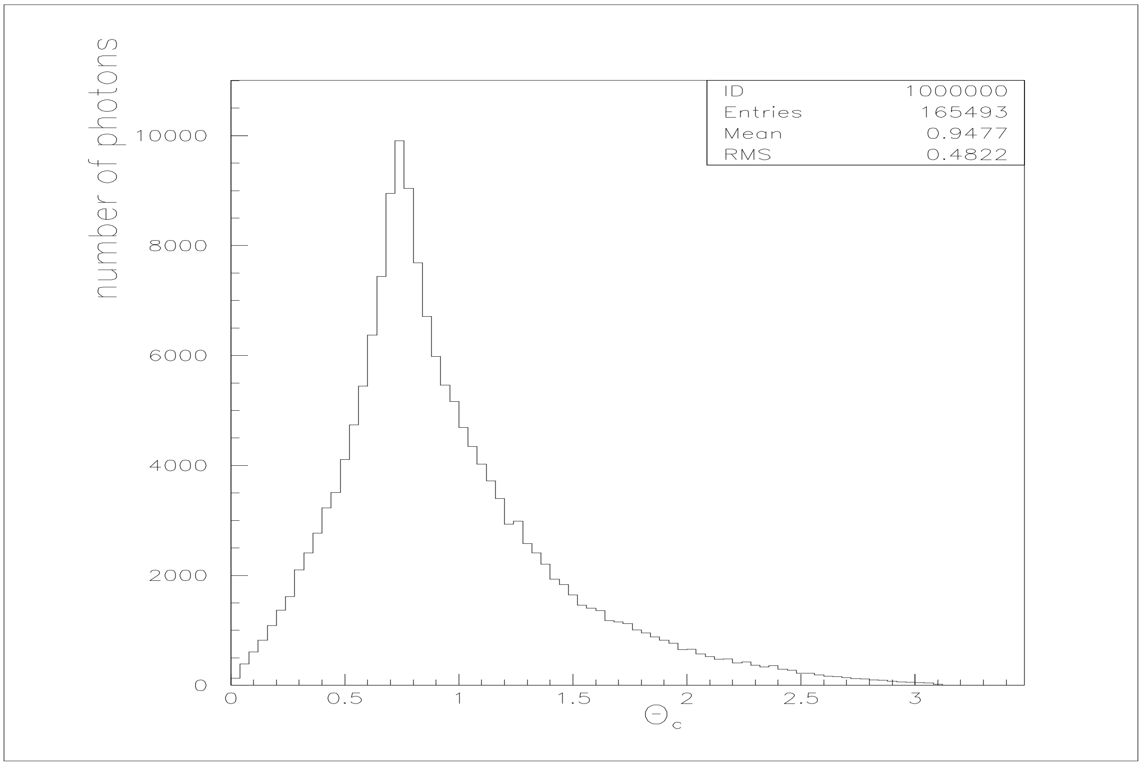

Figure 3.3: **Angle between the direction of the emitted čerenkov photons and the initial direction of the electron.**

in the final state), while under universality the NC reaction is equally sensitive to all three types of neutrinos. As discussed later, this unique feature may enable the SNO experiment to provide the first unambiguous evidence of neutrino oscillations.

Thus neutrinos only feel the weak interaction, which has a typical interaction range of around 10^{-18} meter and a cross section of roughly 10^{-44} m^2, is therefore the weakest among all known interactions (except gravity). It is therefore very difficult to detect neutrino themselves. In principle, neutrinos are detected by looking for products of their CC or NC reactions with the target matter. In order to increase event rates for a neutrino experiment, we could either increase the incoming neutrino flux or have a larger detector which simply enhances probability of neutrino interactions inside the detector. In fact, for many neutrino experiments such as reactor or accelerator based neutrino experiments, both methods have to be used in order to get a decent number of neutrino-induced events. For a solar neutrino experiment such as SNO, as there is nothing we could do to enhance the incoming neutrino flux, the only way to get a large number of neutrino-induced events is to have a detector as large as possible. The other major difficulty for a neutrino experiment is how to get a clean set of neutrino-induced events. Weak interactions are so weak that they are normally overwhelmed by electromagnetic and strong interactions. In a typical neutrino experiment, the number of neutrino-induced events is often several order magnitude less than number of background events. Generally speaking, there are two basic ways to enhance the event/background ratio:

1. we could minimize the background event rate directly by adding external shielding to the detector or/and using carefully-chosen materials during construction of the detector.

2. We could use some unique signal from a neutrino-induced event to distinguish it from other background events.

The necessity to suppress background events has a huge impact on the design and construction of a neutrino experiment such as SNO. For example, the SNO experiment, as all other solar neutrino experiments, is deep underground in order to shield from cosmic ray muon backgrounds. All materials used in the construction of the detector are carefully chosen to contain minimal levels of radioactivities which, as discussed in the next chapter, produce most the troublesome backgrounds to events induced by solar neutrinos. A complex water system has been developed to purify both the light and heavy

Table 3.1: **Neutrino interactions in the SNO detector.**

Interaction Name	Reaction	Q-value (MeV)	σ at 10MeV (10^{-42} cm^2)
Charged current	$\nu_e + d \to p + p + e^-$	-1.44	2.7
Neutral current	$\nu_x + d \to n + p + \nu_x$	-2.22	1.1
Elastic scattering	$\nu_x + e^- \to \nu_x + e^-$	0	0.092
Charged current	$\overline{\nu_e} + d \to n + n + e^+$	-4.03	1.2
Charged current	$\overline{\nu_e} + p \to n + e^+$	-1.80	5

Table 3.2: **The expected number of events per year in SNO under various hypotheses [48].** The detector threshold is assumed to be 5MeV for the electron's kinetic energy. Note the difference in the number of NC events between the astrophysical solution and the neutrino oscillation solution to the solar neutrino problem. All hypotheses assume the neutrino fluxes predicted by SSM [7], except the third column where 1/3 of SSM predicted neutrino fluxes is assumed.

Reaction	SSM (full)	SSM $\times$ 1/3	Vacuum oscillation	MSW Adiabatic	MSW Non-adiabatic
CC	9750	3255	3260	3750	3750
ES	1100	360	480	645	488
NC	2800	933	2800	2800	2800

water. Huge efforts have been put in to minimize possible contaminations to the detector during its construction. Some attempts (such as the look back technique discussed later) have also been made to find a difference in signals between a NC event and a neutron background event in order to suppress background events.

As mentioned before, SNO is sensitive to all three electroweak neutrino flavors by various interaction channels. These interactions are listed in table 3.1, figure 3.5 shows their cross sections, and table 3.2 presents the expected number of events in SNO under different hypotheses.

Figure 3.4: **Feynman diagrams of CC(upper plot) and NC(bottom plot) reactions in SNO.**

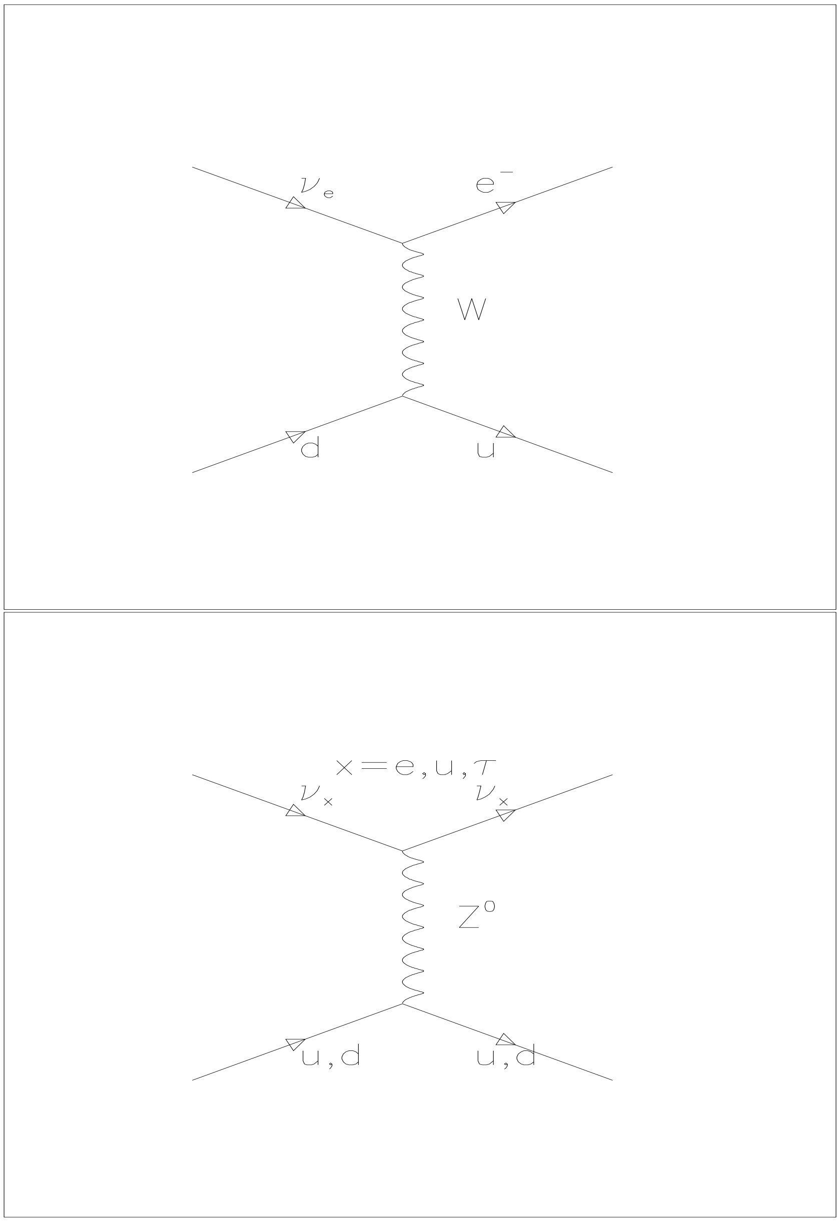

Figure 3.5: **Cross sections of various neutrino reactions in the SNO detector [48].**

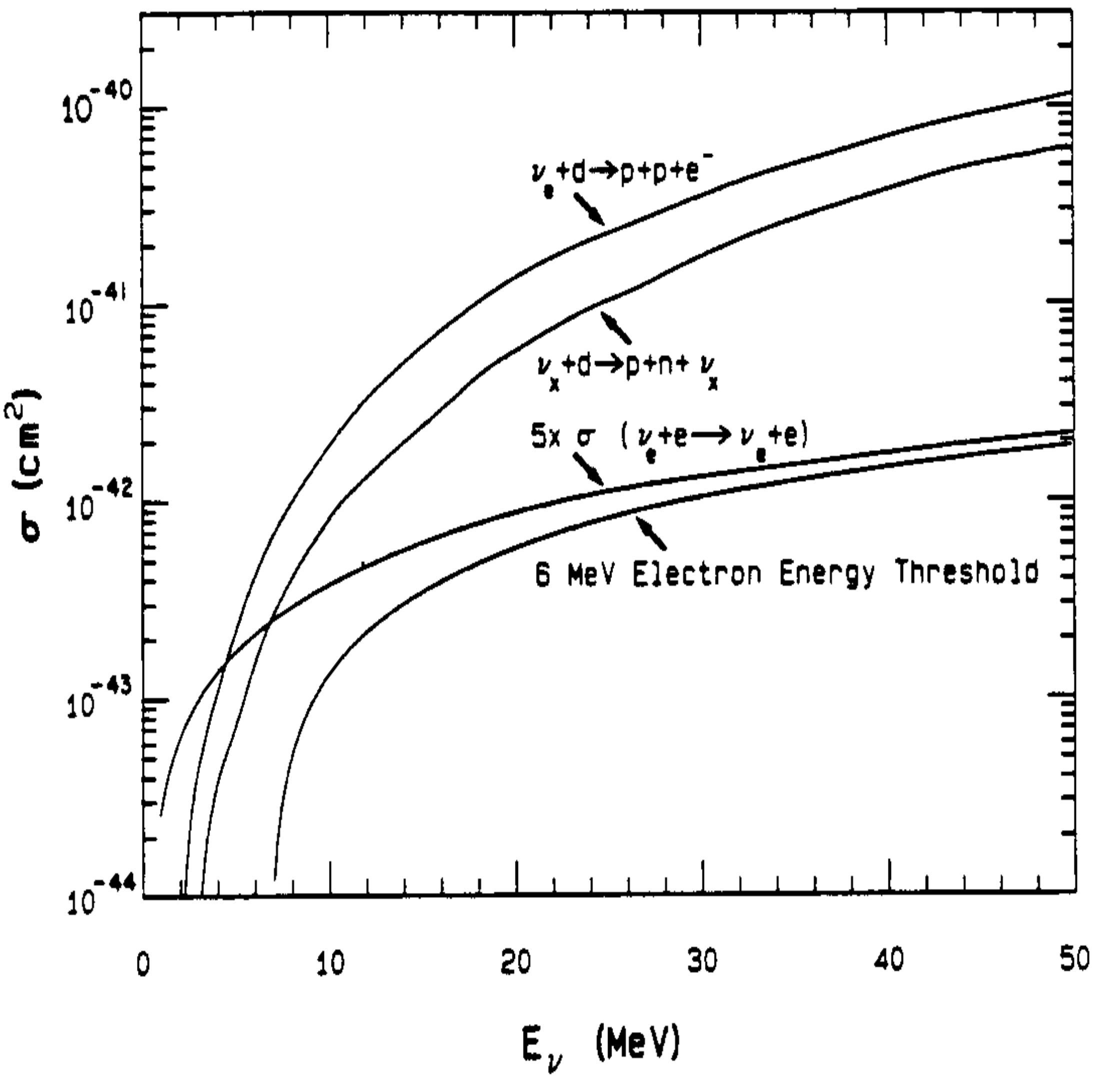

The Charged Current Reaction

The first detection channel used in SNO is the charged current reaction (CC):

$$\nu_e + d \rightarrow p + p + e^- \tag{3.3}$$

The energy threshold of this reaction is 1.442MeV, which means this channel is sensitive only to ^8B, pep and hep solar neutrinos. The kinematics of reaction 3.3 leads to the following expression for the energy of the recoil electron:

$$T_e = E_\nu - Q - \frac{P^2}{m_p} - \frac{(p_e - p_\nu)^2}{4m_p}[53] \tag{3.4}$$

where p_ν and E_ν are the neutrino's three-momentum and energy, p_e and E_e are the electron's three-momentum and energy, P is the relative momentum of the protons in the proton center-of-mass system (c.m.s.), and the energy threshold Q = 1.442MeV. One thing worth mentioning is that in most of the literature, the third term in equation 3.4, which describes the kinetic energies of the two protons in the proton c.m.s., and the fourth term, which describes the small recoil energy of the two-proton center-of-mass system, are ignored. This leads to a simple delta function for the difference between the energy spectrum of the recoil electron and the energy spectrum of the incident neutrino, which is quite different from the results of detailed calculations shown in figure 3.6.

The angular distribution of the recoil electrons produced in CC reactions is:

$$I(\theta_{sun}) = 1 - \frac{1}{3}(\frac{v}{c})cos\theta_{sun} \approx 1 - \frac{1}{3}cos\theta_{sun} \tag{3.5}$$

which leads to a 2 to 1 asymmetry in terms of number events in the backward and forward directions (θ_{sun} is the angle between direction of the recoil electron and direction of the sun). This feature could be useful in future data analyses such as separating CC events from the other kind of events in SNO.

The Neutral Current Reaction

The most important detection channel for solar neutrinos in SNO is the neutral current reaction (NC). H.H.Chen pointed out that the neutrino-induced disintegration of the deuteron nucleus is sensitive to all three electroweak neutrino flavors [56]:

$$\nu_x + d \rightarrow n + p + \nu_x \;\; (x = e, \mu, \tau) \tag{3.6}$$

The energy threshold of NC reaction is 2.22MeV, which enables SNO to detect ^8B solar neutrinos, but at the same time, the low binding energy of deuteron means the SNO

Figure 3.6: **Comparison of the CC differential cross section at various energies T_e and scattering angles ϑ [53].** Solid line represents the calculation without considering the details of deuteron nuclear physics [54], Dotted line is the result of more sophisticated calculation [55].

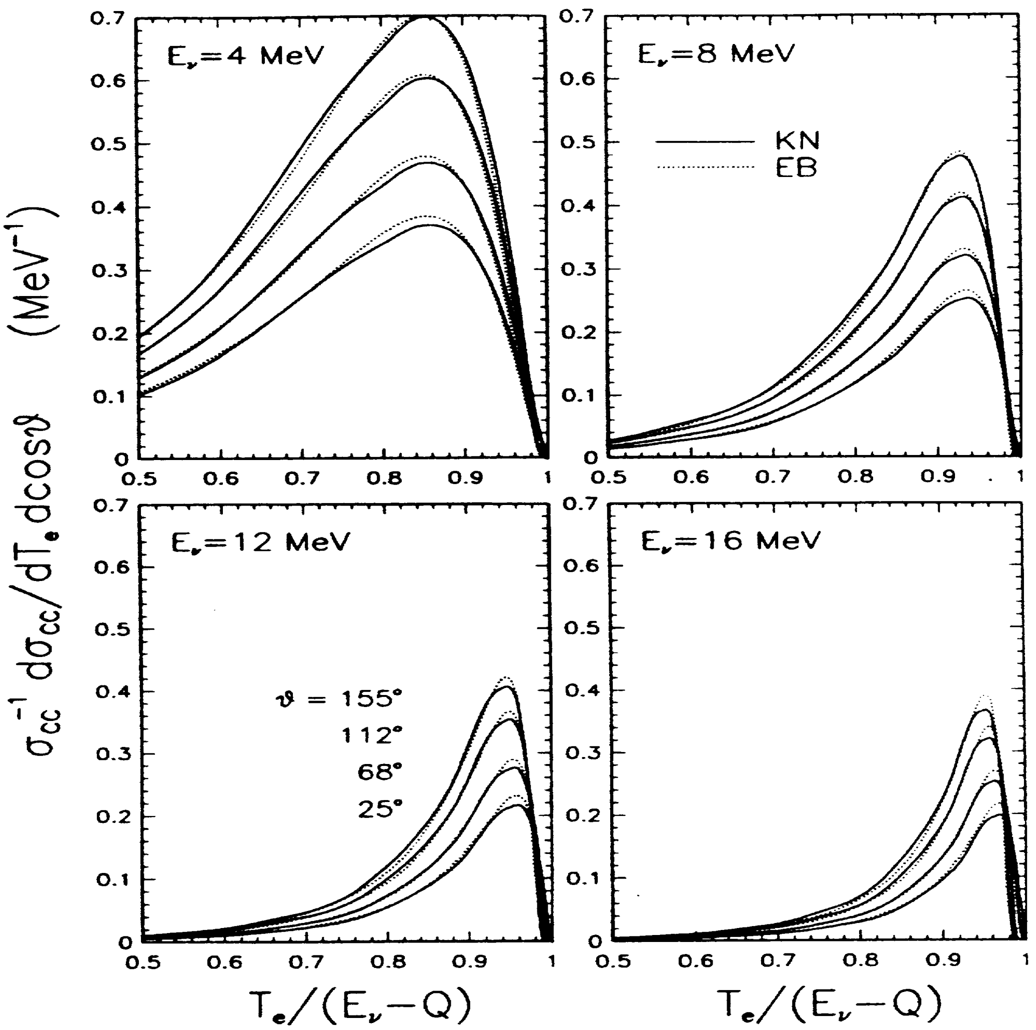

experiment requires a very low level of radioactive impurities in the detector as discussed in the next chapter. The final state neutrinos escape without leaving any trace in the detector. The only signature of the NC reaction is the free neutron, which will be detected by several methods as discussed in the next section. Neutrons are thermalized before they are captured in the target, which means that the information about the initial directions and energies of neutrons are lost. The latest calculation for the cross section of the NC reaction can be found in [57].

The Elastic Scattering Reaction

The elastic scattering reaction (ES) used in SNO is identical to that used in the Kamiokande II experiment:

$$\nu_x + e^- \rightarrow \nu_x + e^- \tag{3.7}$$

which has no energy threshold. The most important feature of this reaction has been shown in the Kamiokande II experiment: the angular distribution of the recoil electrons is peaked in the direction of the incident neutrinos, which provides a unambiguous indication of the source of these neutrinos. Thus the measurement of the direction of the ES events is able to give us the confidence that the detected neutrinos really come from the sun.

The ES scattering reaction is also sensitive to all three electroweak neutrino flavors. However, the cross section of a ν_e ES reaction is approximately 6 times larger than that of a ν_μ or ν_τ scattering since the electron flavour has a $W^\pm$ channel open to it as well as the Z^0 channel available to all three neutrino flavors. As shown in table 3.1, the cross section of the ES reaction is much smaller than those of the CC and NC reactions. However, the number of ES events is somewhat enhanced by the fact that there are 5 times as many electrons as deuterons in one D_2O molecule and electrons are also available in the light water. The ES reaction could provide some “cross-check” information in addition to the other neutrino reactions in SNO.

Anti-Neutrino Reactions

In addition to the three main neutrino reactions above, the SNO detector is also sensitive to anti-neutrinos, which is critical in the case of a supernova. These neutrinos can be detected in D_2O via the analogue of the charged current reaction:

$$\overline{\nu_e} + d \rightarrow n + n + e^+ \tag{3.8}$$

The signature of this reaction is the positron signal followed by one or two delayed neutron signals. The $\overline{\nu_e}$ can also interact in the H_2O via the inverse β decay of the proton:

$$\overline{\nu_e} + p \rightarrow n + e^+ \tag{3.9}$$

which may be identified by the Čerenkov light emitted by the final state positron (The number of PMT hits (nhits) produced by the neutron capture on the hydrogen nucleus is well below the detector's threshold.).

3.4 Running Modes of the SNO detector

Basically there are two ways to prove the hypothesis that flavor-changing neutrino oscillations (except those involved with sterile neutrinos) are the correct solution to the solar neutrino problem:

1. The observation of more NC events than CC events since the sun only produces the electron neutrinos in any significant quantities.

2. A distortion of the neutrino energy spectrum since the shape of the spectrum is not affected by astrophysics, while many of neutrino oscillation solutions inevitably lead to a change in the spectrum. The shape of the spectrum may also be distorted by oscillations of electron neutrinos into sterile neutrinos.

The charged current reactions enable SNO to measure the energy spectrum of ^8B solar neutrinos. The interesting range of the CC spectrum lies between 5MeV and 7.5MeV. Below 5MeV, the signals due to radioactive impurities in the detector become dominant while above 7.5MeV, as shown in figure 3.7, the difference among neutrino spectra induced by various hypotheses may be smaller than the pure statistical error of the SNO data. However, there will exist a contamination in this window. The capture of neutrons produced by NC reactions on the deuterium nuclei leads to emissions of single 6.25MeV gamma rays. The number of PMT hits (nhits) produced by a γ event is somewhat lower than nhits produced by a electron event with the same amount of energy. Nevertheless, these neutral current events can not be ignored when we deduce the shape of CC spectrum, as shown in figure 3.8. There are two ways to solve this problem:

1. A neutron "poison", an isotope which has a much larger neutron absorption cross-section than the deuteron, can be added into the heavy water to get rid of this

contamination. ^6Li is a suitable candidate for such a poison [58]. Monte Carlo simulation shows that by adding 300kg of $LiNO_3$ salt (95% ^6Li) into the heavy water, almost all the neutrons are captured on ^6Li to produce ^7Li, which is stable. The disadvantage of the "poison" run is just its advantage in measuring the CC spectrum: the SNO detector loses its capability of detecting NC events, which is a nightmare in the case of a supernova.

2. Since the Nhits spectrum of single 6.25MeV gamma can be well determined by calibration, if we know the number of free neutrons, the contribution by the NCd (neutrons captured on the deuteron nuclei) events to the combined spectrum shown in figure 3.8 can be deduced and then subtracted from the data. This would leave us with a measurement of the CC spectrum with slightly bigger error bars.

As mentioned before, the neutral current reaction, which is sensitive to all three electroweak flavors of neutrinos, is the most important reaction in the SNO detector. The top priority of the SNO experiment is to measure the ratio between the number of CC events and the number of NC events R_{cc}/R_{nc} since the cross sections of CC and NC reactions are known to 10% while their ratio is known to 0.5% [60]. Observation of a larger flux of neutrinos detected by neutral current reactions than that detected by charged current reactions is a clear signature of flavor-changing neutrino oscillation, as shown in figure 3.9, since astrophysical solutions to the solar neutrino problem are not able to generate new flavors of neutrinos. There are three distinct ways to measure the CC/NC ratio:

1. **Without and With Salt**

   The default method of detecting neutrons produced by NC reactions is by adding ^{35}Cl, which has a much larger neutron absorption cross section (43b) than ^2H (0.53mb), to the heavy water. The de-excitation of ^{36}Cl after neutron capture leads to a γ cascade with a total energy of 8.6MeV. Gamma rays produce energetic electrons through the Compton-scattering and pair-production processes. These electrons then create Čerenkov photons which are detected by the surrounding PMT arrays. Monte Carlo simulation shows that with 2 tons of $MgCl_2$ (salt) in the heavy water, the capture efficiency of neutrons produced in the D_2O is 83% [61]. Figure 3.10 shows the nhits spectrum of neutron capture events in the D_2O. The higher peak is due to neutron captures on chlorine (8.6MeV gamma cascade) or deuteron (6.25MeV gamma) nuclei while the smaller peak corresponds to neutron

Figure 3.7: **CC spectra for the standard solar model and various neutrino oscillation scenarios [53].** STD stands for the standard solar model, VAC stands for vacuum oscillation, LMA stands for the large mixing angle MSW theory, and SMA stands for the nonadiabatic MSW theory with the small mixing angle. Note that the LMA and STD solutions cannot be distinguished on this plot.

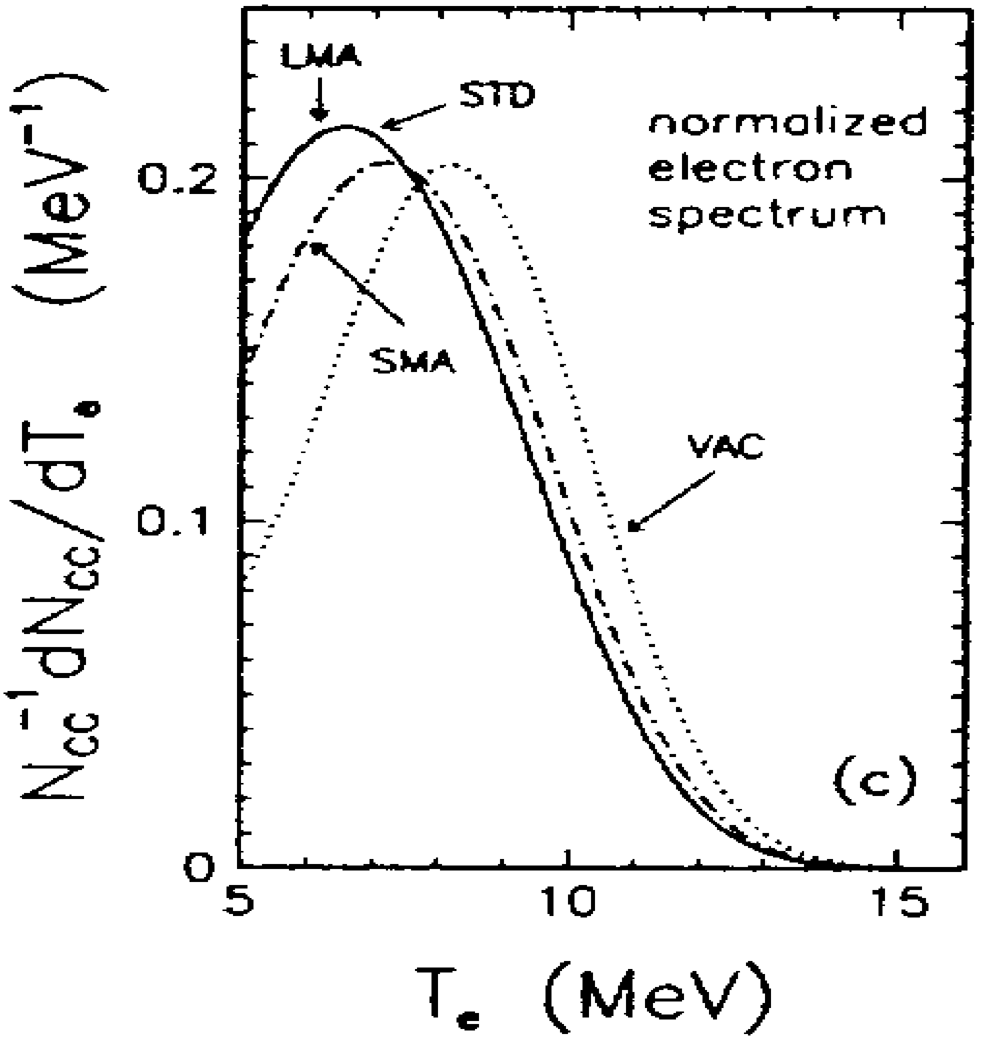

Figure 3.8: **Pure CC (charged current) spectrum (dashed line) compared with the combined spectrum (solid line) of CC and NCd (neutrons captured on deuteron nuclei) events.** The number of CC and NCd events per year is assumed to be 14200 and 1888 respectively, taken from [59]. The energy scale here is ≈ 9 nhits/MeV.

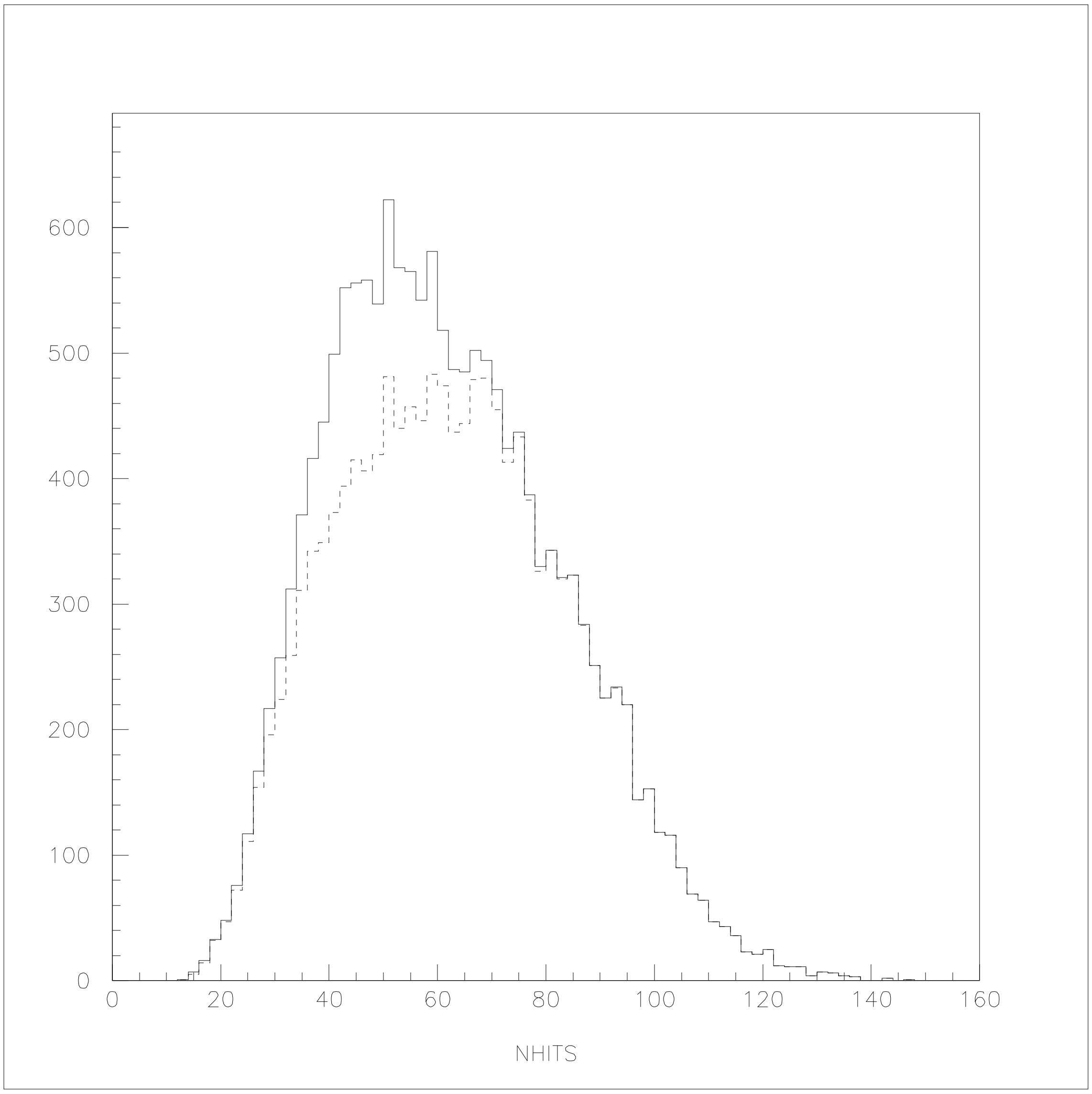

Figure 3.9: **Values of the characteristic CC-shape variable, the average energy $< T_e >$, and of the CC/NC ratio, R_{CC}/R_{NC}, together with 3σ error bars.** Uncertainties due to the backgrounds are neglected, cited from [53]. Symbols are same as those used in figure 2.6.

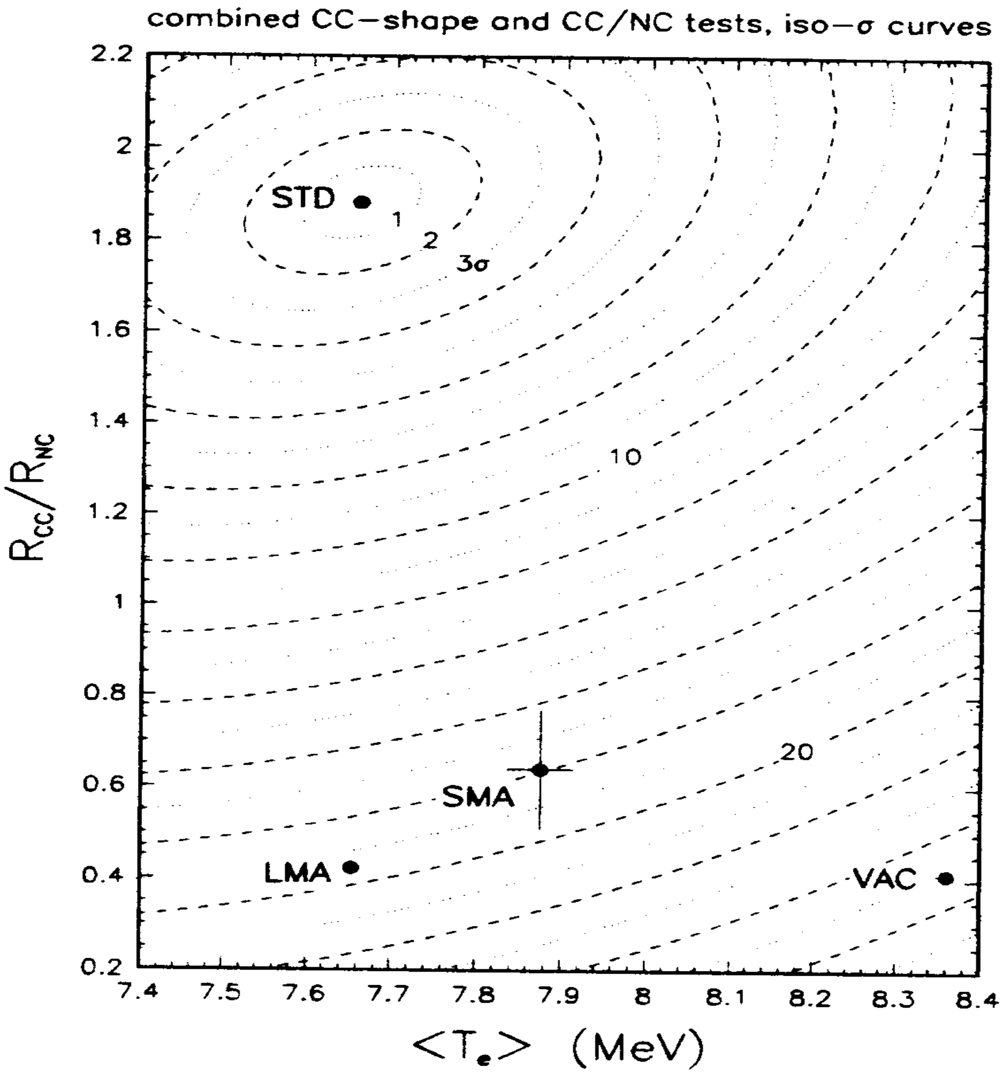

captures on hydrogen nuclei (2MeV gamma) with a cross section of 330mb.

The operating plan for SNO is to start the experiment with a period of pure D_2O running to measure the number of CC events followed by another period of D_2O running with salt to measure the number of (NC+CC) events. A prerequisite of this running mode is that the background level in the detector is known during the period of two years. Another worry is the level of radioactive impurities introduced into the detector by adding the salt, which is still a unknown quantity. Arguably the simplest way to put a upper limit to this contamination is by adding the salt in stages and monitoring the variation of the background spectrum [62].

2. **Neutral Current Detector (NCD)**

The cross section for the reaction

$$^3He + n \rightarrow t + p + 0.764MeV \tag{3.10}$$

is enormous, 5330b. Thus it is possible to distribute ^3He proportional counters sparsely throughout the heavy water to detect neutrons produced by NC events [63]. Such an array of detectors is currently under construction in U.S.A.. In order to minimize radioactive backgrounds, the cylindrical counters, which have a diameter of 5cm and thickness of 0.4mm, are made of ultra-pure nickel. The counters will have a total length of $\sim$ 900 meters and are arranged in a square grid of 1 meter spacing. Each counter string is anchored at the bottom of the acrylic vessel. Neutron captures deposit 764 keV of energy in the counter gas, creating around 30,000 ion pairs that can be detected easily. Pulse shape discrimination has been shown to be able to eliminate the backgrounds from β and α decays in the detector walls with an acceptable loss in efficiency. The advantages of this running mode are:

(a) NCDs are able to detect neutrons on an event-by-event basis.

(b) NCD running mode provides a cross check to the result of the first running mode since the detecting mechanism used here is quite different from that of salt-in and salt-out running mode, and independent of the creation, propagation and detection of Čerenkov photons.

Again the major concern here is the radioactive impurities in the materials used to make these NCDs.

Figure 3.10: **Nhits spectrum of neutron captured events in the D_2O.** SNOMAN code is used to simulate these events with energy scale of roughly 9 nhits/MeV.

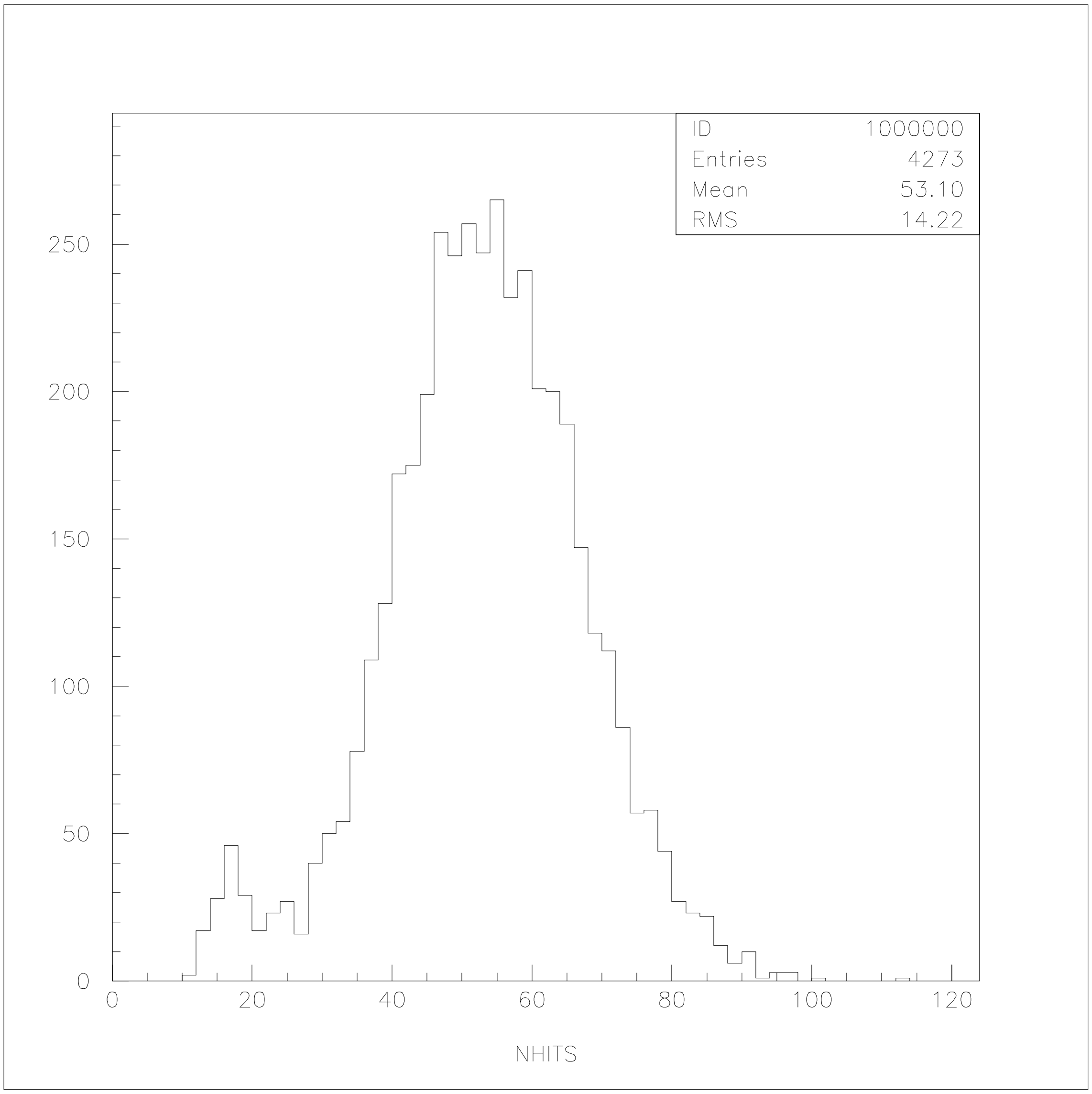

3. **Pattern Recognition**

   The product of a charged current reaction is one energetic electron, while the product of a neutral current reaction is a gamma cascade (usually with 2 or 3 energetic gammas). The difference between the angular distribution of the Čerenkov photons produced by single particle in the D_2O and that produced by multiple particles can be utilized to distinguish between CC and NC events. A pattern recognition technique has been developed to fulfill this task based on the neural network technique and chi square fitting methods [64]. Monte Carlo simulation shows that this technique is able to provide an event by event or a statistical discrimination of NC events from CC events, and thus determine their numbers as above the detector's threshold, the contaminations of other kind of events can probably be ignored (we will have to confirm this once we have data from the experiment.). The simultaneous measurement of the CC spectrum may be achieved by using this technique to determine the numbers of CC and NC events respectively in every nhits bin [65] although the statistical error may be large. This technique has the advantage of only needing 6 months of D_2O running with the salt [59] (although data from a poison run is shown to be highly desirable) as well as not requiring any additional hardware or complex installation procedures. The current major weakness of this technique is its complete reliance on the correctness of Monte Carlo Simulation (although in future we will use calibration sources to verify the simulation results). However, primary studies have been carried out to prove that it is robust against plausible systematic errors in the simulation of the detector [59]. A similar technique is used by the author to determine the level of the major backgrounds in the SNO detector, the details of which will be discussed in chapter 5.

3.5 Calibration Sources

Correct interpretation of the future data from the SNO experiment depends heavily upon our understanding of the response of the detector. This is why calibration sources are needed to check the performance of the Monte Carlo simulation.

The first source consists of a pulsed nitrogen dye laser at a wavelength of 384nm, shining into a diffusing ball. This laser ball technique has been successfully used in the IMB [66] and the Kamiokande II [67] experiments to determine the detection efficiency of

PMTs and the performance of the data acquisition system. By placing this laser ball at different positions in the detector, the angular response of individual photomultipliers can be determined as well as the optical qualities of the acrylic vessel and water. Similarly, by comparing the calibration data between a run with an air fill and a run with a water fill, the optical parameters of both light and heavy water, such as photon attenuation length, could be deduced. By counting the number of late PMT hits, the magnitude of photon scattering inside the detector can be determined.

Through-going muon events have been used in other underground experiments as a ideal calibration source to determine the energy scale of the detector. However, the depth of the SNO experiment makes this source infeasible since the number of penetrating muons is small. Experience with other large water Čerenkov light detectors suggests that an overall scaling factor is needed in order to reconcile the light output of the detector and the prediction of the Monte Carlo code. The IMB collaboration found this scale factor to be 0.52 [68] and the corresponding value for the Kamiokande II experiment is 0.85. The SNO collaboration's own work on the small test detector [69] produced a factor of 0.82. Some work has been carried out in Oxford to measure the absolute quantum efficiency of the photomultiplier used in SNO, this should lead to a scaling factor fairly close to 1.

Useful CC events in SNO have an energy ranging from 5MeV to 20MeV. Several calibration sources have been proposed to check the response of the detector within this energy range:

- The decay of ^{8}Li produces a single electron whose energy spectrum has an end point of 13.1MeV. ^{8}Li can be produced by neutron capture on ^{7}Li. However, isotopes with decay products of high energy electrons normally are short lived. The half life of ^{8}Li is only 0.84s, which means this calibration source has to be made *in situ* near the detector. A devise based on the circulation of a solution of lithium salt which flows between an activation site, where neutrons are produced by a D-T tube, and a transparent reservoir inside the detector is being built in Canada. The beneficial feature of this source is that it produces a continuous β spectrum which is analogous to the energy spectrum of ^{8}B decay, the neutrinos from which are captured in the detector. The major problem is that the emitted electrons inevitably interact with the boundary of the calibration source and thus the energy spectrum is distorted. Monte Carlo simulation is required to make the correction.

- 68% of ^{16}N decays produce an energetic electron and ^{16}O which then decays with emission of a 6.1 MeV gamma. A D-T tube will be used to produce free neutrons which then interact with ^{16}O to produce ^{16}N. Then ^{16}N will be transported into the detector using the same device as that used in the ^{8}Li calibration source.

- An (n,γ) reaction on a ^{3}He target can be used to calibrate the detector response for high energy events. This reaction produces gamma rays with energies up to (20.6MeV + 0.75*E), where E is the energy of the incident neutron. The proposed calibration source consists of a spherical container with ^{3}He gas at 3 atmospheric pressures. At the center of the container, there is a spherical inner source made of stainless steel, which contains a neutron source such as ^{252}Cf. The inner source is filled with lead in order to absorb thermal neutrons and other fission products of ^{252}Cf. The most serious difficulty with this source is the high rate of lower energy γ-rays from neutron captures in materials other than ^{3}He. An accurate Monte Carlo simulation is needed in order to extract information from this calibration data.

The detector response to the neutral current events will be calibrated by introducing free neutrons from spontaneous fission of ^{252}Cf into the heavy water. The Californium is mixed with a small amount of scintillator before being inserted into a block of acrylic, which is then put into the detector. The spontaneous fission of the Californium is tagged by the scintillation light. On average, every fission reaction produces 2.67 free neutrons, which are then thermalized before they are captured on H, D or Cl nuclei. This source exactly reproduces the energy spectrum of NC events induced by the neutrino disintegrations of deuteron in the detector. The major concern is whether we can separate the less frequent neutron capture events from the other products of the fission reaction.

Table 3.3 lists some of proposed calibration sources in SNO.

The detector response to low energy events (below threshold) is not critical for the data analysis of CC and NC events since they have higher energies than the threshold. However, as discussed in chapter 4, the accuracy of Monte Carlo codes in simulating background events (normally with energies below threshold) is critical in applying pattern recognition techniques to determine background levels in the detector. The only available source at present is a triggered NaI detector. The NaI is activated by thermal neutrons, and the subsequent β decay of ^{24}Na is used as a trigger, which is followed by γ decays with one 2.75MeV and one 1.37MeV gamma. The proposal for a background calibration source,

Table 3.3: **Some of proposed calibration sources in SNO.**

Source reaction	Energy	Comment
$^7Li(\alpha,\gamma)^{11}B$	E_γ = 10.3MeV	
$^3He(n,\gamma)^4He$	E_γ = 21MeV	Require fast (4MeV) neutrons
$^3H(p,\gamma)^4He$	E_γ = 20MeV	
$^{11}B(p,\gamma)^{12}C$	E_γ = 11.7 + 4.4MeV	Requires 163keV protons
$^{16}N \rightarrow^{16} O + e^- + \overline{\nu_e}$	Q = 10.4MeV	26% B.R., τ = 7.13 s
	Q = 4.3MeV, E_γ = 6.1MeV	68% B.R.
$^8Li \rightarrow^8 Be + e^- + \overline{\nu_e}$	Q = 13.1MeV	τ = 0.84 s
^{252}Cf fission	$E_n \approx 1MeV$	3-4neutrons per fission

which not only can be used to calibrate the detector response to low energy event but also provides a overall check of the Monte Carlo simulation of the background events in SNO, is presented in chapter 6.

3.6 Supernova Neutrinos

As with solar neutrinos, supernova neutrinos are able to carry information from space inaccessible to other particles (e.g. interstellar dust usually blocks out most of emitted photons.). Detection of neutrinos from SN 1987A by the Kamiokande II and IMB experiments provided a reliable check on the theory of stellar collapse and the properties of neutrinos [70, 71]. Since predictions for the probability of a type II supernova occurring in our galaxies ranges from 1 in 10 to 1 in 100 years, it is hard to estimate the chance of the SNO detector to see such a event during its lifetime (10 years). However, if we are lucky enough that such a supernova happens in the next 10 years, SNO should be able to provide unique information about the relevant physics. Predicted number of events in SNO in the case of a supernova occurring at the distance of 10kpc are listed in table 3.4.

The mechanism of a supernova burst is outlined as follows. After a star has exhausted it's hydrogen fuel and evolved away from the main sequence, its central mass begins to contract into an iron core. When the core mass exceeds the Chandrasekhar limit, $M_{CH} = 5.76Y_e^2M_\odot$, where Y_e is the electron to nucleon ratio, the pressure due to a degenerate electron gas is no longer able to balance its gravitational force, and the star

Table 3.4: **Predicted number of events in SNO from a stellar collapse at 10 kpc, at 100% detection efficiency [72].**

Reaction	Target medium	Events in ν_e burst (kt^{-1})	Events in cooling phase (kt^{-1})
$\nu_e + d \rightarrow p + p + e^-$	D_2O	10	33
$\nu_x + e^- \rightarrow \nu_x + e^-$	D_2O/H_2O	1	16
$\nu_x + d \rightarrow \nu_x + p + n$	D_2O	6	760
$\overline{\nu_e} + d \rightarrow n + n + e^+$	D_2O	0	20
$\overline{\nu_e} + p \rightarrow n + e^+$	H_2O	0	120

starts its final infall. During the transformation of an iron core to a protoneutron star, protons change into neutrons by electron capture reactions:

$$p + e^- \rightarrow n + \nu_e \tag{3.11}$$

This collapse process lasts for a few tens of milliseconds with the emission of electron neutrinos whose average energies are around 15MeV. Then the protoneutron star cools down by transporting energy from its core to the surrounding space. Due to the high density of this protoneutron star, the only efficient way to transport energy is through neutrino emissions. During this cooling process, roughly equal numbers of neutrinos and anti-neutrinos of all types are produced by neutral current processes. Figure 3.11 shows the time distribution of neutrinos produced in a supernova. The average energies of these neutrinos and anti-neutrinos are in the range of 10-30MeV. Because of their larger interaction length in matter, ν_μ ($\overline{\nu_\mu}$) and ν_τ ($\overline{\nu_\tau}$) may be able to escape from a higher density region than ν_e ($\overline{\nu_e}$), and hence have higher energies, as shown in figure 3.12.

The SNO detector will make a unique contribution to the study of these neutrinos because of its sensitivity to all three neutrino flavors, because of its low-energy threshold and large fiducial volume, and because of its good time resolution. The supernova neutrino events can be easily distinguished from solar neutrino events through their higher energy and much higher fluxes in a short time. The SNO detector is able to accurately measure the fluxes of ν_e (through reaction: $\nu_e + d \rightarrow p + p + e^-$ in D_2O) and $\overline{\nu_e}$ (through reaction: $\overline{\nu_e} + p \rightarrow n + e^+$ in H_2O and reaction: $\overline{\nu_e} + d \rightarrow n + n + e^+$ in D_2O) respectively. In addition, the neutral current reaction, $\nu_x + d \rightarrow \nu_x + p + n$, in the heavy water can be used to measure the total neutrino flux regardless of flavor. Thus the flux of $\nu_\mu(\overline{\nu_\mu})$ and

Figure 3.11: **The production of the different types of neutrinos is shown against the time of a supernova [73].** If the neutrino production ceases after a few milliseconds, the formation of a black hole is very possible.

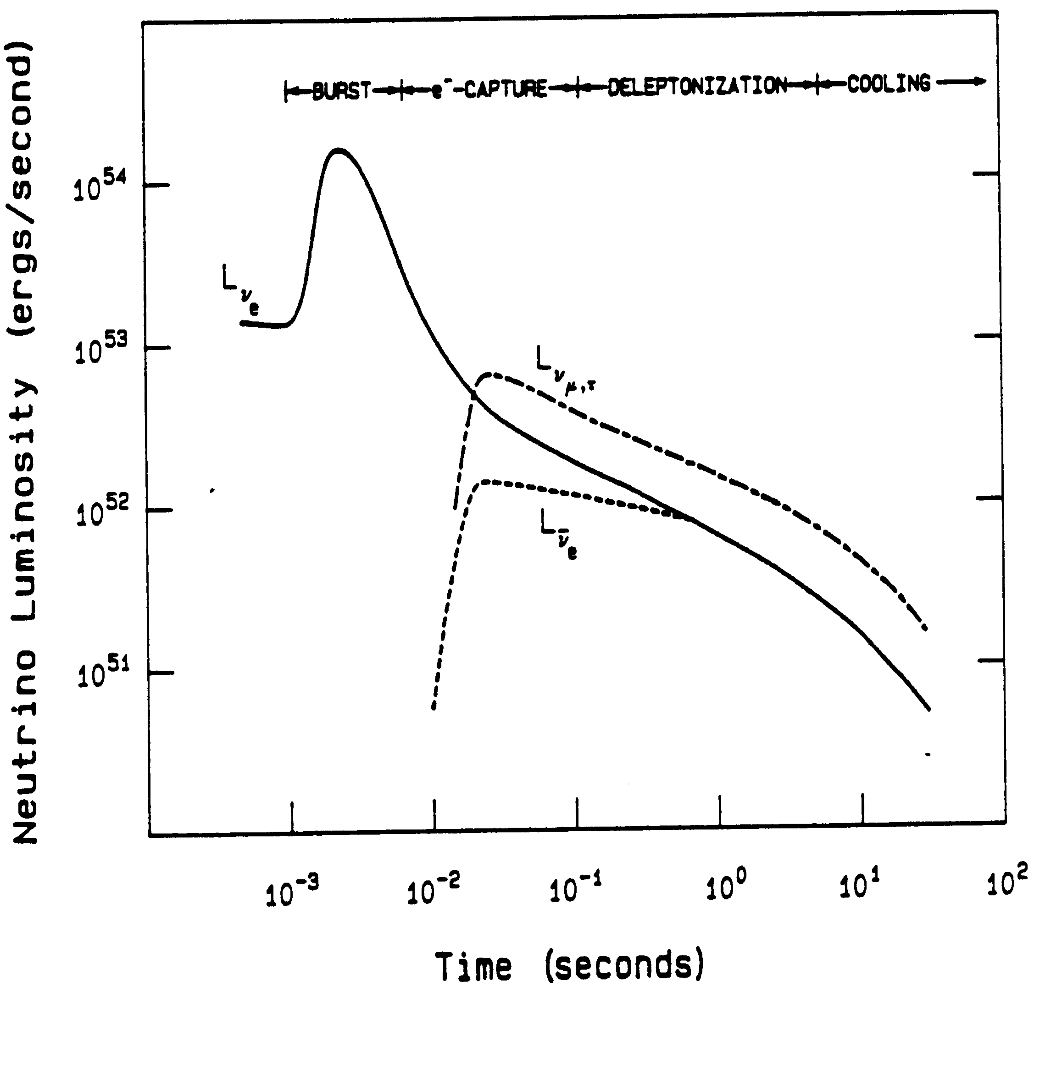

Figure 3.12: **The time-integrated neutrino spectra for a supernova of a 12 $M_\odot$ star as calculated in [74].**

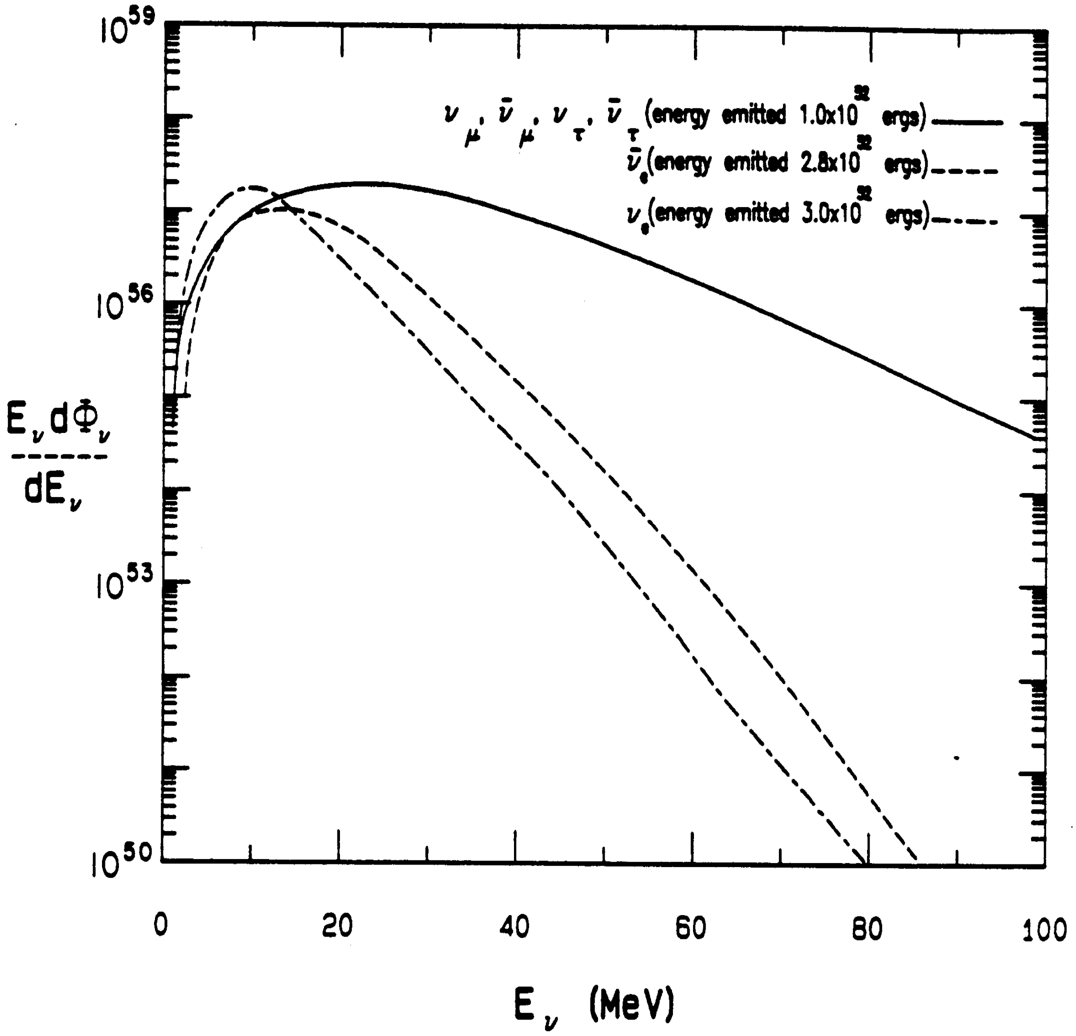

$\nu_\tau(\overline{\nu_\tau})$ can be deduced. All these data should be very useful in verifying the theory of stellar collapse. The early detection of a neutrino burst may lead to the discovery of a new supernova, hours before any optical display can be expected. This would make it possible for astronomers to study the very important early phases of the explosion in the electromagnetic domain.

More importantly, the upper limits of neutrinos' masses can be deduced from their relative arrival time at the earth. Much lower mass limits could be achieved than those probed by the terrestrial experiments. If a neutrino is massive, it's speed is less than the speed of light and hence it takes a longer time for this neutrino to travel from the collapsing star to the earth than a massless neutrino. If a neutrino has mass in the range 50ev $< m_\nu <$ 100keV, it could be readily measured through its delay in arriving relative to other types of events. Below 50eV, it is difficult to decouple the small delay time from the period of the cooling phase which is a few tens of seconds. Above 100keV, the delay time is so long that it may be impossible to separate this supernova neutrino signal from the dominant solar neutrino signals. The upper limit for ν_e may be difficult to deduce because of the relatively small number of events, as shown in table 3.4.

Above all, the capability of the SNO experiment to study supernova neutrinos strongly depends on the distance between the supernova and the earth. If this distance is too short, the time delay due to the non-zero masses of neutrinos may be too small to be separated from uncertainties in supernova models. If the distance is too large, we may not have enough events to do a good mass measurement.

3.7 SNOMAN

The SNOMAN (*SNO* *M*onte Carlo and *AN*alysis) code is a set of FORTRAN routines written and used by the SNO collaboration to simulate physics inside the SNO detector [75, 76, 77]. It is capable of simulating the generation of relevant particles in the various parts of the detector, the propagation of these particles through the complex detector geometry, the response of the PMTs, and the collection of signals by the data acquisition system. The code also provides several software tools (such as event vertex fitter) essential in the off-line data analysis.

The core of the SNOMAN code is a data structure supported by the ZEBRA memory manager [78], by which the code circumvents the lack of dynamic memory management in the FORTRAN routines. Various software processors take the inputs from this data structure, fulfill their own tasks, and then append the outputs to the data structure. This basic frame work ensures that different processors are independent of each other, which makes the endless job of updating the code much easier and enhances the compatability between various tasks.

All of the Monte Carlo simulations carried out during the process of finishing this thesis were done with the SNOMAN code.

Chapter 4

Backgrounds in SNO

4.1 Overview

Since the signature of an event in SNO induced by a solar neutrino is tens of PMT triggers (or PMT hits), any physical processes except neutrino interactions capable of producing such PMT triggers are regarded as backgrounds. The first candidate for such background is PMT noise, a false PMT trigger caused by the dark current. The current estimate for the noise rate in the Hamamatsu R1408 photomultiplier used in SNO is 1kHz. Taking into account the number of PMTs used in SNO, which is approximately 10000, the average number of PMT hits caused by such noise is 2.5 in the trigger window of 250ns. The contribution of PMT noises to the total background level in SNO can be ignored since the average number of PMT hits for a typical neutrino-induced event is larger than 40.

The major backgrounds in SNO are those physical processes which are able to produce a large number of Čerenkov photons since obviously there is no way for a photomultiplier to distinguish between the photons produced by a background event and those produced by a neutrino-induced event. Any charged particles travelling faster than the speed of light in water are able to produce Čerenkov photons. Since SNO is deep underground, high energy cosmic ray muons are the only such candidates which do not come from the materials used to construct the detector. The backgrounds due to penetrating muons are discussed in section 4.2. Electrons with energy higher than the Čerenkov threshold (kinetic energy 262 keV in water) also are able to produce Čerenkov photons. Sources of these electrons are natural radioactive $\beta-\gamma$ decays or high energy gammas which undergo Compton-scattering and/or pair-production. It is because of these troublesome electron backgrounds that the SNO detector needs 4 meters of water shielding, a complex water purification system and a high energy threshold. The contributions of these processes to the total background level depend on their positions relative to the center of the detector. The background processes happening outside the acrylic vessel (external backgrounds) contribute less to the contamination of neutrino-induced events than those occurring inside the AV (internal backgrounds) because of the water shielding and the specially designed PMT concentrators. The external and internal backgrounds are discussed in section 4.3 and section 4.4 respectively.

The unique background to a heavy water detector is free neutrons produced by the photodisintegrations of deuterium nuclei in the D_2O (By comparison, the number of neutrons from other sources such as spontaneous fission of ^{238}U is negligible and this type of background can be easily vetoed due to its characteristic time correlation between the neutron capture signal and the fission signal.):

$$\gamma + d \rightarrow p + n \quad (Q = -2.223 MeV) \tag{4.1}$$

The neutrons produced by these reactions are totally indistinguishable from the neutrons produced by the neutral current reactions. The dominant sources for the γ rays with energy higher than 2.223 MeV are natural radioactive $\beta - \gamma$ decays. Since the top priority of the SNO experiment is to measure the number of NC events, the level of these NC backgrounds place a strict requirement on the radioactive purity of all of the detector components.

In order to meet the requirement of solar neutrino detection, complex water purification systems have been installed to extract radioactive impurities from both the heavy and the light water. A outline of the system's design is presented in section 4.5.

Some software techniques have been developed to provide real time and in situ determination of background levels in the SNO detector. Section 4.6 presents some of these techniques.

4.2 Muon Backgrounds

The SNO detector is located in a cavity at a depth of 2070 meters underground. At this depth, the only penetrating cosmic ray components are muons and atmospheric neutrinos. The flux of atmospheric neutrinos is much smaller than that of solar neutrinos and even if these neutrinos undergo electron scattering, their energies usually are much higher than those of solar neutrinos and can be rejected easily. Through-going muons deposit a huge amount of energy inside the detector, which are easily vetoed as events with a high number of PMT hits. The trouble would be those through-going muons which "skip" the edge of the detector (i.e. only a small fraction of emitted Čerenkov photons are detected by the PMT array.). The vertex fitter can be used to reject this kind of background, a more reliable method is to install some outlooking photomultipliers in the PSUP in order to detect lights coming from the surrounding water shielding just as the Kamiokande II experiment.

The other kind of backgrounds caused by penetrating muons are ^{16}O spallation products, such as ^{8}B, ^{12}B and ^{12}N which decay with high energy electrons (13 to 16MeV endpoint energy) and have relative long half-lives (10-800 ms). The Kamiokande II experiment [79] found that about 1% of the muons produced spallation signals above a 10MeV threshold. In addition (as can be seen in figure 4.1), because of the SNO's depth, the muon intensity at the SNO site is a factor of 200 lower than that at the Kamiokande II experiment. It is estimated that only 24 muons per day pass through the D_2O volume, of which about 1.5 per day produce detectable spallation events above the detector threshold. These events are readily identified by their characteristic time signature, a high energy through-going muon signal followed by a β-decay signal.

4.3 External Backgrounds

4.3.1 Backgrounds from the Cavity Wall

The most troublesome background from the cavity wall comes from the high energy gamma rays. High energy electrons lose energy through multiple Coulomb scatterings immediately after their creation and are normally stopped within a few tens of centimeters, while the thermal length of a free neutron is 21 cm in the light water and the capture of a neutron on a hydrogen nucleus only leads to a low energy (2.223 MeV) γ-ray(well below the detector's energy threshold (5 MeV)).

Gamma rays with energy up to 10 MeV are principally from neutron captures in the norite rock or the other construction materials. The spontaneous fissions of ^{238}U nuclei also produce some high energy gamma rays at a lower level. The source of neutrons is (α, n) reactions primarily on light elements with the α-particles originating from the radioactive decays of ^{238}U nuclei, ^{232}Th nuclei and their daughters. The (α, n) interactions

Figure 4.1: **Cosmic-ray muon flux as a function of overburden (mwe) or depth underground (feet in standard rock) for various underground laboratories [48].**

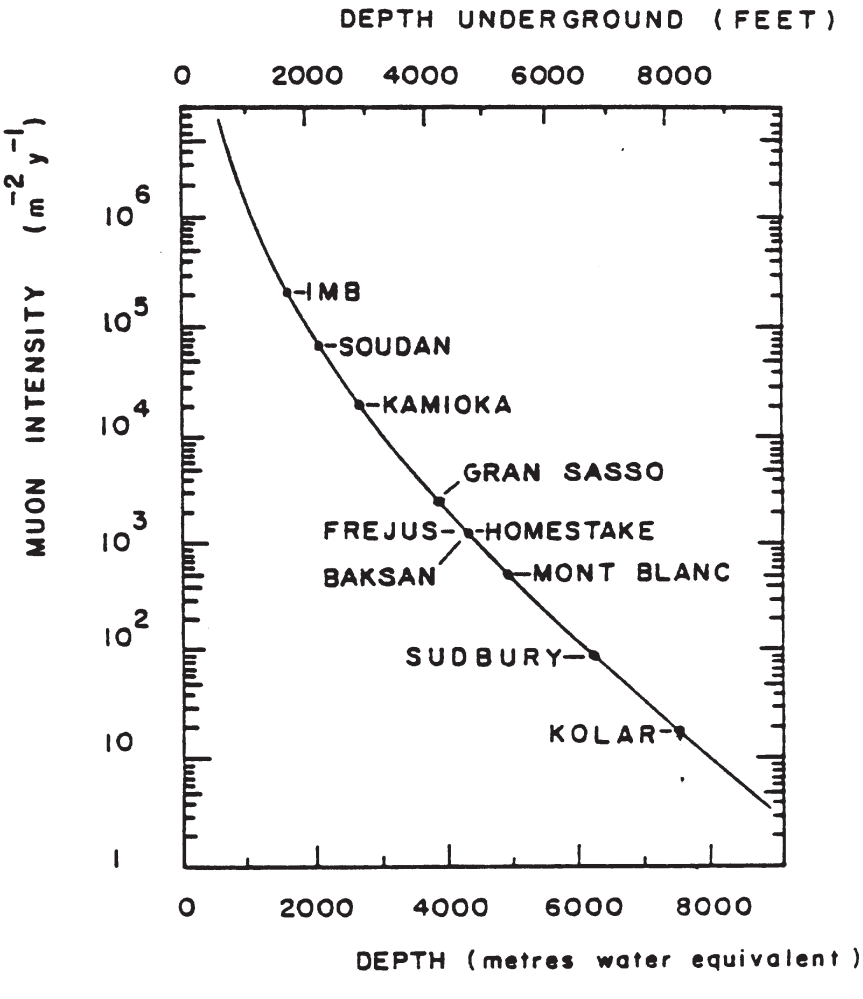

Table 4.1: **High energy gamma-ray fluxes from norite [48].**

E_γ (MeV)	Measured Flux gamma $m^{-2}d^{-1}$	Calculated Flux $m^{-2}d^{-1}$
4.5-5	510$\pm$200	
5-7	360$\pm$200	320
> 7	180$\pm$90	250
> 8	< 20	15

mainly happen in high density materials (such as the PMT support structure and the cavity wall) because α-particle tends to stop in low density materials (such as water) before undergoing such interactions. The norite rock and the concrete used to construct the cavity, whose ^{238}U and ^{232}Th concentration levels are of the order 10^{-6} g/g, are the dirtiest materials in the SNO detector. The flux of high energy gamma-rays from the norite rock at the 5400 feet level of the Creighton mine has been measured with NaI and BGO detectors [80] and is given in table 4.1. The calculated results also shown in table 4.1 agree with the experimental data, which gives the confidence in the Monte Carlo code used below to estimate the background level due to these high energy gamma-rays.

Obviously shielding is needed to prevent these high energy gamma rays from coming into the D_2O region. One layer of shielding is 8000 tons of light water which fills the whole cavity and surrounds the acrylic vessel. The minimum thickness of this water shielding is $\approx$ 400 cm at the waist and the bottom of the vessel.

Monte carlo simulation of high energy γ-rays from the cavity wall is carried out in three steps [81]:

1. A neutron Monte Carlo code is used to simulate the neutron creation, propagation, and capture in the cavity wall. Then the total γ-ray production, binned into 5, 7, and 9 MeV, is calculated based on the number of thermal neutron captures for all elements.

2. The EGS[1] code [82] is used to track 5, 7, and 9 MeVs γ-rays to the PMT sphere (8.5m away from the center of the detector), where the energy and directions of these γ-rays are binned into two histograms.

[1]Electron Gamma Shower

3. The standard Čerenkov Monte Carlo code produced by the collaboration at Queens' university is used to further propagate these γ-rays into the detector following their initial energy and direction distributions.

Following step 2, the estimate is that the numbers of gamma rays arriving at the PMT sphere with energy of 5, 7, and 9 MeV are 35.8, 28.0, and 2.4 per day respectively. Step 3 predicts that a flux of 0.027 γs per day from the cavity wall arrive at the D_2O sphere (600cm away from the center of the detector) with energy higher than 5MeV. Taking into account the reconstruction error of the vertex fitter, the background level due to the high energy γ-rays from the cavity wall is estimated to be 0.11 per day above 5MeV detector threshold. However, it is difficult to determine precisely the level of this kind of background because of the large statistical errors due to the relatively small number of events simulated by the Monte Carlo code. The data from the partial-fill operating mode of the detector, where these gamma rays create Čerenkov photons when they pass through the acrylic vessel or water, should be able to provide a rough estimate of the magnitude of this background. Nevertheless, since the numbers of CC and NC events in SNO are expected to be at the order of 30 per day, the contamination due to the high energy gamma rays from the cavity wall can be ignored.

4.3.2 Backgrounds from the PMT region

The 9600 photomultipliers together with their supporting structure, which is a geodesic sphere made of stainless steels, are also sources of high energy gamma rays. As shown in table 4.2, the materials used to make the photomultipliers have high concentrations of ^{232}Th and ^{238}U. The natural radioactive decays of these two nuclei and their daughters produce α-particles, which then produce free neutrons through (α, n) reactions. The captures of these free neutrons on the high density materials lead to high energy gamma rays. The other major source of high energy gamma rays from the PMT region is (α, pγ) reactions on some light elements, especially Al [83]. This background source is unique to the PMT region since some parts of the photomultiplier, especially the reflector, contain high levels of aluminum. Monte carlo simulations have been carried out to estimate the number of high energy gamma rays from the PMT region with the assumption of the ^{232}Th and ^{238}U concentration levels listed in table 4.2 [81], the results are presented in table 4.3.

Table 4.2: **Masses and activities of PMT components, cited from [81].**

Component	Mass(g)	Th(μg)	U(μg)
Bulb	540	16.2	16.2
Neck	60	1.8	1.8
Pinout glass	34	19.7	47.4
Ceramic spacers	20	31.4	33.4
Dynode	90	0.74	0.41
Gel	80	<1.84	<0.96
capacitors	6	1.65	0.48
Resistors	0.21	0.13	0.25
Kapton	0.7	0	0

Table 4.3: γ**s per year from the PMT region, cited from [81].**

Reaction	5 MeV	7 MeV	9 MeV
(α,n) / (n,γ)	13685	31071	11458
(α,pγ)	28971	10150	490

Given the estimate of the number of high energy gamma rays from the PMT region, the standard SNOMAN code has been used to determine the contribution of these γ-rays to the total background level in the SNO detector. Gamma rays were simulated originating from the front glass of the PMTs going into the 4π directions isotropically. These gamma events are able to contaminate the data set of CC and NC events in the following two ways:

1. Gamma rays penetrate the 2.5 meters water shielding between the PMT sphere and the acrylic vessel, reaching the D_2O region with enough energy ($E_\gamma > 2.223 MeV$) to photodisintegrate the deuterons. The free neutrons produced by the photodisintegrations of the deuterons are totally indistinguishable from those produced by the NC reactions on an event-by-event basis. Rows 6 and 7 of table 4.4 show respectively the numbers of gammas with energy higher than 2.223 MeV reaching the D_2O region and within 1 meter of the region. These numbers are negligible compared to the number of gamma rays produced by the radioactive impurities in 1000 tons of D_2O, as discussed in the next section.

2. Some of the Čerenkov photons produced by gamma rays may scatter. None of the existing vertex fitters in the SNOMAN code has the algorithm capable of completely eliminating this effect. Misreconstructions of event vertices may place some of these gamma events into the D_2O region. However, Monte carlo simulation shows this effect is fairly small, as seen in table 4.4.

Besides high energy gammas, the most difficult-to-model background in the whole SNO detector also comes from the PMT region. As mentioned before, the photomultipliers used in SNO are made of materials which contain relatively high levels of Thorium and Uranium. The natural radioactive decays of these impurities and their daughters produce low energy electrons and gammas which mimic signals of neutrino-induced events. The largest difficulty in estimating the contribution of this kind of background is the large statistical uncertainty due to the impossibility of generating enough Monte Carlo events. The detailed study of PMT $\beta - \gamma$ events is covered in another chapter (chapter 4).

4.3.3 Conclusion

The number of background events due to high energy gamma rays from the cavity wall and the PMT region should be negligible compared to numbers of NC and CC events.

Table 4.4: **Simulation of high energy gamma rays from the PMT region.** r_γ stands for the radius of sphere penetrated by gamma rays with energy higher than 2.223 MeV. r_{fit} is the distance between the center of the detector and the fitted vertex, using the time fitter in the SNOMAN code.

Energy of gamma	5 MeV	7MeV	9MeV
Number of Monte Carlo events	50000	50000	50000
$r_\gamma < 700cm$	126	272	401
$r_\gamma < 600cm$	2	8	24
$r_{fit} < 600cm$ and $Nhits > 5MeV^2$	1	9	20
Number of events per year	42656	41221	11948
$r_\gamma < 700cm$ (per year)	108	224	96
$r_\gamma < 600cm$ (per year)	2	7	6
$r_{fit} < 600cm$ and $Nhits > 5MeV$ (per year)	0.85	7.5	4.8

Some topological cuts could be imposed to further suppress and measure this background, such as the direction cut, similar to that used in the Kamiokande experiment, which is based on the fact that external gamma rays have to go inwards to the D_2O region in order to make event triggers while the directions of CC and NC events are isotropic.

4.4 Internal Backgrounds

Internal backgrounds in the SNO detector refer to those background events occurring in the regions enclosed by the PMT sphere, which includes 1000 tons of heavy water, 1668 tons of light water and 30 tons of acrylic vessel. The major backgrounds in these regions arise from naturally occurring radioactivities. The main isotopes of interest are those that decay to produce high energy electrons and gammas (although much less energetic than those from the cavity and PMT region)since

- Energetic electrons, which are capable of creating Čerenkov photons, mimic the signals from electrons produced by the charged current reactions so that they mask the low energy part of the CC spectrum. As mentioned in chapter 2, the accurate measurement of the CC energy spectrum around the detector's threshold is useful in distinguishing among different solutions to the solar neutrino problem.

- Gamma rays with energy higher than 2.223 MeV are capable of producing free neutrons, which are totally indistinguishable from neutrons produced by the neutral current reactions, through photodisintegrations of deuterons.

Nuclei undergo alpha (strong), beta (weak), and gamma (electromagnetic) decays because by these decays they could go to a somewhat lower energy state which is more stable. For example, the binding energy per nucleon decreases when Z increases for heavy nuclei, thus it is energetically more favorable for a heavy nucleus to undergo an alpha decay to produce two lighter nuclei. An alpha decay changes A (atomic number) value of a nucleus by 4 and Z (proton number) value of a nucleus by 2. A beta decay changes Z value of a nucleus by 1 and does not change its atomic number. A gamma decay only de-excites a excited state and does not change its A and Z values.

There are only 4 possible decay chains relevant to the SNO experiment: namely the thorium, neptunium, uranium and actinium decay chains. Such a decay chain will be observed in nature only if the longest-lived member in the chain has a half decay life comparable to the age of the Earth. For example, the neptunium decay chain does not exist in nature as its longest-lived member, ^{237}Np, only has a half-life of 2.14×10^6 years, which is much shorter than the age of the Earth ($\approx 4.5 \times 10^9$ years). On the other hand, radioactive species with A=230 are abundant on earth as they come from ^{238}U decays which have half lives of 4.47×10^9 years.

According to the semi-empirical mass formula for nuclei, for a fixed A, there exists a Z_{min} which corresponds a largest binding energy among nucleons or a lowest mass of the nucleus. Normally a beta decay tends to push Z value of a nucleus to Z_{min}. A natural decay chain normally consists of many alpha decays followed by one or two beta decays. For example, alpha decays of nuclei with A=230 terminate on $^{214}_{82}$Pb. For a nucleus with A=214, its Z_{min} equals 84. Thus $^{214}_{82}$Pb has to undergo two beta decays to get its beta stable state.

Many decay chains stop at Pb or Bi as these two nuclei have so called magic number of protons or neutrons. In the shell model, nucleons are supposed to fill in different energy levels one by one. Experiments show that the energy gaps around these magic numbers (2,8,20,28,50,82,126) are somewhat larger than elsewhere. For example, Pb has a Z value of 82, $^{209}_{83}$Bi has 126 neutrons and especially $^{208}_{82}$Pb, where the thorium decay chain ends, is a so-called double magic nucleus (it has 82 protons and 126 neutrons).

Among the nuclei which undergo $\beta - \gamma$ radioactive decays, we only need to consider those which have long decay half lives, are present in relatively high abundances in the materials used to construct the detector, and have decays in their decay chains which produce gammas energetic enough to break deuterons. This limits the discussion to two heavy nuclei (^{232}Th and ^{238}U) and their subsequent decay chains.

These two heavy nuclei decay via a number of radioactive daughters, with many alphas, betas and electrons being emitted over the chain of the decays. The two decay chains are shown in figure 4.2 and figure 4.3, the data are taken from [84].

Most of decays in these two decay chains only produce α-particles, which do not contribute to the total background level in water since they are not able to produce Čerenkov photons. Much more serious problems come from those decays which produce electrons and gammas. The number of emitted Čerenkov photons and the subsequent number of PMT hits are more or less proportional to the energy of initial electrons and gammas, thus decays with higher Q values are more troublesome than those with lower Q values. As shown in figure 4.2 and figure 4.3, the decay of ^{208}Tl nucleus has largest Q value of decays in thorium chain while the decay of ^{214}Bi nucleus has largest Q value of decays in uranium chain (The decay of ^{210}Tl in the uranium decay chain is ignored because of its small branch ratio.). Figure 4.4 and figure 4.5 show the relative contributions to total background levels for various decays in the two chains. Obviously the decays of ^{208}Tl and ^{214}Bi nuclei play the dominant roles in their corresponding decay chains. Most events of other decays are below the detector's hardware threshold (10 hits). The most troublesome feature of these two decays is not their large Q values, but their capability of producing high energy gamma rays. The decays of ^{208}Tl and ^{214}Bi nuclei are the only $\beta - \gamma$ decays in the two chains which are able to produce gamma rays energetic enough to break the deuterons. Thus the internal background problem is limited to these two decays in various regions. Simplified decay schemes for ^{208}Tl and ^{214}Bi are shown in figure 4.6.

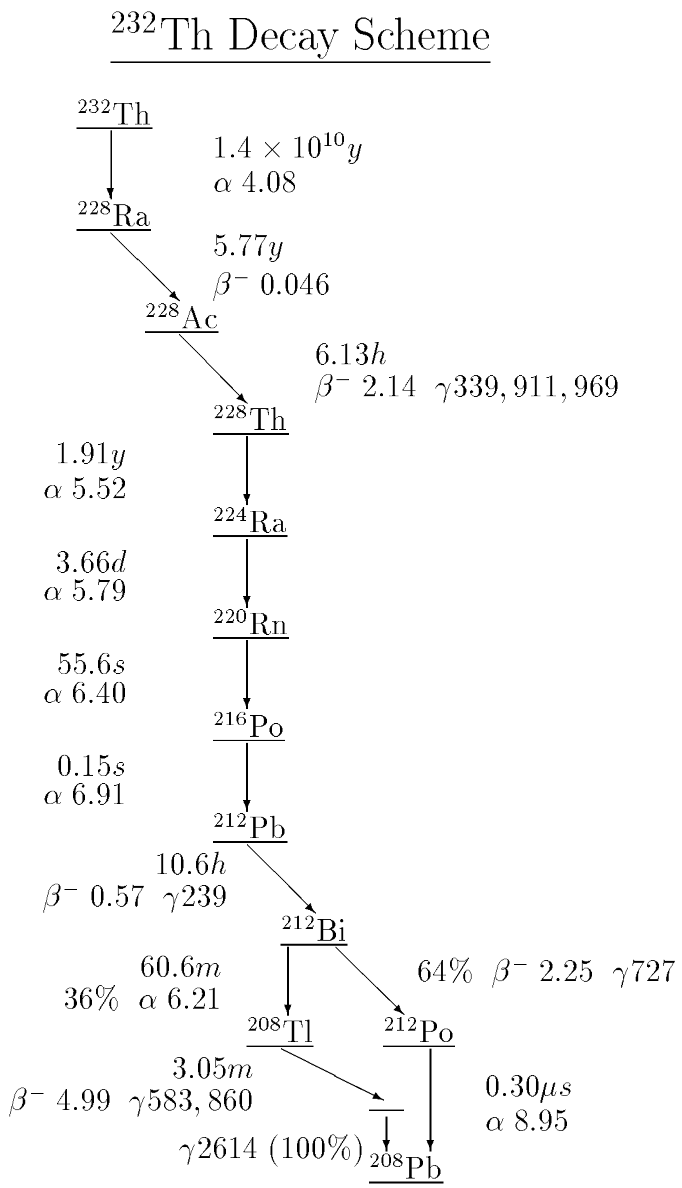

Figure 4.2: The thorium decay chain. All half-lives are shown, with the Q values of beta and alpha decays in MeV, and gamma rays in keV. (Taken from [84]).

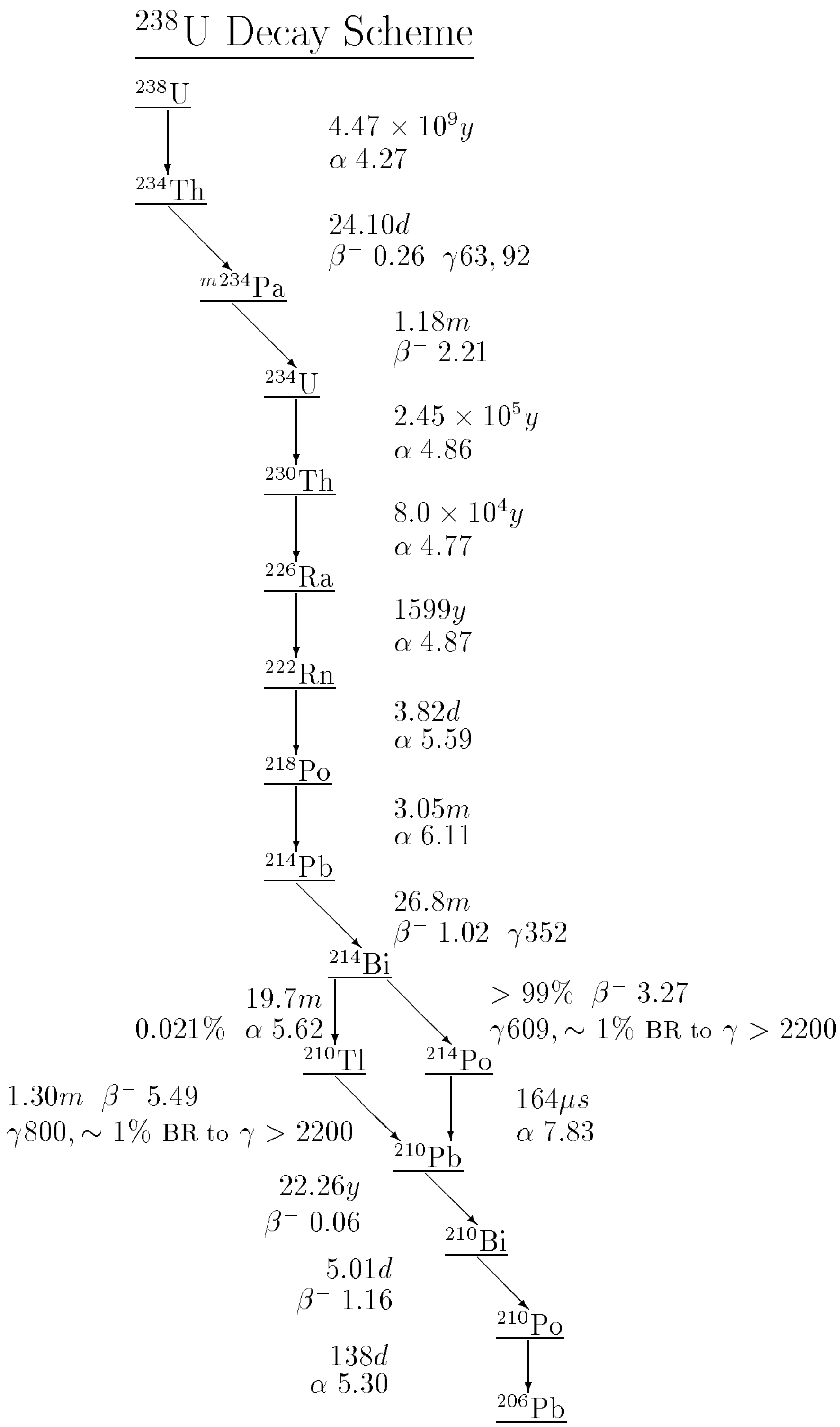

Figure 4.3: The uranium decay chain. All half-lives are shown, with the Q values of beta and alpha decays in MeV, and gamma rays in keV. (Taken from [84]).

More detailed discussion is presented in appendix A.

An energy threshold (5 MeV) will have to be imposed on the data in order to obtain a good signal/background ratio since the number of ^{208}Tl and ^{214}Bi decays , whose Q values are 4.99MeV and 3.26MeV respectively, is much larger than that of NC and CC events. However, high energy gamma rays from these two decays are able to photodisintegrate deuterons to produce free neutrons.

The NC background due to high energy gamma rays is somewhat suppressed by the fact that the cross section for the photodisintegration reaction is much smaller than that of Compton scattering reaction of gamma ray and there are 5 times as many electrons as deuterons in a D_2O molecule. For example, the 2.615 MeV γ-ray from the ^{208}Tl decay has a cross section for photodisintegration of deuteron of 1.2 mb [85] and a cross section for collision with an electron of 125 mb. However, some of the Compton-scattered gammas have enough residual energy to cause photodisintegrations. Monte Carlo simulation shows every 521 2.615 MeV gammas generate one free neutron in the D_2O region. Similar simulation has been carried out for the 2.445MeV gamma rays from the ^{214}Bi decay, the Monte Carlo result is that one free neutron is produced by on average 714 such gamma rays in the D_2O region.

Table 4.5 lists the current estimates of concentration levels of radioactive impurities in various regions of the detector. As discussed before, the major concerns are the decays of ^{208}Tl in the thorium decay chain and ^{214}Bi in the uranium decay chain. The number of these two decays can be calculated with the assumption of secular equilibrium, where the decay rate of daughter nucleus is equal to its parent nucleus. This assumption may be invalid for radioactive nuclei with long decay half lives. Nevertheless, the rough calculation can be carried out as the follows to estimate the number of ^{208}Tl decays per year in the D_2O:

$$Number\ of\ ^{232}Th\ atoms\ in\ D_2O = \frac{(7.94\times10^{-15})\times(8\times10^{9})\times(6.02\times10^{23})}{232} = 2.06\times10^{16} \tag{4.2}$$

$$Number\ of\ ^{208}Tl\ decays = Number\ of\ ^{232}Th\ decays = \frac{(2.06\times10^{16})\times\ln\ 2}{1.4\times10^{10}}\times0.36 = (3.65\times10^{5})/year \tag{4.3}$$

Similar calculations have been done to estimate the number of radioactive decays in the detector with results shown in table 4.5. Figure 4.7 shows energy spectra for CC and NC events and backgrounds from various regions of the detector with these assumed contam-

Figure 4.4: **Nhits spectrum of various decays with Q values larger than 2MeV in the thorium decay chain.** 1800 ^{208}Tl decay events were generated at the center of the detector using standard SNOMAN code, the numbers of Monte Carlo events for other decays are proportional to their relative branch ratios. Solid line stands for the ^{208}Tl decay while dashed and dotted lines stand for the ^{212}Bi and the ^{228}Ac decays respectively. A hardware threshold of 10 Nhits is imposed. Energy scale $\approx$ 9 Nhits/MeV.

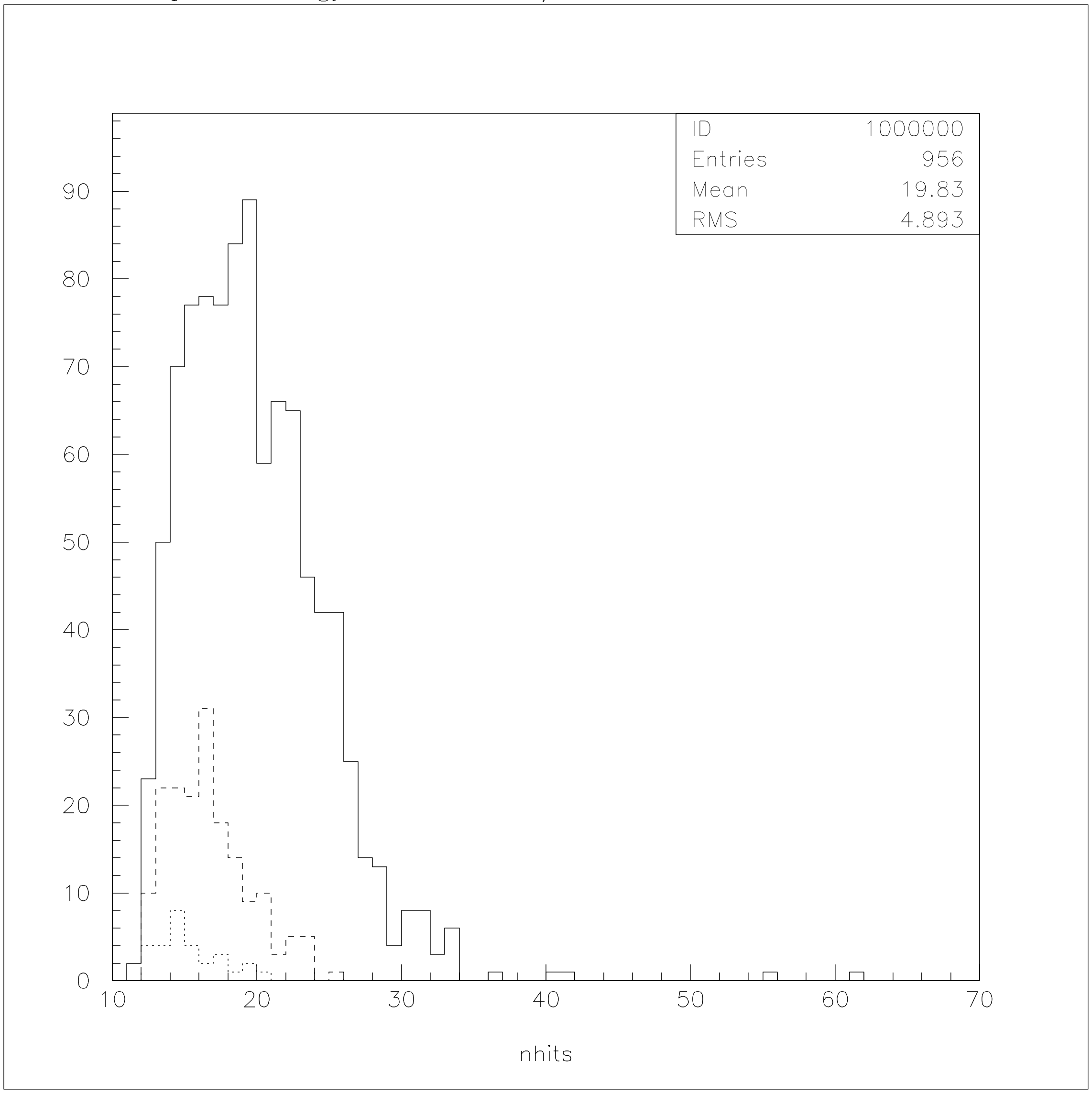

Figure 4.5: **Nhits spectrum of various decays with Q values larger than 2MeV in the uranium decay chain.** 15000 ^{214}Bi and 15000 ^{234}Pa decay events were simulated using the standard SNOMAN code. The solid line stands for the ^{214}Bi decay while dashed line stands for the ^{234}Pa decay. A hardware threshold of 10 Nhits is imposed. Energy scale $\approx$ 9 Nhits/MeV.

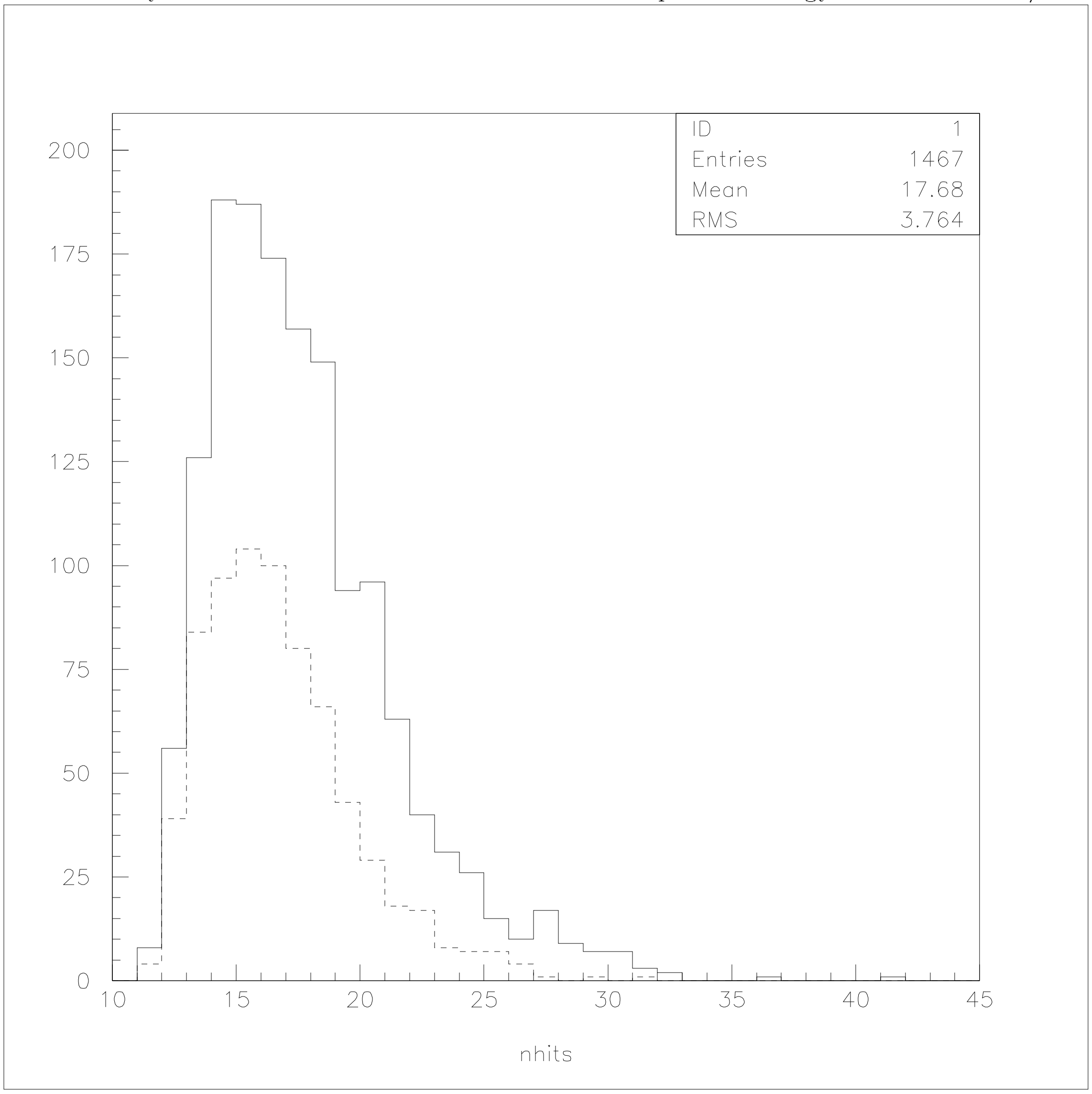

Figure 4.6: **Simplified decay schemes for ^{214}Bi and ^{208}Tl, taken from [48].**

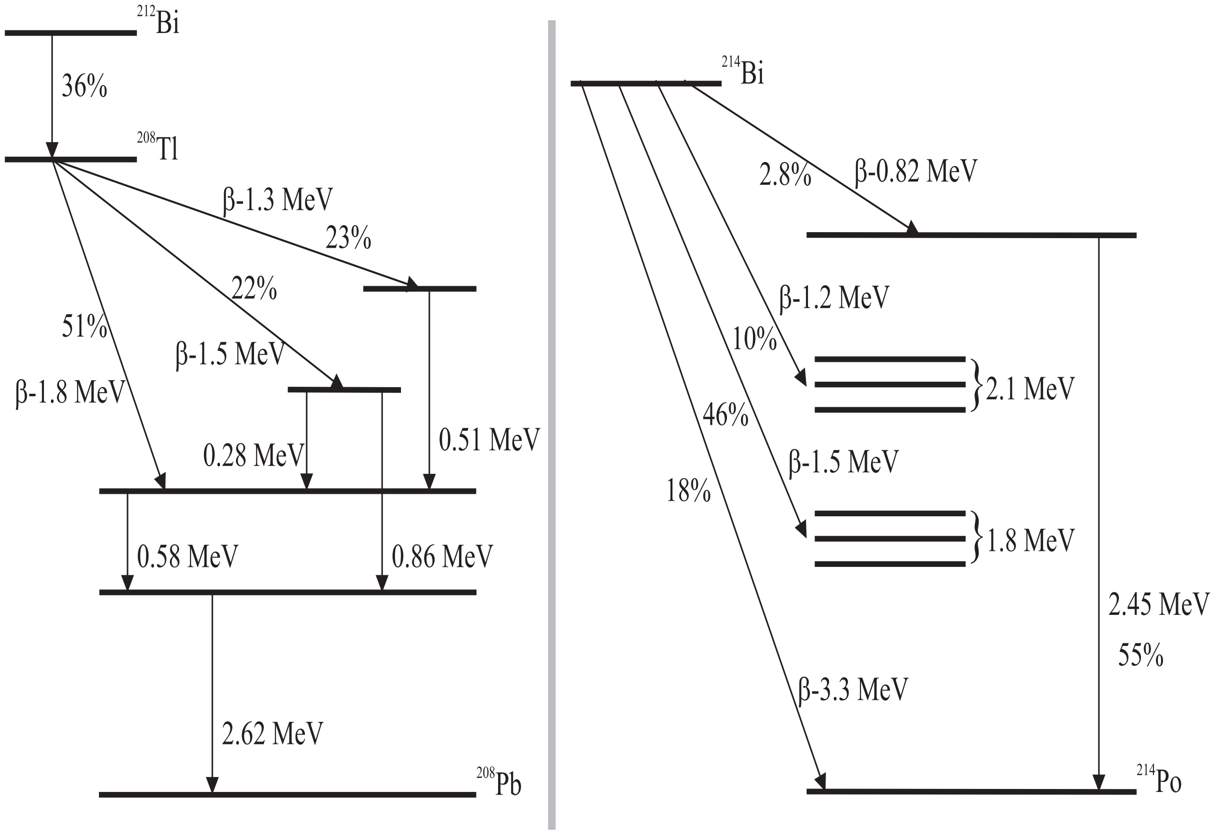

ination levels. CC and NC events become dominant above 52 hits. The only significant background above this threshold is due to the free neutron produced by high energy gamma rays. Taking into account the fact that the branching ratio of ^{208}Tl decay is 36% and only 1.54% of ^{214}Bi decays produce gamma rays energetic enough to photodisintegrate of deuterons, the expected levels of thorium and uranium concentrations in the D_2O produce 252 and 95 free neutrons respectively (which is much smaller than the number of neutrons (6570) produced by the neutral current reactions per year.). Gamma rays from the decays of ^{208}Tl and ^{214}Bi in the AV produce 114 and 36 free neutrons respectively in the D_2O. Since Monte Carlo simulation shows that half of these neutrons escape from the D_2O region and the other half are captured within 50 cm of the acrylic vessel, a simple fiducial cut is able to reject almost all of these. The number of free neutrons produced by gamma rays coming from the regions outside the AV is negligible because of short attenuation lengths of gammas in the AV and the light water.

The only major backgrounds in SNO excluded in figure 4.7 are the ^{208}Tl and ^{214}Bi decays in the PMT region, which are discussed in the next chapter.

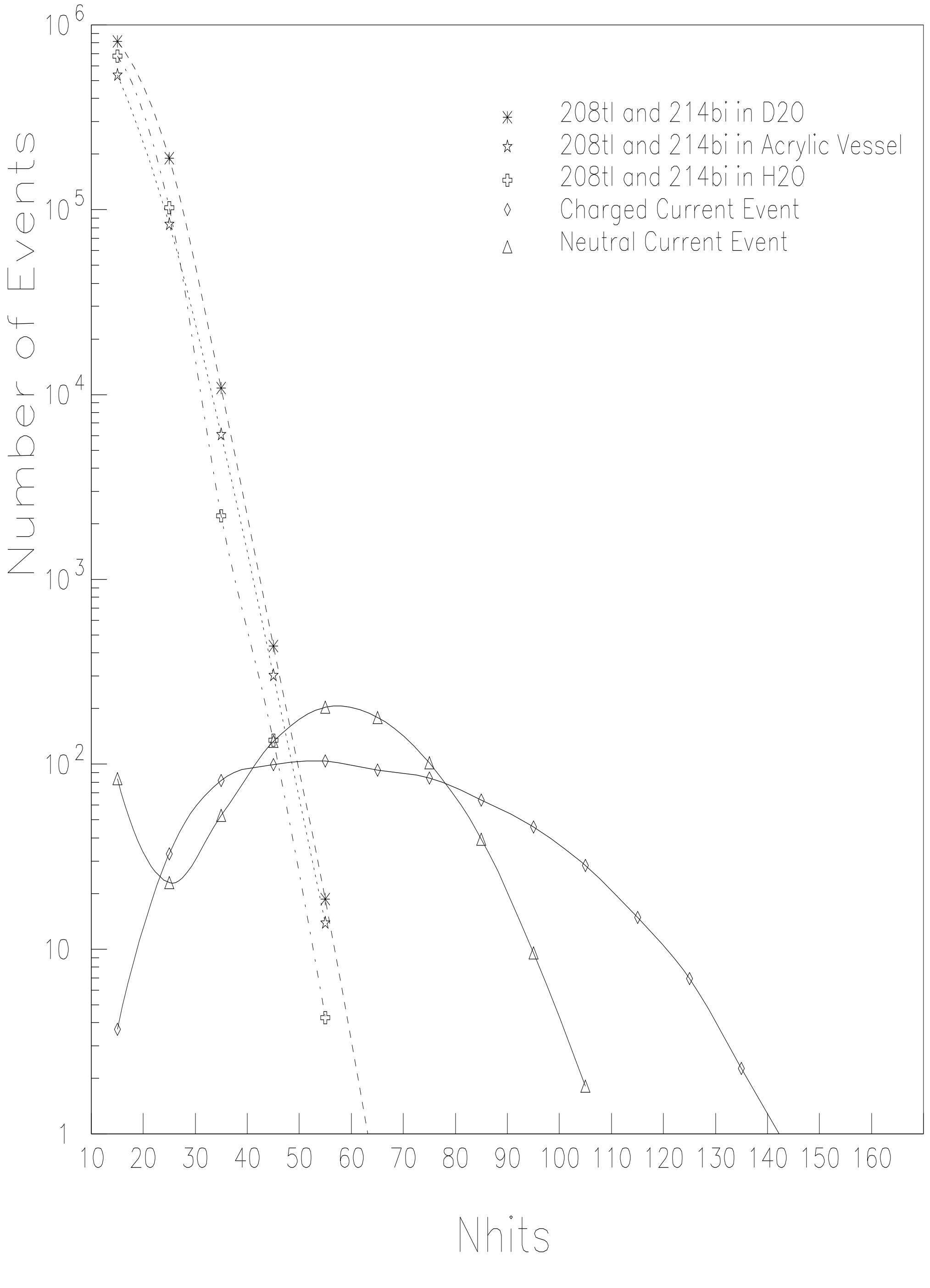

Figure 4.7: **Event energy distribution from a year data, reconstructed inside 600cm per year per 10 hits.** Unit=nhits (number of PMT hits), The CC energy spectrum assumes a neutrino flux equal to $\frac{1}{2}$ of the SSM value while the NC energy spectrum assumes the SSM rate and that 2 tonnes of salt has been added to the heavy water.

Table 4.5: **Number of the ^{208}Tl and the ^{214}Bi decays per year**

region	Thorium Concentration(g/g)	^{208}Tl decay per year
1000 tons D_2O	7.94×10^{-15}	365000
30 tons Acrylic Vessel	4.6×10^{-13}	6.35×10^{5}
8000 tons H_2O	7.52×10^{-14}	2.75×10^{7}
region	Uranium Concentration(g/g)	^{214}Bi decay per year
1000 tons D_2O	11×10^{-15}	4.38×10^{6}
30 tons Acrylic Vessel	6.3×10^{-13}	7.5×10^{6}
8000tons H_2O	8.6×10^{-14}	2.7×10^{8}

4.5 Water System

Both heavy and light water have to be purified in order to achieve the radioactive contamination levels described in the previous section, and assayed in order to determine the background rate. The purification and assay of water is likely to be a continuous process throughout the lifetime of the experiment since the pure water is a very good solvent and there will be constant leaching of contaminants from various detector components into the water (There is certain probability that the water system will have to be stopped in order to check the source of radon breakthrough which happened in the Kamiokande experiment.). The time needed to circulate 1000 tonnes of heavy water is expected to be around 4 days.

The purification and assay of water is done with a combination of different systems, all integrated into an overall water system which allows different techniques to be used at different times. Two types of techniques have been developed to extract radioactive impurities from the water:

1. **RO technique**

   Reverse Osmosis (RO) [86] is the best known technique for removing heavy nuclides from a solvent. It works by applying an external pressure to counteract the osmotic pressure established across a membrane with very small pores. By the application of this reverse osmotic pressure, there is a concentration of solute molecules on the retentate side, and hence the solvent has impurities removed. There are several problems with this technique, the most serious of which is the fact that RO system extracts the added $MgCl_2$ as well as the elements of the Th and U decay chains.

Thus the RO system can not be used when salt is in the detector. This leads to the development of the second technique.

2. **Ion exchange**

   Manganese dioxide (MnO_2) and hydrous titanium oxide (HTiO) are well known ion exchanger for the heavier elements. The use of small acrylic beads coated with MnO_2 enables the water system to extract both the ^{224}Ra in the Th decay chain and the ^{226}Ra in the U decay chain with good efficiency. The major problem about this technique is that it is not able to remove Rn which is present in the cavity. The HTiO is used in a technique known as seeded ultra-filtration, or SUF [87], which is able to extract ^{224}Ra, ^{226}Ra, ^{228}Th, and ^{212}Pb. The major concern of the SUF technique is the possible radioactivities introduced by the complex chemical procedures.

Various assay techniques have been developed to measure the radioactive concentration levels in the water:

- Extraction of ^{222}Rn by a vacuum degasser, followed by α counting in a Lucas cell (an acrylic cell lined with zinc sulphide scintillator).

- Extraction of ^{224}Ra and ^{226}Ra on MnO_2 beads, followed by the emanation and α counting of the radon daughters.

- Concentration of ^{212}Pb complex by reverse osmosis, followed by the precipitation of lead chromate to make a source for β-α coincidence counting [88].

- Extraction of ^{224}Ra, ^{226}Ra, ^{228}Th, and ^{212}Pb by seeded ultrafiltration, followed by the use of a liquid scintillator for β-α coincidence counting.

A common problem with many of these assay techniques is that they do not assay the thorium or uranium chains at the points where they cause trouble in the detector, the decays of ^{208}Tl and ^{214}Bi. In such cases, the assumption of secular equilibrium has to be made. In addition, almost all of these techniques require certain amount of time to accomplish the assay, during this time some of radioactive nuclei decay and the assay efficiency is decreased. I would also point out that all of the techniques mentioned above require complex chemical procedures and a check based on other techniques may be helpful. The next section describes some of the so-called 'real time' assay techniques which have been developed to avoid these problems.

4.6 Direct Assay Techniques

Direct assay techniques analyze the hit patterns of PMTs produced by background events inside the detector and extract information which enables us to determine background rates in SNO. These techniques provide efficient and simple ways to monitor background levels in real time and in situ; they do not involve any of the hardware and complex chemical procedures described in the previous section, and thus are much easier to perform and do not have the risk of introducing extra background into the detector. However, all of these techniques are based (at present) on the Monte Carlo simulation of the detector by the SNOMAN code. Thus the performance of techniques heavily depends on the accuracy of the SNOMAN simulation. Several calibration sources have already been built in order to check the difference between reality and the prediction of the SNOMAN code. Hopefully, the data from the calibration sources will give us confidence in the performance of SNOMAN and the robustness of these direct assay techniques.

4.6.1 Fitting the Background Wall

From a study of the energy spectra generated by different backgrounds in the detector, an assay technique has been proposed [120] to use the shapes of background walls to determine the relative concentration of thorium, uranium and possibly potassium. It is well known that the spectra of ^{208}Tl and ^{214}Bi decays are different since the two decays have different Q values (4.99 MeV for ^{208}Tl decays and 3.27 MeV for ^{214}Bi decays). As shown in figure 4.8, the energy spectrum of ^{208}Tl decays peaks around somewhat higher nhits than that of the ^{214}Bi decays and the spectral width of the ^{208}Tl decays is somewhat larger than that of the ^{214}Bi decays since every decay branch of ^{208}Tl has a high energy gamma ray which normally produces a larger spectrum width than an electron. Given the combined energy distributions of ^{208}Tl and ^{214}Bi decays, a standard chi square fitting method can be carried out to determine the relative ratio of theses two decays. Since these two decays are the dominant backgrounds in the detector, the concentration levels of thorium and uranium can be deduced.

As shown in figure 4.8, the difference between two spectra at low energy (14-25 nhits) is critical in distinguishing between two types of decays. However, the SNO detector is not optimized for such low energy events and the performance of the SNOMAN code is most fragile at this region. A more serious problem for this technique is that at such low energy,

Figure 4.8: **Energy spectra of ^{208}Tl (dashed line) and ^{214}Bi (solid line) decays in the D_2O with a R_{fit} cut: $R_{fit} < 400cm$ (R_{fit} is distance between the fit vertex and center of the detector).**

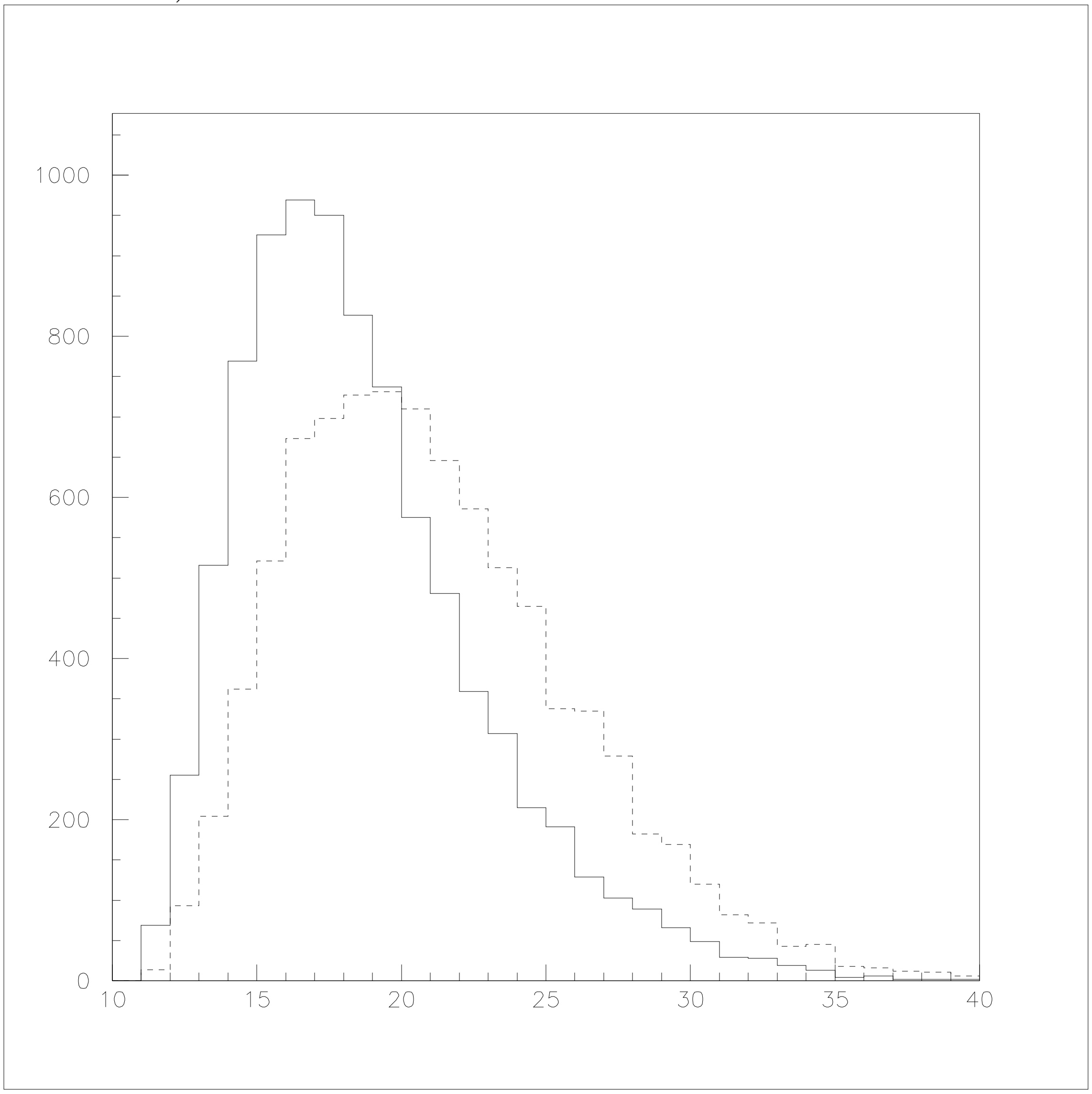

the spectra of ^{208}Tl and ^{214}Bi decays are severely contaminated by events such as decays of ^{40}K (Q value = 1.35 MeV) which is abundant in the salt, decays of other elements in the thorium and uranium decay chains (^{228}Ac, ^{212}Bi and ^{234}Pa) and mis-reconstructed events which occurs outside the AV (especially the beta-gamma decays from the glass of the PMTs). Despite all these problems, this technique of fitting the background wall may give an order of magnitude estimate of the background levels in the D_2O.

4.6.2 Look Back Technique

Another technique uses a time correlation measurement to determine the level of NC background in the detector. As mentioned before, most NC backgrounds are induced by high energy gamma rays from ^{208}Tl decays in the thorium decay chain and ^{214}Bi decays in the uranium decay chain. These two decays always produce single electron and multiple low energy gamma rays along with the high energy gamma rays which cause photodisintegrations of deuterons. The resulting free neutrons are thermalized in the D_2O and then captured on ^{35}Cl (in a salt run), which leads to a cascade of high energy gammas (E_{total} = 8.6 MeV) just as a neutral current event. However, for such a NC background event, there is a low energy signal (^{208}Tl or ^{214}Bi decay without the high energy gamma) followed by a high energy signal (neutron capture on ^{35}Cl) in the detector separated by a certain time. This delayed coincidence relation could in principle be used to distinguish between the free neutron produced by the photodisintegration of the deuteron nucleus and that produced by neutrino-disintegration of the deuteron nucleus. The mean time for a free neutron to reach thermal energy in the D_2O is 125 ns [61]. Figure 4.9 shows the time (thermalization and capture time) and the distance between the production of the free neutron and the capture of the free neutron with salt in the D_2O.

The procedure for this technique is as follows: from the time of a neutron capture signal, look back for 5 ms to see whether there is a low energy signal during that period. A more stringent cut can be imposed to require that such low energy event is reconstructed within 100 cm of the neutron capture vertex. The major problem of this technique is that its efficiency is low. Q values of ^{208}Tl decay (4.99 MeV) and ^{214}Bi decay (3.27 MeV) are so low that very few events can make signals with nhits above the hardware threshold (10 nhits) without their high energy gamma rays. Monte Carlo shows that only 5% of ^{208}Tl decays and almost none of ^{214}Bi decays can make a visible signal in the detector after losing the high energy gamma. None of vertex fitters currently in the SNOMAN

Figure 4.9: **The time (unit=ns) and distance (unit=cm) distributions between the production of the free neutron and the capture of the free neutron with 2 tonnes of $MgCl_2$ in the D_2O.**

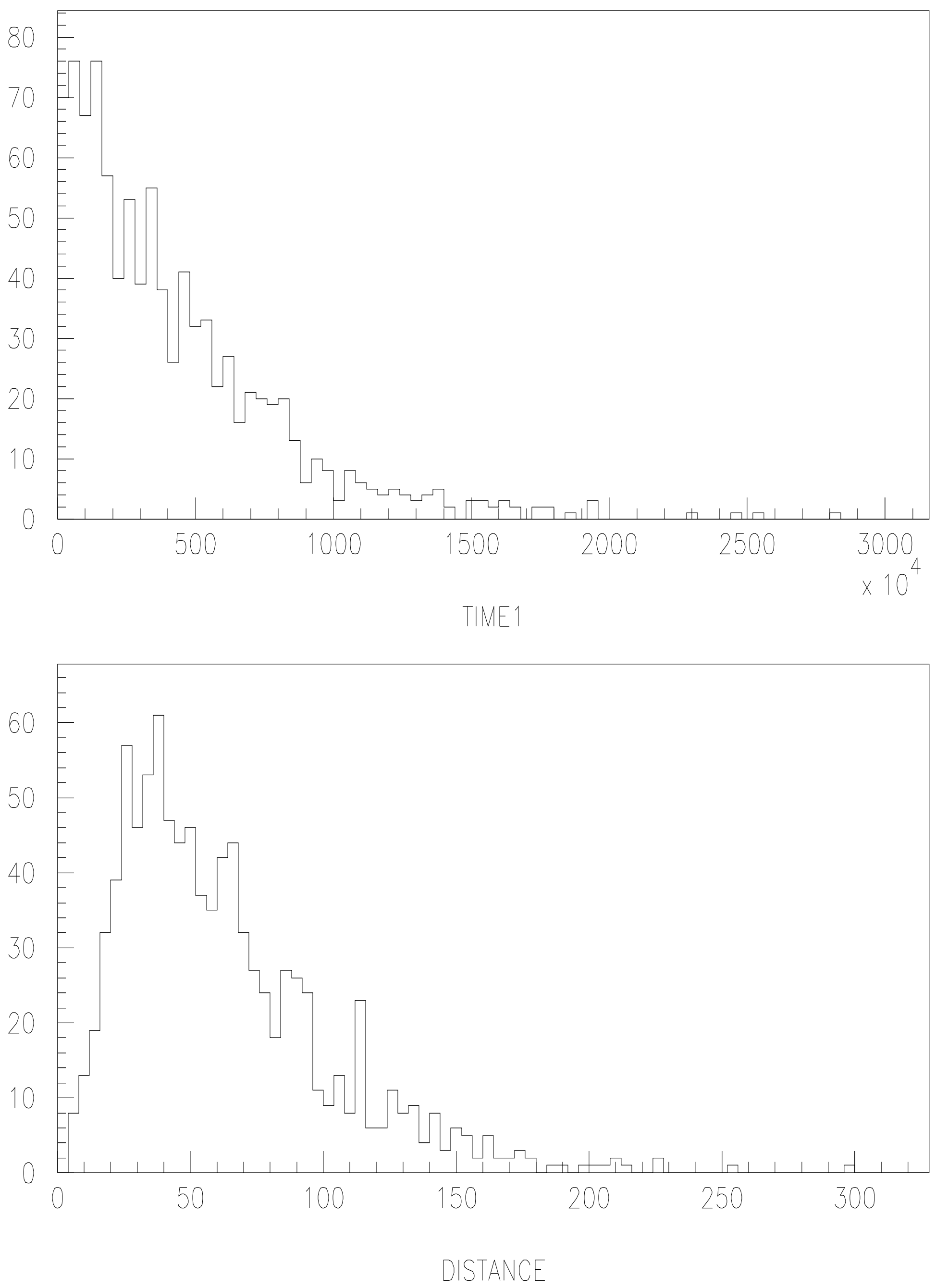

code is able to reconstruct such low energy events with the error of 100 cm. However, the contamination to this 5 ms window is small. The major concern is the decay of ^{40}K in the D_2O and the beta-gamma decays from the PMT glass. The decay rate of ^{40}K is 0.07 ms^{-1} and only 2% of these decays are visible to the detector. The rate of beta-gamma decays from PMT glass is around 1 KHz and only 5% of these signals are visible.

Although with some difficulties, the pursuit of this look back technique may be worth while since it is the only known technique capable of identifying the NC background on a event-by-event basis. A look back hardware trigger will be installed along with the standard detector trigger to keep records of events with nhits smaller than 10 for a certain period in order to wait for the possible delayed neutron capture signal.

4.7 Summary

The major backgrounds in the SNO detector come from ^{208}Tl and ^{214}Bi decays in the thorium and uranium decay chains. Based on simulations carried out with the current version of the SNOMAN code, a detector threshold of 5 MeV may be needed to be imposed on the data in order to get clean signals of NC and CC events. I should point out that without data from calibration sources, there are great uncertainties with the performance of the SNOMAN code. Given the expected level of radioactive impurities in the detector, the amount of NC background is on the order of one magnitude less than that of NC events. The largest uncertainty is on the effect of beta-gamma decay events from glasses of PMTs, which is discussed in the next chapter.

Several techniques have been developed to determine background levels in the SNO detector. However, most of them either involve complex chemical procedures or have extremely low efficiencies. A method based on pattern recognition technique has been developed by author to determine background levels while avoiding these problems. This method is described in chapter 5.

Chapter 5

PMT β-γ Backgrounds

5.1 Overview

This chapter tackles possibly the hardest problem in the study of backgrounds in the SNO detector: β-γ decays from the PMT region, especially the 10000 photomultipliers. Although the stainless steel used to construct the PSUP (PMT SUPporting structure) contains high levels of uranium and thorium, the background level due to the β-γ decays from the steel is thought to be fairly low since the supporting structure is behind the photomultipliers and the gaps between the PMTs are covered by the black plastic sheets with low levels of radioactive impurities which prevent light produced outside the PSUP from being detected.

As mentioned before, the photomultipliers used in the SNO experiment are made of materials with relatively high concentrations of uranium and thorium compared to the heavy and the light water, as shown in table 5.1. Approximately, 10000 photomultipliers contain 0.3456 grams of uranium and 0.12 grams of thorium, which are much higher than the corresponding values in 1000 tonnes of heavy water (7.94×10^{-6} grams of thorium and 1.1×10^{-5} grams of uranium at the purity levels expected in SNO). Thus 2.5 meters of water shielding is needed to separate the much cleaner D_2O region from the highly radioactive PMT region. The main difficulty in the study of these PMT β-γ backgrounds originates from two factors:

- It is almost impossible to measure accurately the amounts of thorium and uranium in all of the photomultipliers, thus there is a big uncertainty in the absolute radioactivities in the PMTs.

Table 5.1: **Measurements of radioactivity in a photomultiplier used in SNO.** The values, averaged over all components of the photomultiplier, are given in ppb by mass. The mass of a photomultiplier is around 800g, cited from [90].

Measurement	^{238}U	^{232}Th
Guelph	47.6 ± 4.8	19.9 ± 2.5
Birkbeck	38.8 ± 4.6	10.1 ± 1.5
Average	43.2	15.0

- Even if, somehow, the absolute radioactivities in 10000 photomultipliers were known precisely, it would still be difficult to estimate how large the contribution of these radioactivities to the total background level in the SNO detector would be because of the unfeasibility of generating enough Monte Carlo events.

Decays of ^{208}Tl and ^{214}Bi, because they have the largest Q values in the corresponding decay chains, are the only major components of PMT β-γ backgrounds which cause concern. Given the data about uranium and thorium levels in the photomultiplier shown in table 5.1, the numbers of these two decays per year from 10000 photomultipliers can be estimated with the assumption of secular equilibrium in the decay chains. The corresponding values are shown in table 5.2. Using the SNOMAN code, Monte carlo simulations have been carried out to study the effects of these β-γ decays. In order to speed up the simulation, one assumption was made that the total radioactivity in a photomultiplier is evenly distributed throughout it's front glass, taking a glass mass of 800g. This simplification, which condenses all radioactivities in the PMT's front glass (the nearest part to the center of the detector), would result in a overestimation of background levels from PMT β-γ decays. However, it should be kept in mind that the data shown in table 5.1 are very rough measurements on just one photomultiplier, thus it is possible that the real contaminations are higher than those values. The results of Monte Carlo simulations are shown in table 5.2, the deduced one year worth of PMT background data are shown in figure 5.1.

The combination of a energy threshold of 6 MeV (a energy scale of 9 hits/MeV) and a event position cut ($R_{fit} < 600cm$) seems to be able to eliminate almost all of the PMT β-γ backgrounds from the experimental data if both the Monte Carlo simulations and the measurements of radioactive impurities in PMTs are correct. However, these two

Figure 5.1: **Nhits spectra of the PMT β-γ backgrounds reconstructed within the D_2O region.** Black points stands for ^{208}Tl decays and white points stands for ^{214}Bi decays, the time fitter was used. Also shown are the error bars because of the huge scaling factors.

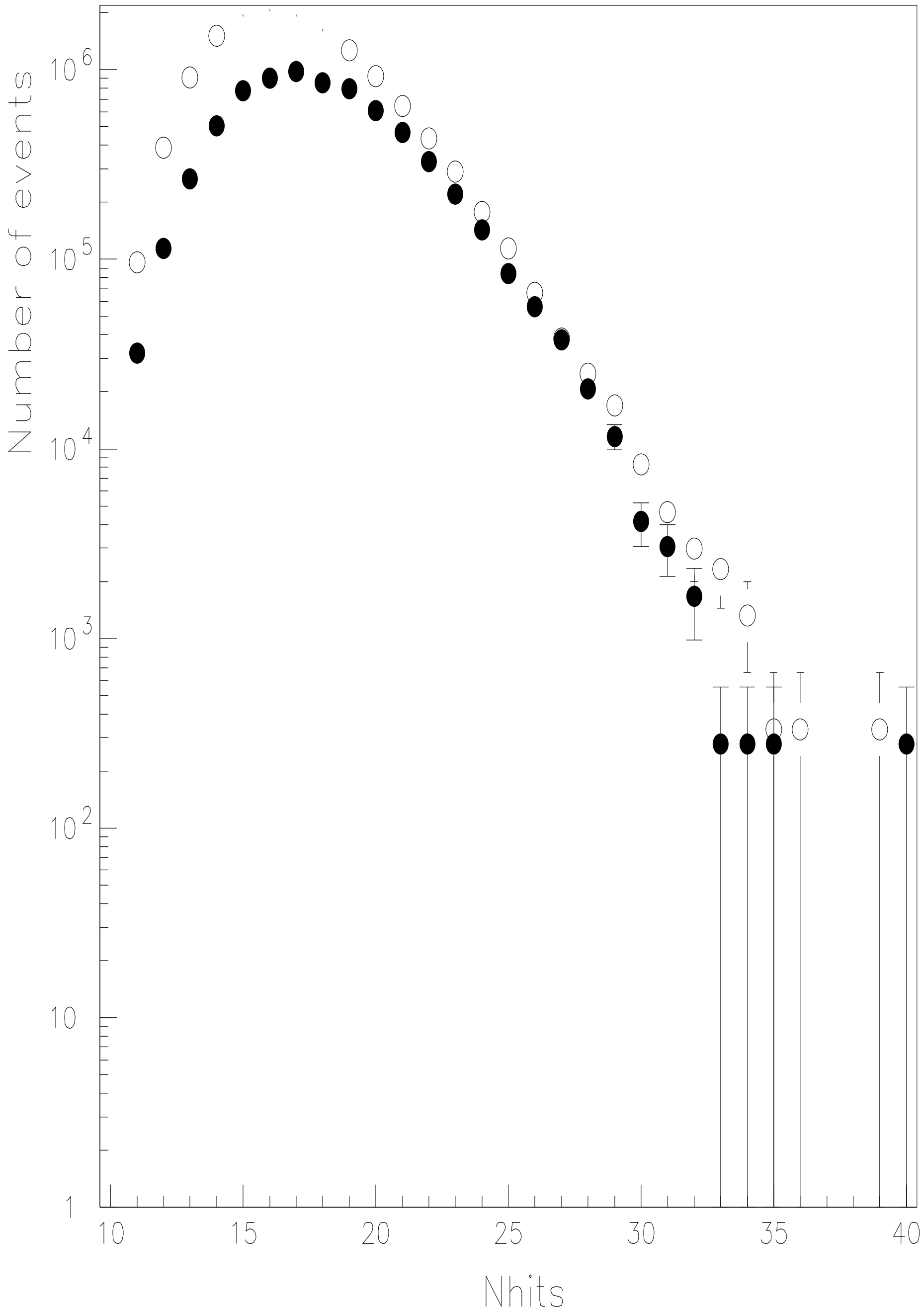

Table 5.2: **Monte Carlo simulation of ^{208}Tl and ^{214}Bi decays in the front glass of SNO PMTs.** Columns one and two show the sources of decays and the expected rates respectively, columns 3 to 6 show the number of Monte Carlo events, the number reconstructed inside the D_2O and inside 4m by the time fitter, and the total number of events over threshold. Columns 7 and 8 show the scaling factor to 1 year, and the expected number of events reconstructed in the D_2O per year. The numbers in brackets are the maximum Nhits in any categories. A threshold of 3MeV is imposed (energy scale: $1MeV \approx 9Nhits$)

Source	Rate (yr^{-1})	Run	In D_2O	In 4m	Total	Scale	in D_2O (yr^{-1})
^{208}Tl	5.55E9	2E7	289(40)	16(32)	9183(42)	277.5	80198
^{214}Bi	1.36E11	2.6E8	141(39)	7(30)	4059(42)	523	7.38E4

conditions are difficult to verify. Even if somehow these two conditions are successfully calibrated, the data still need to be extrapolated to the high energy region in order to get the above conclusion. As shown in figure 5.1, the spectrum of the PMT background has the largest uncertainty at its high energy end. Furthermore, if we want to lower the energy threshold in order to measure the CC spectrum at the energy where it is most sensitive to various solutions to the solar neutrino problem, the PMT β-γ background could become a serious problem. The other concern is the contamination of this type of background in the window used to monitor D_2O backgrounds as described in the next chapter.

The following sections present some techniques which try to tackle the problems mentioned above. Section 5.2 investigates why some of PMT β-γ background events are mis-reconstructed by 2.5 meters into the D_2O region. Sections 5.3 and 5.4 discuss some software tools which are able to reduce these backgrounds significantly by applying new vertex fitter and imposing various special background cuts.

In theory, a high energy gamma ($E_\gamma > 2.223$ MeV) from a ^{208}Tl or ^{214}Bi decay in a photomultiplier could penetrate 2.5 meters of water shielding, reach the D_2O region and produce a free neutron by photodisintegrating a deuteron nucleus. However, the probability of such an event is very small. The attenuation factor of water shielding can be easily estimated:

$$\frac{I}{I_0} = exp(-\frac{l\rho}{\lambda}) = exp(-\frac{250}{11}) \approx 1.3 \times 10^{-10} \quad (5.1)$$

where l and ρ are the thickness and the density of the shielding respectively while λ is the attenuation length of the energetic gamma in water[91]. This huge factor, combined with the small probability of photodisintegration (roughly 1 in 600), makes the number of this kind of NC background negligible when compared with the inherent NC background in the heavy water.

The other kind of background worth mentioning is the double or triple coincident event, i.e., two or three radioactive decay events which happen to occur within a single trigger window. Obviously it is difficult to distinguish between this kind of event and a single event since the DAQ system records all detected photons regardless of their origins and offline analyses often assume they are from single event. This kind of background is able to deposit energy one or two times higher than that of a single decay event in the detector, which may lead to contamination of events above the detector threshold. Furthermore, the normal vertex fitter may perform badly for the double or triple coincident events since the decays could occur in different regions of the detector. The probability for a double coincidence event occurring within a single trigger window can be calculated as follows:

$$P_{double} = P_{single} \times P_{single} = (l(\frac{N_1}{A}))(l(\frac{N_2}{A})) \quad (5.2)$$

where N_1 and N_2 are numbers of individual decays per year respectively, A is number of nanoseconds a year which equals 3.1536×10^{16}, and l is the length of the trigger window which equals 250 ns. Similar calculations have been carried out for triple events. The number of double and triple coincident events are shown in table 5.3 and table 5.5 for various combinations. As shown in table 5.4 and table 5.6, the effect of this kind of background is fairly small compared to the single PMT β-γ decay events. The main reason for this is that normally in this case the vertex fitter (here the time fitter in SNOMAN was used) does not converge to a single point within the D_2O since the detected photons come from sources at different positions (especially for the triple coincident events). Double ^{214}Bi decay events play a major role in this kind of background. A detector threshold of 5 MeV (45 Nhits) should be able to eliminate all of these backgrounds if the predictions of MC simulation are not too far away from reality.

Table 5.3: **Number of double coincident events per year in the SNO detector.**

Decay types	^{208}Tl(D_2O)	^{214}Bi(D_2O)	^{208}Tl(AV)	^{214}Bi(AV)	^{208}Tl(H_2O)
^{208}Tl(D_2O)	0.0011	0.0127	0.00191	0.0226	0.0157
^{214}Bi(D_2O)		0.152	0.022	0.26	0.018
^{208}Tl(AV)			0.0032	0.038	0.0262
^{208}Tl(AV)				0.446	0.31
^{208}Tl(H_2O)					0.214

Events types	^{214}Bi(H_2O)	^{208}Tl(PMT)	^{214}Bi(PMT)	$^{40}K(D_2O)$
^{208}Tl(D_2O)	0.01537	17	410	6
$^{208}Bi(D_2O)$	1.77	193	4723	77
^{208}Tl(AV)	0.257	28	685	11
^{214}Bi(AV)	3.03	330	8086	132
^{208}Tl(H_2O)	2.1	42	1028	100
$^{208}Bi(H_2O)$	20.6	410	10055	901
^{208}Tl(PMT)		2.44×10^5	5.99×10^6	98000
^{214}Bi(PMT)			1.47×10^8	2.4×10^6
$^{40}K(D_2O)$				39400

Table 5.4: **Monte Carlo simulation of double background events in the SNO experiment.** Columns two and three show the number of background events expected per year and MC events respectively. Columns four and five show number of MC events after different rfit cuts. Column six shows number of events per year after the rfit cut. The numbers in parentheses are the maximum Nhits in any category. A Nhits threshold of 27 is imposed (energy scale: 1MeV =9Nhits).

Events type	No. of real events per year	No. of MC events per year	$r_{fit} < 600$ (MC)	$r_{fit} < 400$ (MC)	$r_{fit} < 600$ (per year)
Bi(PMT)Bi(D_2O)	4723	5000	23(35)	12(29)	22
Bi(PMT)Bi(AV)	8086	10000	8(36)	0	6
Bi(PMT)Bi(H_2O)	10055	10000	13(36)	0	13
Tl(PMT)Tl(PMT)	2.44E5	2E5	68(37)	21(37)	83
Tl(PMT)Bi(D_2O)	192	200	0	0	0
Tl(PMT)Bi(AV)	330	500	0	0	0
Tl(PMT)Bi(H_2O)	410	500	1(29)	0	1
Bi(PMT)Tl(D_2O)	410	500	33(37)	9(33)	27
Bi(PMT)Tl(AV)	685	1000	31(41)	3(28)	21
Bi(PMT)Tl(H_2O)	1028	1000	5(32)	0	5
K(D_2O)K(D_2O)	3.94E4	3.94E4	0	0	0
K(D_2O)Bi(H_2O)	161	1000	3(32)	0	0
K(D_2O)Tl(PMT)	9.8E4	9.8E4	12(31)	2(29)	12
K(D_2O)Bi(PMT)	2.4E6	2E6	16(37)	4(31)	19
Bi(PMT)Bi(PMT)	1.47E8	1E7	41(34)	13(34)	603
Bi(PMT)Tl(PMT)	5.99E6	5E6	201(37)	23(36)	240

Table 5.5: **Number of triple events per year in the SNO detector.**

Decay types	Tl(PMT)/ Tl(PMT)	Tl(PMT)/ Bi(PMT)	Bi(PMT)/ Bi(PMT)
Tl(PMT)	11	263	6451
Bi(PMT)	263	6451	163429
K(D_2O)	3	78	1984

Table 5.6: **Monte Carlo simulation of triple coincident events in the SNO detector.** Notation is same to that of double coincident events. A threshold of 3 MeV (27 Nhits) is imposed.

Events type	No. of real events per year	No. of MC events per year	$r_{fit} < 600$ (per year)	$r_{fit} < 400$ (per year)
Tl(PMT)Tl(PMT)Bi(PMT)	263	500	0	0
Tl(PMT)Bi(PMT)Bi(PMT)	6451	6451	0	0
K(D_2O)Bi(PMT)Bi(PMT)	1984	2000	0	0
Bi(PMT)Bi(PMT)Bi(PMT)	163429	163429	4(34)	1(30)

5.2 Causes of Mis-reconstructions

PMT β-γ decay events occur in the PMT region, which is 2.5 meters away from the D_2O region where CC and NC events occur. However, the detector DAQ system records Čerenkov photons regardless of their origins. Thus special software tools, which are called vertex fitters, are required to work offline and deduce the origin of the photons from the pattern of triggered PMTs. By using these vertex fitters, backgrounds from regions outside the acrylic vessel could be separated from events occurring in the D_2O region. At present, the most basic and frequently used vertex fitter in the SNOMAN code is the time fitter. As shown in the previous section, many of PMT β-γ decay backgrounds are mis-reconstructed inside the AV by the time fitter. In order to investigate the reasons behind these mislocations, it is necessary to first outline the procedure of the time fitter [76]:

1. All of PMT triggers are assumed to be caused by Čerenkov photons travelling in straight lines from one point (the event vertex) in the detector to the PMTs.

2. Based on the assumption in step one, a series of equations can be constructed as follows:
$$t_{ic} = \frac{\sqrt{(x_{ip} - x_o)^2 + (y_{ip} - y_o)^2 + (z_{ip} - z_o)^2}}{c'} + t_o \tag{5.3}$$
where i=1,2...N and N is number of hits (or number of triggered photomultipliers); x_o, y_o, z_o, and t_o are the three spatial and one temporal coordinates of the fit vertex

respectively while x_{ip}, y_{ip}, z_{ip} are the three spatial coordinates of the i^{th} triggered (hit) photomultiplier; c' is the average speed of light in the heavy and light water and t_{ic} is the calculated trigger time for the i^{th} detected photon (hit).

3. There always exists a deviation between the calculated and the recorded trigger time of an individual photon due to the finite time resolution of the photomultipliers and electronics. Thus a Chi-square function is defined as the following:

$$\chi^2 = \sum_{i=1}^{N} \frac{(t_{ip} - t_{ic})^2}{\sigma^2} = \sum_{i=1}^{N} \frac{(t_{ip} - t_{ic})^2}{t_{jitter}^2} \tag{5.4}$$

where t_{ip} and t_{ic} are the recorded and the calculated trigger time of the i^{th} detected photon and t_{jitter} is the spread of mean transit time of the photomultiplier. The Levenberg-Marquart nonlinear least-square algorithm (using numerical routines from [92]) is then applied to find the current best fit vertex position and time by minimizing the χ^2 function.

4. Based on the current best fit vertex position and time determined in step 3, the current best calculated trigger time for each detected photon t_{ic} is deduced from equations described in step 2. Then for each triggered photomultiplier, t_{ic} is compared with the recorded trigger time t_{ip}. The single photomultiplier with the largest value of $|t_{ip} - t_{ic}|$ is regarded as the bad PMT hit and discarded from the data set.

5. Step 3 and 4 are repeated cyclely until the calculated times agree with recorded times (by defining a tolerance window around t_{ip}) for all of the remaining photomultipliers. This iteration is fairly effective in throwing away photons which violate the assumption described in step 1. Based on the data from the remaining PMTs, step 3 is carried out for the last time to get spatial and temporal coordinates for the fit vertex.

Figure 5.2 shows the mechanism of production of Čerenkov photons by a charged particle in the SNO detector. The charged particle travels along the direction shown by the arrow at a speed higher than the speed of light in the water. Most probably photons are emitted at directions along the surface of a cone defined along the initial direction of the charged particle with a Čerenkov angle θ (see figure 5.2). If this particle travels exactly in the radial direction, given the spherical symmetry of the SNO detector, the series of equations defined in step 2 of the time fitter are no longer independent of each other. In theory, if all of the hit photomultipliers (no matter how many) are located in a plane perpendicular to the initial direction of the particle, only three independent equations are required to describe the relations between the spatial and the temporal coordinates for all PMTs. It is impossible to solve three equations with four unknown variables (three spatial and one temporal coordinates of the event vertex). Thus such an event could be reconstructed at any point along the initial direction of the charged particle, which may lead to a mislocation. However, the probability for such an event to occur is extremely low. In order for above mechanism to work for PMT β-γ decay events, all of gammas and electrons produced from the radioactive decays must travel in the same radial direction and there are no other photons emitted off the surface of the Čerenkov cone. Both requirements are highly unlikely since the correlations between the directions of gammas and electrons produced by radioactive decays are ignorably small (Even if this does happen, the emitted photons have to travel through the whole detector in order to be detected by the PMTs.) and the angular distribution of emitted photons has a quite large width as discussed in the last chapter.

The assumption made in step 1 of the time fitter is the most vulnerable procedure in the whole algorithm. In reality, not all PMT triggers are caused by Čerenkov photons and not all of the photons travel in straight lines. However, in theory, this false assumption is more or less rescued by the iterations carried out in step 5 which enable the time fitter to throw away some bad PMT triggers which are not caused by straight-line travelling photons. Since the χ^2 fitting procedure is carried out with a fixed point as the starting vertex every time after a bad PMT trigger is purged from the data set, the final results (fit coordinates of the event vertex) are only dependent on the spatial and temporal information of those remaining PMT triggers whose calculated time t_{ic} lie within a predefined window (currently this window is from -8 ns to 4 ns in the standard SNOMAN code) around the recorded time t_{ip}. Thus the result of the fitter is fully dependent on these remaining PMT triggers. In other word, if all of these triggers are caused by photons travelling in straight lines, the event is expected to be reconstructed fairly accurately relative to the true vertex. A parameter is defined to reflect the quality of one PMT hit (trigger):

$$R_{dev} = c' \times (t_p - t_e) - \sqrt{(x_p - x_e)^2 + (y_p - y_e)^2 + (z_p - z_e)^2} \tag{5.5}$$

where x_p, y_p, z_p, and t_p are the recorded spatial and temporal coordinates for this PMT trigger respectively; x_e, y_e, z_e, and t_e are corresponding values for the event vertex, i.e.,

Figure 5.2: **Production of Čerenkov photons by a charged particle travelling in the SNO detector (see text).**

14cm

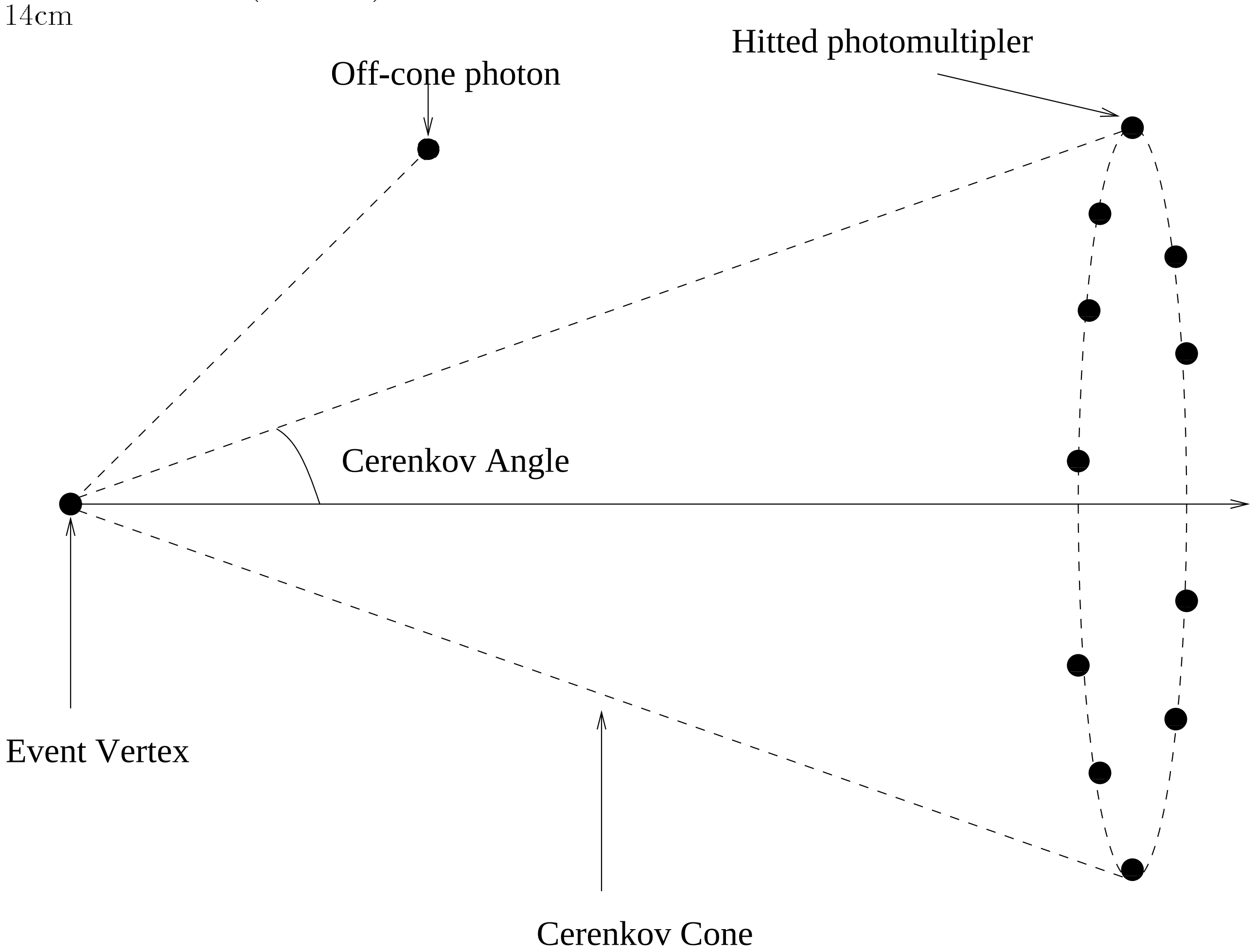

the source vertex where this photon came from, which is not available for real events; and c' is the average speed of the light in the heavy and light water which equals to 22.397 cm/ns. If R_{dev} is approximately equal to zero, the trigger is thought to be caused by a photon travelling in a straight line since there are always fluctuations due to non-zero spread of transit time of the photomultiplier. Figure 5.3 shows R_{dev} distributions for a well fit PMT β-γ decay event before and after the use of the time fitter. The effect of the fitter is obvious: some of the very bad PMT hits, which deviate significantly away from the assumption in step 1, are thrown out from the data set. The largest R_{dev} value for the remaining PMT triggers is no more than 150 cm. Figure 5.4 shows a similar R_{dev} distribution for a badly fit PMT background event, which has a PMT trigger with R_{dev} value of -1000 cm. No wonder this event is reconstructed 10 meters away from the real vertex.

The reasons behind misreconstructions of PMT β-γ backgrounds are complex and often dependent on each other. Theoretically it is difficult to separate them and judge which one plays the major role as the cause of the failure of the fitter. We must use detailed Monte Carlo simulation to show the whole physical picture behind the mis-reconstruction. The following studies are based on 17 MC PMT β-γ decay events mislocated inside the AV, whose full data structures were saved on disk to record every step through their generation, propagation and detection in the detector. Although the number of events is small, they represent all the events mis-reconstructed inside the D_2O from 10 million ^{208}Tl decay events in the glass of the PMTs simulated by the SNOMAN code[1].

The first candidate for a bad PMT hit is PMT noise, i.e. the false PMT trigger caused by dark current in the photocathode. Obviously a PMT trigger caused by noise has no relation at all with the event vertex. The average number of PMT noise hits (2.5) in a trigger window (250 ns) is much lower than the number of PMT hits for events considered here ($>$ 25 hits). However, since we are studying events whose probability to occur is extremely low (17 in 10 million), it is possible that these special events contain many more noise hits than average. Furthermore, it is the fraction of noise hits in the remaining PMT triggers after the time fitter throws out bad hits that determines the quality of the reconstruction. Monte Carlo simulation shows these seventeen events together contain 96 PMT noise hits. Thus on average each of these events has 5.6 noise hits which is more than double the value for a common event. This is expected because the PMT β-γ event,

[1] The 2_09 version of the SNOMAN code was used, where energy scale is: 1 MeV $\sim$ 7 Nhits.

Figure 5.3: R_{dev} **distributions for a well fit PMT β-γ decay event.** Upper plot contains all PMT hits while lower plot only contains the remaining PMT hits after the time fitter is used (see text).

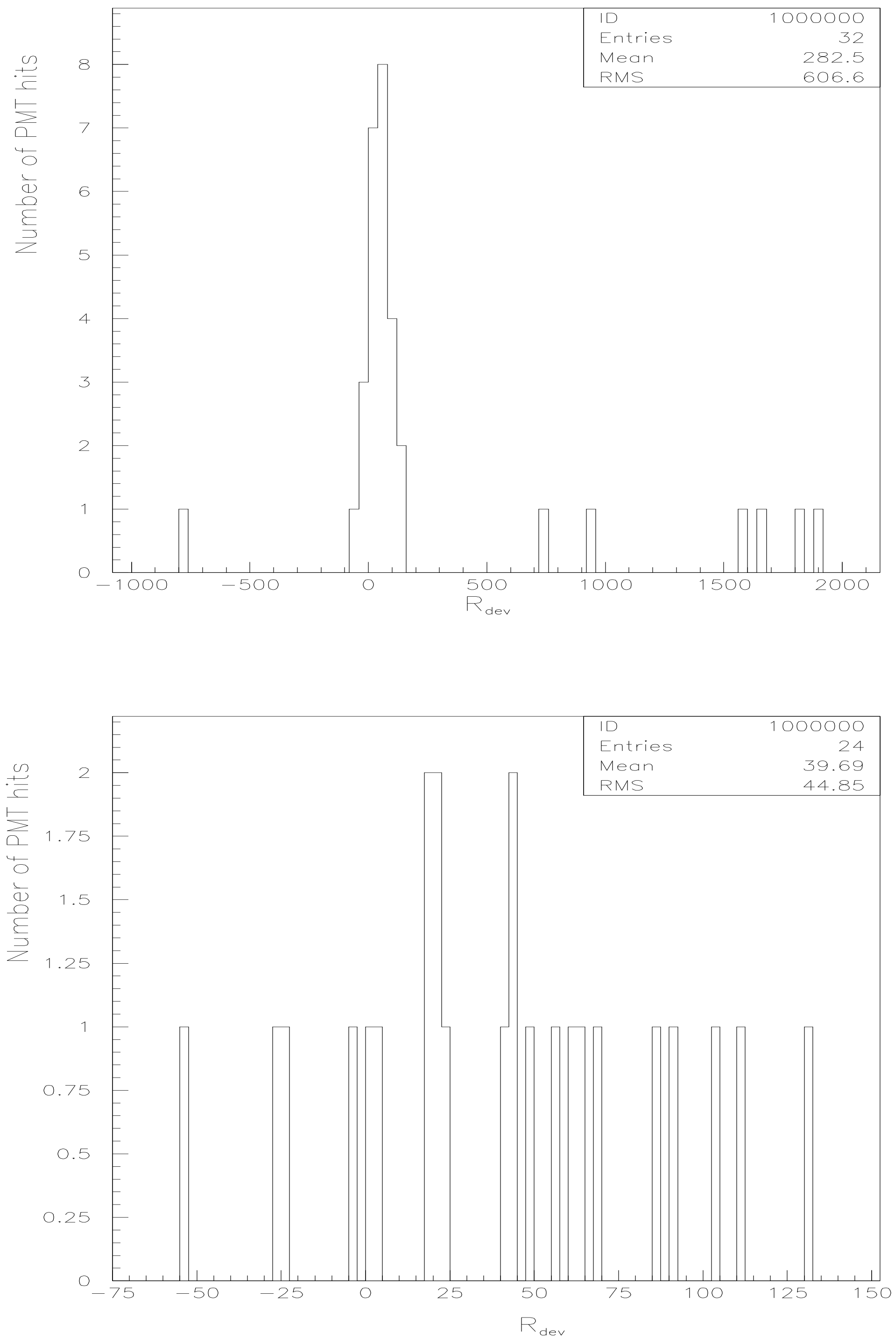

Figure 5.4: R_{dev} **distribution for a badly fit PMT** β-γ **decay event.** Plot only contains the remaining PMT hits after the time fitter is used (see text).

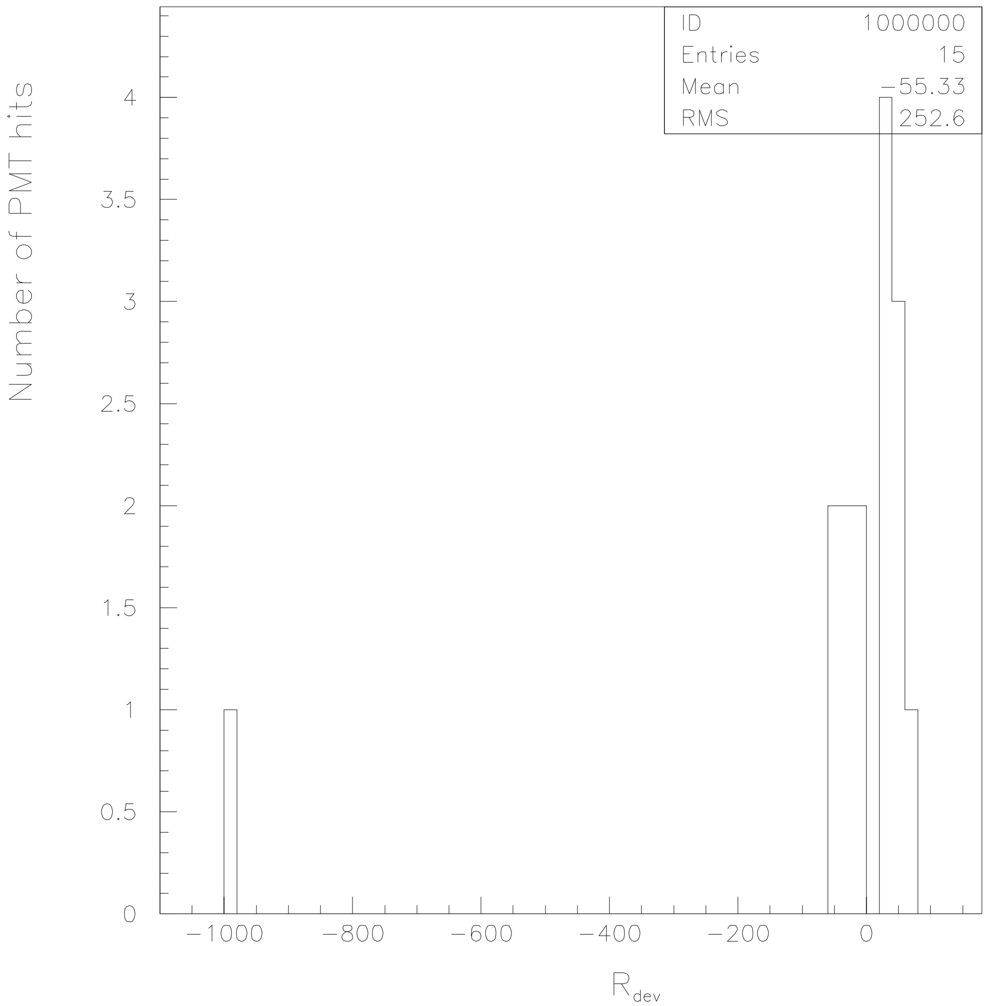

which has an average nhits less than 10, are more likely to be above threshold when they have more noise hits than average. The time fitter successfully purges 87 out of the total of 96 noise hits from the data. Figure 5.5 shows the R_{dev} distribution of a badly fit event where a single noise hit causes the event to be mislocated to a radius of 505 cm. Note if we replace coordinates of the true event vertex with coordinates of the fit vertex, all of the remaining PMT hits have rather small R_{dev} value, as shown in figure 5.5. This is because during fitting process, the fitter threw out some good PMT hits in order to accommodate that bad hit caused by the noise. Three out of the 17 mis-reconstructed events were caused purely by noise.

Another way to break the assumption in step 1 of the time fitter is if Čerenkov photons come from two, instead of one, points in the detector. Thus the fitter may be confused and unable to reconstruct the event accurately since there is not a unique source for all photons. PMT β-γ decays only produce electrons and gammas. These electrons lose energy fairly quickly and produce photons within a few centimeters, which is well below the spatial resolution (35 cm) of SNO as the photomultiplier has a 1.6 ns spread in the transit time . Thus the electron vertex can be thought as a point vertex, which produces photons right at the position where the PMT β-γ decay occurs (the PMT front glass). It is a different situation for a gamma ray, which has a certain probability of penetrating through several meters of water shielding and then losing energy by producing electrons or positrons through Compton scattering or pair production reactions. These electrons or positrons produce Čerenkov photons at positions which may be meters away from the original source (the PMT front glass). As discussed before, the probability of such an event is extremely low due to the short attenuation length of energetic gammas in the water. However, this small probability may be compensated by large number of PMT β-γ decays. Careful studies have been carried out on the 17 mis-reconstructed events, only one of which was found to be caused by a penetrating gamma. Figure 5.6 shows the positions where photons were created in this event. The majority of the photons were generated by a gamma which penetrated through more than 1 meter of light water toward the center of the detector. Figure 5.7 shows R_{dev} distribution for this event. Mis-reconstruction of this event was caused mainly by three PMT noise hits and at a less significant level by the penetrating gamma since this gamma did not reach the D_2O region.

One alternative way to break the assumption in step 1 of the time fitter is simply that Čerenkov photons do not always travel in straight lines. Normally, there are two factors

Figure 5.5: R_{dev} **and** R_{dev}**(fit) distributions for a badly fit PMT** β-γ **decay event.** R_{dev}(fit) is defined by replacing coordinates of the true event vertex with coordinates of the fit vertex in the R_{dev} definition. Plot only contains the remaining PMT hits after the time fitter is used. (see text).

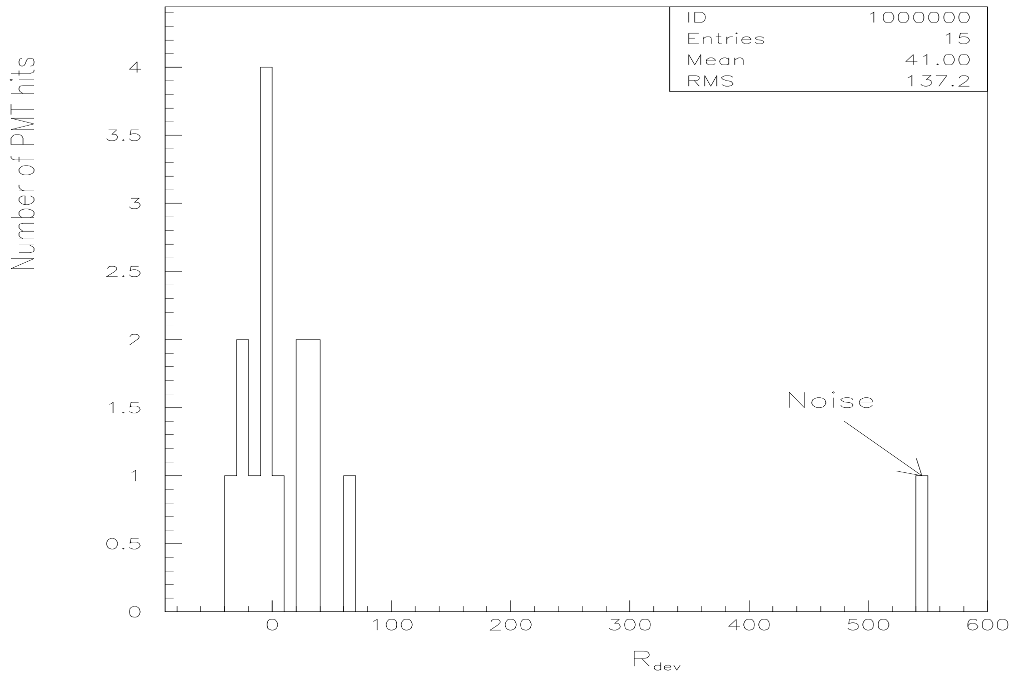

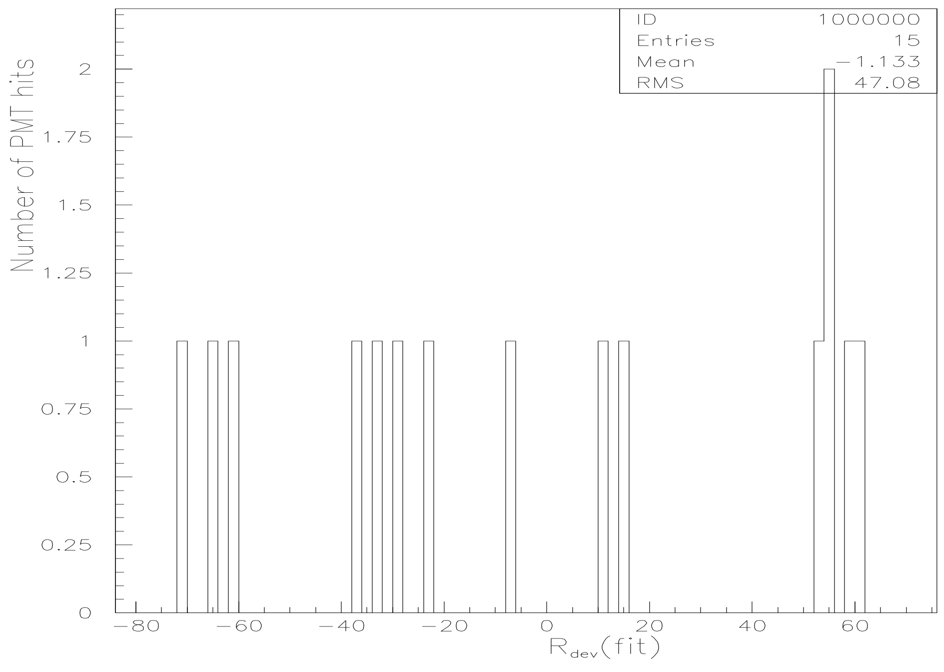

Figure 5.6: R_{pos} **distribution for a badly fit PMT β-γ decay event.** R_{pos} is the distance between the center of the detector and the source vertex of photons (see text).

Figure 5.7: R_{dev} **distribution for a badly fit PMT β-γ decay event.** Plot only contains the remaining PMT hits after the time fitter is used (see text).

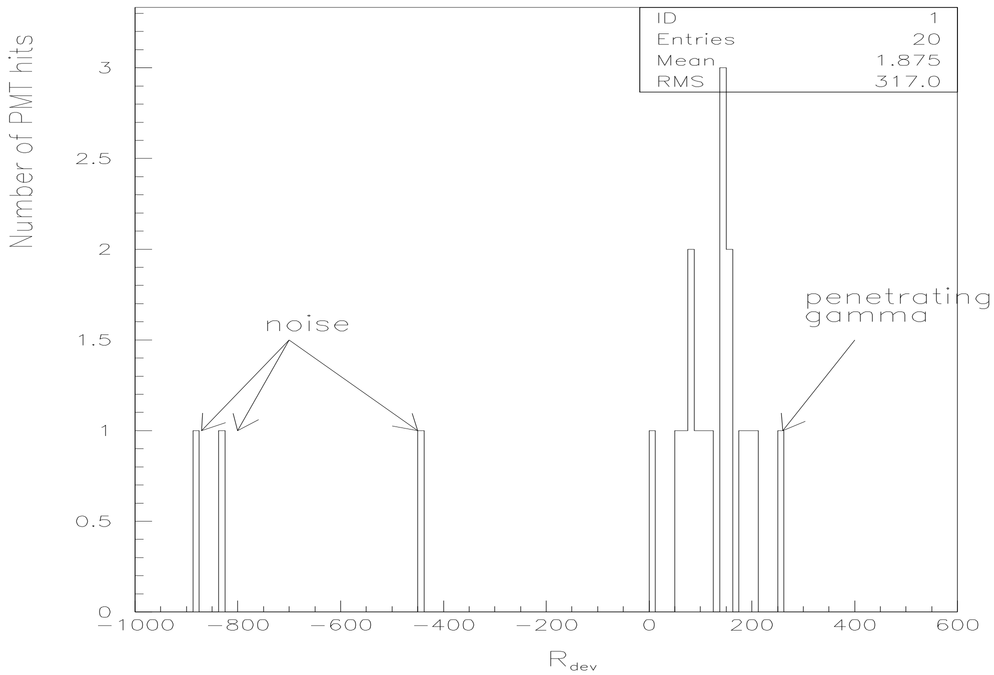

which can change the direction of a photon:

- Refraction or reflection.

  The SNO detector is made of different materials, thus it is not homogeneous in terms of the refractive index. A photon, which is created somewhere near the PMT sphere, may pass through boundaries between the H_2O region and the acrylic vessel or/and between the acrylic vessel and the D_2O region before it hits a photomultiplier and makes a trigger. The difference between the refractive index of water (D_2O: 1.337, H_2O: 1.342) and the AV (1.5) may lead to refraction or reflection at these boundaries. Reflection is able to do more damage to the reconstruction of the event vertex than refraction since it changes the direction of the incident photon more significantly. The mechanism behind the mis-reconstruction due to reflections is shown in figure 5.8. Photons change their directions when they meet the boundary between the AV and the light water. Since photons are assumed to travel in straight lines, from the fitter's point of view, these reflected photons are thought to come from a point in the D_2O region instead of the source PMT (Although PMT is not able to determine direction of the incoming photon, it could use the temporal information to deduce how far way the photon is generated.). Thus the event is mislocated. However, the probability for photons undergoing reflection is fairly low, especially for those with small angles of incidence [93]. This probability increases with the incident angle. However, this is more or less compensated by the decrease in the difference of path lengths between photons travelling straight and those reflected as the incident angle increases. Monte Carlo results show that 2 out of the 17 mis-reconstructed events are caused by reflections.

- Rayleigh Scattering

  Photons can change their directions by many physical processes even when they travel in a homogeneous media. One of those processes is Rayleigh Scattering, which is mainly caused by fluctuations in the number of scattering particles per unit volume encountered by a throughgoing photon. For single component liquid such as heavy water or light water, this is directly related to fluctuations in the density. The photon tends to retain its original polarization after being scattered. Since the polarization is perpendicular to the direction of travel, this leads to a restriction on the angular distribution of the scattered photon. However, the scattered photon has

Figure 5.8: **Two dimensional schematic diagram of a mis-reconstructed event due to reflections.** (see text).

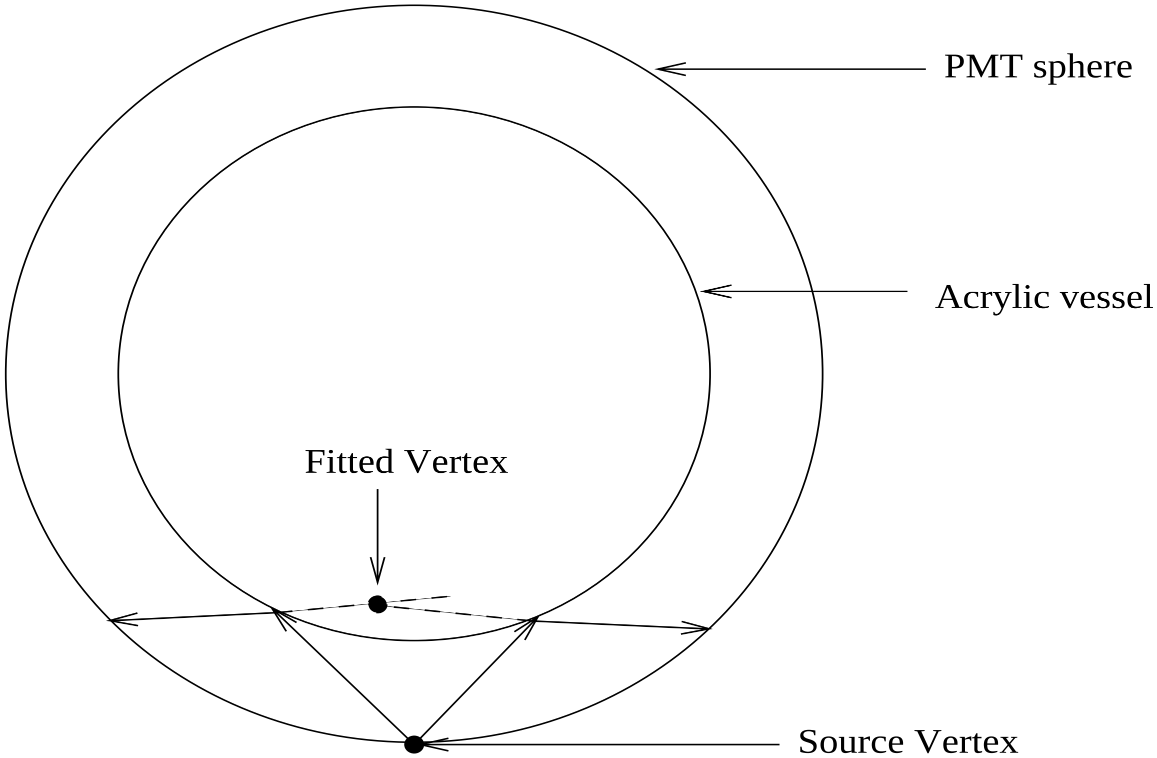

the same probability for going backward as for going forward. Thus it is able to cause the same problem for the fitter as a photon undergoing the reflection. The probability for Rayleigh scattering is low (roughly 2×10^{-4} per centimeter in the water). But again the large number of PMT β-γ decay events makes this process highly likely. Eight out of seventeen mis-reconstructed events were found to be caused by Rayleigh scatterings. Figure 5.9 shows a PMT β-γ decay event wrongly fit at a radius of 336 cm after a photon changed its direction by 129^o.

Scattering from discrete particles in the water (so-called Mie scattering) is not included in the Monte Carlo. Given the required cleanliness of the water in SNO, it is unlikely that there will be sufficient number of particles in the water to make this a significant effect [94].

The reasons for mis-reconstructing 17 PMT β-γ decay events are summarized in table 5.7. Rayleigh scattering seems to be the dominant reason followed by PMT noise hits although the statistics are not good. Data about how much scattering we should see in SNO are extracted from experiments which have difficulty distinguishing between light attenuation due to absorption of photons and that due to scattering of photons. This may

Figure 5.9: R_{dev} **distribution for a badly fit PMT** β-γ **decay event.** Plot only contains the remaining PMT hits after the time fitter was used (see text).

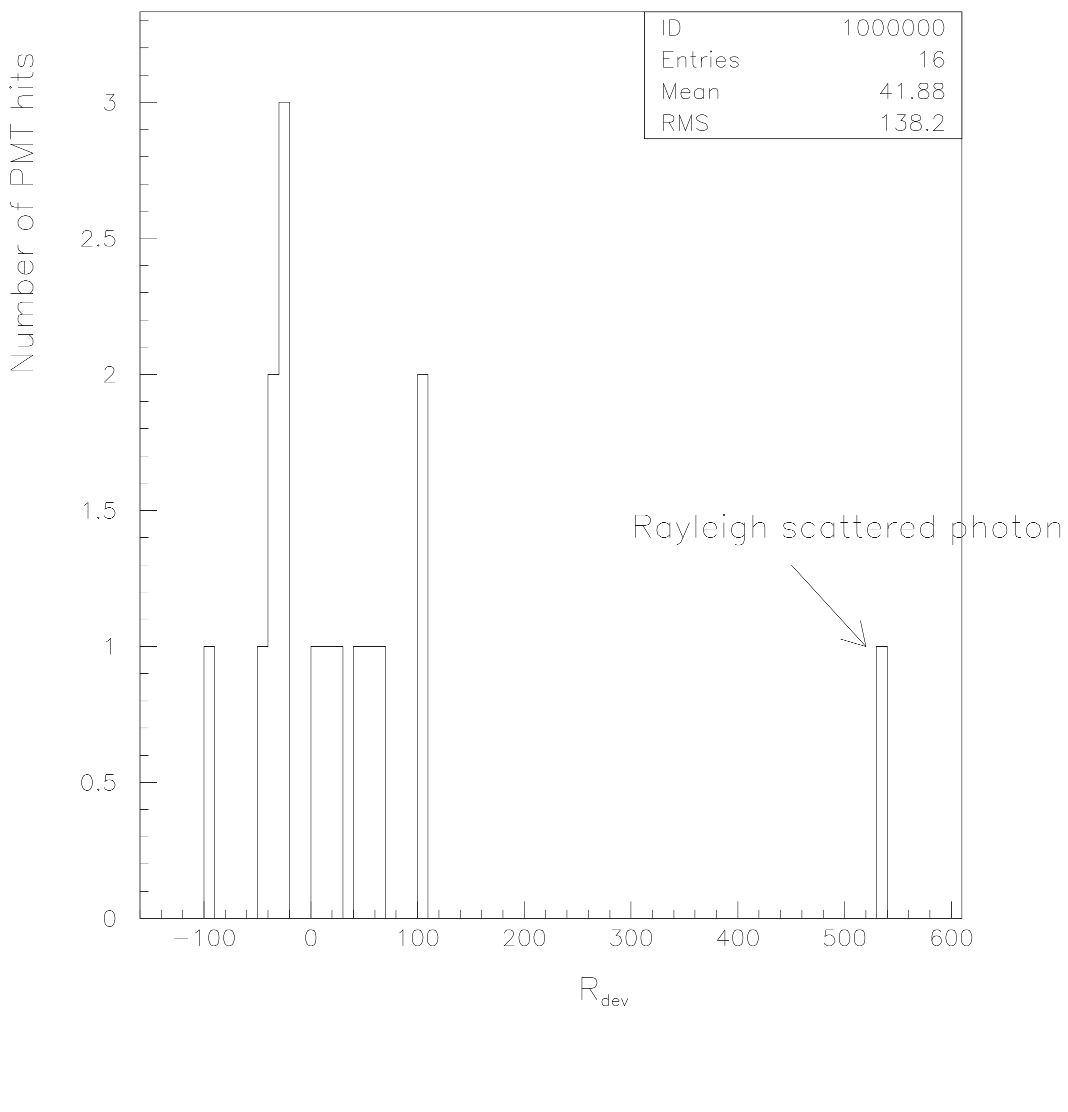

Table 5.7: **Causes of mis-reconstructions of 17 PMT β-γ decay events simulated by the SNOMAN code.**

	Rayleigh scatterings	Noises	Specular reflections	Penetrating gammas	Combination of 2 or more reasons
Number of events	8	3	2	0	4

lead to large errors in the Monte Carlo simulation. These 17 events were generated by the old version of the SNOMAN code. In the latest version of the code, which represents our current best guess of properties of the water, the magnitude of the Rayleigh scattering is higher than that in the old version. Thus it is expected that the Rayleigh scattering will play a more significant role in the mis-reconstruction of the event vertex by the vertex fitter.

5.3 A Lorentzian Fitter

5.3.1 The Theory

In step 3 of the time fitter, a χ^2 function is defined and then minimized in order to determine values of input parameters (spatial and temporal coordinates of the fit vertex). At the minimum of the χ^2 function, we have:

$$\frac{\partial \chi^2}{\partial a_k} = 0 = \sum_{i=1}^{N} \frac{2}{\sigma^2}(t_{ic} - t_{ip})\frac{\partial t_{ic}}{\partial a_k} \qquad k = 1, 2, 3, 4 \tag{5.6}$$

where a_ks are the four parameters to be fit. Thus the four coordinates of the fit vertex are approximate solutions to equations 5.6. To the first order of approximation, $\frac{\partial t_{ic}}{\partial a_k}$ has the same value for both good and bad PMT hits. σ is a constant. The fact that, as described in the last section, bad PMT hits normally have greater effect on the performance of the time fitter than good ones (in some events, even a single bad hit can devastate the reconstruction) can be understood: in equations 5.6, bad PMT hits have much larger weights $(t_{ic} - t_{ip})$ than good ones, thus they may determine the solutions. The larger the deviation of the PMT hits, the greater weight they have, and the larger the effect they can impose on the result of the fitter.

The reason that this specific χ^2 is chosen for the time fitter is that the $(t_{ic} - t_{ip})$

distribution is assumed to be a Gaussian function. This is based on the assumption that every PMT trigger is caused by a photon travelling in a straight line, which is not true as discussed in the last section. In principal, we could choose other p.d.f.s[2] for $(t_{ic} - t_{ip})$. One of alternative functions is called the double (or two-sided) exponential function:

$$Prob(t_{ic} - t_{ip}) \sim exp(-|\frac{t_{ic} - t_{ip}}{\sigma}|) \tag{5.7}$$

The χ^2 function is rewritten as:

$$\chi^2 = \sum_{i=1}^{N} |\frac{t_{ic} - t_{ip}}{\sigma}| \tag{5.8}$$

which gives:

$$\frac{\partial\chi^2}{\partial a_k} = 0 = \sum_{i=1}^{N} \frac{1}{\sigma} sgn(t_{ic} - t_{ip}) \frac{\partial t_{ic}}{\partial a_k} \qquad k = 1, 2, 3, 4 \tag{5.9}$$

The difference between this equation and equation 5.6 is that now the weight for any PMT hit is the sign of $(t_{ic} - t_{ip})$ instead of its value. Thus every PMT hit (bad or good) has the same weight.

The idea of letting every PMT hit have the same weight could be further extended by adopting the Lorentzian (or Cauchy) function as the p.d.f.:

$$Prob(t_{ic} - t_{ip}) \sim \frac{1}{1 + \frac{1}{2}(\frac{t_{ic} - t_{ip}}{\sigma})^2} \tag{5.10}$$

The corresponding χ^2 function is:

$$\chi^2 = log(1 + \frac{1}{2}(\frac{t_{ic} - t_{ip}}{\sigma})^2) \tag{5.11}$$

And:

$$\frac{\partial\chi^2}{\partial a_k} = 0 = \frac{1}{\sigma}(\frac{z}{1 + \frac{1}{2}z^2}) \frac{\partial t_{ic}}{\partial a_k} \qquad k = 1, 2, 3, 4 \tag{5.12}$$

where $z = \frac{t_{ic} - t_{ip}}{\sigma}$. Here the weigh $(\frac{z}{1+\frac{1}{2}z^2})$ increases with z as before. However, it starts to decrease if z is larger than $\sqrt{2}$. For a bad PMT hit with z much larger than $\sqrt{2}$, its weight is almost zero, thus it is expected that this bad hit does not affect fitting results significantly. The general idea here is that weight for given individual point should increase with deviation, then decrease to eliminate effects of bad data points. The major difference between the lorentzian fitter and the time fitter is that one uses the Lorentzian function as its p.d.f. while the other uses the Gaussian function.

[2] Probability Distribution Function

5.3.2 The Simulated Annealing Algorithm

We need to find a algorithm which fulfills the task of finding the minimum of the χ^2 function defined in equation 5.11. One method for minimizing a function is the so-called Variable Metric method in multi-dimensions (the Levenberg-Marquardt algorithm used in the time fitter is one of its implementations.). It looks for the minimum of the function by moving the evaluated point along the so-called down-hill direction in the parameter space where $\frac{\partial \chi^2}{\partial a_k} < 0$. The major advantage of this method is its speed, the algorithm converges to the minimum fairly quickly. There are two major weakness :

1. It requires knowledge of the gradient of the minimized function, i.e., we must be able to calculate the derivation of the χ^2 function explicitly. This requirement is met by the Lorentzian fitter where the derivative of the χ^2 function is defined in equation 5.12.

2. This method becomes unreliable when applied to the function with many local minima. The algorithm could easily converge to a poor, local minimum where the condition of $\frac{\partial \chi^2}{\partial a_k} = 0$ is met. Since the shape of the specific χ^2 function used in the Lorentzian fitter is unknown and thought to be complex, we need to find a algorithm which is able to find the global minimum of the function amongst many local minima.

The method of simulated annealing [95] is a technique that has attracted significant attention as being suitable for finding the global minimum in a large parameter space which contains many local minima. This method was first developed to solve the famous "travelling salesman" problem [96]. It has also been used successfully for designing complex integrated circuits [97]. The name of this algorithm comes from its correspondance to the physical world: if a metal is cooled down slowly, so called annealed, metal molecules are able to find their lowest energy states so that after being annealed, the metal becomes more robust. On the other hand, if the metal is cooled too quickly, it could end up in somewhat higher energy state which is less strong. Thus the whole point is to decrease the temperature sufficiently slowly.

The detailed implementation of the simulated annealing method is based on the idea of downhill simplex method in multi-dimensions [98](the amoeba routine taken from [92] was used.), where a simplex consisting of 5 vertices is formed in the 4-dimension parameter space and this simplex changes its shape and volume and moves in the downhill direction according to the function values of its 5 vertices. The difference here is that we add a thermal fluctuation to each vertex of the simplex according to the Boltzman probability distribution

$$Prob(E) \sim exp(-\Delta E/kT) \tag{5.13}$$

when we evaluate the function values. This fluctuation sometimes causes the simplex to move up-hill and thus go out of the local minimum. The magnitude of the fluctuation is dependent on the temperature. We first start with the high temperature, thus the simplex has a somewhat larger probability to go uphill or go out of the local minimum. As the temperature goes down, this probability decrease. When temperature equals 0, there is no thermal fluctuation and the method of simulated annealing is just the downhill simplex method in multi-dimensions.

There are several techniques worth mentioning used in the Lorentzian fitter:

1. E is the function to minimize, here it is the χ^2 function. The problem is how to decrease T so that the requirement of slow cooling is satisfied. The starting temperature T_{max} should be larger than the maximal value of ΔE, thus at the beginning of annealing the thermal fluctuation would be able to reach the whole parameter space. The maximal value of ΔE could be determined by randomly sampling a large number of points in the parameter space. Monte Carlo calculation shows this value should be set as 200 for the current problem. There are many ways for slowly cooling down the system. There are no theoretical reasons that one of these cooling methods should be preferred over others for a general case. It seems only experiment could decide which method is most suitable for a specific case. I decided to use the following cooling method: Budget a total of K iterations, and reduce the temperature T after every m moves to a value $T = T_{max}(1 - k/K)^{\alpha}$, where k is the cumulative number of iterations so far. Many tests have been done with various k, K and α. It seemed the performance of the fitter was best when $m = 100$, $K = 10000$ and $\alpha = 2$.

2. Another strategic question is whether to do an occasional "restart", where a vertex of the simplex is replaced by the "best-ever" point. Again there is not any theory about whether this kind of restart is beneficial. The only way to find out the answer is trying the algorithm with and without the restart and then comparing the result. Monte carlo experiments seem to show that occasional restarts are somewhat

negative for the problem here.

3. The true p.d.f. of PMT β-γ events is not expected to be identical to the Lorentzian distribution because of many bad PMT hits. The same technique used in the time fitter is also used in the Lorentzian fitter: the thought-to-be bad hit is discarded repeatly and the fitting process is repeated until all of the remaining PMT hits fall in a predefined time window.

4. Finally there is a subtle problem associated with the amoeba algorithm used in the fitter. The global minimum of the χ^2 function is though to be found by the fitter if the algorithm converges. However, sometimes, for some reasons, the simplex used in the algorithms is trapped in a small valley and can not go anywhere. The solution is to reset the vertices of the simplex so that they surround the best minimum found so far and restart the algorithm. It turned out that this simple process is highly beneficial.

Main routines used in the Lorentzian fitter were taken from [92] with some minor modifications.

5.3.3 Results and Comments

When we evaluate the performance of a vertex fitter, two criteria are relevant:

- Since the majority of the events are expected to be fit at positions rather close to true vertices, the positions relative to the true vertices and the sharpness of the event peak is one reflection of the performance of the fitter.

- There are always some events which are reconstructed far away from the true vertices. The number of such badly fit events and the magnitude of the errors are another criterion to judge the performance of the fitter.

The second criterion described above is especially important for fitting PMT β-γ decay events since we only worry about those events mis-reconstructed inside the acrylic vessel. Figure 5.10 shows fitting results of the time and the Lorentzian fitter for 1078 PMT β-γ decay events above 25 hits. Clearly the Lorentzian fitter performs better than the time fitter. Its R_{fit} distribution has a much sharper peak around the true positions of the events, fewer events are mis-reconstructed inside the acrylic vessel, and all of events are reconstructed at positions at least 5 meters away from the center of the detector while the most badly fit event by the time fitter is only 3 meters away from the center of the detector. In addition, 95% of the PMT β-γ decay events are reconstructed within 10 meters of the center of the detector by the lorentzian fitter while the corresponding number for the time fitter is only 85%.

A good fitter should be good for all kinds of events since normally a vertex fitter is merely the first step in identifying the class of the studied event. Monte Carlo tests have been carried out to evaluate the performance of the Lorentzian fitter for other kinds of events in SNO. Figure 5.11 shows the fit results of the time and the Lorentzian fitter for 1489 5 MeV electron events uniformly generated in the D_2O region, where R_{error} is the distance between the fit vertex and the true vertex. The position and the sharpness of peaks are similar for two R_{error} distributions. However, 8.1% of events failed the 1 meter R_{error} cut (see figure) when the time fitter was applied and the corresponding value is 3.8% for the lorentzian fitter

Basically, each vertex fitter is just one implementation of the Maximal Likelihood fitting method with a different probability distribution function. The time fitter assumes the p.d.f. for R_{dev} is a Gaussian function whose standard deviation equals to the averaged speed of light in heavy and light water times 1.6 (because there is always a Gaussian fluctuation (1.6 ns width) in the PMT transit time.) while the Lorentzian fitter takes the Lorentzian distribution as its corresponding p.d.f.. However, these assumptions are just approximations. As shown in figure 5.12, the p.d.f. generated by Monte Carlo simulations are neither Gaussian nor Lorentzian function, it has a much longer tail than these two functions. Nevertheless, the Lorentzian function looks more like the true p.d.f. than the Gaussian function since it has a longer tail. This may, from another angle, explain why the Lorentzian fitter performs better than the time fitter. Let's study the peak of the true p.d.f. shown in the bottom half of figure 5.12. Clearly the p.d.f. is not peaked and symmetric around 0 as assumed in the time and lorentzian fitters. There are many more "late" hits ($R_{dev} > 0$) than "early" ones ($R_{dev} < 0$) because there are many more scattered photons than PMT noise. Obviously the performance of the maximal likelihood fitting method will be best if we choose the right p.d.f.. This is accomplished in the grid fitter [58], a vertex fitter which used the p.d.f. produced by Monte Carlo simulation. Its name comes from the method used to avoid local minima of the maximal likelihood function: a initial grid search in the whole parameter space which determines the starting point by

Figure 5.10: R_{fit} **distribution for 1078 PMT β-γ events above 25 hits.** R_{fit} is the distance between the fit vertex and the center of the detector. Note the position of PMT sphere is $R_{fit} = 850cm$. A cut ($R_{fit} < 1000cm$) is imposed on the data. Upper plot shows results of the Lorentzian fitter while the bottom one shows results of the time fitter.

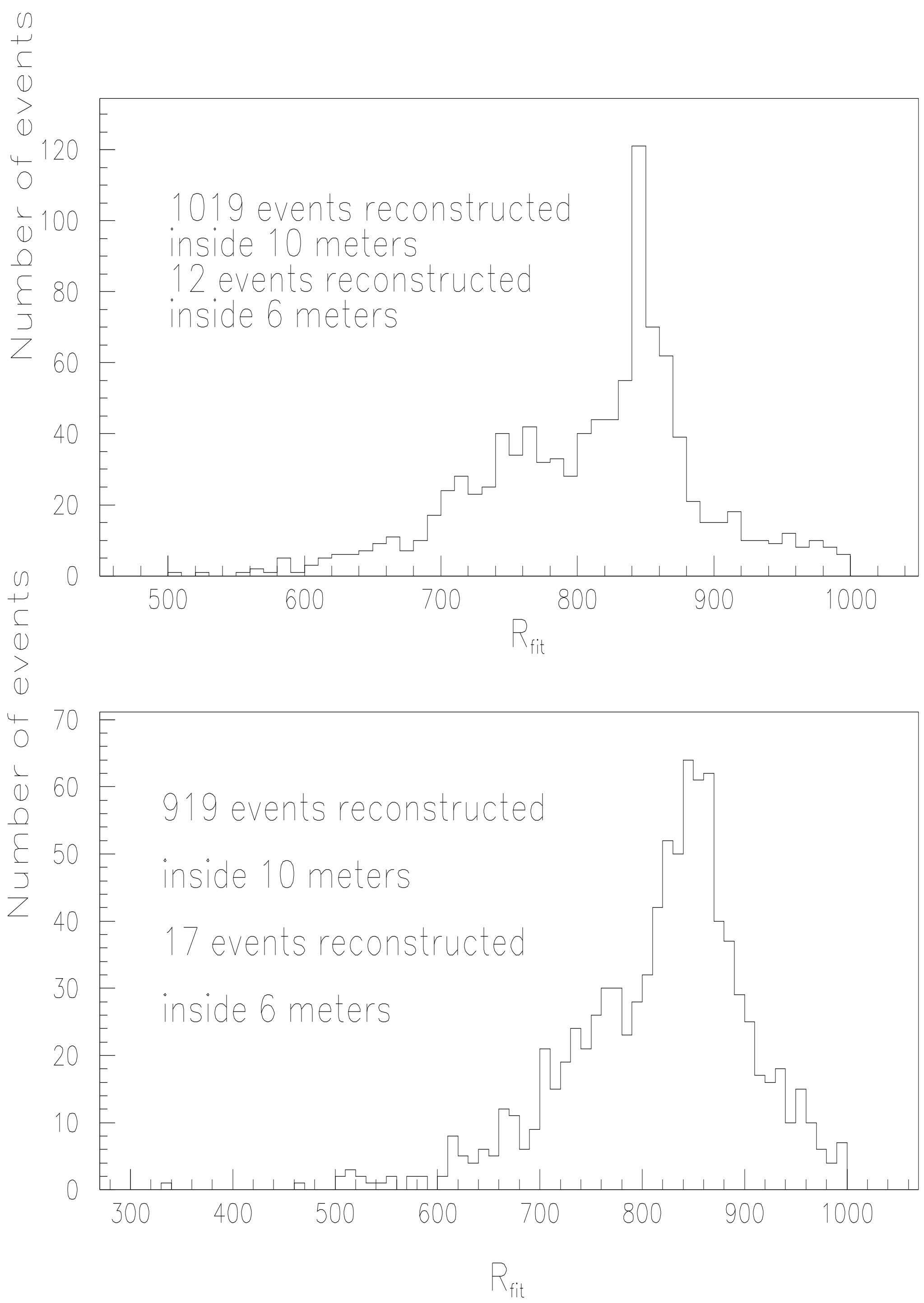

Figure 5.11: R_{error} **distribution for 1489 5 MeV electron events uniformly distributed in the D_2O region.** R_{error} is the distance between the fit vertex and the true vertex. A cut ($R_{error} < 100cm$) is imposed on the data. The upper figure shows the result of the Lorentzian fitter while the bottom one shows the result of the time fitter.

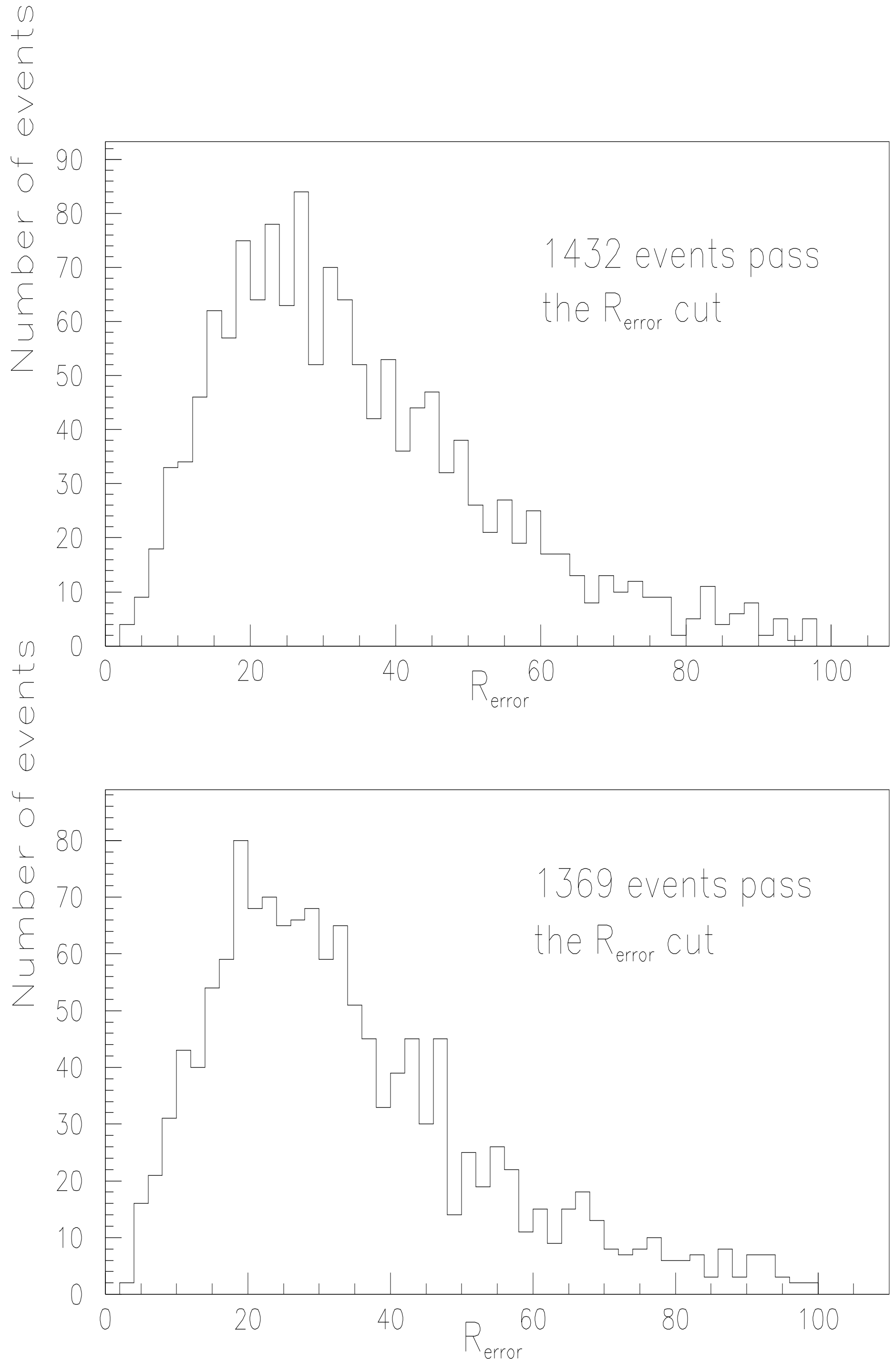

comparing the function values in every pixel. The major vulnerability of the grid fitter is that since the fitter uses p.d.f.s generated by the Monte Carlo, it requires the correctness of the SNOMAN code which is not established. However, future calibration data should give us confidence in the validity of the code (perhaps after modification).

5.4 Background Vetoes

Although the Lorentzian fitter performs better than the time fitter, it (also all other vertex fitters in the current SNOMAN code) is only able to eliminate a small number of PMT β-γ decay events which are wrongly reconstructed inside the acrylic vessel by the time fitter. This section describes some techniques developed by the author to veto those mislocated background events.

5.4.1 The Time Veto

If most of PMT triggers are caused by photons travelling in straight lines from the source vertex to the hit photomultipliers, for an event occurring at the center of the detector, most of the photons should hit photomultipliers at the same time. On the other hand, for a event occurring at the edge of the detector (e.g. one of PMTs), it is possible that some of photons, which have to travel through the whole detector before they hit some PMTs, make PMT triggers much later than others. Thus it is expected that the time distribution of PMT triggers for PMT β-γ decay events is broader than the distribution for internal decay events. However, this did not turn out to be a large effect, as shown in figure 5.13, due to the contamination of bad PMT hits (noise or scattered photons). The mathematical implementation of the time veto is to define a value t_{div}, which is the time difference between two PMT triggers averaged on all possible pairs in a event. As figure 5.14 shows, on average, a PMT β-γ decay event does have a larger t_{div} value than a internal β-γ decay event. However, two distributions do not separate from each other completely and it is difficult to impose a veto to separate the two kinds of events.

Based on the idea similar to that behind the time veto, a special hardware trigger whose time window is much shorter than the standard trigger has been installed in the SNO detector. This trigger suppresses the probability of detecting events occurring outside the acrylic vessel without losing sensitivities to events occurring in the central region of the detector.

Figure 5.12: R_{dev} **distributions for PMT hits of 1000 PMT β-γ decay events.** Also shown are Gaussian (dashed line) and Lorentzian (dotted line) functions normalized to the peak value of the distribution. The bottom figure has a cut $-200 < R_{dev} < 200$.

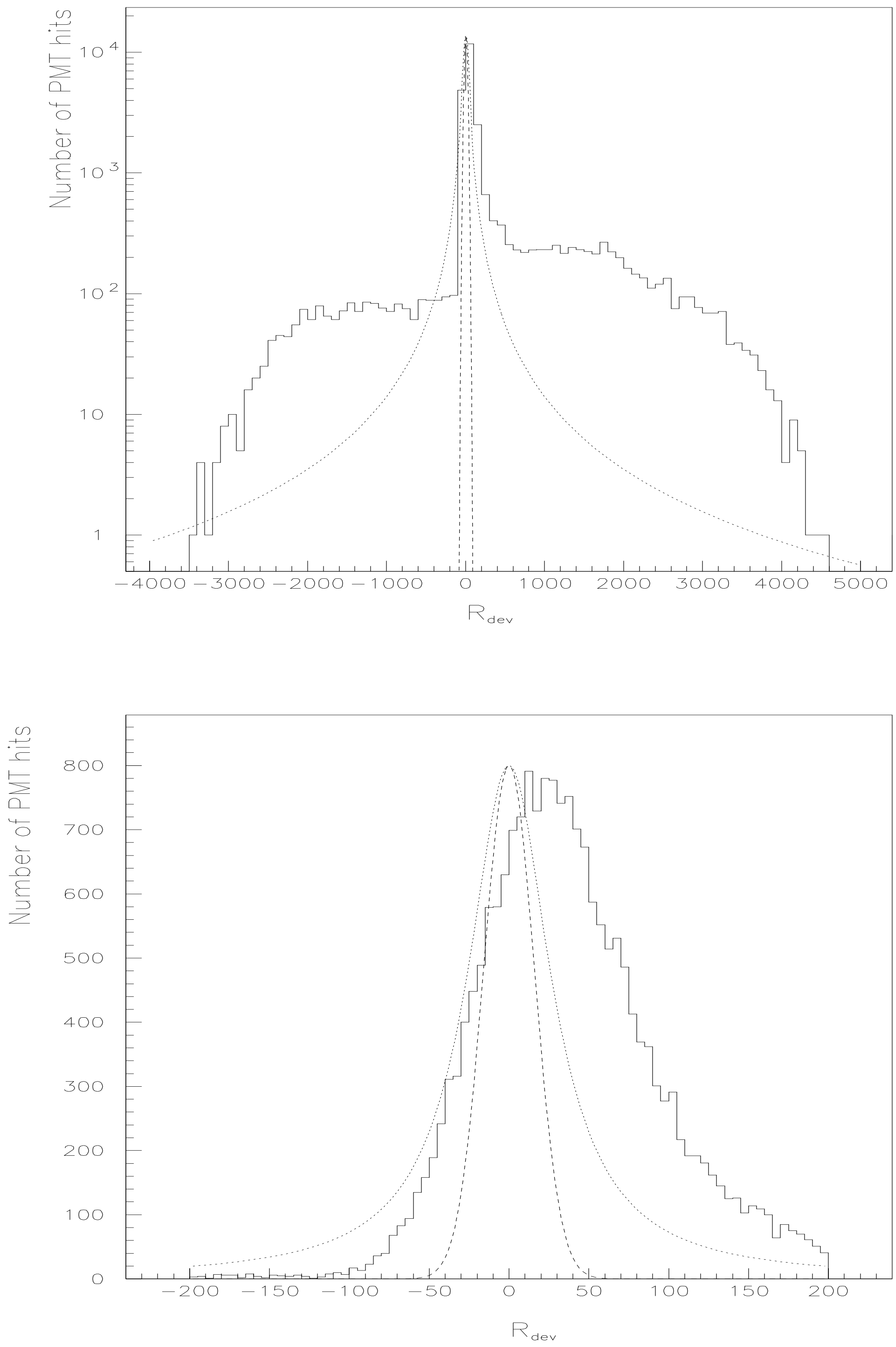

Figure 5.13: **Time distributions for PMT triggers of two sets of events: 1000 PMT β-γ decay events (dashed line) and 1000 internal β-γ decay events (solid line).**

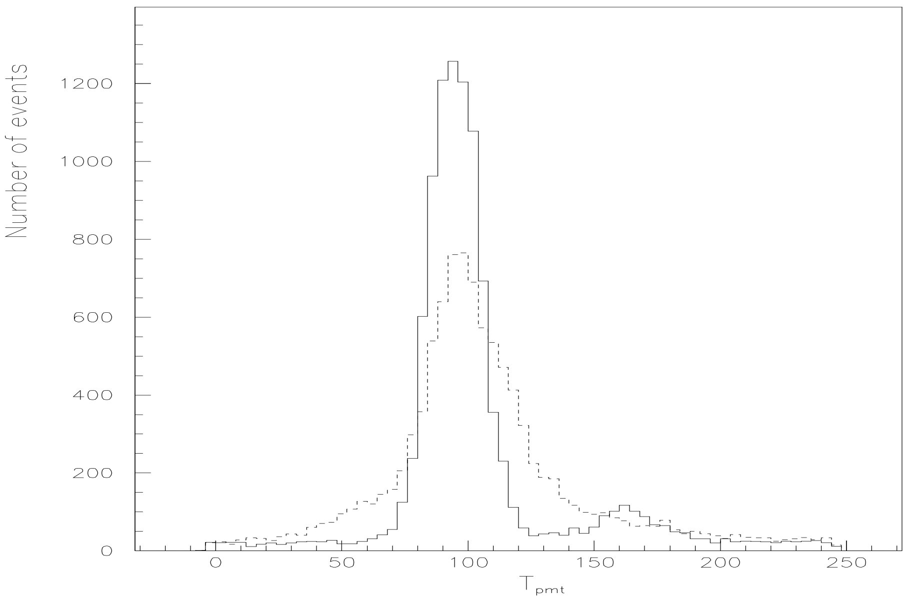

Figure 5.14: T_{div} **distributions of two sets of events: 1000 PMT β-γ decay events (dashed line) and 1000 internal β-γ decay events (solid line).**

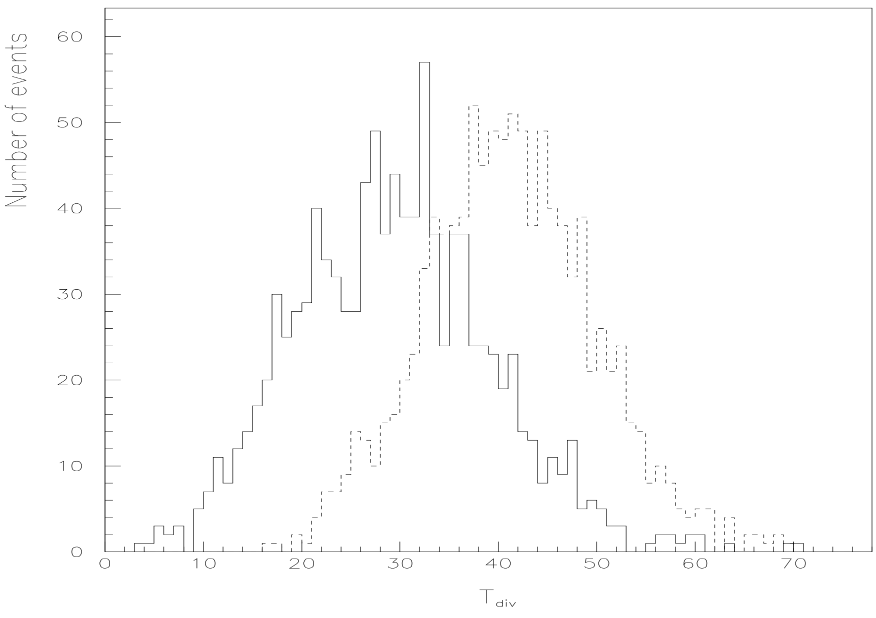

Figure 5.15: Q_{max} **distributions of two sets of events: 1000 PMT** β-γ **decay events (solid line) and 1000 internal** β-γ **decay events (dashed line).** (see text)

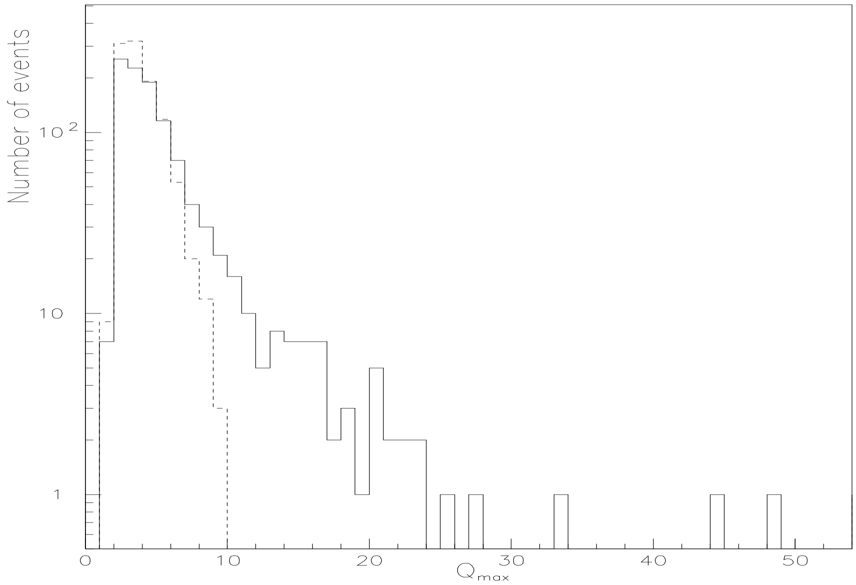

5.4.2 The Charge Veto

Since a PMT β-γ decay event occurs in (or near to) a photomultiplier, it is likely that more than one of the created photons would trigger the same photomultiplier within a single trigger window, which would lead to a large accumulated charge in the PMT. Such scenario is highly unlikely to happen for an internal event where photons are created at least 2.5 meters from the PMTs. Figure 5.15 shows the Q_{max} (the largest charge deposited in a single photomultiplier) distributions for 1000 PMT and 1000 internal β-γ decay events. Although two distributions are not separated from each other at all due to the poor charge resolution of photomultipliers used in the SNO detector, the distribution of the PMT β-γ decay events has a much longer tail than that of the internal events. The charge veto simply cuts off any events with $Q_{max} > 10$, which enables us to reject 3 out of the 17 studied PMT β-γ decay events mis-reconstructed in the D_2O region, as shown in figure 5.16.

5.4.3 The Direction Veto

The direction veto is based on the direction of a event. Since there are several gammas and electrons in a β-γ decay event, the event direction is defined as the averaged direction

Figure 5.16: Q_{max} **distributions of 17 PMT** β-γ **decay events mis-reconstructed in the** D_2O **region.** (see text)

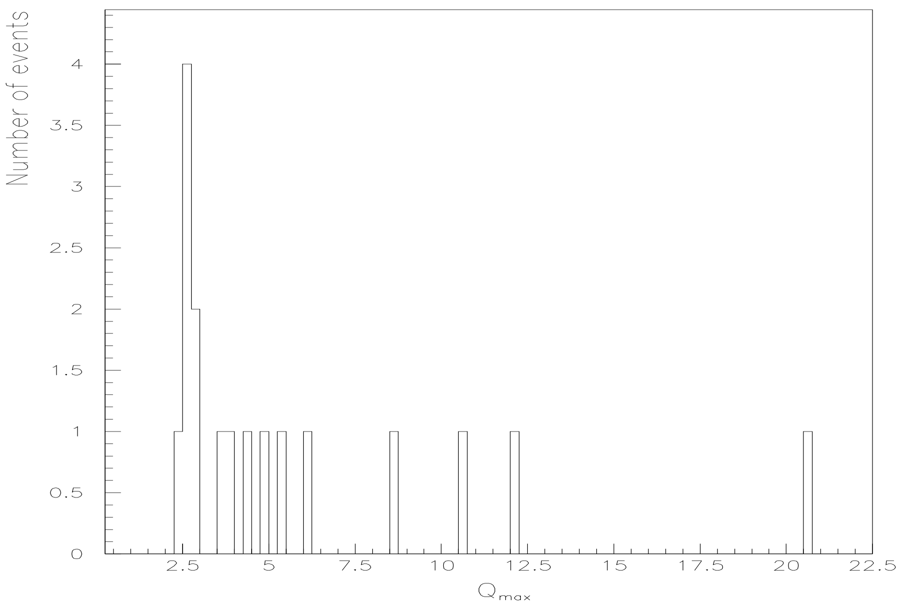

of all detected photons. For a PMT β-γ decay event, almost all of the photons have to come inwards and towards the center of the detector in order to make PMT triggers, thus the event is fit as pointing inwards. The directions of events occurring in the D_2O region are expected to be isotropic or slightly outward relative to the center of the detector since outgoing photons have shorter paths to travel than ingoing ones before they hit photomultipliers. A value θ_{fr} is defined to describe the direction of a event. θ_{fr} is the angle between two vectors: one is the direction of the event and the other is from the center of the detector to the fit event vertex. Thus if θ_{fr} equals 0, the event points outwards along the radial direction while if θ_{fr} equals π, the event travels inwards along the radial direction.

As figure 5.17 shows, most of the PMT β-γ decay events do go inward while the internal β-γ decay events travel at all directions. The direction veto is to cut any events with θ_{fr} larger than 2.5. This veto enables us to cut 77.3% of PMT β-γ decay events while only losing 15% of internal events. Figure 5.18 shows θ_{fr} values for those 17 PMT β-γ decay events mis-reconstructed in the D_2O region. The direction veto is only able to get rid of 5 of them. The small affect of the veto is due to large errors of the vertex fitter for these events.

Figure 5.17: θ_{fr} **distributions for two sets of events: 1000 PMT** β-γ **decay events (solid line) and 1000 internal** β-γ **decay events (dashed line).**

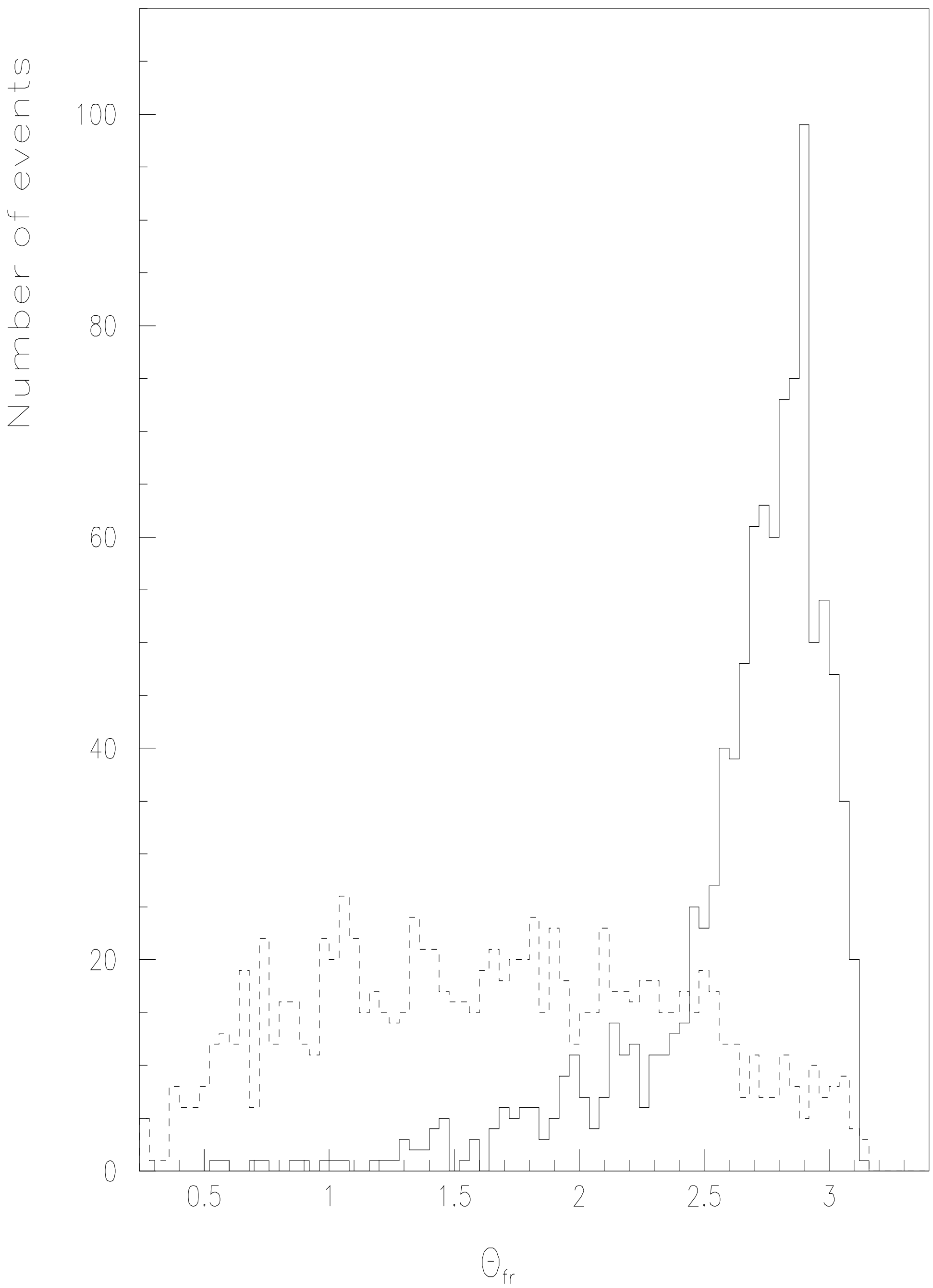

Figure 5.18: θ_{fr} **distributions for 17 PMT** β-γ **decay events mis-reconstructed in the** D_2O **region.**

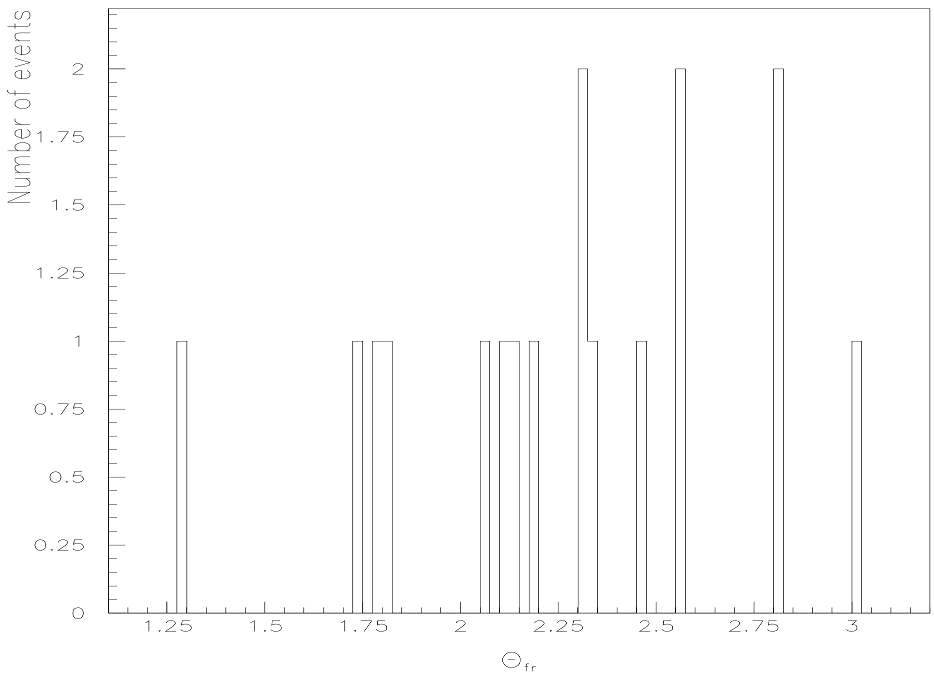

5.4.4 The PMT veto

The major difference between a PMT β-γ decay event and an internal β-γ decay event is that one occurs in the PMT region and the other occurs in the D_2O region. In fact, most of PMT β-γ decay events take place in the photomultipliers themselves. Thus it is very likely that one or more photons produced by such an event would lead to a trigger in the source PMT. If this theory is correct, we have already known the position and the time of a PMT β-γ decay event, which would be recorded in one of PMT triggers, before the vertex fitter is used.

Based on this idea, the procedure of the PMT veto is as follows:

1. Randomly choose one PMT trigger and take its position and time as the spatial and temporal coordinates of the event vertex. Define a value R_{dev_i}:

$$R_{dev_i} = c' \times (t_{pi} - t_e) - \sqrt{(x_{pi} - x_e)^2 + (y_{pi} - y_e)^2 + (z_{pi} - z_e)^2} \tag{5.14}$$

   where x_{pi}, y_{pi}, z_{pi}, and t_{pi} are the recorded three spatial and one temporal coordinates for the i^{th} PMT trigger respectively while x_e, y_e, z_e, and t_e are corresponding values for the assumed event vertex. c' is the average speed of the light in the heavy and light water which equals 22.397 cm/ns. If the true source vertex is near to the selected photomultiplier and the i^{th} PMT trigger is caused by a photon travelling in a straight line, R_{dev_i} should approximately equals 0. Calculating R_{dev_i} for every other PMT trigger, we will get a R_{dev_i} array whose size is equal to Nhits-1, where Nhits is the number of PMT triggers in an event.

2. Sort this array in ascending order. We define another value *res*:

$$res = \sum_{i=1}^{int(Nhits/2)} R_{dev_i} \tag{5.15}$$

Thus *res* is the sum of the first int(Nhits/2) smallest R_{dev_i}. By this way we should be able to eliminate affects of bad PMT hits in the event. Finally we have

$$res = \frac{res}{int(Nhits/2)} \tag{5.16}$$

in order to get rid of the dependence of *res* on Nhits.

3. Repeat step 1 and 2 until every PMT trigger has been chosen to get spatial and temporal information of the assumed event vertex. We end up with a *res* array of size Nhits.

4. Choose the minimal value of this array as the representing value of *res* for the event.

5. The PMT veto is carried out based on this value, which is discussed below.

As figure 5.19 shows, the res_{min} distribution for internal β-γ decay events is fairly flat over a large range while the res_{min} distribution for PMT β-γ decay events strongly peaks at somewhat smaller value. If we put a veto threshold at $res_{min} = 100$ and discard any events with $res_{min} < 100$, we are able to get rid of 74% of PMT β-γ decay events while only losing 12.2% of internal events without using any vertex fitter. Figure 5.20 shows the res_{min} distribution for the 17 PMT β-γ decay events mis-reconstructed inside the acrylic vessel. By using this PMT veto, we are able to get rid of 8 such events. Here the affect of the PMT veto is not as good as the case of normal PMT decay events presented above. It may due to statistic fluctuation since the number of events studied here is small. However, the author believes the main reason is that photons generated by such a PMT β-γ decay event tend to go forward in order to make more PMT triggers, thus they do not make any trigger in the source photomultiplier. Nevertheless, the PMT veto has been proved useful in rejecting PMT β-γ decay events.

Figure 5.19: res_{min} **distributions for two sets of events: 1000 PMT β-γ decay events (solid line) and 1000 internal β-γ decay events (dashed line).**

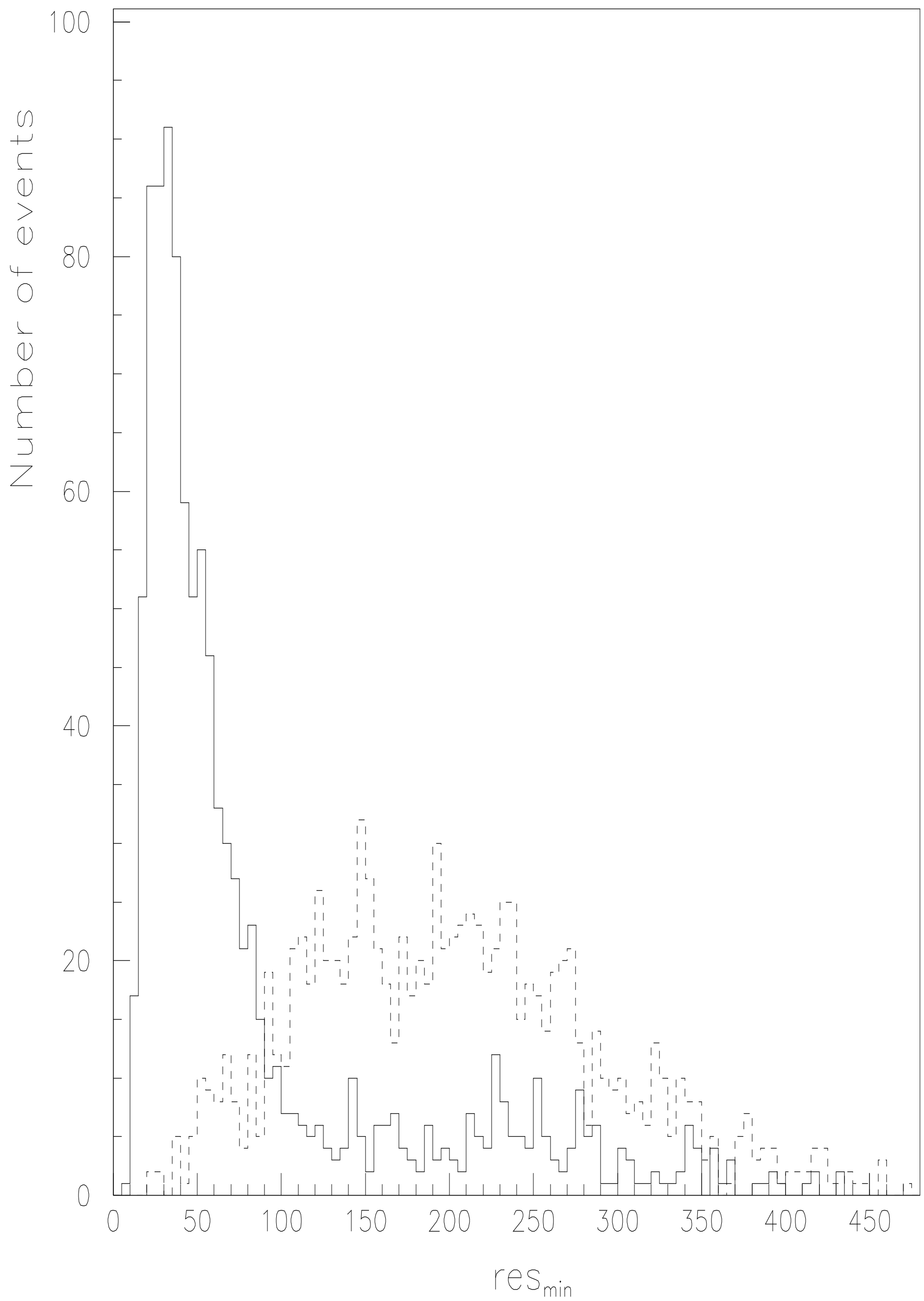

Figure 5.20: res_{min} **distribution for 17 PMT β-γ decay events mis-reconstructed inside the acrylic vessel.**

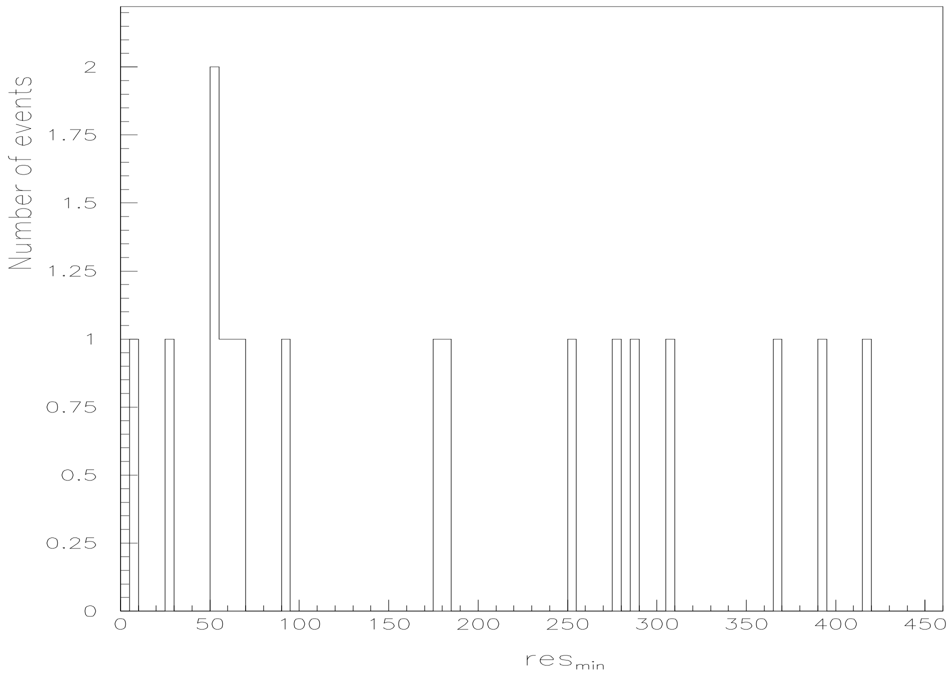

5.4.5 The Divergence Veto

Seventeen mis-reconstructed PMT β-γ decay events have been carefully studied with results described in section 2. It turned out for most of the events, a single bad PMT hit is able to have a great effect on the performance of the vertex fitter. Obviously if we can, somehow, recognize and discard this bad PMT hit, the vertex fitter should be able to reconstruct the event vertex fairly accurately. This seems to enter a endless loop since we can only know which PMT hit is bad **after** the correct original event vertex is determined. However, a background veto is not a vertex fitter, what we need is a method to determine which event is mislocated instead of reconstructing every event accurately. Let's think of the situation of a perfect event where every PMT trigger is caused by a photon travelling from its original vertex to the PMT in a straight line. In such an event, no matter which PMT hit is discarded from the data supplied to the vertex fitter, the fitter is able to reconstruct the event vertex at the same point (the true original vertex) since we always have much more information than we need (the number of PMT hits for an event above the detector threshold is always much larger than the number (4) of parameters to fit.). The situation is totally different for a event containing one or more bad PMT hits. In this case, if we happen to discard that or those bad PMT hits, the vertex fitter will then reconstruct the event vertex at the true vertex which is far away from the wrongly reconstructed vertex when all PMT hits, including bad ones, are taken into account. Based on this idea, the technique of the divergence veto is as follows:

1. Randomly select one PMT hit and purge it from the data set supplied to the vertex fitter.

2. Based on the remaining PMT hits, carry out the fitting process as usual and record the spatial and temporal coordinates of the fit vertex.

3. Discard another randomly selected PMT hit from the data set and include the previously discarded PMT hit in the data.

4. Repeat step 2 and 3 until every PMT hit in a event has been purged from the data once.

5. Determine whether the fit vertices based on various sets of limited data agree with the fit vertex based on the complete set of data.

For example, when this veto is implemented for a event with 30 PMT hits, we need to carry out the fitting procedure for 30 times, each time the vertex fitter takes data from only 29 PMT hits. Finally we will have 30 fit vertices.

Figure 5.21 shows results for two events, one of which is well reconstructed while the other is mislocated 2.5 meters away from the true vertex (the time fitter was used.). For the well fit event, all of the fit vertices are contained in a box with a size of roughly 0.03 cubic meters. For the badly fit event, the corresponding box is around 10 cubic meters. There are a couple of vertices which are far away from the other vertices. In fact these two vertices are fairly close to the true vertex. However, the result of the time fitter, when all PMT hits are taken into account, is close to the other vertices, which are wrong. It is thus expected that the fit vertices for a mis-reconstructed event are much more divergent than those of a well fit event.

There are many mathematical methods to measure the divergence of these fit vertices. The simplest way is to count the number of fit vertices outside a sphere with a radius of 100 cm and its center at the fit vertex based on the data from all PMT hits. The final result, n_{100}, is the ratio of this number to the total number of PMT hits. Figure 5.22 shows n_{100} distributions for two sets of events. Here the divergence veto is simple and powerful: any event whose n_{100} value is not equal to 0 is regarded as being badly fit and thus rejected. With this veto, we are able to reject 16 out of 17 mis-reconstructed PMT β-γ decay events while only 16.4% of well fit events are discarded.

We can move a step further. By imposing this veto, we are able to enhance the performance of the vertex fitter for events other than the PMT β-γ events. By rejecting any event whose n_{100} value is not equal to 0, we discard 75.6% of badly fit events while only 8.3% of well fit events are vetoed, as shown in figure 5.23.

The idea behind the divergence veto is somewhat similar to that behind the quad fitter algorithm [99, 89] in the SNOMAN code. The quad fitter randomly chooses 4 PMT hits from the data set and then directly calculates coordinates of their common original vertex assuming every PMT trigger is caused by a straight-line travelling photon. This resulting vertex is called a quad point. By repeating such procedures for various combinations of 4 PMT hits, the fitter finally form a quad cloud in the 4d (x,y,x,t) parameter space. The location of the maximal density of the cloud is regarded as the final fit vertex [100]. This algorithm becomes vulnerable when the number of bad PMT hits increases since the number of bad combinations, which contain one or more bad PMT hits, increases more than linearly with the number of bad hits and the quad fitter does not have the ability to discard those bad hits recursively as the time fitter (although the quad fitter could implicitly discard some bad hits because the bad hit often does not have a real solution to form a quad point.). However, the character (e.g. the size) of the quad cloud may also be a good indication of the performance of the vertex fitter.

There are many implementations of the idea behind the divergence veto. The n_{100} variable mentioned above is just one of such implementations, which has already been proved to be fairly useful in identifying badly fit events. Personally the author thinks it is worth pursuing this idea further.

5.4.6 Summary

Several software vetoes have been developed to reject PMT β-γ decay events, of which the divergence veto turned out to be most useful. Combining the divergence veto with any one of other vetoes or the Lorentzian fitter described in previous sections, we are able to reject all of studied PMT β-γ decay events mis-reconstructed inside the acrylic vessel while only losing a small proportion of internal events. If Monte Carlo simulations by the SNOMAN code agree with the reality, we are confident that with the help of vertex fitters and background vetoes, the PMT β-γ decay events should not form a severe contamination to the internal events, which is a prerequisite for the technique described in the next chapter to determine the level of internal backgrounds in the SNO detector.

5.5 Conclusion and Comments

It is difficult to measure accurately radioactive concentration levels in the various components of photomultipliers. However, if the SNOMAN code is reasonably correct, we should be able to deduce the number of PMT β-γ decay events fairly accurately from the number of detected events at low nhits. Even if we think all events recorded by the SNO detector are PMT β-γ decay events (maybe with some help from vertex fitters), the error should not be larger than 10% since PMT β-γ decay events are dominant in the detector (PMT sphere is dirtiest part of the detector except the cavity wall which is shielded away by 2 meters of light water.).

If the prediction of the SNOMAN code agrees with the reality, with the help of vertex fitters and background vetoes, we should be able to get rid of almost all of PMT β-γ decay events from the data.

However, author has to point out that the credibility of all these works depends on the correctness of the SNOMAN code. The background calibration source described later should give us confidence in the performance of the code. Personally, the author think the simplest and ultimately the best way to find out whether the PMT β-γ decay is a serious background is a light water fill which will get rid of most of high energy signals from solar neutrinos.

Figure 5.21: **Results of the divergence veto for two events with same number of PMT hits.** The top figure shows the fit vertices for a PMT β-γ event mis-reconstructed inside the acrylic vessel while the bottom figure shows the fit vertices for a well reconstructed ^{208}Tl decay event in the D_2O. Note the difference in the scale of axes between two figures.

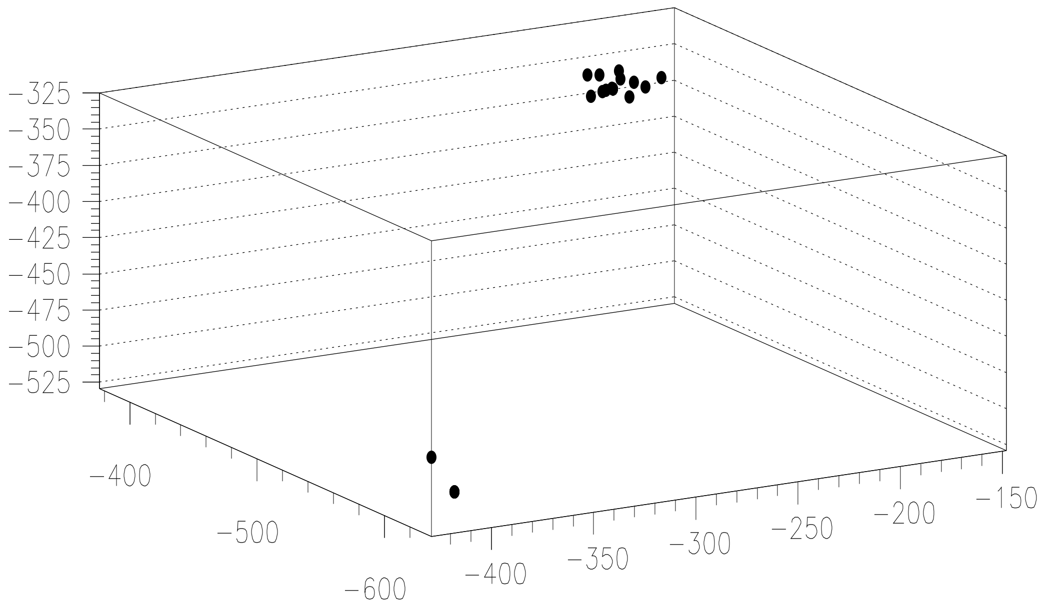

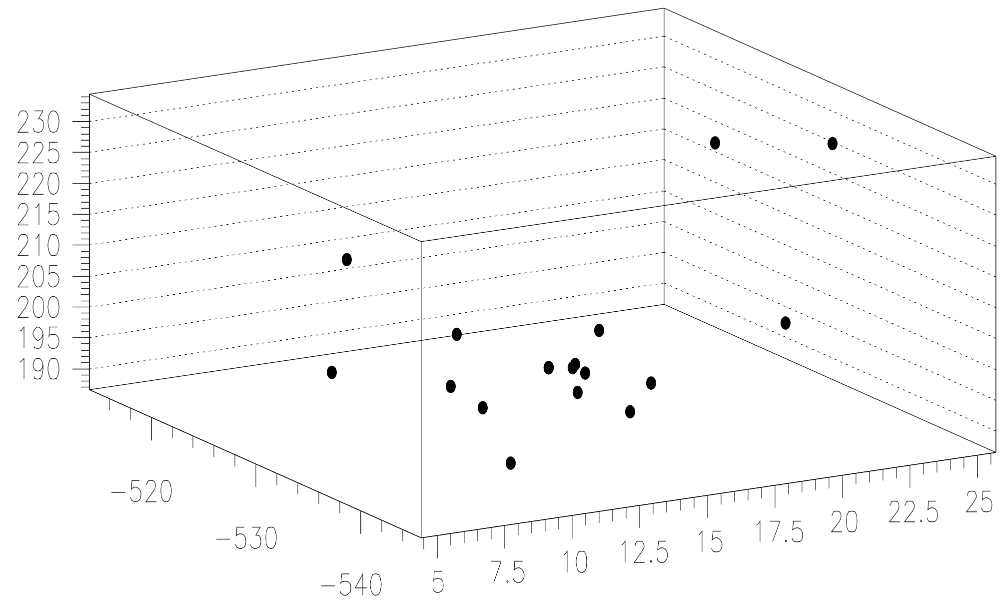

Figure 5.22: n_{100} **distributions for two sets of events.** The lower figure shows the distribution for 17 PMT β-γ event mis-reconstructed inside the acrylic vessel while the upper figure shows the distribution for 1350 well reconstructed ^{208}Tl decay event in the D_2O. Note the vertical axes are at log scale.

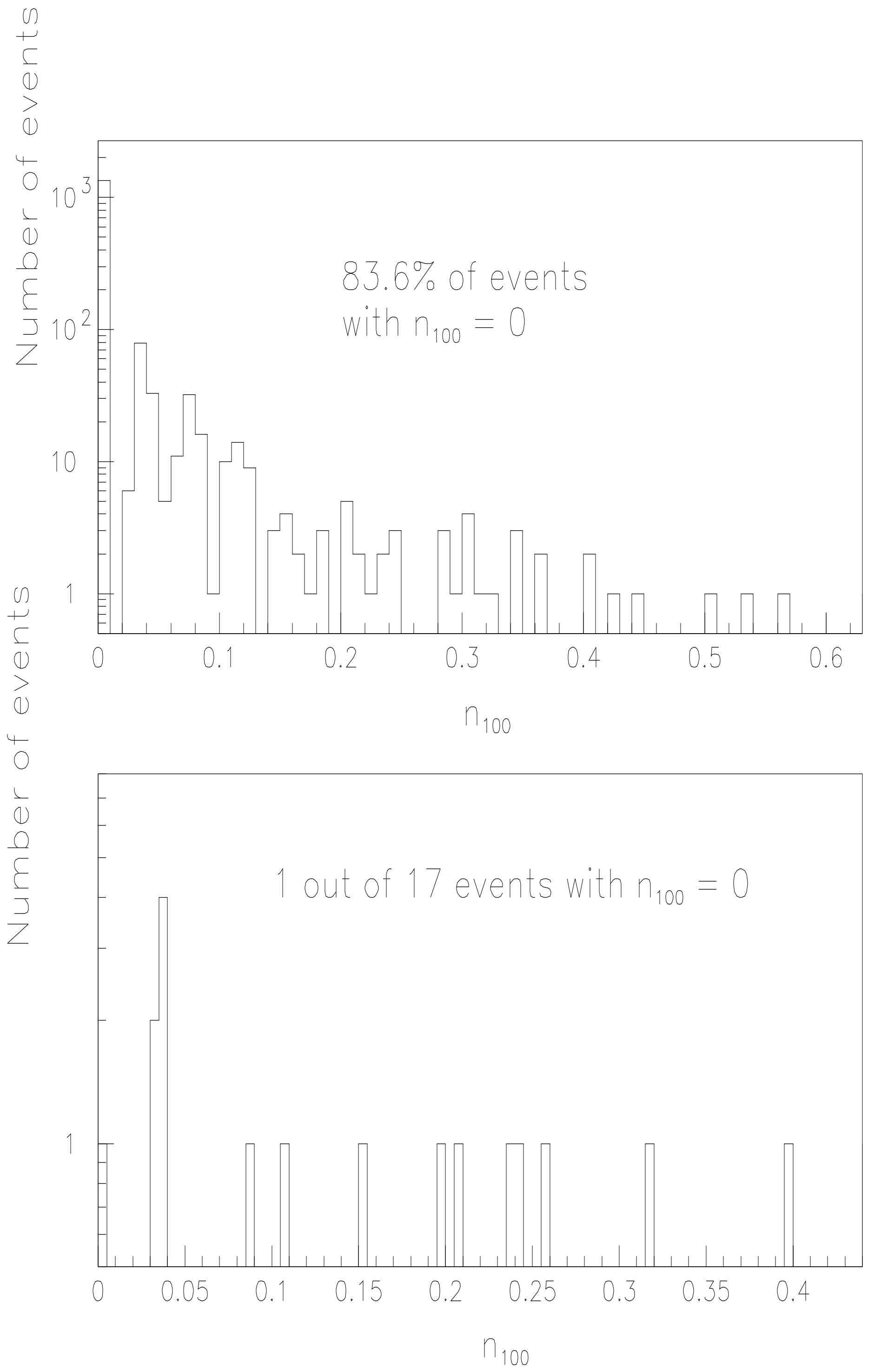

Figure 5.23: n_{100} **distributions for 1500 5 MeV electrons uniformly distributed in the** D_2O **region.** The upper plot shows the distribution for events which are correctly reconstructed within 1 meter of the true vertex while the bottom plot shows the distribution for those events with are wrongly reconstructed at least 1 meter away from the true vertex. Note the vertical axes are a log scale.

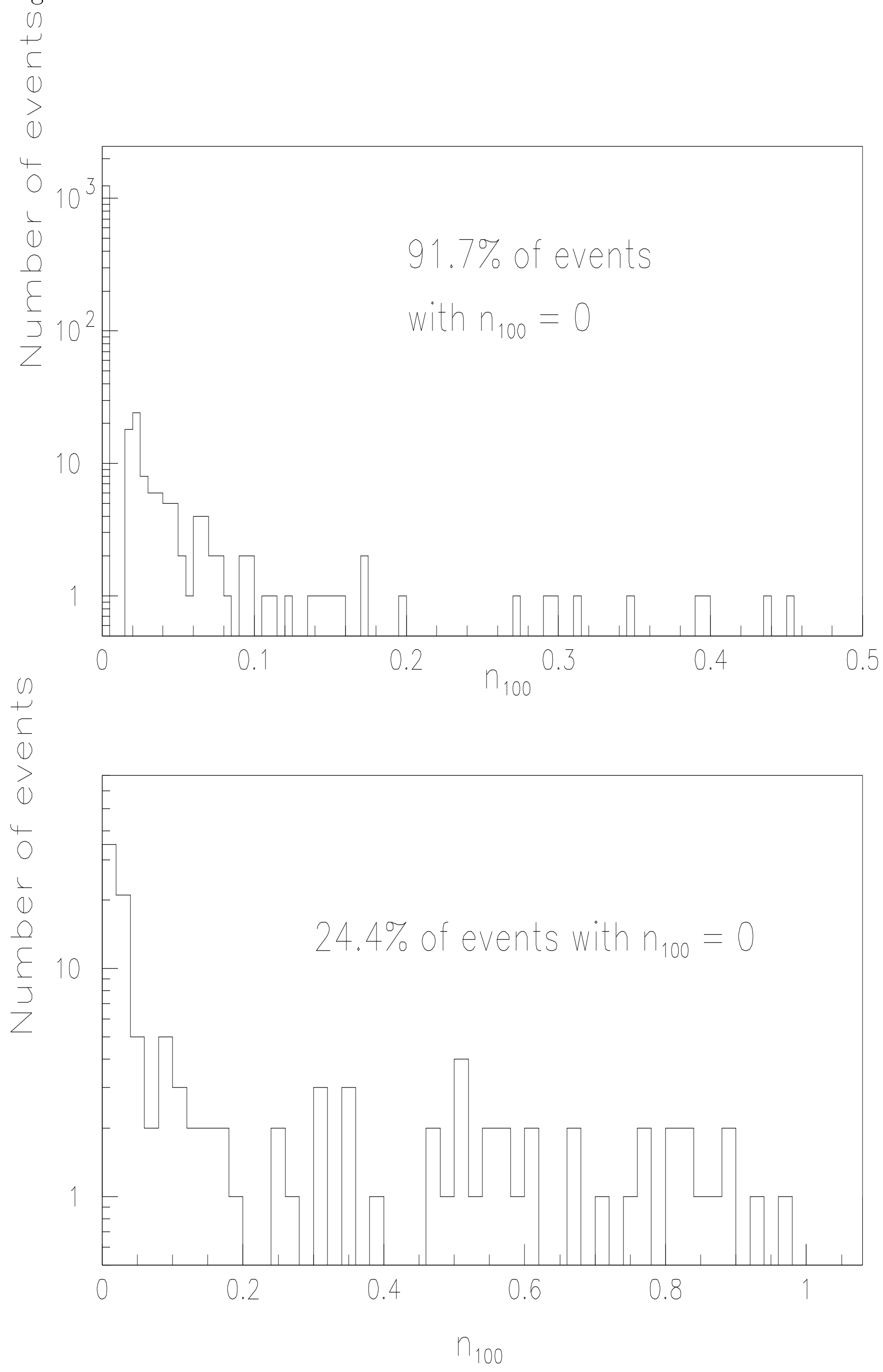

Chapter 6

Determining Background Levels in the SNO detector

6.1 Introduction

As discussed in previous chapters, the major backgrounds in the SNO detector are ^{208}Tl and ^{214}Bi decays in the D_2O region, the acrylic vessel and the H_2O region, of which the most troublesome are the radioactive decays in the 1000 tons of heavy water. These so-called internal backgrounds (or D_2O β-γ decays) are in the same region as the events induced by solar neutrinos (thus vertex fitters are useless for discriminating this background) and they are able to produce free neutrons which are indistinguishable from neutrons produced by neutral current events (thus the standard energy threshold, the nhits cut, is useless.). We must be able to measure the levels of backgrounds, which are critical in terms of determining the energy threshold of the detector. More importantly, we must be able to determine the number of NC background events accurately which must then be subtracted from the number of neutron capture signals in order to get the correct number of neutral current events.

Several assay techniques have been developed, as described in chapter 3, to extract radioactive nuclei in the thorium and the uranium decay chains from the water chemically and then count them, which enables us to deduce the number of ^{208}Tl and ^{214}Bi decays in the water. However, all of these methods require a lot of additional hardware, complex chemical extraction and counting techniques, and the assumption of secular equilibrium below ^{212}Pb in the thorium chain and ^{222}Rn in the uranium chain. This chapter describes some software techniques developed by the author which enable us to determine the levels of the major backgrounds in the SNO detector in-situ, real time, and without involving any hardware, complex chemical procedures or the assumption of secular equilibrium.

Section 6.2 describes the theory and the method used to determine the levels of D_2O backgrounds, the most troublesome ones in the detector. Section 6.3 is a step further from section 6.2. It introduces the neural network technique, which, when combined with a histogram fitting technique, enables us to determine the levels of all the major backgrounds (^{214}Bi and ^{208}Tl decays in the D_2O, the AV and the H_2O region)in the SNO detector.

6.2 Determining levels of Internal Backgrounds

6.2.1 The Theory

The major internal backgrounds are the ^{208}Tl and ^{214}Bi decays in 1000 tons of heavy water since they not only have largest Q values in β-γ decays (although the ^{210}Tl decay has a larger Q value, its effect can be ignored because of its small branch ratio(0.021%) and its equilibrium with the ^{214}Bi decay) in thorium and uranium decay chains but also produce high energy gamma rays which are capable of producing free neutrons by photodisintegrating deuteron nuclei. It should not be difficult to get clean data from these two decays in order to determine their levels by filtering data through an offline window (nhits or r_{fit} cut), as shown later. The problem is how to distinguish between these two types of decays. This is most difficult and important since two decays with different Q values contribute to the total background level differently and they have different probabilities for creating neutral current backgrounds.

The first thought is that it might be easy to distinguish between the two types of decays since they have different Q values. However, the larger Q value of the ^{208}Tl decay is compensated for by the larger number of ^{214}Bi decays. In order to distinguish between the two types of decays, we must know the shape of whole energy spectrum, including the low nhits part which is severely contaminated by various other backgrounds in the SNO detector. This is the major reason that the technique of fitting the background spectra described in chapter 3 did not work. What we need is a technique which is able to distinguish between the two types of decays while only using information contained in the high nhits (30-40) part of the energy spectrum (3MeV-4MeV).

Table 6.1 and table 6.2 show the decay schemes of the ^{208}Tl and the ^{214}Bi β-γ decays.

Table 6.1: **Decay Scheme of the ^{208}Tl nucleus [101].**

Cumulative branching ratio	Energy of electron(MeV)	Number of gammas	Energies of gammas (MeV)
0.000521	0.5115	3	1.2828 0.5831 2.6146
0.000691	0.6091	3	1.1852 0.5831 2.6146
0.000713	0.6336	2	1.7438 2.6146
0.000821	0.6336	3	1.1607 0.5831 2.6146
0.001015	0.6336	3	0.8834 0.8604 2.6146
0.001123	0.6336	4	0.8834 0.2773 0.5831 2.6146
0.001385	0.6958	3	0.8212 0.8604 2.6146
.....	.....	..	....
0.488909	1.517	3	0.2773 0.5831 2.6146
0.999700	1.7943	2	0.5831 2.6146
1.000000	2.3774	1	2.6146

Table 6.2: **Decay Scheme of the ^{214}Bi nucleus [101].**

Cumulative branching ratio	Energy of electron(MeV)	Number of gammas	Energies of gammas (MeV)
0.178417	3.27	0	
0.178587	1.1222	1	2.1478
0.182679	1.1222	2	1.86869 0.60931
0.194613	1.15145	1	2.11855
0.216350	1.15145	2	1.50924 0.60931
0.217381	1.15145	2	0.70307 1.41548
0.221038	1.15145	3	0.70307 0.80617 0.60931
0.221728	1.15145	2	0.38894 1.72961
.....	.....	..	....
0.999144	0.5753	1	2.6947
0.999529	0.5753	2	1.31702 1.37768
1.000000	0.5753	3	1.31702 0.76837 0.60931

Although the schemes are not complete (the complete schemes would take tens of pages.), there are several characteristic differences between the two schemes:

- As said before, the Q values of the two types of decays are different. More importantly, almost every branch of the ^{208}Tl decay has a high energy (2.614 MeV) gamma ray, several low energy gamma rays and one electron while only 1.54% of the ^{214}Bi decays produce a gamma with energy larger than 2.2 MeV.

- There is a unique channel in the ^{214}Bi decay which only produces a single electron (with end point of 3.27 MeV). All other decay channels of the ^{208}Tl and the ^{214}Bi nucleus produce a electron plus one or more energetic gammas.

In addition, we have to consider some other factors:

- A energetic electron is capable of producing more Čerenkov photons than a gamma with the same amount of energy since the gamma has to give its energy to several electrons each of which has 260 keV Čerenkov threshold.

- A single energetic particle produces more photons than multiple particles with the same amount of total energy because of rules governing the production mechanism of Čerenkov photons (Nhits/MeV decreases as energy becomes smaller.) and the non-zero Čerenkov threshold.

Based on the facts described above, we are able to see a difference between the two types of decays. If we impose a high nhits window, which is just what we need in order to get rid of contaminations from other radioactive decays, on the events , it is possible to get almost purely those ^{214}Bi decay events which only produce a single electron while still selecting the ^{208}Tl decay events which produce multiple particles. Figure 6.1 shows the average number of gammas produced by these two types of decays. On average, above the detector threshold (10 hits), each ^{208}Tl decay produces more than 2 energetic gammas while ^{214}Bi decay produces less than 1 gamma. More importantly, as the nhits threshold is increased, number of gammas produced by the ^{214}Bi decay event decreases dramatically, which does not happen for the ^{208}Tl decay event. This is because in order to provide a larger number of hits, ^{214}Bi decay events tend to decay by the single electron channel, which produces more photons. In fact, if we only select those events with nhits larger than 30, 92% of the ^{214}Bi decay events produce a single particle (3.27 MeV electron) while all of the ^{208}Tl decay events produce multiple particles (one electron + one high energy gamma ray + several low energy gamma rays).

Now the problem of how to distinguish between the two types of decays changes to the problem of how to distinguish between the single particle and the multiple particle events. The signals of an event are some PMT triggers induced by Čerenkov photons whose directions, to some extent, depend on the direction of the original charged particle. There is little correlation among the directions of the multiple particles produced by the ^{208}Tl decay. Thus it is expected that, above 30 hits, the hit PMTs produced by ^{208}Tl decay events should be distributed somewhat more isotropically than that of ^{214}Bi decay events. This is the theoretical basis of the following method used to distinguish between the two types of decays.

6.2.2 Implementations and Results

Naturally, the first thought is that above 30 hits, a ^{214}Bi decay event is more or less a cone-like event (because of the Čerenkov cone produced by its decay product: a single electron) while a ^{208}Tl decay event should not have such a character. This leads to the first parameter used to distinguish between the two types of decays: θ_i, which is the angle between two vectors. The first one is the fit direction of the event while the other vector is from the fitted position of the event to the position of the i^{th} PMT hit, as shown in figure 6.2. Figure 6.3 shows θ_i distributions for the ^{208}Tl and the ^{214}Bi decay events above 30 nhits. On average, ^{214}Bi decay events have a θ_i value somewhat less than that of ^{208}Tl decay events because of the reasons mentioned above. A more efficient parameter is $\overline{\theta_i}$, the mean value of θ_i averaged for all PMT triggers in one event. $\overline{\theta_i}$ distributions for the two types of decays are shown in figure 6.4. The difference between these two distributions could be used to distinguish the two types of decays statistically. The problem with this technique is that it depends heavily on the accuracy of fitting the event direction. It is more difficult to fit the event direction than the event position and the average error of the fit direction is 20 degrees when the time fitter is used. Furthermore, there is no point in asking what is the direction for an event with multiple outgoing particles. The algorithm used in the time fitter uses the direction averaged over all detected photons as the fit event direction. Thus the difference between a cone-like event (the ^{214}Bi decay) and a non-cone-like event (the ^{208}Tl decay) is not sufficiently expressed by this parameter.

The second parameter I used is called θ_{ij}. It is the angle between two vectors which

Figure 6.1: **Averaged number of gammas produced by the ^{208}Tl decays (solid line) and the ^{214}Bi decays (dashed line) with nhits threshold set at various values.** Note these decays always produce one electron.

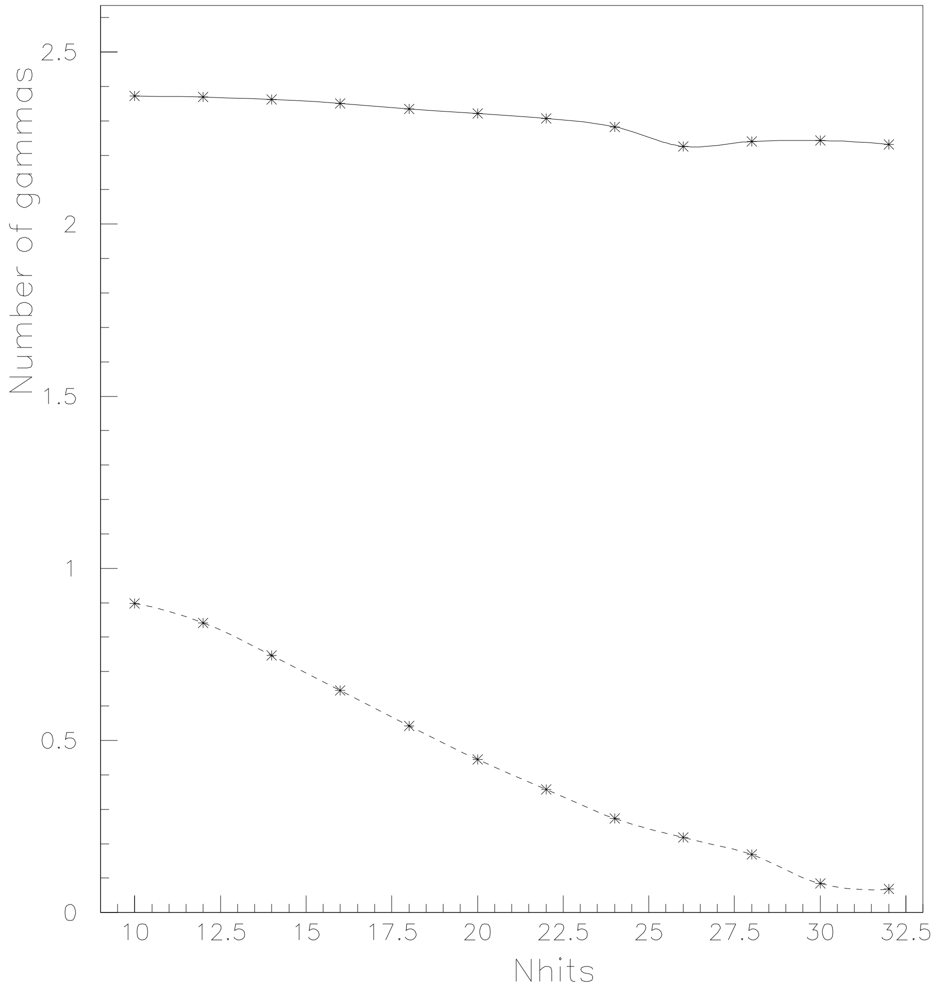

Figure 6.2: θ_i **and** θ_{ij} **parameter used to distinguish between the** ^{208}Tl **and the** ^{214}Bi **decay.** see text.

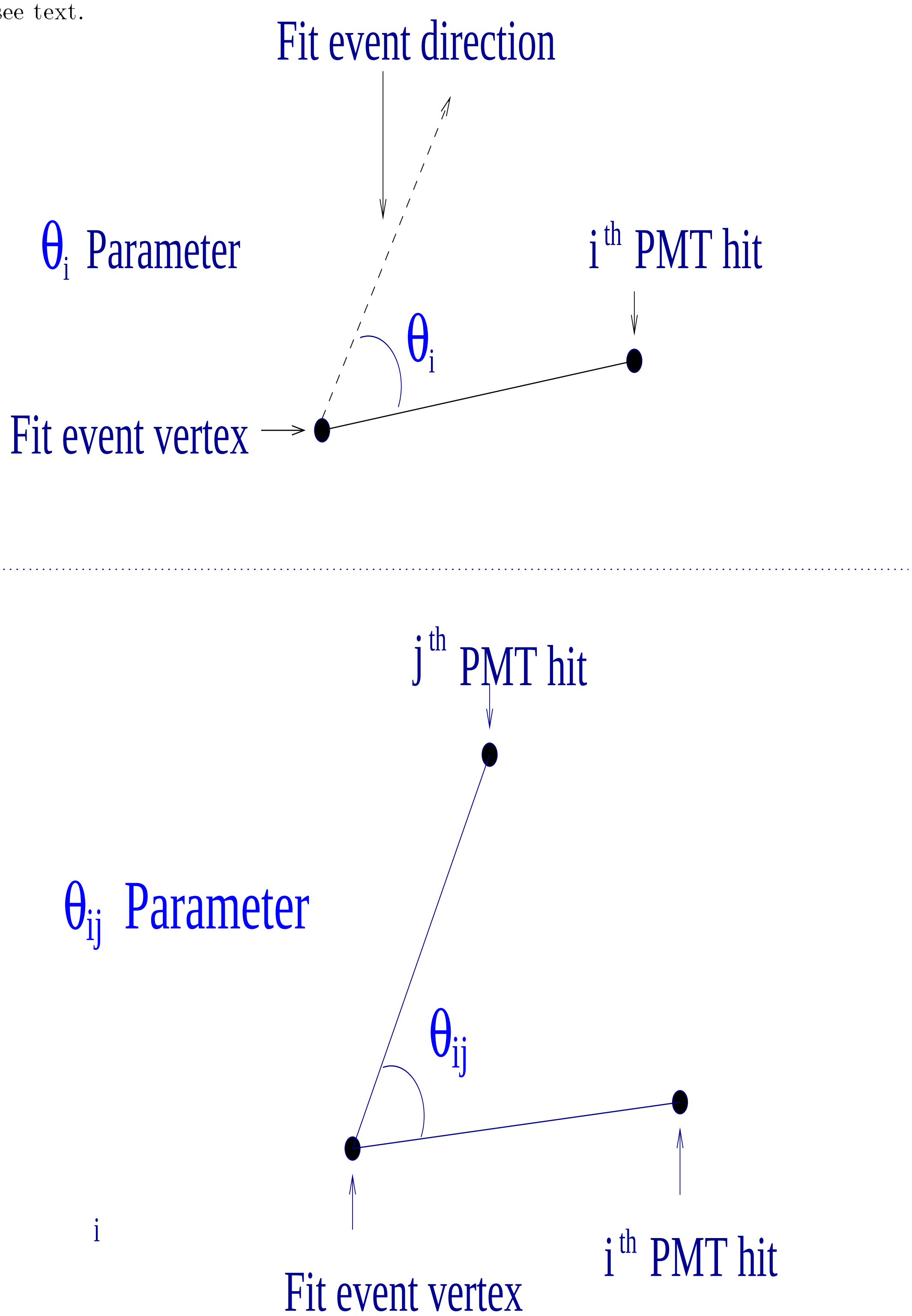

Figure 6.3: θ_i **distributions for equal numbers of** ^{208}Tl **(solid line) and** ^{214}Bi **decay events (dashed line) above 30 hits.**

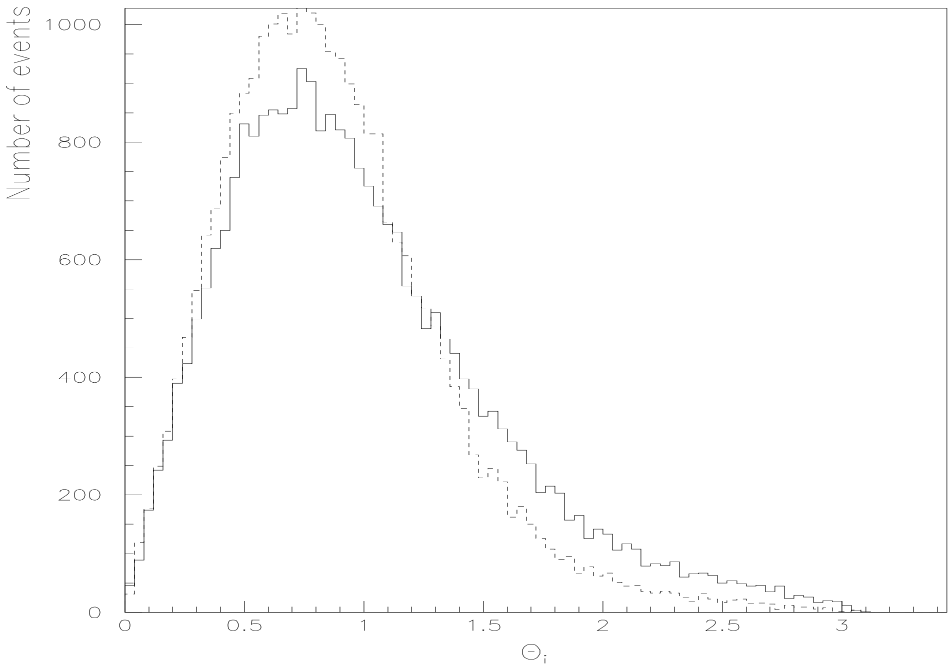

Figure 6.4: $\overline{\theta_i}$ **distributions for equal numbers of** ^{208}Tl **(dashed line) and** ^{214}Bi **(solid line) decay events above 30 hits.**

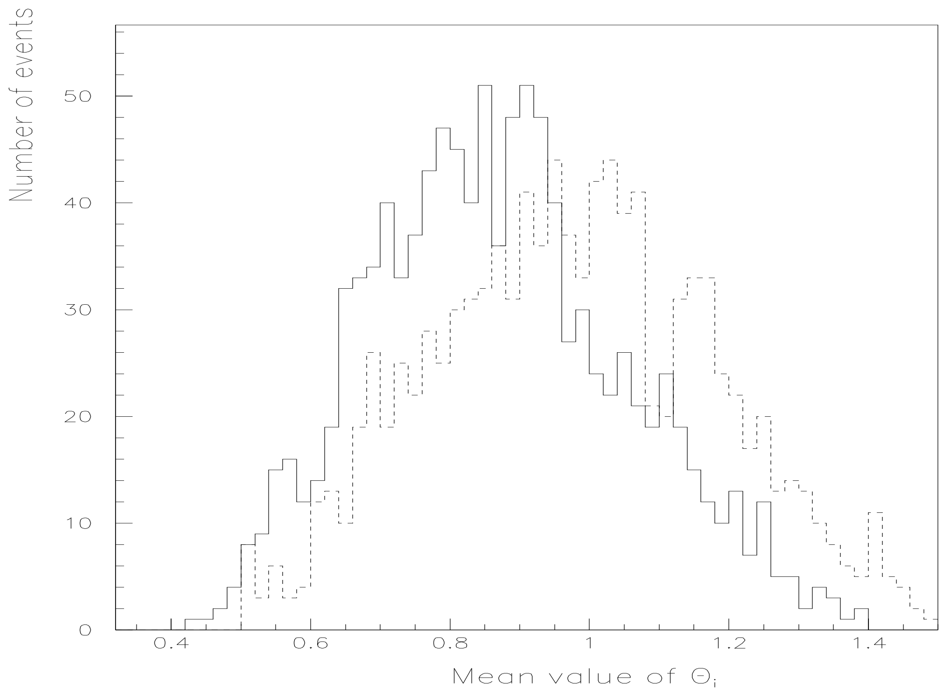

are from the fit vertex to the i^{th} and j^{th} PMT hits respectively, as shown in figure 6.2. The benefit of choosing such a parameter is that it does not depend on the accuracy of the fitted event direction any more, instead it only depends on the accuracy of the fitted event position. Furthermore, this parameter is rotationally invariant because of the spherical symmetry of the SNO detector. Since the average reconstruction error of the time fitter is around 20cm, which is fairly small compared to the dimension of the detector, this parameter is expected to work better than the previous one. In practice, similar to the previous parameter, we use the mean value of θ_{ij} averaged over all combinations of two PMT hits. $\overline{\theta_{ij}}$ distributions for ^{208}Tl and ^{214}Bi decay events are shown in figure 6.5. With the help of the $\overline{\theta_{ij}}$ parameter, the difference between the two types of decays should be large enough to carry out a statistical separation.

The task of the statistical separation is to determine the ratio of two types of decay events in a mixed data set. The procedures are as follows:

1. Equal and large numbers of ^{208}Tl and ^{214}Bi decay events in the D_2O region are simulated to produce the $\overline{\theta_{ij}}$ distributions, which are called calibration distributions, for the two types of decays. The $\overline{\theta_{ij}}$ distribution is also produced for a mixed data set, which is called the data distribution.

2. A standard chi square fitting method is carried out to fit the data distribution to a linear combination of the two calibration distributions:

$$\chi^2 = \sum_i \frac{(d_i - a_1 c_{i1} - a_2 c_{i2})^2}{\sigma_{d_i}^2 + a_1^2\sigma_{c_{i1}}^2 + a_2^2\sigma_{c_{i2}}^2} \tag{6.1}$$

   where d_i is the number of events in the i^{th} bin of the data distribution, c_{i1} and c_{i2} are the number of events in the i^{th} bin of the two calibration distributions respectively. The statistical errors are taken into account as follows:

$$\sigma_{d_i}^2 = d_i; \quad \sigma_{c_{i1}}^2 = c_{i1}; \quad \sigma_{c_{i2}}^2 = c_{i2}; \tag{6.2}$$

3. The Levenberg-Marquart method [92] is used to minimize this χ^2 function with ratios a_1 and a_2 as fitted variables.

In order to verify that this technique works for various admixtures of the two types of decays, various combinations of two types of decay events were tried and the fit results

Figure 6.5: **$\overline{\theta_{ij}}$ distributions for equal numbers of ^{208}Tl (dashed line) and ^{214}Bi (solid line) decay events above 30 nhits.**

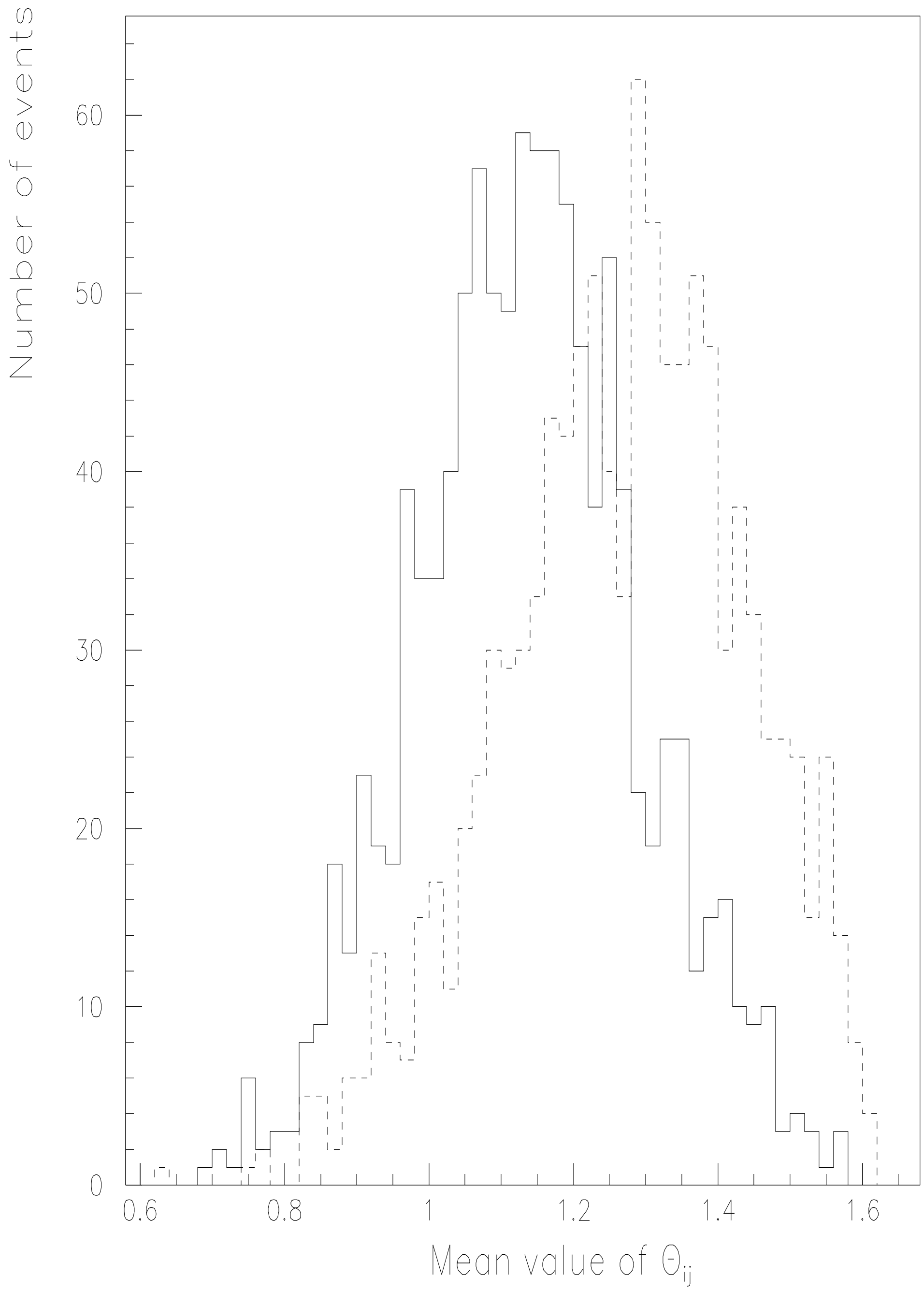

Table 6.3: The results of the statistical separation of the ^{208}Tl and the ^{214}Bi decays in D_2O

Number of events	True fraction for ^{208}Tl	Fitted fraction for ^{208}Tl	True fraction for ^{214}Bi	Fitted fraction for ^{214}Bi
3000Tl+3000Bi	0.5	0.489 +/- 0.030	0.5	0.509 +/- 0.031
4000Tl+2000Bi	0.667	0.665 +/- 0.032	0.333	0.333 +/- 0.030
4000Tl+1000Bi	0.8	0.784 +/- 0.035	0.2	0.214 +/- 0.032
4000Tl+400Bi	0.909	0.897 +/- 0.039	0.091	0.100 +/- 0.034
1500Tl+3000Bi	0.333	0.328 +/- 0.032	0.667	0.669 +/- 0.035
1000Tl+3000Bi	0.25	0.230 +/- 0.033	0.75	0.767 +/- 0.038
300Tl+3000Bi	0.091	0.064 +/- 0.035	0.909	0.933 +/- 0.043
4000Tl+800Bi	0.833	0.820 +/- 0.036	0.167	0.178 +/- 0.032

are shown in table 6.3. This technique is able to distinguish between the ^{208}Tl and the ^{214}Bi decays in D_2O statistically for a large range of relative admixtures (all of the fitted results agree with the true values within the statistical errors.).

The procedure used to determine levels of major backgrounds in the D_2O region is summarized as follows:

1. A cut window (e.g. $30 < nhits < 40$ and $0 < r_{fit} < 400cm$) is imposed on the data so that the dominant events inside this window are the ^{208}Tl and the ^{214}Bi decay events occurring in the D_2O region. The other types of event contribute no more than 5% of the total signals inside this window, as shown in table 6.4.

2. The technique described above is used to distinguish between these two types of decays and determine their numbers in the cut window. Bad PMT hits are discarded from the analysis by rejecting any PMT hits with $|R_{dev}| > 100cm$ where

$$R_{dev} = c' * (t_{pmt} - t_{fit}) - \sqrt{(x_{pmt} - x_{fit})^2 + (y_{pmt} - y_{fit})^2 + (z_{pmt} - z_{fit})^2} \qquad (6.3)$$

   x_{pmt}, y_{pmt}, z_{pmt} and t_{pmt} are three spatial coordinates and one temporal coordinate of the PMT hit respectively and x_{fit}, y_{fit}, z_{fit} and t_{fit} are three spatial coordinates and one temporal coordinate of the fit event vertex. c' is the average speed of light in the light and heavy water.

3. The overall numbers of the ^{208}Tl and the ^{214}Bi decays are deduced by using the probability for each of the two event types to fall within the cut window which is

Table 6.4: The number of the events in the 'Th/U monitoring window'

Event type	Concentration level(g/g)	No. of events reconstructed in this window
^{208}Tl in D_2O	Th: $7.94 * 10^{-15}$	5890/year
^{214}Bi in D_2O	U: $11 * 10^{-15}$	6789/year
^{208}Tl in Acrylic Vessel	Th: $4.6 * 10^{-13}$	95.2/year
^{214}Bi in Acrylic Vessel	U: $6.3 * 10^{-13}$	150/year
^{208}Tl in H_2O	Th: $7.52 * 10^{-14}$	23/year
^{214}Bi in H_2O	U: $8.6 * 10^{-14}$	116/year
Charged Current Event	CC No:4500	84.9/year

determined by the Monte Carlo simulation (1.6% for ^{208}Tl decay events and 0.155% for ^{214}Bi decay events).

Step 1 of the determining procedures is relatively easy to fulfill since we can always tighten the cut window to get clean signals of the ^{208}Tl and the ^{214}Bi decays in the D_2O. The main problem lies within the second and the third steps, where the Monte Carlo simulation plays a fairly important role. Thus the accuracy of the code is essential. Since the hope that the predictions of the code agree with reality completely is unrealistic, we have to check the robustness of this technique against possible systematic errors due to discrepancies between the MC simulation and reality.

6.2.3 Systematic Studies

Fitter residuals

At present we have no ideas how large the errors of the vertex fitters are when they are used on real events. Whether this pattern recognition technique is robust against the discrepancy between the fit errors of MC events and the fit errors of real events should be checked. However, we do not have any data from the detector yet. An alternative but insufficient way to estimate the systematic error due to this possible discrepancy is to check the robustness of this technique when different vertex fitters are used since these fitters have different fitting errors. This is carried out by generating the calibration distributions with the use of the time fitter while producing the data distribution with

Table 6.5: **Results of the systematic study of the pattern recognition technique when using different vertex fitter.**

Number of events	True fraction for ^{208}Tl	Fitted fraction for ^{208}Tl	True fraction for ^{214}Bi	Fitted fraction for ^{214}Bi
3000Tl+3000Bi	0.5	0.472 +/- 0.030	0.5	0.531 +/- 0.032
4000Tl+2000Bi	0.667	0.700 +/- 0.033	0.333	0.301 +/- 0.030
4000Tl+1000Bi	0.8	0.850 +/- 0.037	0.2	0.151 +/- 0.032
4000Tl+400Bi	0.909	0.977 +/- 0.041	0.091	0.025 +/- 0.035
1500Tl+3000Bi	0.333	0.291 +/- 0.032	0.667	0.710 +/- 0.036
1000Tl+3000Bi	0.25	0.203 +/- 0.034	0.75	0.800 +/- 0.039
300Tl+3000Bi	0.091	0.036 +/- 0.036	0.909	0.969 +/- 0.044
4000Tl+800Bi	0.833	0.891 +/- 0.038	0.167	0.110 +/- 0.033

the grid fitter. The difference between the errors of two fitters is large: the grid fitter has 51cm mean value and 34cm width while the time fitter has 59cm mean value and 55cm width. Then the chi square fit is repeated as before. As table 6.5 shows, the fitted results are worse but still lie within two standard deviations of the true values. This technique should be robust against small errors of the vertex fitters and any large reconstruction errors should be identified using the calibration source described in the next chapter.

Energy Scale

A systematic error may arise from the uncertainty of the absolute energy scale. A test of this technique was performed by generating the calibration distributions from events with nhits ranging from 30 to 40, while producing the data distribution from events with nhits ranging from 29 to 39 which was then shifted up by 1 hit. The chi square fit is repeated and the results are shown in table 6.6. This technique is fairly robust against this systematic error. But the problem occurs when we deduce the overall numbers of decay events from the numbers falling in the monitor window because the event numbers drops fairly quickly with the increasing nhits, this resulted in a 30% systematic error. The calibration source described in the next chapter should be able to reduce the uncertainty of the absolute energy scale to 1% level.

Table 6.6: **Results of the systematic study of the pattern recognition technique when using different nhits window.**

Number of events	True fraction for ^{208}Tl	Fitted fraction for ^{208}Tl	True fraction for ^{214}Bi	Fitted fraction for ^{214}Bi
3000Tl+3000Bi	0.5	0.513 +/- 0.030	0.5	0.485 +/- 0.031
4000Tl+2000Bi	0.667	0.657 +/- 0.032	0.333	0.341 +/- 0.030
4000Tl+1000Bi	0.8	0.788 +/- 0.036	0.2	0.210 +/- 0.032
4000Tl+400Bi	0.909	0.890 +/- 0.039	0.091	0.108 +/- 0.034
1500Tl+3000Bi	0.333	0.355 +/- 0.032	0.667	0.642 +/- 0.035
1000Tl+3000Bi	0.25	0.282 +/- 0.033	0.75	0.714 +/- 0.037
300Tl+3000Bi	0.091	0.104 +/- 0.032	0.909	0.898 +/- 0.038
4000Tl+800Bi	0.833	0.818 +/- 0.037	0.167	0.179 +/- 0.033

Incompleteness of the decay schemes

MC Simulations of the ^{208}Tl and the ^{214}Bi decays strongly depend on the correctness and completeness of their decay schemes. These decay schemes are complex and updated almost every year. Before the 2_09 version of the code, only 98.53% of the ^{208}Tl and 74.6% of the ^{214}Bi decay schemes were included in the simulation. Tests have been done on the robustness of this technique against the systematic error due to the incompleteness or/and possible mistakes in the two decay schemes. The calibration distributions were generated with the complete decay schemes while the data distribution was produced with the incomplete decay schemes. The chi square fitting procedure was repeated. The results are shown in table 6.7.

All of the fitted results are consistent with the true values within the statistical errors even with only 74.6% ^{214}Bi decay schemes. This simply confirms the foundation of this separation method: Above 30 nhits, the ^{214}Bi decays are mostly single electron events. The decay branch with the 3.27 MeV single electron has been included in the original incomplete code. The original code renormalized the branching ratios of the ^{214}Bi decay schemes to 100%, which causes problems when we try to deduce the total number of events from the number of events reconstructed inside the window. For example, 3208 out of 3 million ^{214}Bi decay events were reconstructed in the monitor window after the update of the decay schemes, while 4197 out of 3 million events were reconstructed in the monitor

Table 6.7: Results of the systematic study on the pattern recognition technique when using different decay schemes

Number of events	True fraction for ^{208}Tl	Fitted fraction for ^{208}Tl	True fraction for ^{214}Bi	Fitted fraction for ^{214}Bi
4000Tl+4000Bi	0.5	0.495 +/- 0.029	0.5	0.504 +/- 0.029
4000Tl+2000Bi	0.667	0.641 +/- 0.032	0.333	0.356 +/- 0.030
4000Tl+1000Bi	0.8	0.773 +/- 0.035	0.2	0.223 +/- 0.032
2000Tl+4000Bi	0.333	0.336 +/- 0.030	0.667	0.664 +/- 0.032
1000Tl+4000Bi	0.2	0.191 +/- 0.031	0.8	0.810 +/- 0.036
400Tl+4000Bi	0.091	0.072 +/- 0.033	0.909	0.931 +/- 0.040
4000Tl+400Bi	0.909	0.890 +/- 0.039	0.091	0.107 +/- 0.034

window when using the incomplete decay schemes. This causes a 31% systematic error, which illustrates the importance of the update of the decay schemes. Again we have to rely on the background calibration source to verify the correctness of the MC simulation.

Inaccuracy of the EGS4 code

The performance of this pattern recognition technique heavily depends on the accuracy of the code used to simulate the angular distribution of Čerenkov photons generated by the event. The SNOMAN code uses the EGS4 (Electron and Gamma Shower) code system [82] to simulate the propagation of the electron or/and the gamma. One suggestion [102] from some members of the SNO collaboration is that the Moliere multiple-scattering theory used in the EGS4 code system is not good enough to describe accurately the angular distribution of Čerenkov photons induced by a energetic electron in the D_2O. Instead the Dedrick single-scattering theory should be used in the simulation. It was claimed that the SNOMAN code underestimated the width of the angular distribution of Čerenkov photons, which might lead to the failure of the technique used to distinguish between the two types of decays.

We have analyzed the data from [102] and found out that the difference between angular distributions calculated according to two theories is fairly small [103]. We also carried out a study to verify that this pattern recognition technique is robust against such small errors even if it turns out that the Dedrick theory is right. We artificially widened the width of the angular distribution of photons by adding a 20% (+10%, -10%)

Table 6.8: **Results of the systematic study of the pattern recognition technique on possible errors in the angular distribution of photons.** see text.

Number of Events	True Fraction for ^{208}Tl	Fitted Fraction for ^{208}Tl	True Fraction for ^{214}Bi	Fitted Fraction for ^{214}Bi
1500Tl+1500Bi	0.5	0.48 +/- 0.04	0.5	0.51 +/- 0.04
3000Tl+1500Bi	0.667	0.641 +/- 0.036	0.333	0.359 +/- 0.035
4000Tl+1000Bi	0.8	0.79 +/- 0.037	0.2	0.21 +/- 0.034
4000Tl+400Bi	0.909	0.904 +/- 0.041	0.091	0.095 +/- 0.036
1000Tl+1500Bi	0.4	0.36 +/- 0.042	0.6	0.637 +/- 0.044
750Tl+1500Bi	0.333	0.292 +/- 0.041	0.667	0.7 +/- 0.045
500Tl+1500Bi	0.25	0.21 +/- 0.044	0.75	0.79 +/- 0.049

fluctuation to the Čerenkov angle calculated by the SNOMAN code. The distortion of the angular distribution due to this artifact is at least at the same order as (if not larger than) the difference between distributions calculated by two theories. The systematic study was carried out as follows:

1. Using the standard SNOMAN code, equal numbers of the ^{208}Tl and the ^{214}Bi decays in D_2O were simulated respectively to produce the $\overline{\theta_{ij}}$ distributions (calibration distributions) for the two types of decays.

2. The non-standard SNOMAN code with the varied Čerenkov angle is used to generate a certain number of the two types of events and the combined $\overline{\theta_{ij}}$ distribution(data distribution) was obtained.

3. The standard chi square fitting method was used to fit the data distribution to some linear combination of two calibration distributions and the relative numbers of the ^{208}Tl and the ^{214}Bi decay events were calculated.

Different combinations of the two types of events were tried and the results are presented in table 6.8. All fitted results lie within the statistical errors of the true values, the systematic error is ignorable compared with the statistical error.

6.2.4 Summary

The pattern recognition technique, which uses a simple $\overline{\theta_{ij}}$ parameter, is able to distinguish between the ^{208}Tl and the ^{214}Bi decay event statistically. Based on this technique, we should be able to determine the levels of major backgrounds in the D_2O region of the SNO detector accurately (within 1σ). This technique has the advantages of determining background levels in-situ, in real time and without the involvement of any additional hardware or complex chemical extraction and counting methods. It has been shown to be robust against some systematic errors due to possible discrepancies between the prediction of the MC code and reality.

6.3 Determining the levels of Major Backgrounds in the SNO Detector

6.3.1 The Theory

High energy gamma rays produced by radioactive decays in the acrylic vessel and the H_2O regions could easily travel into the D_2O region and produce free neutrons through photodisintegrations of deuteron nuclei. An accurate determination of background levels in these regions is also important since it would decide where should we put our fiducial cut in the D_2O region for the neutrino-induced events. Our ambition is to extend the technique described in the previous section further so that we are able to determine the levels of all major backgrounds (the ^{208}Tl and ^{214}Bi decays in the D_2O, the acrylic vessel and the H_2O region) in the SNO detector in-situ and in real time. If we achieve our object, we will have a technique which is completely different to the methods used in the water system and thus provide an independent cross check to the results from the water assay. Furthermore, the radioactive concentration levels in the AV, which can not be measured by the water system, could be determined by this technique (note the AV is much dirtier than the water in terms of radioactivities and it is just next to the D_2O region.).

There is little problem in finding a monitor window in which the ^{208}Tl and the ^{214}Bi decay events in the D_2O, the AV and the H_2O regions are dominant since they are major backgrounds in the detector (except for the PMT $\beta-\gamma$ backgrounds and we believe the techniques described in the previous chapter should be able to reject most of backgrounds from the PMT region.). The main task is to separate these six types of events (2 types of decays in three regions) and determine their numbers in the monitor window (table 6.12) respectively. Then we could use the Monte Carlo to determine the overall numbers of these decays respectively, as with the method used to determine major background levels in the D_2O.

First we need to distinguish between the ^{208}Tl and the ^{214}Bi decay events in the same region. We have succeeded in using $\overline{\theta_{ij}}$ parameter to distinguish between these two types of decays in the D_2O region. It seems that only the MC simulations (verified by the calibration sources) are able to tell whether the detector is still able to "see" the difference between the angular distributions of photons generated by these two decays in the AV or H_2O region. Figure 6.6 shows θ_{ij} distributions for equal numbers of ^{208}Tl and ^{214}Bi decays in the acrylic vessel (note in this figure every entry corresponds to a pair of PMT triggers instead of a decay event). At small values of θ_{ij}, the number of entries for the ^{208}Tl decay events is smaller than that of the ^{214}Bi decay events. At large value of θ_{ij}, the situation is the opposite. Thus on average, a ^{208}Tl decay event in the acrylic vessel should have a larger mean value of θ_{ij} than a ^{214}Bi decay event in the same region, just as the situation for events in the D_2O region. MC simulation shows that a similar situation occurs for the decay events in the H_2O region.

After we have found a way to distinguish between the two types of events in the same region, the next task is to find a way to separate the same type of events in different regions. A natural solution to this problem is a vertex fitter which is able to determine the position of the event. We used the time fitter, the basic and the fastest (although not the best) fitter in the SNOMAN code. Figure 6.7 shows R_{fit} (the distance between the center of the detector and the fitted event vertex) distributions for the ^{208}Tl and ^{214}Bi decay events in the D_2O, the acrylic vessel and the H_2O regions. Since the fitter reconstructs most of events fairly close to their true positions, the R_{fit} distribution for the events occurring in the AV should peak at the position of the acrylic vessel (corresponding to $PAR \approx 0.94$ in the plot) while the R_{fit} distribution for the events occurring in the light water should peak at the position just out of the AV and the R_{fit} distribution for decay events in the heavy water is fairly flat between 0 and 1 (Due to the spherical geometry of the detector, the distribution is slightly peaked at the edge of the AV.).

The difference between the R_{fit} distributions of events in the AV and the H_2O region is small because two regions are next to each other and we have to impose a tight R_{fit}

Figure 6.6: θ_{ij} **distributions for equal numbers of** ^{208}Tl **(dashed line) and** ^{214}Bi **(solid line) decays in the acrylic vessel.**

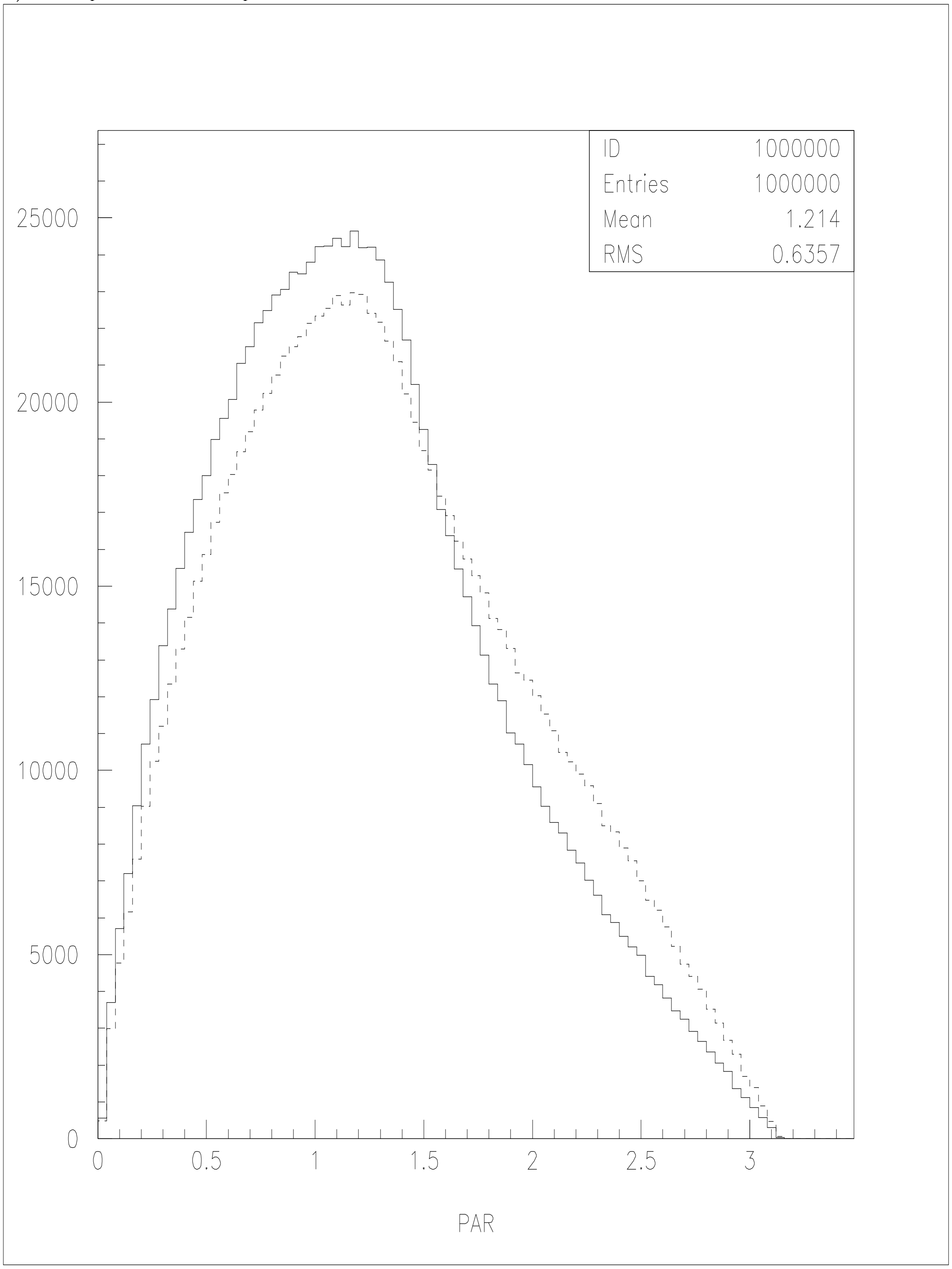

Figure 6.7: R_{fit} **distributions for equal numbers of** ^{208}Tl **decay events (upper plot) in three regions:** D_2O**(dashed line), the acrylic vessel (dotted line) and** H_2O **(solid line) ; equal numbers of** ^{214}Bi **decay events (bottom plot) in three regions:** D_2O**(dashed line), the acrylic vessel (dotted line) and** H_2O **(solid line).** The R_{fit} value is normalized to lie between 0 and 1. Thus $PAR = 1$ corresponds to $R_{fit} = 640$ and $PAR = 0$ corresponds to $R_{fit} = 0$

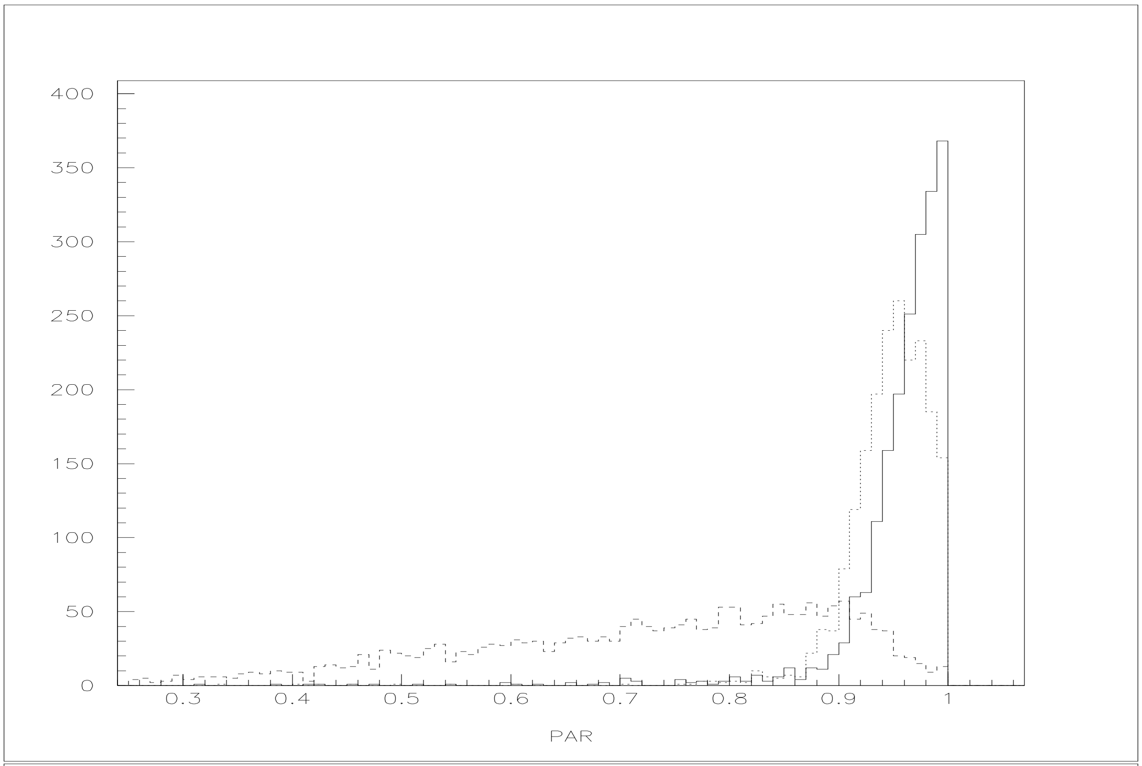

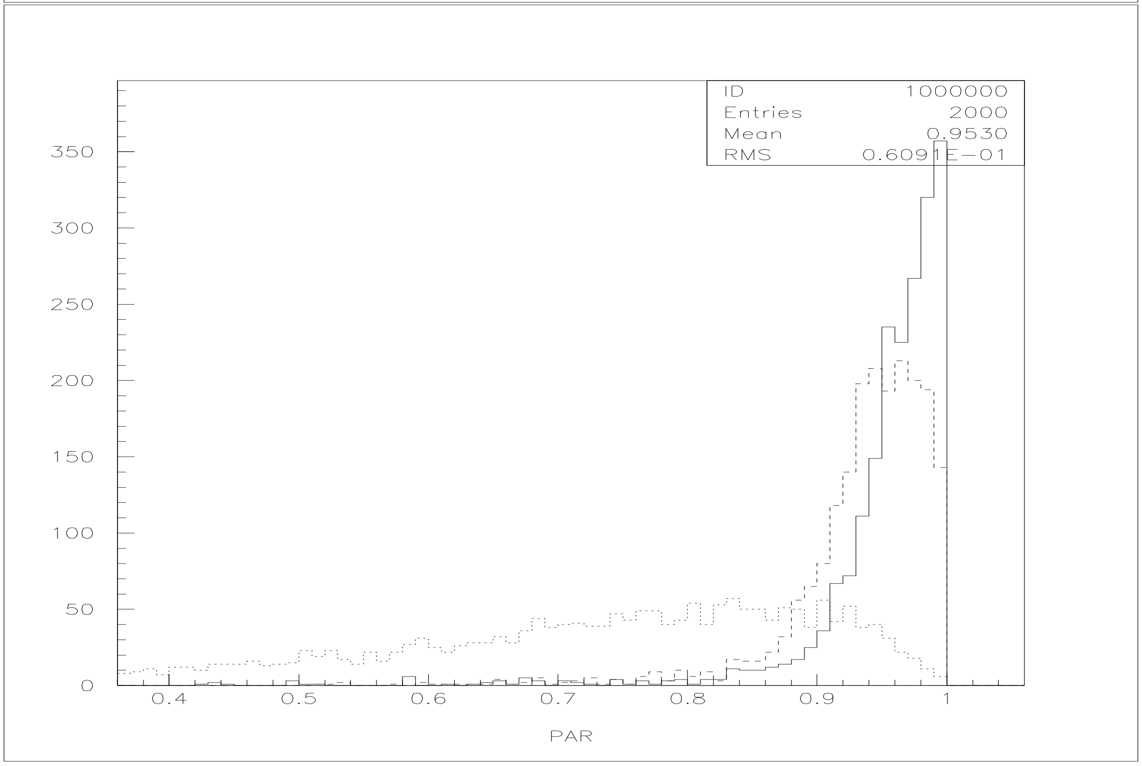

cut (eg. $R_{fit} < 640cm$) in order to reject mis-reconstructed PMT β-γ decay events. This difference also heavily depends on the accuracy of the vertex fitter. We have come up with another method to separate events in different regions. For a decay event in the acrylic vessel, a Čerenkov photon travelling approximately along the vessel (normal to the radial direction) is much more likely to be absorbed than the photon travelling at other directions since the attenuation length of the photon in the acrylic is much shorter (orders of two magnitude less) than that in the water and by travelling along the vessel, the photon has to traverse the longest path in acrylic before entering the water region. Furthermore, such a photon has largest probability to undergo total internal reflection. We defined a parameter θ_{ir}, which is the angle between two vectors: one is from the center of the detector to the fit event vertex (the radial direction) and the other is from the fit vertex to the i^{th} PMT hit. Figure 6.8 shows the θ_{ir} distributions for the ^{208}Tl decay events in three regions. For the ^{208}Tl decay events in the heavy water, an outgoing photon is more likely to make a PMT hit than an ingoing one. Thus the number of PMT hits with low values of θ_{ir} is slightly larger than those with high values of θ_{ir}, which lead to a smooth peak in the corresponding θ_{ir} distribution. The θ_{ir} distribution from the ^{208}Tl decay events in the AV has a fairly deep valley around 90 degrees because of the reasons mentioned above. For the ^{208}Tl decay events in the H_2O region, the Čerenkov photons travelling inward in such a direction so as to travel a long distance through the AV has the smallest probability to produce a PMT hit. Thus in the corresponding θ_{ir} distribution, there is also a deep valley but this time around somewhat larger value of θ_{ir} than that of the events occurring in the AV. Similar situation also happens for ^{214}Bi decay events in the three different regions.

Generally speaking, an outward travelling photon has a larger probability of generating a PMT hit because it has much less attenuation path to travel before it hits one of the photomultipliers. Photons travelling outwards have a somewhat larger probability to make PMT hits if they are generated in the H_2O rather than the D_2O region. Thus the nhits distributions for events occurring in different regions are expected to be different. Figure 6.9 shows the nhits distributions for ^{208}Tl decay events in three different regions. At low nhits, the number of the ^{208}Tl decay events in D_2O is smaller than those in H_2O while the number of decay events in the acrylic vessel is between them. At high nhits, this rank is reversed. This is because the outgoing photons produced by the decays in the H_2O region make more PMT hits than those from the decays in the D_2O region.

Figure 6.8: θ_{ir} **distributions for equal numbers of** ^{208}Tl **decay events in three regions:** D_2O**(dashed line), the acrylic vessel (solid line) and** H_2O **(dotted line).**

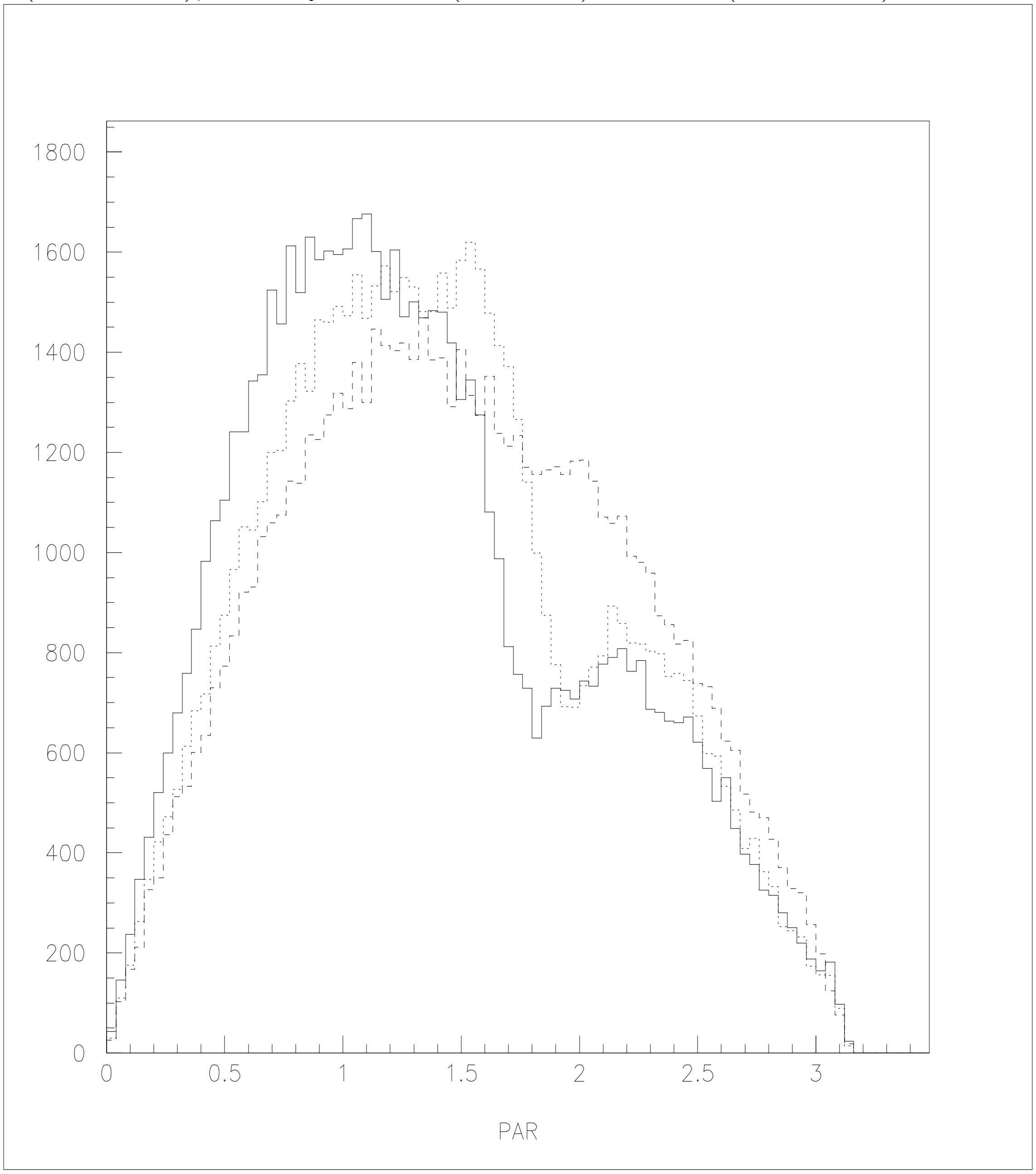

Figure 6.9: **Nhits distributions for equal numbers of ^{208}Tl decay events in three regions: D_2O(dotted line), the acrylic vessel (dashed line) and H_2O (solid line).**

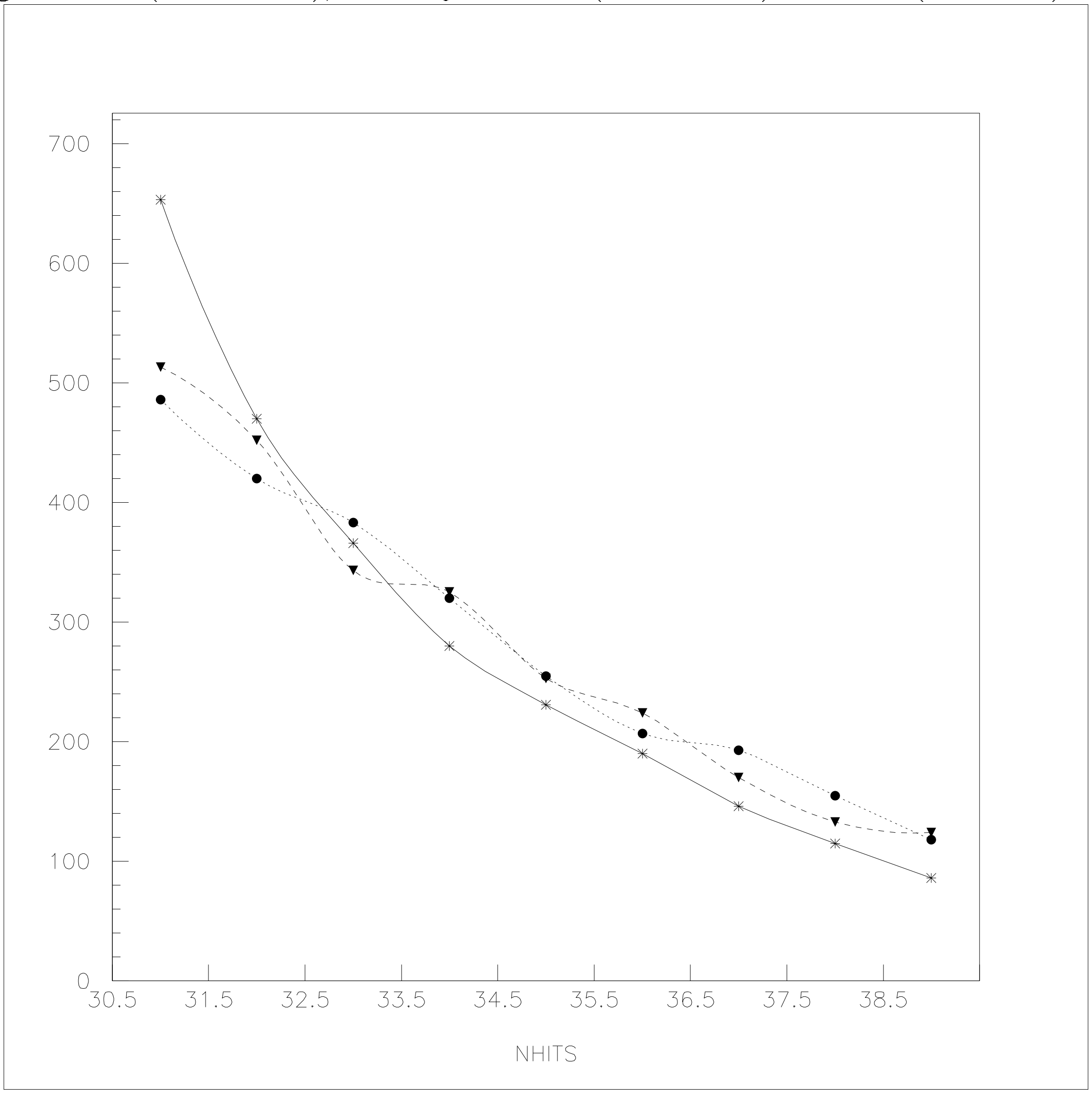

6.3.2 Implementation

Parameterization

In order to separate patterns of PMT hits generated by the six types of events, a large amount of information must be extracted from distributions presented above and taken into account in the analysis. Neural network techniques [104] are one of the most successful techniques developed to accomplish complex pattern recognition tasks. By using this technique, we are able to simplify the analysis procedure. The neural network technique we used is described in the next section. Below we present some mathematical implementations of parameters which extract information from the data distributions and constitute the inputs to the network:

- **Nhits parameter**

  Nhits parameter is chosen to reflect the difference in energy spectrum among various event classes. It is defined as the number of PMT hits produced by an event normalized within the monitor window:

  $$Par_{nhits} = \frac{nhits}{nhits_{max} - nhits_{min}} \tag{6.4}$$

  where $nhits_{max}$ and $nhits_{min}$ are the minimal and maximal nhits value of the cut window respectively.

- **R_{fit} parameter**

  R_{fit} parameter uses information provided by the vertex fitter to determine position of the event. It is defined as:

  $$Par_{rfit} = \frac{r_{fit} - r_{min}}{r_{max} - r_{min}} \tag{6.5}$$

  where r_{fit} is the distance between the center of the detector and the fit event vertex, r_{min} and r_{max} are the minimal and maximal r_{fit} cut of the window respectively.

- **θ_{ir} parameter**

  As discussed before, events occurring in different regions have different θ_{ir} distributions. Because by definition outputs of the neural network range between 0 and 1, it will be natural and convenient that the inputs of the network also vary from 0 to 1. In order to describe all information contained in a θ_{ir} distribution (instead of just its mean value), we use a cumulative function to represent the distribution. The definition of the θ_{ir} parameters are:

$$Par_{\theta_{ir}}(k) = \frac{number\ of\ PMT\ hits\ with\ \theta_{ir}\ less\ than\ \frac{k*\pi}{9}}{total\ number\ of\ PMT\ hits\ in\ the\ event} \tag{6.6}$$

where k ranges from 1 to 9,

- **θ_{ij} parameter**

  θ_{ij} parameters are used to distinguish between two types of decay events in the same region. Again we use a cumulative function to describe the θ_{ij} distribution. The definitions of the θ_{ij} parameters are:

$$Par_{\theta_{ij}}(k) = \frac{number\ of\ entries\ with\ \theta_{ij}\ less\ than \frac{k*\theta_c}{2}}{total\ number\ of\ entries\ in\ the\ event} \tag{6.7}$$

  where k ranges from 1 to 9 and θ_c is the Čerenkov angle. Thus $\frac{9}{2} * \theta_c$ is approximately equal to 180 degree. Each entry in the distribution corresponds to a pair of PMT hits.

During calculations of these parameters, we also impose a R_{dev} cut on the data to discard any bad PMT hits in the event.

The Neural Network Technique

At present, the most popular and widely used pattern recognition technique is the neural network technique which simulates the performance of neurons of human brain in terms of learning, recording and applying knowledge. This technique has been successfully used in many high energy physics experiments [105, 106] to solve problems such as online fast hardware triggers [107] and offline event separation [108]. This technique was first used by D. W. Dong and Y. Chan [109] of the SNO collaboration to distinguish between true and false Čerenkov radiation signals that are produced by certain types of events in the SNO detector. S. Brice also used this technique to distinguish between the neutral current events and the charged current events and achieved great success [64, 59]. Such a network technique was further extended by the author to separate six types of backgrounds, as described below.

We used the simplest and most widely used network: the feedforward and error back-propagation network. The layout of such a network is shown in figure 6.10. Generally speaking, a feedforward neural network is made up of several layers: one input layer, one or more hidden layers and one output layer. Each layer is made of several nodes (or neurons). Each node in the input layer corresponds to a input parameter to the network. All of these input parameters must be carefully chosen to reflect the character of the studied event. The function of the input layer is just to feed these parameters into the next layer, which is the first hidden layer. Each node in the hidden layers takes the input from every node of the previous layer, performs some operations on the inputs according to a specific function and then feed the outputs into the next layer. It was the definition of these specific functions and addition of the hidden layers that lead to today's wide applications of neural network techniques. For an individual node, the function is defined as:

$$Y = \left[1 + exp - (\sum_i \omega_i X_i - \theta)\right]^{-1} \tag{6.8}$$

Y is the output of the node and X_i is the output of the i^{th} node of the previous layer. θ is called the node threshold, which is compared with the weighted sum (weight ω_i) of the outputs from the previous layer. If $\sum_i \omega_i X_i$ is larger than θ, the output Y is larger than 0.5 and the node is said to be active (a notion inherited from the old perceptron algorithm). Otherwise the node is said to be off or inactive. Different node has different threshold and weights. Finally the output layer is able to output some information which enable us to recognize the input patterns. The flow of information in the network is shown as arrows in figure 6.10. The information is feed from one layer to another (from left to right in the figure) until the output layer. This is why such a network is called the (information) feedforward network.

The origin of the error backpropagation is from the algorithm used to train the network, by which the values of weights and thresholds of each nodes are determined. Training the network to set its internal parameters requires the use of a training set of patterns. For example, if we want to train the network to separate N classes of events, this training set should contain equal numbers of N classes of events in oder to avoid a *priori* biasing, and the true class of each event must be known. The output value of a node in the output layer ranges between 0 and 1 because of the use of the sigmoid function mentioned before. In the case of two classes separation, there is only one node in the output layer and we can simply define that the node output of $Y > 0.5$ is to signify the input of a Class 1 event and $Y < 0.5$ a Class 2 event. This enables a targeted network output to be assigned to each pattern of the training set:

Figure 6.10: **Layout of a feedforward and error backpropagation neural network.**

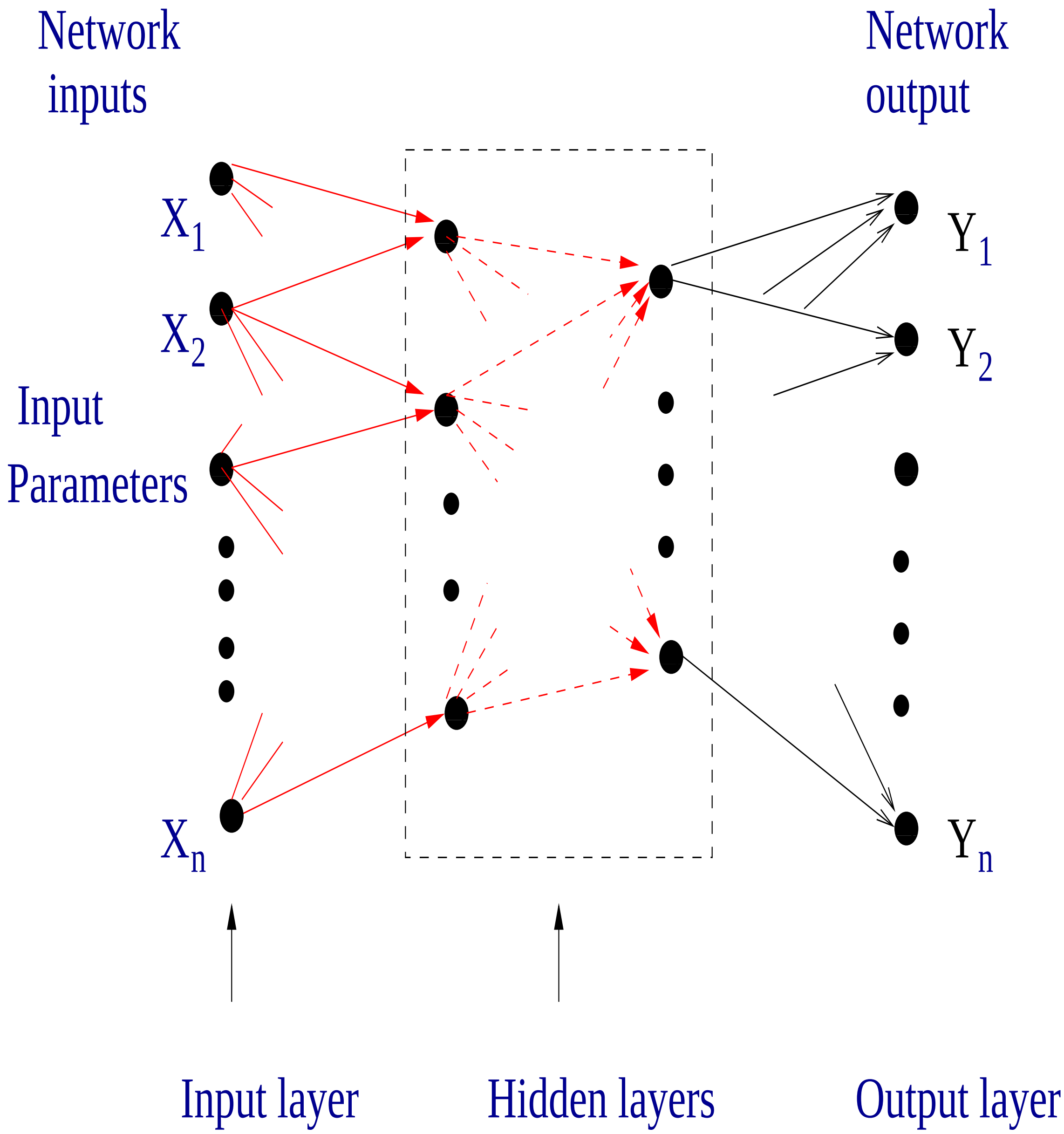

$$\text{For true Class 1 events,} \quad \text{Target: } T = 1.0$$
$$\text{For true Class 2 events,} \quad \text{Target: } T = 0.0$$

A error function of the network is defined as:

$$E(\omega_i, \theta) = \frac{1}{2} \sum_p [Y(\underline{X^p}) - T^p]^2 \tag{6.9}$$

P is the label of the hit patterns in the training set. $\underline{X^p}$ is the vector of the input parameters for the p^{th} pattern of the set and Y is the corresponding network output. T^p is the targeted network output. The situation is a bit more complex if we try to separate more than 2 classes of events. In the case of N classes separation, there are N nodes in the output layer, each of which corresponds to one class of event. Thus the assignment rule is: if the output of a certain node is highest among all the outputs, the network determines that the input event belongs to the event class corresponding to this node. The targeted network outputs of a training set is:

For Class 1 events, targets: $T_1 = 1.0$, $T_i = 0.0$ (i=2,...,N)

For Class 2 events, targets: $T_2 = 1.0$, $T_i = 0.0$ (i=1,3,...,N)

... ...

For Class N events, targets: $T_N = 1.0$, $T_i = 0.0$ (i=1,2,...,N-1)

The definition of the error function is similar to equation 6.9 with expansion of output nodes from 1 to N:

$$E(\omega_i, \theta) = \frac{1}{2} \sum_p [\underline{Y}(\underline{X^p}) - \underline{T^p}]^2 \tag{6.10}$$

where T and Y are vectors. The training process is a process of minimizing this error function while determining the optimum values of the weights and the threshold of all nodes in the network. The problem of finding the minimal value of a function is somewhat similar to the fitter problem described in the last chapter. Many ways of implementations lead to many types of network techniques. For example, stochastic learning networks use the Monte Carlo method (similar to algorithm used in the grid fitter) or the simulated annealing method (similar to algorithm used in the Lorentzian fitter) to find the minimal of the function and determine the internal parameters of the network. The algorithm used in the error backpropagation learning technique is somewhat similar to that used in the time fitter.

In order to simplify the discussion, we choose a simple feedforward and error back-propagation neural network which has only a single hidden layer, as shown in figure 6.11. In this case, the error function is explicitly written as:

$$E(w_{ij}, \theta_j, W_{jk}, \Theta_k) = \frac{1}{2} \sum_p [\underline{Y}(\underline{X}^p) - \underline{T}^p]^2 \tag{6.11}$$

The weights w_{ij} and W_{jk} and the thresholds θ_j and Θ_k are updated along the so called "down-hill" direction in the parameter space:

$$\begin{aligned}
\triangle W_{jk} &= -\eta \frac{\partial E}{\partial W_{jk}} \\
\triangle w_{ij} &= -\eta \frac{\partial E}{\partial w_{jk}} \\
\triangle \Theta_k &= -\eta \frac{\partial E}{\partial \Theta_k} \\
\triangle \theta_j &= -\eta \frac{\partial E}{\partial \theta_j}
\end{aligned}$$

where η is known as the learning rate and controls the size of the update steps. Iterations continues until the error function converges to its minimal value. If convergence is slow or/and the error surface has very narrow minimum valleys, there are extensions of this method such as the addition of a momentum term [104].

It is instructive to calculate these partial derivatives explicitly. The following two definitions are useful in the calculations:

$$\delta_k^p = Y_k^p(Y_k^p - 1)(Y_k^p - T_k^p) \tag{6.12}$$

$$\delta_j^p = H_j^p(H_j^p - 1) \sum_k W_{jk} \delta_k^p \tag{6.13}$$

where δ_k^p is known as the error of the output node Y_k and δ_j^p is known as the error of the hidden node H_j respectively for the p^{th} pattern in the training set. With these two definitions, replacing E with the sigmoid function and calculating the derivations explicitly, we have:

$$\begin{aligned}
\triangle W_{jk} &= \eta \sum_p \delta_k^p H_j^p \\
\triangle w_{ij} &= \eta \sum_p \delta_j^p X_i^p \\
\triangle \Theta_k &= -\eta \sum_p \delta_k^p \\
\triangle \theta_j &= -\eta \sum_p \delta_j^p
\end{aligned}$$

Figure 6.11: **Layout of a feedforward and error backpropagation neural network with only one hidden layer.**

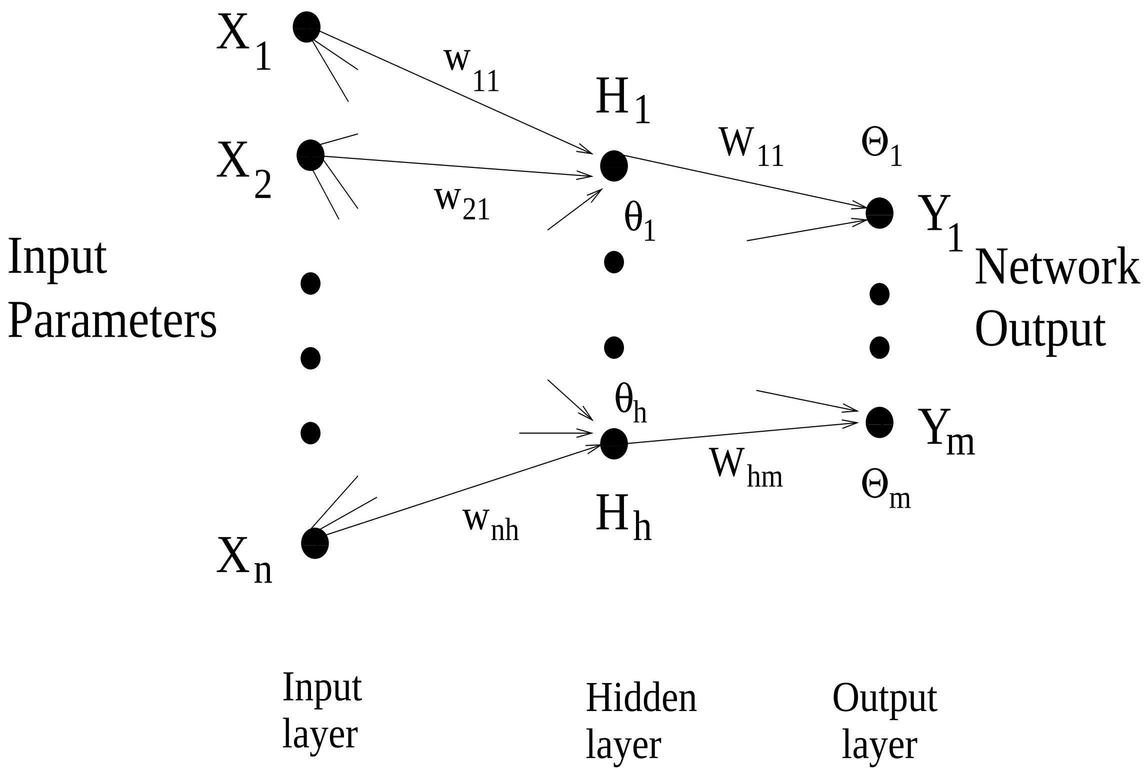

The interesting thing here is that the error of a hidden node (δ_j^p) can be calculated only after the calculation of the error of a output node (δ_k^p). Thus the updates of w_{ij} and θ_j can only follow the updates of W_{jk} and Θ_k. Note all these equations remain same when we update the weights and the thresholds of a network with more than one hidden layer. The errors of the nodes are backpropagated from the output to the input in order to update the weights and the thresholds one layer by one layer. This is why the algorithm is called as a feed forward and error backpropagation neural network.

The knowledge learned through the training process is stored in the topology of the network and the weights and thresholds of its nodes. It is hoped that after proper training, the network is able to draw some optimal boundaries in the multi-dimensional (input) parameter space. These boundaries divide the parameter space into several regions, each of which corresponds to one class of event need to be identified.

In practice, we used the Neural Network Simulator (SNNS) developed by Stuttgart university [110] of Germany, which could be obtained via anonymous ftp from the host. This simulator enables us to choose networks with different topologies and various training method without rewriting any codes. Two externally set parameters in the network algorithm are the number of hidden layers and the number of hidden nodes. The inclusion of more than one hidden layer in the network is perfectly feasible, but may not be necessary. This follows principally from the theorem which states that any functional mapping between the input space and the output space of the network can be approximated to arbitrary accuracy by a feedforward neural network with just one hidden layer [111]. Obviously with too few nodes in a hidden layer, there is insufficient flexibility to form the optimal boundaries in the parameter space. However, too many nodes may lead to the overtraining of the network, in which case the network begins to learn the features of the individual input patterns instead of the common characteristics of one class of events. To avoid the overtraining, the size of the training set should be much larger than the number of internal parameters (weights and thresholds) need to be adjusted.

While there are some very elegant pruning and growing techniques to kill off or add hidden nodes during the training process, a network for SNO events probably has no need of them. Typically the task of SNO event classification requires a number of hidden nodes that is of the same order as the number of input nodes and often considerably less. We did some experiments by using networks with various numbers of hidden nodes or/and hidden layers. Results show that the capabilities of the networks to classify SNO events are more or less the same regardless of the numbers of hidden nodes or/and layers as long as the overtraining situation is avoided.

6.3.3 The Results

Two Class Separation

We began with the separation of two event classes to test the performance of the network. The task is to determine the uranium and thorium concentration levels in 1000 tons of heavy water. The methods are similar to that are described in the last section. The difference is that instead of directly fitting the θ_{ij} distributions, we feed the θ_{ij} distributions through a trained network and then fit on its output distributions. In this case, the network only has one output node. If its value is larger than 0.5, we assign the input event as a ^{208}Tl decay event. Otherwise the input event is considered as a ^{214}Bi decay event. There are 9 nodes in the input layer, each of which corresponds to one θ_{ij} parameter. The network has a hidden layer with 6 nodes. A training set consisted of 1000 ^{208}Tl decay

Table 6.9: **Results of the event-by-event separation of ^{208}Tl and ^{214}Bi decay events in the D_2O.**

	$0.5 \leq Y_{out} \leq 1.$	$0. \leq Y_{out} \leq 0.5$
Tl decay event	1118	882
Bi decay event	259	741
Percentage of Correct = (62.0 +/- 0.9)%		

events and 1000 ^{214}Bi decay events is used to train the network. In order to optimize the capability of the network to generalize the characters of the events and avoid the overtraining, a validation set consisted of same numbers of the two types of events with known identities (not used in the training set) were used to evaluate the performance of the network. The training algorithm will stop if the average output error of the validation set reaches its minimum. Finally a testing set is used to determine the performance of the network on patterns that are not used during the training process. Results of the test with a pattern set consisting of 2000 ^{208}Tl and 1000 ^{214}Bi decay events are shown in table 6.9. It appears that the network recognizes the ^{214}Bi decay events better than the ^{208}Tl decay events. It is also clear that the network is not able to distinguish between these two types of events on the event-by-event basis.

However, our object is to distinguish them statistically. Figure 6.12 shows the output distributions of the network for ^{208}Tl and ^{214}Bi decay events. These plots could be compared with figure 6.5. The difference between two distributions shown in figure 6.12 is larger than that shown in figure 6.5. The network somewhat enlarges the difference between the angular distributions of photons produced by two classes of events and it may generalize the information contained in the two distributions which is not fully represented by the mean value of θ_{ij}. The standard chi square fitting techniques is used to determine the numbers of ^{208}Tl and ^{214}Bi decay events in a predefined window (e.g. $40 > nhits > 30$ and $r_{fit} < 400cm$). In order to check the performance of the chi square fitting, two methods (Simulated annealing and the Levenberg-Marquart methods) were used to minimize the chi square function. Various combinations of two classes of events have been tried with fitting results shown in table 6.10. The two tables show similar results: the performance of the network technique and the chi square fitting is satisfactory. All fitting

Figure 6.12: **Output distributions of the network for 1000 ^{214}Bi decay events (upper plot) and 2000 ^{208}Tl (bottom plot) events(bottom plot). The vertical axis represents the number of the events.**

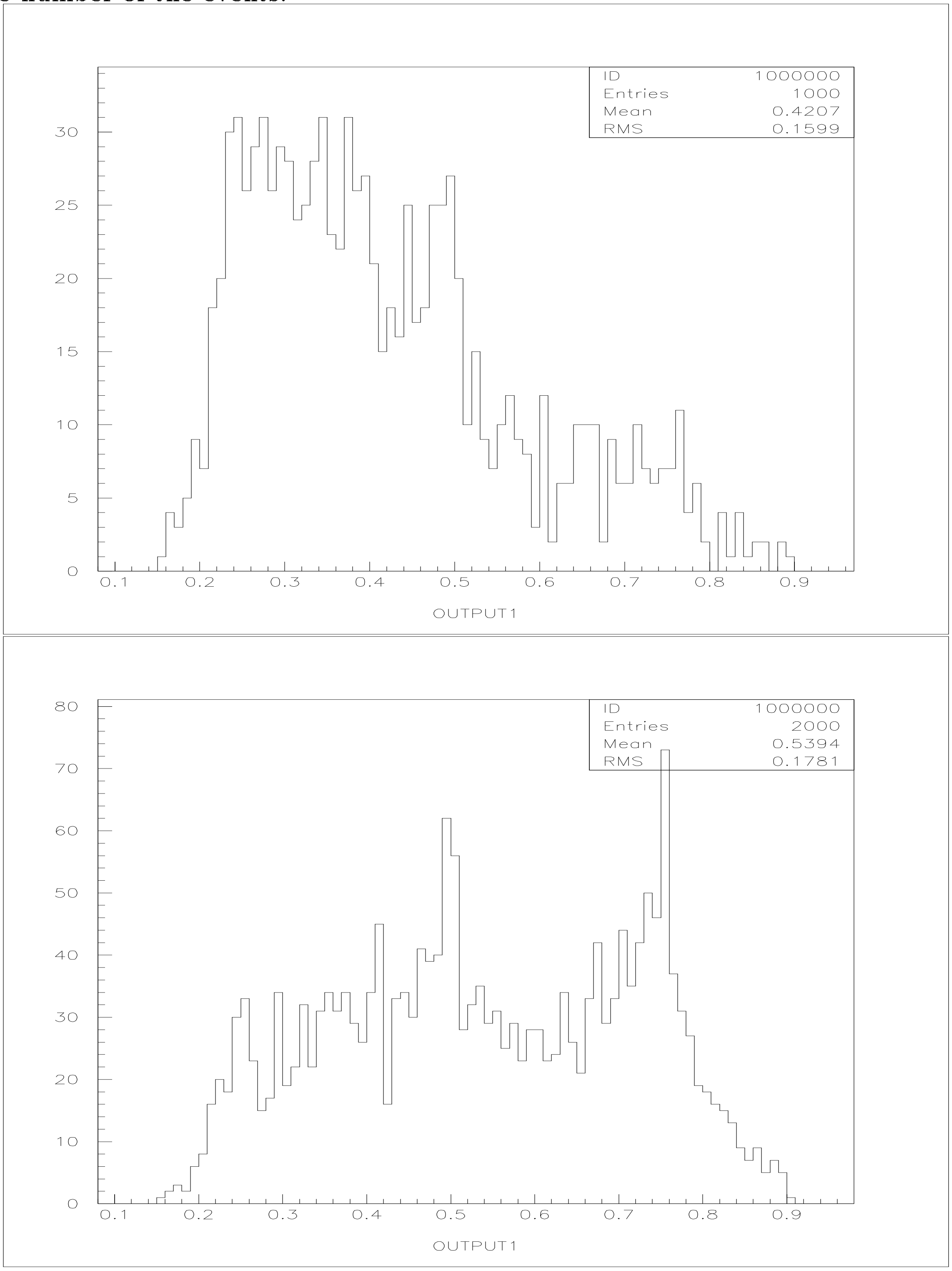

Table 6.10: **Results of the statistical separation of the ^{208}Tl and ^{214}Bi decay events in D_2O.**

Data set	true Bi fraction	Anneal-Amoeba method		
		Fitted Bi-fraction	Chi2 value	Degree of freedom
2800Tl+700Bi	0.2	0.199 +/- 3.9E-02	79	65
1000Tl+2000Bi	0.66	0.65 +/- 3.6E-02	65.6	64
1000Tl+1000Bi	0.5	0.52 +/- 4.47E-02	68	59
2000Tl+1000Bi	0.33	0.35 +/- 3.89E-02	78	65
1000Tl+3000Bi	0.75	0.73 +/- 3.34E-02	74	65

Data set	true Bi fraction	Levenberg-Marquart method		
		Fitted Bi-fraction	Chi2 value	Degree of freedom
2800Tl+700Bi	0.2	0.244 +/- 4.06E-02	63.6	65
1000Tl+2000Bi	0.66	0.63 +/- 3.99E-02	47	64
1000Tl+1000Bi	0.5	0.52 +/- 4.59E-02	51.5	59
2000Tl+1000Bi	0.33	0.37 +/- 4.09E-02	57.5	65
1000Tl+3000Bi	0.75	0.70 +/- 3.73E-02	53.7	65

values agree with the true values within the statistical errors.

Six Class Separation

A simple extension of the neural network described in the last section enables us to separate six classes of events: the ^{208}Tl and the ^{214}Bi decay events in three regions (D_2O, AV and H_2O). The input layer of this extended network has 18 nodes: one represents the Nhits parameter, one represents the R_{fit} parameter, nine come from the θ_{ij} parameters and nine are the θ_{ir} parameters. The hidden layer has 10 nodes. There are six nodes in the output layer, each of which corresponds to one of event classes need to be identified. We hope that the neural network is able to use not only the information from the individual parameters but also possible correlations among these parameters to recognize different kind of events. Again we use a training set and a validation set to train the network and avoid overtraining. Each of these sets contains equal numbers of the 6 classes of decay events. A testing set consisting of patterns not used in the training is used to evaluate

Table 6.11: **Neural network outputs for 6 event classes.** 1. the ^{208}Tl decay events in D_2O, 2. the ^{214}Bi decay events in D_2O; 3. the ^{208}Tl decay events in the acrylic vessel, 4. the ^{214}Bi decay events in the acrylic vessel; 5. the ^{208}Tl decay events in H_2O, 6. the ^{214}Bi decay events in H_2O.

		event class decided by neural network					
		1	2	3	4	5	6
true event class	1	850	918	185	64	42	45
	2	394	1403	143	89	20	55
	3	25	110	910	283	303	473
	4	11	85	701	707	143	457
	5	11	43	480	118	741	711
	6	3	33	392	149	411	1116
Percentage Correct = (45.4 +/- 0.4)%							

the performance of the network with results shown in table 6.11. The network is able to recognize some events otherwise the correct rate would be 16.6%.

Although the event-by-event separation is impossible, the statistical separation is feasible, which is good enough. In order to determine the major background levels in the SNO detector by this technique, firstly a cut window should be imposed on the data so that within this window the dominant events come from the ^{208}Tl and the ^{214}Bi decays in the three regions. Based on some reasonable assumptions of radioactive concentration levels in the detector, a cut window with $30 > nhits > 40$ and $0 < r_{fit} < 640$, where nhits is the number of PMT hits produced by an event and r_{fit} is the distance between the center of the detector and the fit vertex, seems to be suitable for the analysis. Contamination in this window is negligible compared to the numbers of these six classes of events, as shown in table 6.12 (Contamination due to PMT β-γ events is not known exactly because of poor statistics. However, with the background veto techniques described in the previous chapter and adjustable window thresholds, affects of this kind of background are expected to be small.)

Then the hit patterns generated by events inside the cut window were fed into the trained network to produce a six-dimensional output distribution. This distribution was fit as a linear combination of six calibration distributions, each of which is generated by

Table 6.12: **Number of events reconstructed inside the window** ($30 > nhits > 40$ **and** $0 < r_{fit} < 640$) **per year.**

region	Thorium Concentration(g/g)	^{208}Tl decay per year
1000 tons D_2O	$11 * 10^{-15}$	29031
30 tons Acrylic Vessel	$4.6 * 10^{-13}$	35093
8000 tons H_2O	$7.53 * 10^{-14}$	63336

region	Uranium Concentration(g/g)	^{214}Bi decay per year
1000 tons D_2O	$11 * 10^{-15}$	26514
30 tons Acrylic Vessel	$6.3 * 10^{-13}$	13815
8000tons H_2O	$8.6 * 10^{-14}$	82314

other types of events	events per year reconstructed inside the window
Charged Current Events	282 (1/3 SSM level)
Neural Current Events	192 (Full SSM level)
^{228}Ac decay events in D_2O	11 (equilibrium)
^{212}Bi decay events in D_2O	207 (equilibrium)
^{234}Pa decay events in D_2O	1643 (equilibrium)
^{40}K decay events in 2.5 tons $MgCl_2$	< 426 (1ppm K concentration level in $MgCl_2$)

one class of events. Figure 6.13 shows fit results with same numbers of the six types of events. Since we do not know the numbers of the 6 classes of events inside the window (that is what we are trying to determine), various combinations have been tried to check the performance of this technique with results shown in table 6.13 and table 6.14. Almost all of fitted results agree with the true data within the statistical errors. The combination of the neural network technique and the chi square fitting method is able to separate six classes of events statistically even when the number of one class of events is no more than 5% of the total event number. The use of the network simplifies the task of chi square fitting since it greatly reduce the dimensions of the distribution which need to be fitted (from 20 to 6). After the numbers of the six classes of decay events within the cut window are determined, we can use Monte Carlo simulations to deduce the overall numbers of radioactive decays in various regions of the detector by calculating the fraction of total decays which produce events within the cut window and hence the numbers of NC and CC background events.

So far we have only used the spatial information to separate different classes of events. Temporal information is used to reject bad PMT hits as described before. Temporal information may also be useful when we try to separate events generated in different regions since the amount of travel time of a Čerenkov photon before it hits a PMT depends on where it is created. The addition of some temporal parameters is a possible method to improve the performance of the neural network.

6.3.4 Systematic Studies

Up to now, this pattern recognition technique fully relies on the Monte Carlo simulations: all patterns in the network's training, validation and testing sets are generated by the SNOMAN code. The technique involves a feedforward neural network and histogram fitting in the six dimension space. Logically, the more complex a technique, the less robust it is. Thus we have to check the robustness of this technique against systematic errors in the code since there are always discrepancies between reality and the prediction of the code.

One simple way to quantify the background levels in the SNO detector is to calculate the number of free neutrons produced by various kinds of backgrounds since they contaminate signals from the neutral current events which are important and unique to the experiment. The numbers of free neutrons produced by various backgrounds in the de-

Figure 6.13: **Results of statistical separation of six classes of events with same number of each kind of events.** Figure is shown as ratio between fit and true data.

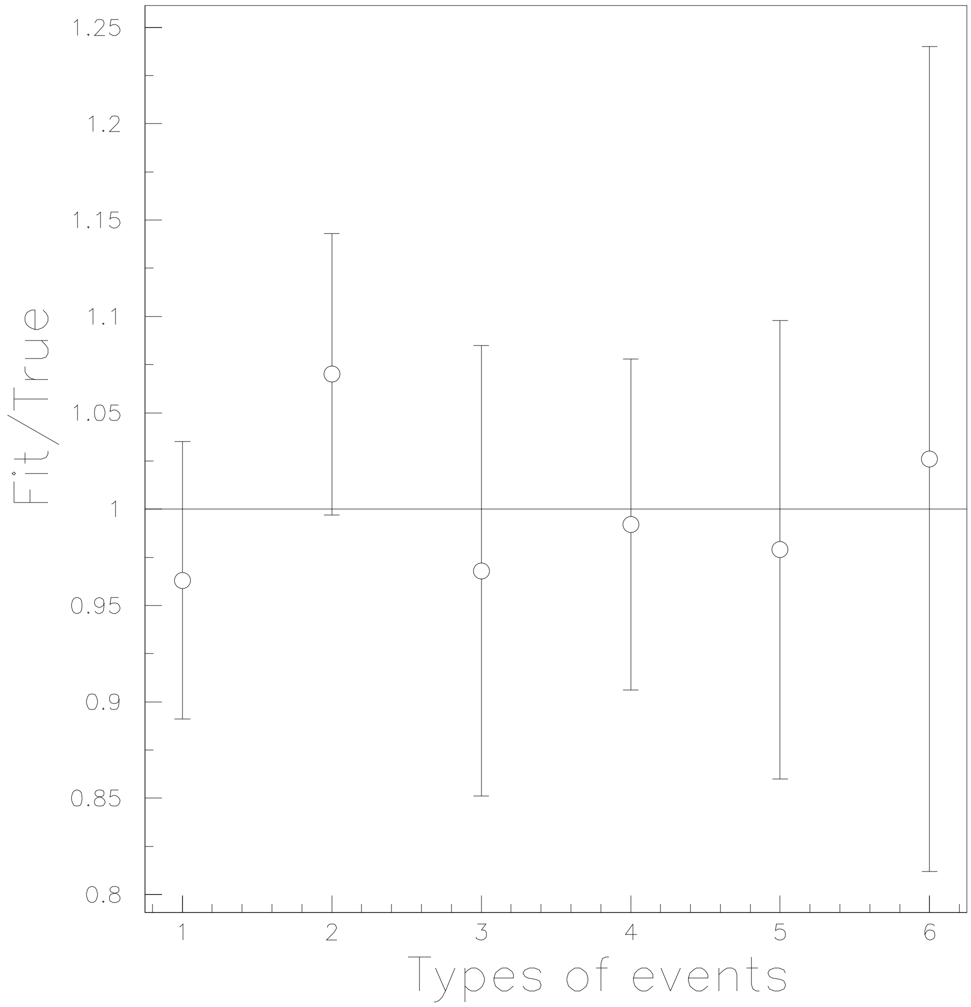

Table 6.13: **Results of statistical separation of six classes of events.** see text, notations is same as in table 6.11.

	true event number	true class fraction	fitted class fraction
1	2104	0.1667	0.1606 +/- 0.0120
2	2104	0.1667	0.1784 +/- 0.0122
3	2104	0.1667	0.1614 +/- 0.0195
4	2104	0.1667	0.1653 +/- 0.0143
5	2104	0.1667	0.1632 +/- 0.0199
6	2104	0.1667	0.1711 +/- 0.0357

	true event number	true class fraction	fitted class fraction
1	5000	0.277	0.267 +/- 0.014
2	2000	0.111	0.127 +/- 0.013
3	5000	0.277	0.268 +/- 0.018
4	2000	0.111	0.114 +/- 0.012
5	2000	0.111	0.114 +/- 0.017
6	2000	0.111	0.111 +/- 0.033

	true event number	true class fraction	fitted class fraction
1	4000	0.3077	0.2941 +/- 0.0161
2	2000	0.1538	0.1757 +/- 0.0153
3	2000	0.1538	0.1501 +/- 0.0191
4	2000	0.1538	0.1517 +/- 0.0135
5	2000	0.1538	0.1653 +/- 0.0181
6	1000	0.0769	0.0632 +/- 0.0370

	true event number	true class fraction	fitted class fraction
1	1000	0.0909	0.0988 +/- 0.0106
2	2000	0.1818	0.1773 +/- 0.0114
3	3000	0.2727	0.2549 +/- 0.0221
4	2000	0.1818	0.1887 +/- 0.0161
5	1000	0.0909	0.1125 +/- 0.0206
6	2000	0.1818	0.1678 +/- 0.0377

Table 6.14: As table 6.13.

	true event number	true class fraction	fitted class fraction
1	3000	0.2857	0.2791 +/- 0.0160
2	1000	0.0952	0.1099 +/- 0.0147
3	1000	0.0952	0.0879 +/- 0.0220
4	2000	0.1905	0.1945 +/- 0.0160
5	2500	0.2381	0.2467 +/- 0.0219
6	1000	0.0952	0.0818 +/- 0.0410

	true event number	true class fraction	fitted class fraction
1	2000	0.1481	0.1469 +/- 0.0111
2	2000	0.1481	0.1547 +/- 0.0112
3	4000	0.2963	0.2643 +/- 0.0210
4	2000	0.1481	0.1621 +/- 0.0147
5	2000	0.1481	0.1649 +/- 0.0206
6	1500	0.1111	0.1072 +/- 0.0365

	true event number	true class fraction	fitted class fraction
1	600	0.0909	0.0962 +/- 0.0109
2	600	0.0909	0.0920 +/- 0.0108
3	900	0.1364	0.1232 +/- 0.0249
4	300	0.0455	0.0574 +/- 0.0146
5	1800	0.2727	0.2644 +/- 0.0330
6	2400	0.3636	0.3669 +/- 0.0464

	true event number	true class fraction	decided class fraction
1	300	0.0455	0.0696 +/- 0.0478
2	300	0.0455	0.0247 +/- 0.0240
3	1500	0.227	0.2564 +/- 0.0506
4	750	0.114	0.1037 +/- 0.0198
5	3000	0.454	0.4044 +/- 0.0451
6	750	0.114	0.1414 +/- 0.0886

Table 6.15: **Number of free neutrons produced by various radioactive decay backgrounds in the SNO detector.**

		Number of decay per year	Number of events in the cut window	Number of neutrons produced per year
D_2O	^{208}Tl decay	505890	29031	759
D_2O	^{214}Bi decay	$4.78 * 10^6$	29031	80
Acrylic	^{208}Tl decay	$5.26 * 10^5$	29031	263
Vessel	^{214}Bi decay	$1.57 * 10^7$	29031	63
H_2O	^{208}Tl decay	$1.28 * 10^7$	29031	256
H_2O	^{214}Bi decay	$9.66 * 10^7$	29031	48

tector under certain conditions are shown in table 6.15. In order to simplify the analysis, the numbers of six classes of decay events falling within the cut window ($30 < nhits < 40$ and $0 < r_{fit} < 640$) are assumed to be same.

Impurity in the Testing Set

The first step of the technique is to impose a cut window on the data from the detector so that within the window the dominant events are the ^{208}Tl and the ^{214}Bi decay events in the heavy water, the acrylic vessel and the light water. Under some reasonable assumptions, this task should be achieved readily, as shown in table 6.12. Major contaminations come from the decays of ^{234}Pa nuclei in the uranium decay chain which produce a 2.21 MeV electron. The number of the ^{234}Pa decays is more or less constrained by secular equilibrium. However, we could artificially increase the decay rates in order to estimate the effects of other unexpected signals on the performance of the pattern recognition technique:

- The contamination to the ^{208}Tl and ^{214}Bi decay events in D_2O is set at 5% level, all of which come from the ^{234}Pa decays.
- The contamination to the ^{208}Tl and ^{214}Bi decay events in the acrylic vessel is set at 5% level, all of which come from the ^{234}Pa decays.

Table 6.16: **The systematic study of the performance of the pattern recognition technique on a contaminated testing set.**

		The percentage change of the results of the network	Change in the number of the background neutrons
D_2O	^{208}Tl	5.29%	40.2
D_2O	^{214}Bi	-9%	-7.2
Acrylic	^{208}Tl	-14%	-36.8
Vessel	^{214}Bi	6.2%	3.9
H_2O	^{208}Tl	-13.7%	-35
H_2O	^{214}Bi	24.2%	11.6
Net change in the deduced number of NC background events = 23.3			

- The contamination to the ^{208}Tl and ^{214}Bi decay events in the H_2O is set at 10% level (because of the possible extra contaminations from the PMT β-γ decay events), all of which come from the ^{234}Pa decays.

The robustness of the pattern recognition technique is checked by feeding the contaminated pattern set into the network and fitting its output distribution. The fitted results are shown in table 6.16. The number of NC background events deduced by this technique only changes by -1.59%. This systematic error is surprisingly small. The fact that all of these radioactive decays produce free neutrons more or less reduce the errors of the fit results. After all, what we are concerned directly is the number of NC background events instead of some less meaningful numbers of radioactive decays in the detector.

Impurity in the Training and Validating Sets

Basically there are two ways to prepare the training and the validating sets for the network: by Monte Carlo simulations, or for some of the sets, from some calibration sources. If the latter method is used , there will be some impurities in the sets due to the mixing of the six classes of events. For example, when using ^{222}Rn gas pumped into the heavy water to get the set of patterns for ^{214}Bi decay events in the D_2O, the other 5 classes of decay events occur in the detector at the same time. Because of the reconstruction errors of the vertex fitters, there will always be some contamination in the pattern set.

Table 6.17: **The systematic study of the performance of the pattern recognition technique on a contaminated training set.**

		The percentage change of the results of the network	Change in the number of the background neutrons
D_2O	^{208}Tl	8.28%	62.8
D_2O	^{214}Bi	-4.4%	-3.5
Acrylic	^{208}Tl	14.7%	38.7
Vessel	^{214}Bi	2.3%	1.45
H_2O	^{208}Tl	-9.44%	-24.2
H_2O	^{214}Bi	17.5%	8.4
Net change in the deduced number of NC background events = 83.65			

It means that the neural network would be told some events from the other 5 classes are ^{214}Bi decays in the D_2O when it is trained. The robustness of this pattern recognition technique against such systematic errors was checked by training the network with the contaminated pattern sets (10% impurities) and repeating the analysis. The results are shown in table 6.17. The deduced number of NC background events only changes by 5.7%.

Scattering of Čerenkov Photons in the Detector

If the scattering probability of a photon in the detector varies from time to time or does not agree with the Monte Carlo, there will be errors in the angular distribution of photons produced by an energetic electron in our simulation, which is the foundation of this pattern recognition technique. Increased scattering would make the hit pattern of an event more isotropic, which may wash out the difference between a single-particle event and a multi-particle event. Whether the technique is robust against such systematic errors was checked. We artificially increases the scattering of a photon in the D_2O and H_2O region by 20% and redid the analysis. The results are shown in table 6.18. Since it is claimed that a light source is able to determine the photon scattering level to much better than 10%, the level of NC background deduced by this technique should not be wrong by more than 4.76%.

Table 6.18: **The systematic study of the performance of the pattern recognition technique on a testing set generated with high scattering probability of the photon..**

		The percentage change of the results of the network	Change in the number of the background neutrons
D_2O	^{208}Tl	6.5%	49.3
D_2O	^{214}Bi	-12.6%	-10.1
Acrylic	^{208}Tl	5.9%	15.5
Vessel	^{214}Bi	2.8%	1.76
H_2O	^{208}Tl	6.7%	17.2
H_2O	^{214}Bi	-7.7%	-3.7
Net change in the deduced number of NC background events = 69.96			

Attenuation Probability of Photons in the Detector

If the attenuation length of the photon in the detector does not agree with the value used in the Monte Carlo codes, there will be some error in deducing the total background levels from the number of decay events falling inside the cut window. By increasing the attenuation probability of a photon in the D_2O and H_2O by 10% and the acrylic vessel by 20% and repeating the analysis, we check the robustness of this technique against such a systematic error. As shown in table 6.19, although this is a very dramatic systematical change (with laser ball calibration source, we should be able to determine this value accurately to the few percent level [112]), the deduced level of NC backgrounds only changes by -18.9%.

Complexity of the Acrylic Vessel

The most complex geometry of the SNO detector simulated by the SNOMAN code is the acrylic vessel. In the default running mode of the code, in order to save the CPU time, the vessel is only simulated as a spherical shell. But in reality it is made up of 122 acrylic tiles and some attachments such as belly plates and grooves which accomodate the supporting ropes. It is difficult to simulate this part of the detector precisely and the code is usually run in its default mode in order to speed up the simulation process. Thus

Table 6.19: **The systematic study of the performance of the pattern recognition technique on a testing set generated with short attenuation length.**

		The percentage change of the results of the network	Change in the number of the background neutrons
D_2O	^{208}Tl	-20%	-151.8
D_2O	^{214}Bi	-16.1%	-12.9
Acrylic	^{208}Tl	-33.8%	-88.9
Vessel	^{214}Bi	-12.2%	-7.7
H_2O	^{208}Tl	-4.4%	-11.3
H_2O	^{214}Bi	-10.1%	-4.85
Net change in the deduced number of NC background events = -277.45			

whether the simplifications of the code affect the performance of the technique should be checked. We carried out a systematic check by producing the training and validating sets with the simplified simulation of the vessel (i.e. as a spherical shell) while producing the testing set with the full simulation of the vessel (i.e. turn on its tiles and attachments). As shown in table 6.20, the number of free neutrons produced by major radioactive decays only changed by 0.8%.

Direction of the PMTs

In the SNOMAN code, all photomultipliers are simulated to point towards the center of the detector. There will always be some fluctuations in the directions of the PMTs in reality, which means that the angle of the incident photon would be different to what is simulated in the code and so does the probability to detect this photon. In order to simulate such kind of systematic errors, a gaussian jitter (mean = 0^o and 1σ = 2^o) was added to the directions of the PMTs and then a testing pattern set was produced. The analysis was carried out as before and results are shown in table 6.21. The deduced number of background neutrons only changes by 7.84%. This test also verified that the pattern recognition technique is fairly robust against uncertainty in the angular response of the PMT used in SNO.

Table 6.20: **The systematic study of the performance of the pattern recognition technique on a testing set generated with the full simulation of the acrylic vessel.**

		The percentage change of the results of the network	Change of the number of the neutrons
D_2O	^{208}Tl	3.83%	29.1
D_2O	^{214}Bi	1.6%	1.28
Acrylic	^{208}Tl	-8.41%	-2.21
Vessel	^{214}Bi	1.33%	0.84
H_2O	^{208}Tl	-6.87%	-17.6
H_2O	^{214}Bi	0.65%	0.31
Net change in the deduced number of NC background events = 11.72			

Table 6.21: **The systematic study of the performance of the pattern recognition technique on a testing set generated with jittered PMT directions.**

		The percentage change of the results of the network	Change of the number of the neutrons
D_2O	^{208}Tl	20.2%	153.3
D_2O	^{214}Bi	-17.8%	-14.2
Acrylic	^{208}Tl	-11.6%	-30.5
Vessel	^{214}Bi	5%	3.2
H_2O	^{208}Tl	-1.7%	-4.35
H_2O	^{214}Bi	1.3%	0.62
Net change in the deduced number of NC background events = 108.07			

Noise of the PMTs

In the SNOMAN code, the PMT noise (1 KHZ) is simulated to be evenly distributed among all tubes. It is expected that in reality, there wil be some tubes with more or less noise than average. This so-called "hot" PMT effect may distort the hit pattern of an event. We analyzed this systematic effect by doubling the noise rate in 900 photomultipliers and then producing the testing set for the network. The results are shown in table 6.22. Higher noise rates lead to higher nhits, thus the number of decay events falling inside the cut window is increased and so is the deduced number of free neutrons. There are also some errors from the pattern recognition technique. The overall change in the deduced number of free neutrons produced by radioactive decays is 11.2%.

Detection Efficiency of the PMTs

Up to now, the information about the detecting efficiency of the photomultiplier used in SNO only came from the measurement of 4 Hamamatsu eight inch PMTs [94]. The average deviation of the data from 4 tubes is 4.5%. In the SNOMAN code, all of the 10000 photomultipliers are simulated to have same detecting efficiency, which is the average value of the experimental data. This is definitely not true in reality. There are always some discrepancies among the detecting efficiencies of different photomultipliers. We estimated effects of such kind of systematic errors by artificially reducing the detecting efficiencies of 3030 PMTs by 5%. Since all of these PMTs are located in a certain band (300cm $< z <$ 900cm), the hit patterns of an event may be distorted, which may lead to the mis-identification of the event by the network. We used non-standard code to produce the testing set and then repeated the analysis with results shown in table 6.23. The systematic error in the deduced number of free neutrons produced by major radioactive decays is 4.1%.

Summary

Table 6.24 is a summary of the studies on the robustness of this pattern recognition technique on some possible systematic errors of the code. The total systematic error (quadratic sum) in the number of NC backgrounds deduced by this technique is 24.9%. If the number of NC events is 10 times as large as that of NC background events, such systematic errors could be ignored. Furthermore, the largest systematic error is due to

Table 6.22: **The systematic study of the performance of the pattern recognition technique on a testing set generated with high noise rate.**

Systematic error when deducing the total number of decay events from the number of the events inside the cut window.

		The percentage change of the results of the network	Change in the deduced number of the background neutrons
D_2O	^{208}Tl	8.4%	63.8
D_2O	^{214}Bi	9.3%	7.4
Acrylic	^{208}Tl	6.4%	16.8
Vessel	^{214}Bi	12.5%	7.88
H_2O	^{208}Tl	8.1%	20.7
H_2O	^{214}Bi	11.4%	5.47
Net change in the deduced number of NC background events = 122.05			

Systematic error when using the neural network and chi square technique to determine the relative ratio of 6 classes of the events

		The percentage change of the results of the network	Change in the deduced number of the background neutrons
D_2O	^{208}Tl	13.9%	105.5
D_2O	^{214}Bi	-11%	-8.8
Acrylic	^{208}Tl	2%	5.26
Vessel	^{214}Bi	1.9%	1.2
H_2O	^{208}Tl	4.9%	12.5
H_2O	^{214}Bi	-10%	-4.8
Net change in the deduced number of NC background events = 110.86			

Table 6.23: **The systematic study of the performance of the pattern recognition technique on a testing set generated with decreased detection efficiency of the PMTs.**

		The percentage change of the results of the network	Change of the number of the neutrons
D_2O	^{208}Tl	1.2%	9.2
D_2O	^{214}Bi	5.27%	4.2
Acrylic	^{208}Tl	-9.75%	-2.6
Vessel	^{214}Bi	-5.54%	-3.5
H_2O	^{208}Tl	16.2%	41.5
H_2O	^{214}Bi	-3.15%	-1.5
Net change in the deduced number of NC background events = 47.3			

the change of the photon attenuation probability in the detector (18.9%). This systematic uncertainty seems to be too large given the fact that a laser ball will be used to calibrate this value.

6.4 Conclusion and Comments

.

A pattern recognition technique has been developed to distinguish between the ^{208}Tl and the ^{214}Bi decays in the heavy water statistically, which enables us to directly determine the levels of the most troublesome backgrounds in the SNO detector in real time, in-situ and with little cost. The technique is extended, by including a neural network, to determine the levels of radioactive decays in all regions of the detector (the D_2O, the acrylic vessel and the H_2O regions). The performance of the technique is satisfactory and it has been proved to be robust against various kind of systematic errors in the code. However, the best way to verify this technique is to have some background calibration sources, which are described in the next chapter.

Table 6.24: **Summary of the systematic studies on the performance of the pattern recognition technique.**

Systematical Change	change in the number of the neutrons
Impurity of the testing set	-1.59%
Impurity of the training and calibrating sets	5.7%
Scattering efficiency of the photons	4.76%
Attenuation probability of the photons	-18.9%
Simulation of the acrylic vessel	0.8%
Direction of the pmts	7.84%
Noise of the pmts	11.2%
Detecting efficiency of the pmts	4.1%

Chapter 7

Background Calibration Sources

7.1 Introduction

Almost all of the work described in previous chapters is based on Monte Carlo simulations using the SNOMAN code. Thus the correctness of the code is critical to the creditability of the proposed software techniques. Calibration sources are essential for verifying the agreement between reality and the Monte Carlo prediction. As described in chapter 2, many calibration sources have been proposed to verify various aspects of the code; and many of them are being built in Canada and America. However, none of proposed sources is designed to verify simulations of background events in SNO. This chapter describes background calibration sources proposed and constructed by the author which are able to calibrate simulations of backgrounds in various regions of the detector.

The benefits of such background calibration sources are huge:

- These sources enable us to verify the angular distribution of Čerenkov photons produced by electrons or gammas in the detector which is the foundation of the pattern recognition technique described in the last chapter.

- More importantly, they should give us great confidence (or destroy it) in the performance of the code. No matter which method is used to determine background levels in the detector(the pattern recognition or the water assay technique), we have to use the code to determine where the detector threshold should be. In the worst case where the pattern recognition technique does not work, we have to rely solely on the water system to determine background levels in the detector. However, the water system only tells us the numbers of radioactive decays in the detector. We still need the SNOMAN code to interpret these numbers and extract tangible information such as how large contamination these backgrounds contribute to the energy spectrum of the charged current events and how many neutral current background events they will produce.

As discussed before, major backgrounds in the SNO detector are radioactive decays of nuclei in the thorium or the uranium decay chain, especially the decays of ^{208}Tl and ^{214}Bi nuclei. Thus background calibration sources are just Th or U decay sources. The next section describes the designs and some MC simulations of these sources.

7.2 Monte Carlo Simulation

7.2.1 The Design

There are several things we need to be consider in the design of the sources:

- **The strength of the source**

  The Th or U solution contained in the source should be easy to make and store. Radioactivity in the source should be strong enough to complete the whole calibration process in short period of time.

- **The material**

  The material used to construct the source should be transparent because we want to "see" Čerenkov photons from the source. The material should be very clean in terms of thorium and uranium concentration levels since we do not want to add extra backgrounds to the detector when we put in the source. The material should be strong. If the source breaks, tens of becquerels of thorium or uranium will go into the detector and that would be a disaster for the experiment.

- **The geometry**

  The first thought is that this source should be a sphere with some thorium or uranium at the center. This design minimizes the probability of a photon undergoing reflection or refraction at the source's boundary.

Generally speaking, we want this calibration source to generate data, in a short time (eg. 3 hours), equivalent to half a year's data from backgrounds in 1000 tons of heavy water. Simple calculations show that the required amount of Th and U are 17 and 204 becquerel respectively. In practice, we use ^{228}Th and ^{226}Ra solutions which are commercially available. The half lives of these two decays are 1.91 year and 1599 year, which should be long enough for source to be stored for several months.

"Polycast" acrylic is chosen as the material used in construction. The same acrylic is used in SNO to construct the vessel which contains the heavy water. As discussed above, the concentration levels of thorium and uranium in this material are extremely low. Obviously, the acrylic vessel is transparent and very strong. The other thing we need to worry about is the radiation damage. Glass and other transparent materials such as the acrylic become colored when exposed to radiation. The physical processes which are responsible for the coloring are reasonably well understood. When glasses and other transparent materials are formed, they contain many invisible defects and impurities. When these materials are exposed to radiation, free electrons are trapped in these defects or around these impurities. A large fraction of the centers formed in this way are optically active: they absorb or emit light. The study of Goldberg et al. [113] shows the effects of radiation damage on lead glasses. As far as I know, there are not any theoretical calculations of the radiation damage in the acrylic. Since the dose of the proposed background calibration source is much smaller than 1 rad per month, the radiation damage is not expected to be a serious problem. Of course the best way is to measure the optical quality of the acrylic several months after construction of the source.

The plan of the calibration source is shown in figure 7.1. Two hemispheres of acrylic are bonded together to form an acrylic ball. At the center of the ball, a pre-drilled cylindrical hole contains the radioactive material. The dimensions of the sphere and the cylindrical hole are not critical as long as the radius of the sphere is much larger than that of the hole, thus minimizing the probability of total internal reflection. The height of the cylindrical hole should be small because of practical reasons mentioned later. We choose the radius of the acrylic ball to be 4 cm, the radius and the height of the cylindrical hole to be 0.3 cm and 0.2 cm respectively. Also shown in figure 7.1 is a cubic calibration source. For practical reasons, it is much more difficult to make a spherical source than a cubic one. It is expected that the construction of a perfect source will consume many acrylic prototypes because of the difficulties in bonding and filling the inner volume of the source with the acrylic monomer as discussed later. If the cubic source performs as well as the spherical one, we prefer the cubic one.

Figure 7.1: **Geometry of the background calibration sources.** Upper plot is a spheric source while the bottom one is a cubic source. see text.

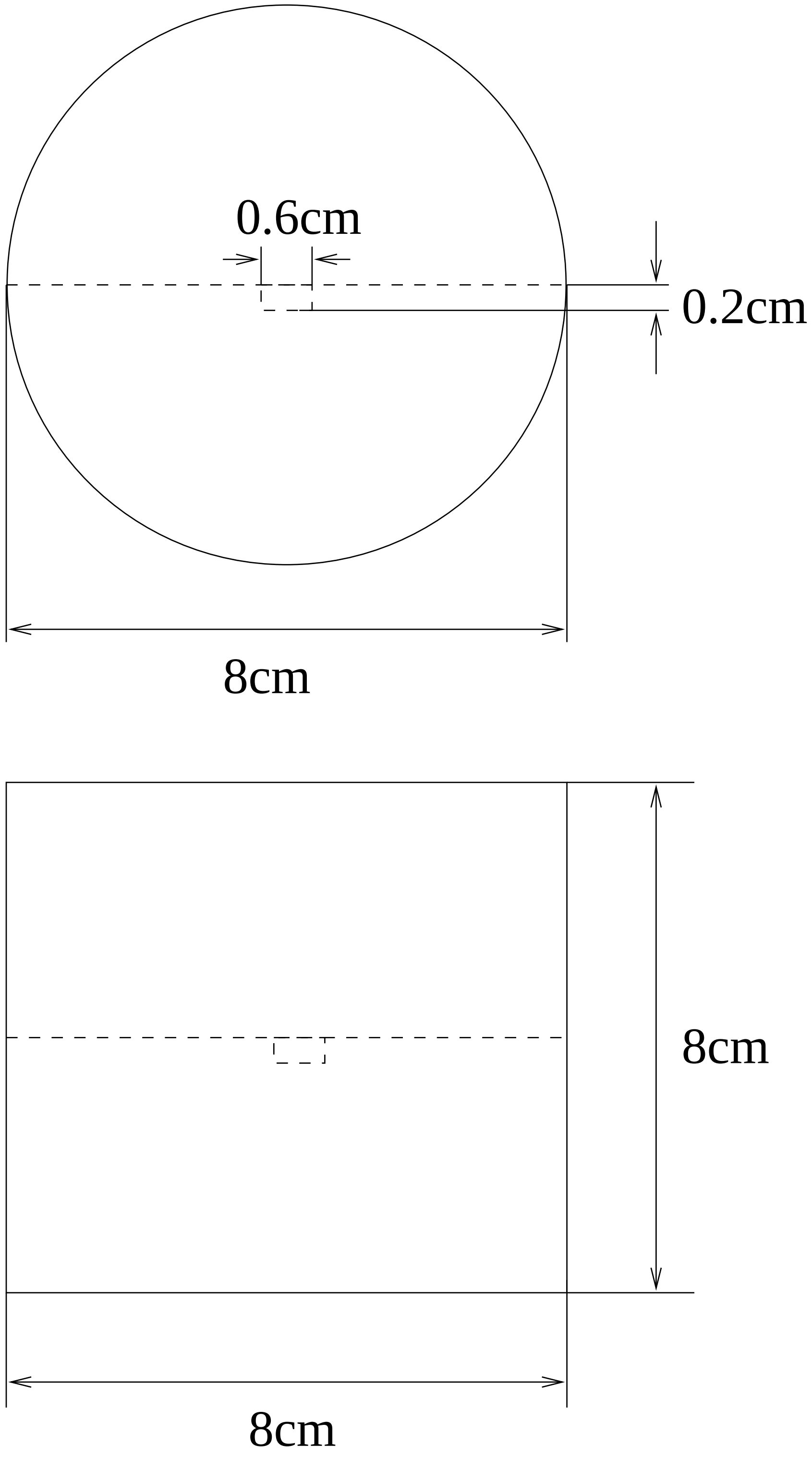

7.2.2 Results of MC simulations

The calibration source is simulated as a cylinder embedded in an acrylic ball using the SNOMAN code. A simple but powerful method to check the geometry of the simulated source is to generate thousands of neutrinos at the center of the source travelling in all directions and record all boundary vertices of the outgoing neutrinos. This method produces a neutrino image of the source, as shown in figure 7.2, which agrees with the design. Also shown in figure 7.2 is the neutrino image of the cubic calibration source.

A calibration source should be strong enough to overwhelm any other backgrounds in the detector. Hundred of thousands of MC ^{208}Tl and ^{214}Bi decay events were generated in the cylindrical hole of the source with results shown in table 7.1. With such a strong source at the center of the detector, contamination due to other events in the detector can be ignored. The only possible background comes from double or triple coincident events. Since the source is so "hot", it is possible two or more decay events (eg. one happens in the source, the other happens in the PMT sphere) could occur within the same trigger window. However, since the vertex fitter would put this kind of coincident event at anywhere in the detector or just fail to find a converged vertex, an r_{fit} cut , which rejects any events reconstructed further than 1 meter away from the center of the source, should be able to get rid of most of such backgrounds. Calculations showed that only 8 double ^{208}Tl decay events and 2360 double ^{214}Bi decay events would happen in 3 hours. Monte Carlo simulations showed that only 8 such events fall into the monitor window ($30 <$ nhits < 40 and $r_{fit} < 100$cm).

θ_{ij} distributions for two types of decays are shown in figure 7.3. We hope these sources are able to tell us whether the SNO detector is sensitive enough to see the difference between the angular distributions of Čerenkov photons generated by the two types of decays. As figure 7.3 shows, the distributions produced by the sources with different geometries (sphere and cube) are similar. It may be due to the fact that the difference between the refraction indexes of the acrylic (1.5) and the heavy water (1.337) is not too large. From other point of view, it simply proves that these background calibration sources are fairly robust against any systematic errors in their geometries. I have also carried out simulations of sources with different sizes and/or made of different materials. With large sources or sources made of materials less transparent than the UV stabilized acrylic, the difference between the θ_{ij} distributions produced by two types of decays becomes smaller.

Figure 7.2: **Neutrino images of the background calibration sources.** It was generated by recording all intersection vertices of MC neutrinos with the source, see text.

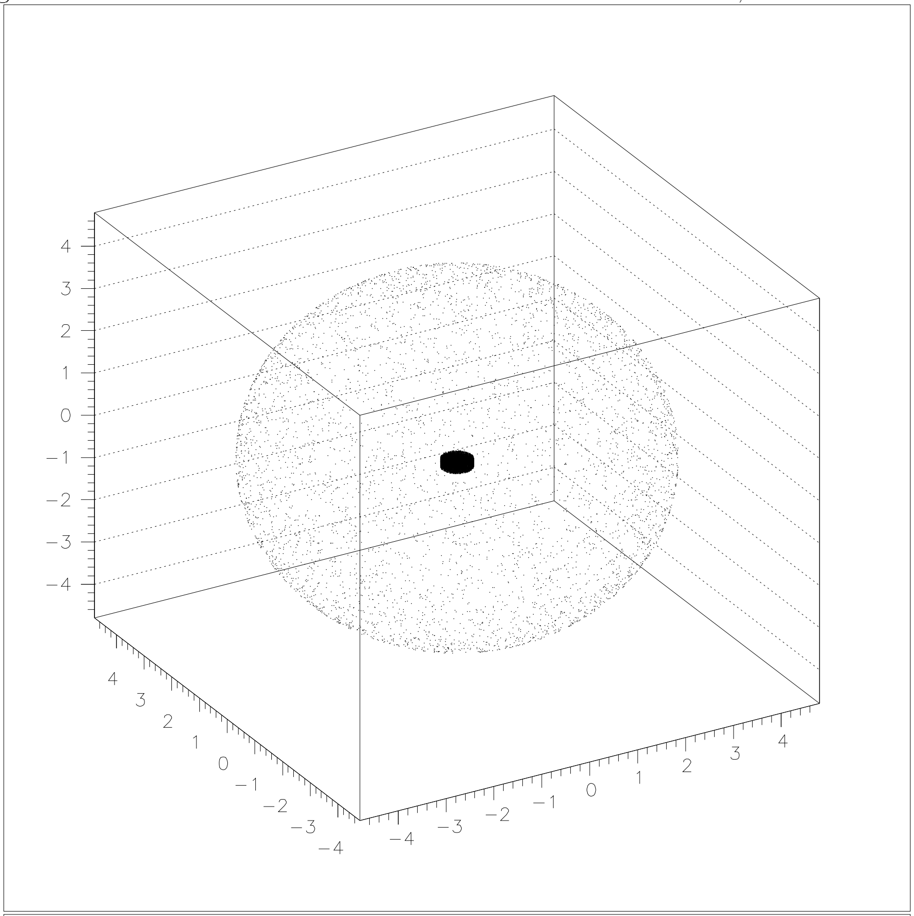

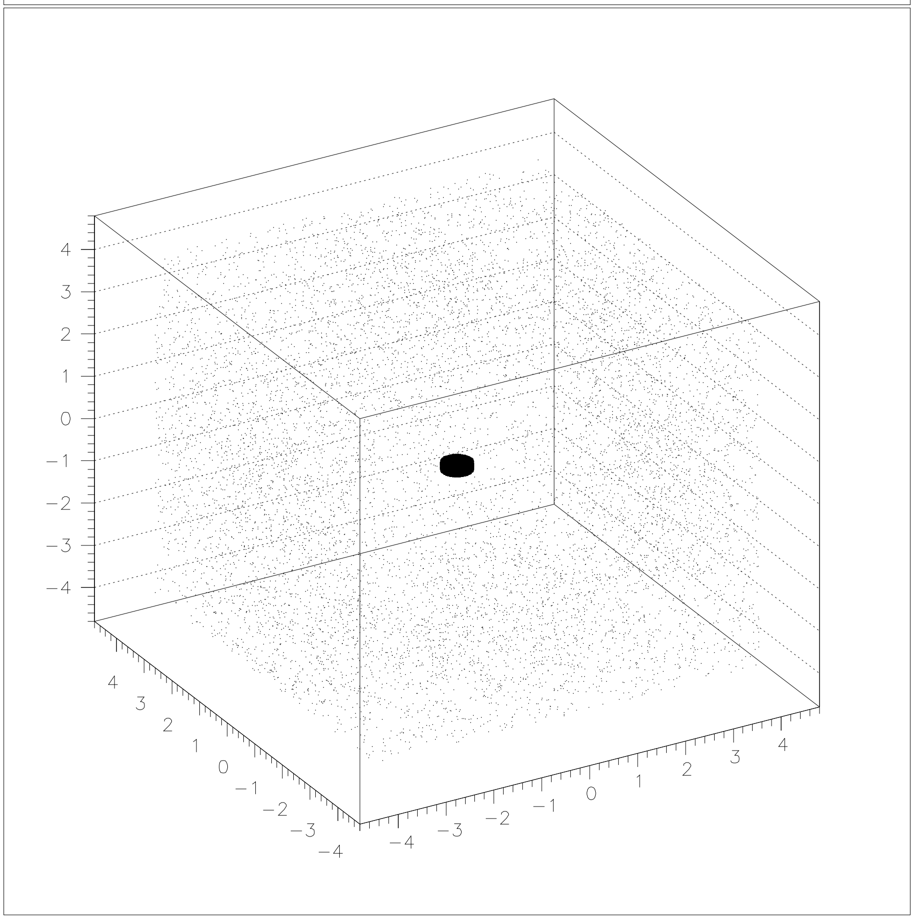

Table 7.1: **MC results of background calibration sources.** The source is placed at the center of the detector. A window ($30 < nhits < 41$ and $r_{fit} < 100cm$) is imposed on the data.

A spherical calibration source with radius of 4cm

Type of decay	No. of MC events	No. of MC events in the window	No. of events in three hours	No. of events in the window
^{208}Tl decays	100000	2491	182500	4546
^{214}Bi decays	900000	1935	2.19E6	4709

A cubic calibration source with each side of 4cm

Type of decay	No. of MC events	No. of MC events in the window	No. of events in three hours	No. of events in the window
^{208}Tl decays	70000	1786	182500	4656
^{214}Bi decays	600000	953	2.19E6	3478

This is because the photons produced by low energy gammas or/and electrons from the ^{208}Tl decay are more likely to be absorbed by the source material than the high energy gamma (2.613 MeV), which makes a ^{208}Tl decay event look like a single particle event, and thus similar to a ^{214}Bi decay event.

7.3 Source Construction

Polymethacrylate is, commercially, the most important member of a range of acrylic plastics. It was found in 1880 [114] that this material could be easily made through the polymerisation of the acrylic monomer. The process discovered by Crawford [115], which enabled people to prepare the monomer using cheap and readily available chemicals, started wide applications of this material in many fields. This material is used to build the background calibration sources as well as the acrylic vessel in the SNO detector.

Methyl methacrylate will polymerise readily and the effect may be observed with uninhibited samples of monomer during storage. This is the main reason to choose this material. We can easily pour the liquid monomer into the inner volume of the calibration source where the radioactive thorium or uranium powders are contained. After the monomer polymerises, the inner volume of the source will become a solid acrylic cylinder

Figure 7.3: θ_{ij} **distributions for equal numbers of** ^{214}Bi **(solid line) and** ^{208}Tl **(dashed line) decay events uniformly generated in the background calibration source.** The upper plot shows the distributions from a spherical source while the bottom plot shows the distributions from a cubic source.

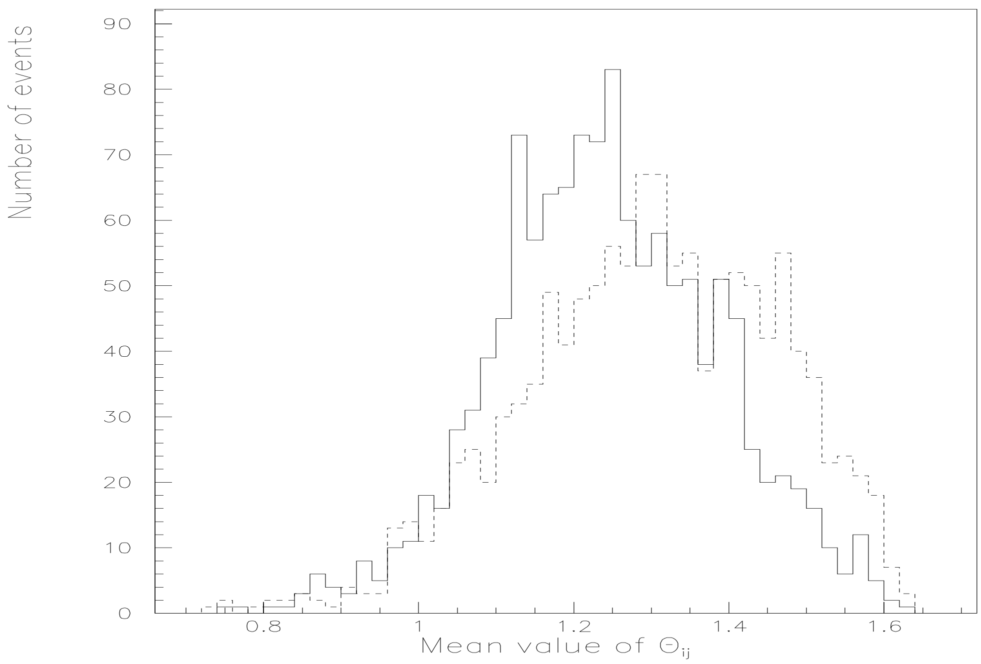

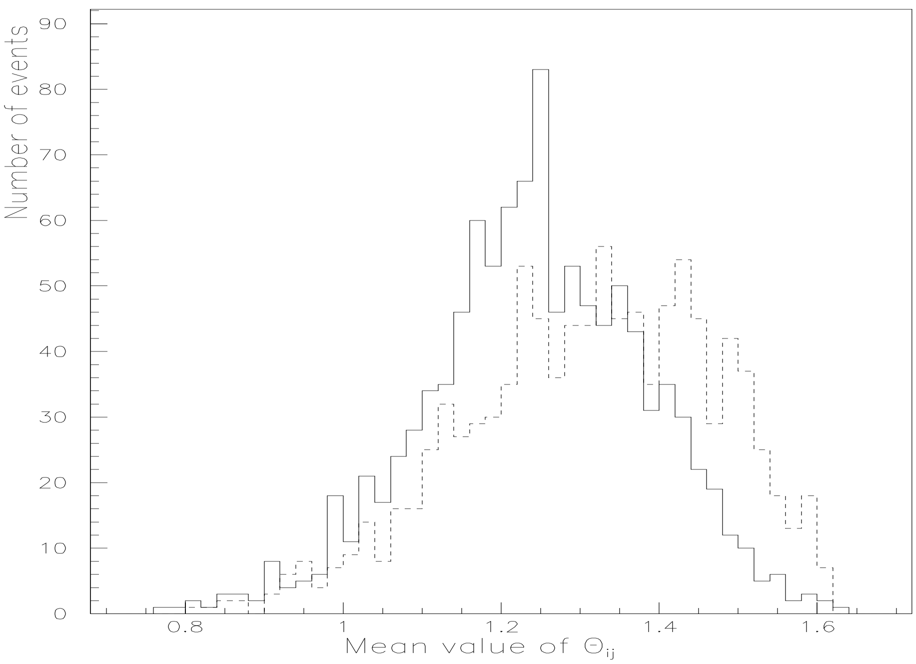

which is unseparatable from the outer volume of the source. The radioactivity will be contained hermetically and there should not be any chance that it could leak out of the source and contaminate the detector.

The original design of the calibration source is shown in figure 7.4, which is a solid acrylic ball with a long cylindrical hole. The plan was that we could fill the whole hole with the monomer after the radioactivities were placed at the bottom of the hole. We hoped that the polymer would seal the hole hermetically and this procedure might end with a solid acrylic ball with radioactivities at its center. However, experiments showed otherwise. A couple of problems occurred:

- The acrylic is a poor thermal conductor. Lots of heat was generated when the monomer polymerised, which led to regional exotherms. These exotherms produced bubbles along the cylindrical hole.

- Extensive shrinkage ($\approx 20\%$) occurred in the conversion from the monomer to the polymer. More seriously, we could not control which part of monomer cured first. If the monomer in the higher region of the cylindrical hole cured first, we would end up with a big voids in the middle of the hole since there was not enough monomer left to fill the whole hole.

Obviously both bubbles and voids are unacceptable since they seriously affect the optical character of the calibration source which is essential in the measurement of the angular distribution of Čerenkov photons. Many techniques had been tried to avoid these bubbles and voids during the polymerization of the monomer:

- We tried holes with various shapes. For example, we filled a conical hole with the monomer and hoped the gravity would force the monomer at the bottom of the hole to cure first.

- We built a monomer reservoir above the hole and hoped that it would supply extra monomer to compensate the shrinkage during the polymerization.

- We provided air pressure (≈ 15 p.s.i.) on the open end of the hole and hoped this pressure would push the monomer towards the closed end of the hole and thus avoid the shrink voids.

- In order to minimize the shrink voids, we used so-called "prepolymer" syrup, which is available on the market, instead of the pure monomer. This kind of syrup consists

Figure 7.4: **Geometry of the original design of the calibration source.**

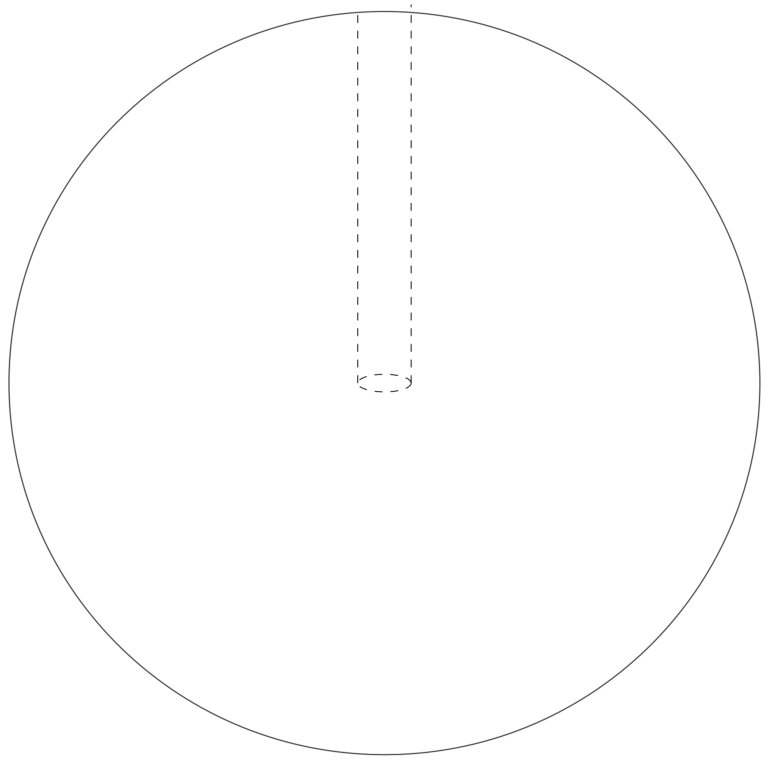

of a solution of polymer in monomer with a small amount of ($\approx$ 0.5%) benzoyl peroxide dissolved as a catalyst.

All of these techniques helped to avoid bubbles and voids to some extent, especially the "prepolymer" syrup. However, bubbles and voids still occurred in all experiments. Similar situations occurred in the construction of the acrylic vessel in the SNO detector, which caused several months of delay. In fact, it is more difficult in our case because we needed to fill a half-through hole while in the case of the construction of the AV, only through holes needed to be filled. After consulting with experts in the SNO AV group, we adopted the design shown in figure 7.1. It seemed to be a simple task to construct the sources. However, we met many problems in the practice.

As said before, we used the ^{228}Th and the ^{226}Ra solutions as radioactive sources. The standard procedure was to place several drops of solutions in the cylindrical hole pre-drilled in one half of the source. Then the source was placed in the fume cupboard for one or two days. During this period, the water vaporized naturally and the radioactive contents were left inside the hole. All these processes ran smoothly until we poured the acrylic monomer into the cylindrical hole. The polymerized monomer turned completely yellow. The ^{228}Th solution is in 1M HNO_3, otherwise ^{228}Th would deposit on the container. It was suspected that the acid interacted with the monomer, which led to the change of color. However the neutralization of the HNO_3 solution with NaCl did not make things better. Barry Knox [116] pointed out that the yellowness of the monomer may be due to the oxidization by HNO_3. We reprepared the ^{228}Th solution with HCl (it was not easy because of radioactive safety) and it worked fine with the monomer. The ^{226}Ra is now stored in an HCl solution.

7.4 Optical Qualities of the Calibration Sources

The performance of the background calibration source heavily relies on its optical quality as any loss of transparency in the source may wash out the small difference between angular distributions of Čerenkov photons produced by the two types of radioactive decays. The optical transparencies of acrylic blocks used in SNO have been measured before and relevant data have been included in the SNOMAN code to carry out previous simulations. The problems left lie with the optical qualities of the acrylic glue used to attach the two blocks together and the monomer syrup used to fill the inner volume of the source as shown in figure 7.1. Two experiments have been set up to measure these physical qualities:

- A spectrophotometer was used to measure the transmission of light, from 300 nm to 600 nm, through a polished acrylic block. Then the block was cut into two pieces and then bonded together with the acrylic glue. The spectrophotometer was again used to measure the light transmission of the block. The two sets of measured data are shown in figure 7.5. Comparison of the two curves could eliminate many systematic errors in the experiment such as possible bias of the spectrophotometer. A clear feature of the plot is that the acrylic glue absorbs light with wavelength less than 400 nm. The discrepancy of two curves at high wavelength may be due to the reflection of light at the boundary between the upper and the lower half of the block.

- Similar measurements have been carried out to quantify the optical quality of the monomer syrup. It is expected that we are going to use the same syrup which is used to bond the acrylic panels together in the SNO experiment. A test sample (shown in figure 7.6) with 3mm wide bonding region sent from the SNO AV group was measured, the data is shown in figure 7.7. The data of light transmission along z direction of the block was used to deduce the attenuation length of light in this acrylic block (taking into account reflection of light (4%) at the air-acrylic and the

Figure 7.5: **Transmission of light through a acrylic block before (solid line) and after (dashed line) the bonding measured by a spectrophotometer.** See text.

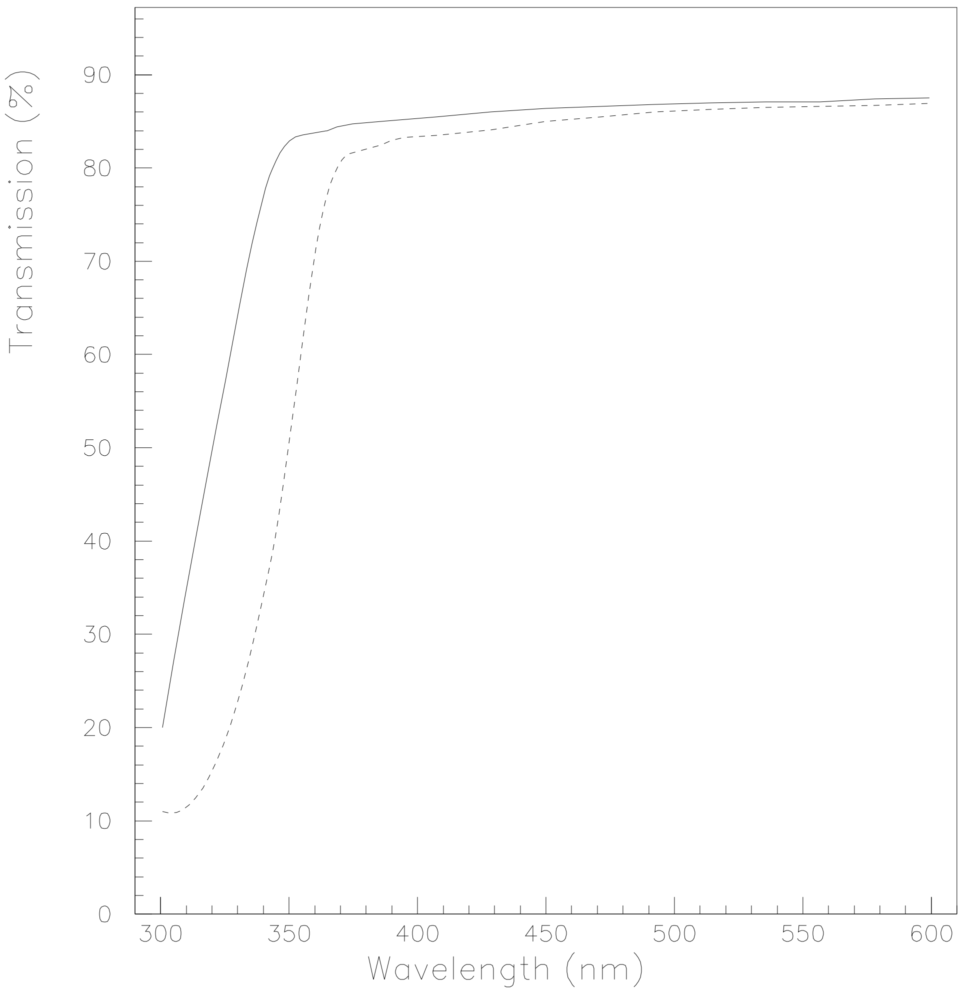

Figure 7.6: **A acrylic bond sample.** see text

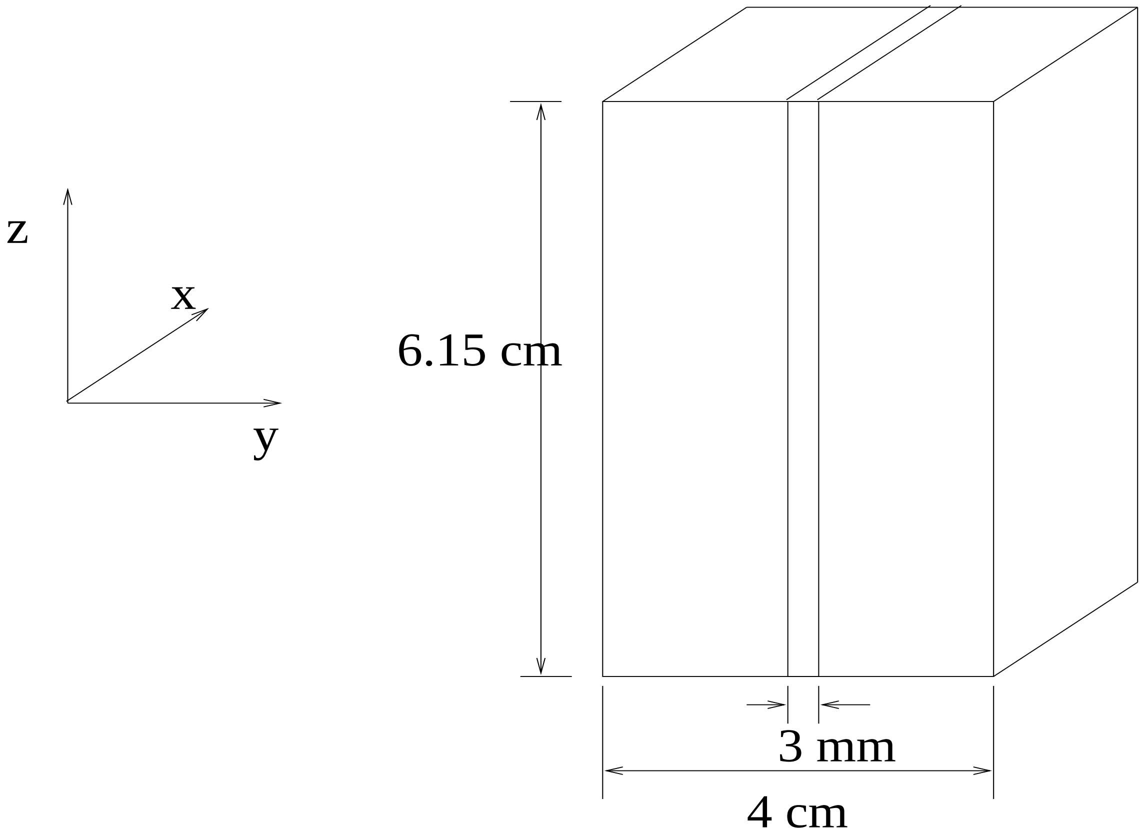

acrylic-air boundaries). Then we estimated how much light would pass through the block along the y axis if there was no bond region. Comparing these deduced values with real data, we could deduce the attenuation length of light in the monomer syrup used to bond the two acrylic block together. This method minimizes possible systematic errors in the experiment. The monomer syrup also strongly absorbs UV light.

7.5 Systematic Studies

As shown in the previous section, both acrylic glue and monomer syrup strongly absorb UV light. Monte Carlo simulations have been carried out to determine whether the attenuation of light at low wavelengths would have significant effects on distinguishing between ^{208}Tl and ^{214}Bi decays. A systematic study was carried out with the assumption that there existed a boundary between the upper and the lower half of the source , through which any photon with wavelength less than 400 nm would be absorbed and 5% of photon with wavelength larger than 400 nm would undergo diffuse scattering (i.e. the scattered

Figure 7.7: **Transmission of light through two pieces of acrylic blocks bonded by the monomer syrup.** Solid line represents data of light transmission along the y axis direction shown in figure 7.6 while dashed line shows the corresponding data along z axis direction. The dotted line represents the deduced data of light transmission along y direction if there was no bond, see text.

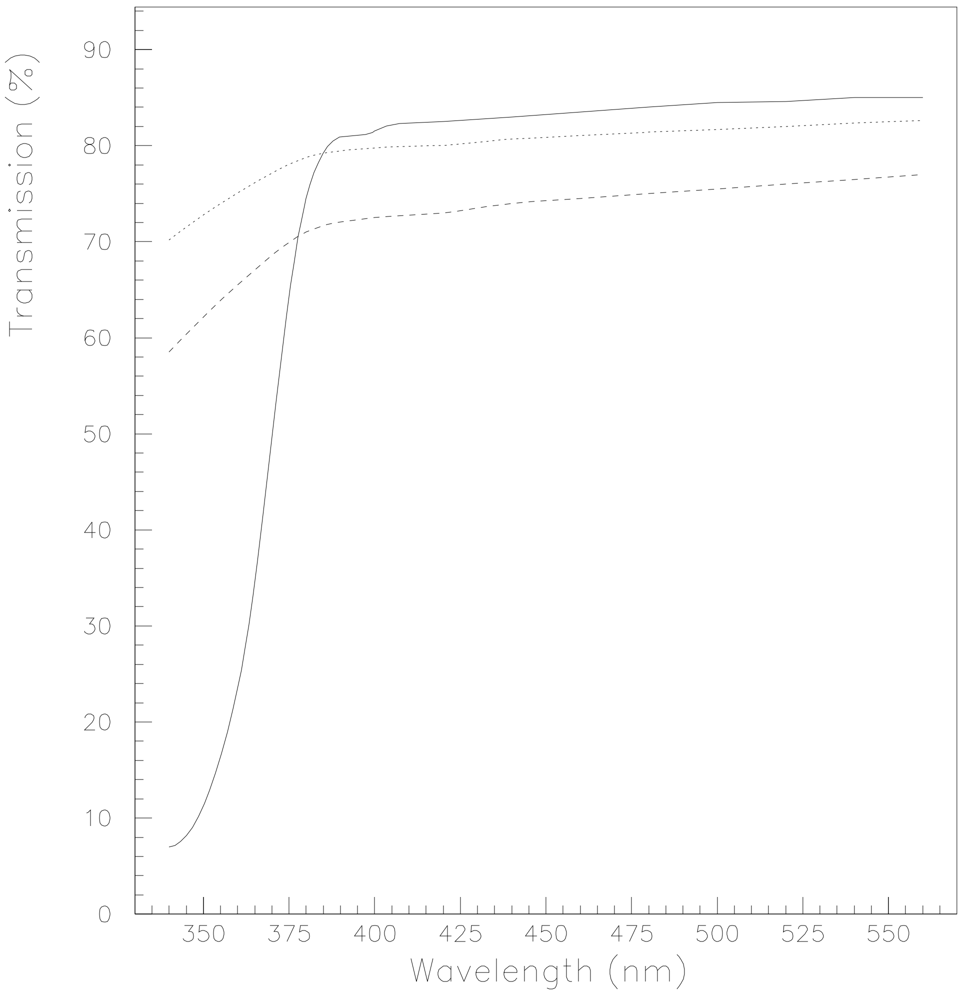

Table 7.2: **Results of the Kolmogorov-Smirnov test to verify whether two histograms come from the same parent distribution, see text.** D is the largest normalized deviance between two histograms.

Names of compared histograms	D	Probability($D > observed$)
standard thorium source thorium source with systematic changes	0.045	0.077
standard uranium source uranium source with systematic changes	0.089	0.0018
standard thorium source standard uranium source	0.195	3.32E-34

photon is assumed to be isotropically distributed in the backward hemisphere of the incoming photon). Attenuation lengths of light at various wavelengths in the monomer syrup, which was used to fill the inner volume of the source, were deduced from figure 7.7 and are shown in table 7.3. $\overline{\theta_{ij}}$ distributions for two types of radioactive decays were generated with these assumptions, which are compared with distributions generated by standard sources. As figure 7.8 shows, the changes in the simulations of the sources do not produce significant changes in the distributions. A more mathematical approach has been done to verify whether two histograms generated with and without the systematic changes in the calibration source agree with each other by using the Kolmogorov-Smirnov test (see appendix 1). Results of the test are shown in table 7.2. The difference between histograms generated by the thorium and uranium source is much larger than that generated by the sources with and without systematic changes. Although the boundary and the inner volume of the source strongly attenuate light at low wavelengths, the net affect is more or less minimized by the fact that even without these systematic changes, these photons are fairly likely to be absorbed by the source itself and 5cm thick acrylic vessel. However, the number of PMT hits is less robust than the angular distribution of the hits. Table 7.4 shows discrepancies between numbers of events falling within the cut window ($r_{fit} < 100$ cm and $30 <$ nhits < 41) generated with standard and non-standard sources. This would lead to $\approx 30\%$ systematic errors when we use these sources to calibrate the energy scale of the detector at low energy range. Thus the optical quality of the source must be measured and taken into account by the MC simulations.

Table 7.3: **Deduced attenuation lengths of light in the monomer syrup at various wavelength.**

Wavelength (nm)	340	360	380	400	420	440	500	600
Attenuation length (cm)	0.13	0.26	5.26	100	100	200	200	200

Table 7.4: **Systematic study about the ability of the source to calibrate the energy scale of the detector at the low energy range.** see text.

Type of sources	No. of MC	No. of events in the window events $30 < nhits < 40$ and $r_{fit} < 100cm$
standard thorium source	70000	1786
thorium source with systematic changes	70000	1501
standard uranium source	600000	953
uranium source with systematic changes	600000	672

Figure 7.8: **Systematic study of the background calibration source Solid lines show the $\overline{\theta_{ij}}$ distributions generated with a boundary between the upper and the lower half of the source and a less transparent inner volume while the dashed lines are standard distributions as before. The upper plot comes from the ^{208}Tl decays while the bottom plot comes from the ^{214}Bi decays.**

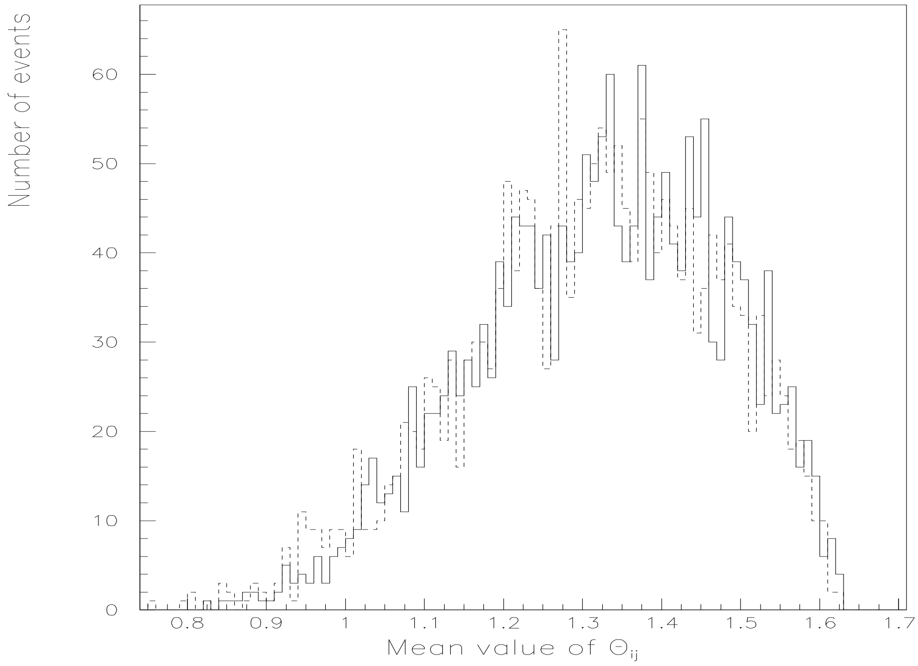

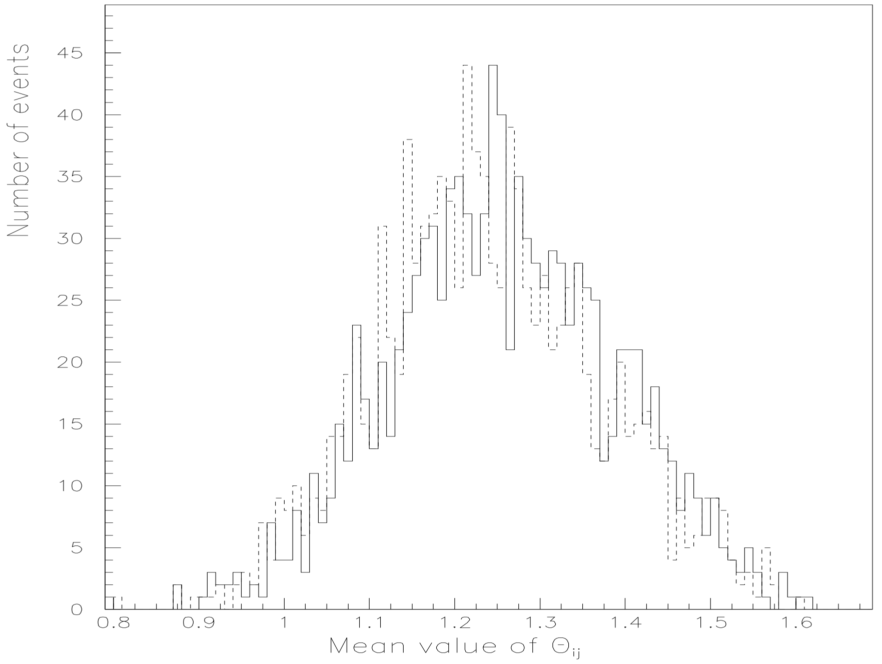

Table 7.5: **Results of the Kolmogorov-Smirnov test to verify whether two histograms come from the same parent distribution, see text.** D is the largest normalized deviance between two histograms.

Names of compared histograms	D	Probability($D > observed$)
thorium source filled with the water thorium source filled with the polymer	0.03	0.288
uranium source filled with the water uranium source filled with the polymer	0.045	0.077
thorium source filled with the polymer uranium source filled with the polymer	0.195	3.32E-34

The inner and outer volume of the calibration source is made of the same material. However, the outer volume is solid acrylic while the inner cylindrical hole was filled with the acrylic monomer which then polymerized and became solid. There exists a boundary between two regions which can be seen if one looks carefully. Photons have small but non-zero probabilities of undergoing reflections or refractions when they traverse the boundary, which may affect the net angular distributions. A systematic study was carried out by assuming the inner cylindrical hole of the source was filled with water and then θ_{ij} distributions were generated for both thorium and uranium calibration sources. These distributions agree with the distributions generated with the standard sources, as shown in figure 7.9. We also carried out the Kolmogorov-Smirnov test to verify whether the histogram generated with the inner volume of the source filled with the water and the histogram generated with the inner volume of the source filled with the acrylic polymer come from the same parent distribution. Results of the test are shown in table 7.5. Again the difference between histograms generated by the thorium and the uranium source is much larger than that generated by the same source with different filling material. In reality, the distortion in the angular distribution of Čerenkov photons due to the boundary between the inner and outer volume of the source is much smaller than the situation assumed here with a boundary between the water and the acrylic. Data from the calibration source should be robust against any systematic errors due to this boundary.

Figure 7.9: **Systematic study of the background calibration source for the boundary between the inner and outer volume of the source.** The solid line shows θ_{ij} distributions generated with water in the inner volume of the source while the dashed line stands for distributions generated with the standard source. The upper plot comes from the ^{214}Bi decays while the bottom plot comes from the ^{208}Tl decays.

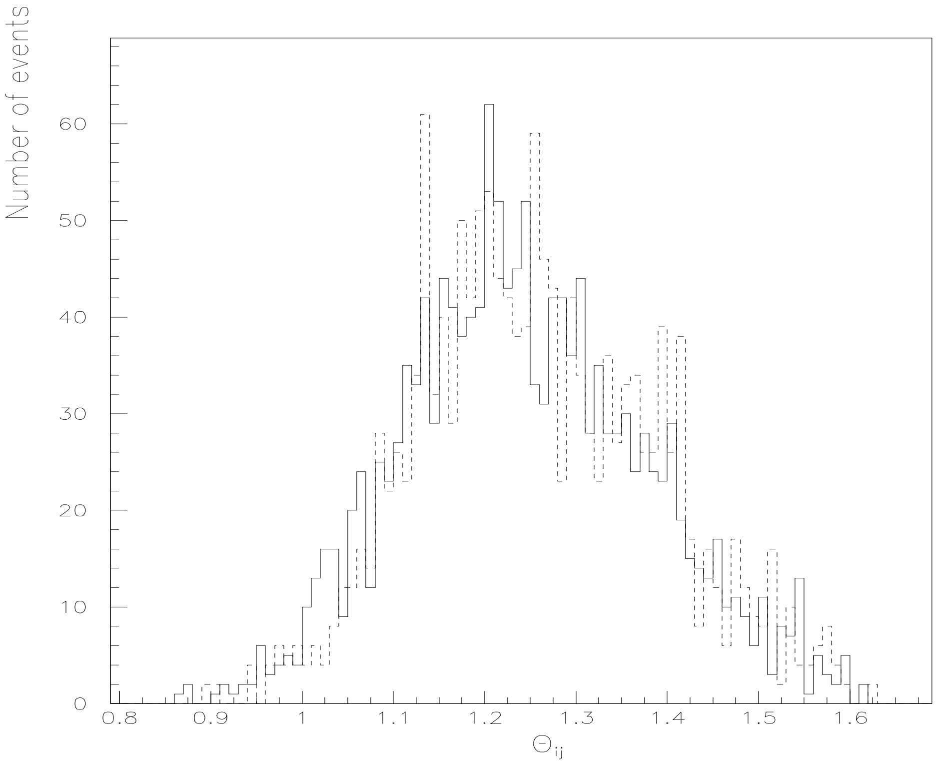

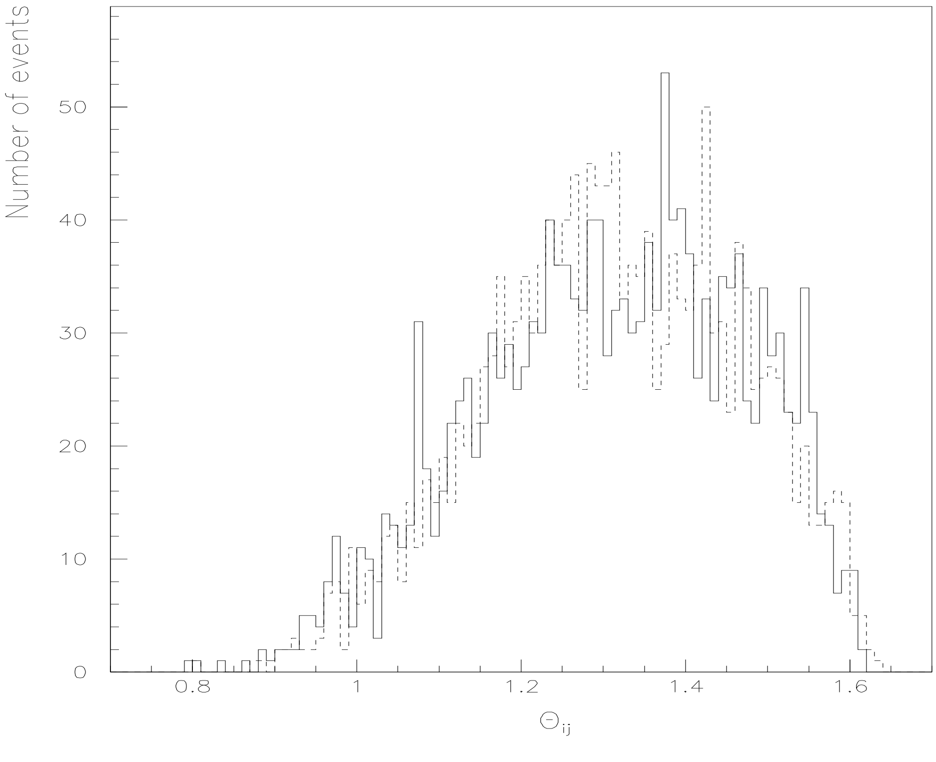

7.6 Leakage test

Since there are tens of Becquerels of radioactive materials in the background calibration source and the expected total background level in 1000 tons of heavy water is 1000 radioactive decays per day, it is critical that the ^{228}Th or the ^{226}Ra solution contained in the source does not leak out. A test has been carried out by putting a prototype of the calibration source, which contained 10 Becquerel of ^{228}Th, into a plastic container which is full of HCl solution (HCl is a much more powerful solvent than water in terms of washing off radioactive contaminations). After 10 hours, a beta-alpha counter [86] was used to measure the background level in the HCl solution, which turned out to be 1 decay per day. This small value is not statistically significant compared with results from a blank test without embedded radioactivities (0.5 decay per day). This low background level may come from possible contaminations on surfaces of the container or the acrylic instead of the inner volume of the source. Even if all backgrounds in the HCl solution come from the calibration source, it is much less than 1% of the expected background level in the heavy water.

7.7 Summary

Background calibration sources are able to verify the simulations of backgrounds in SNO based on the SNOMAN code. They could check not only the angular distributions of photons produced by various radioactive backgrounds, which is the foundation of the pattern recognition technique described in the previous chapter, but also, more importantly, the energy spectrum of the background events, which determine the energy threshold of the SNO detector. The benefits of these sources can not be achieved by any other methods. A simple design of the source has been described. Some prototypes of the sources have been built and tests proved that they are feasible for the SNO experiment.

Chapter 8

Final Conclusions

This thesis presents work done by the author during three years' D.Phil study at Oxford university. The main subject is Monte Carlo simulations of various backgrounds in the SNO detector and some software tools developed by the author which will be useful in future analyses of data from SNO.

Chapter 3 gives a detailed discussion about backgrounds in the detector, of which β-γ decays of ^{208}Tl and ^{214}Bi nuclei are dominant. Extensive Monte Carlo simulations have been carried out to evaluate effects of these two types of backgrounds in various regions of the detector. If the expected levels of radioactive contaminations in various components of the detector are achieved, a energy threshold of 6 MeV should be enough to reject most of the backgrounds. One of the most difficult problem in the background studies comes from the so called PMT β-γ background, which was discussed in chapter 4. Monte Carlo simulations showed that Rayleigh scattering was the dominant reason behind mis-reconstructions of PMT β-γ background events. Many software techniques have been developed to reject this kind of background. The so-called divergence veto technique seemed to be the most powerful one, which is able to reduce the level of this kind of background by roughly an order of magnitude. As is well known, the most troublesome background in the SNO experiment is the neutral current background which has a identical signal as that of a neutral current event. The thing we can do is to determine the level of this kind of background accurately and then subtract it from the number of neutron capture events in the detector in order to measure the number of neutral current events. Thus accuracy in determining the level of NC backgrounds is crucial in terms of the ultimate goal of the SNO experiment: the NC/CC ratio. Chapter 5 presents a pattern recognition technique which could fulfill this task. Monte Carlo simulations showed that this technique is able to determine the levels of the major backgrounds in the detector with only 5% error. Even taking into account some possible systematics, the error is not larger than 20%. Finally chapter 6 presents designs of background calibration sources which will play a critical role in our understandings of backgrounds in the detector, the most important and difficult problem for a neutrino experiment such as SNO.

Appendix A

Online Monitor

A.1 Introduction

There are many physical parameters (such as attenuation length of the photon in the detector and the response of individual photomultiplier) in the SNOMAN code which are set as constants at present. These values are expected to change from time to time in the real detector, which requires frequent calibrations. Each calibration process will produce enormous amounts of data which in normal cases are stored in hundreds of ntuple files. It is impossible and unnecessary for people to spend a long time in looking through all these data and finding out whether there are any changes in the relevant parameters. The purpose of the online monitor is to let the computer do the comparison and report any significant changes in these parameters automatically. If some of parameters change, the computer may automatically write the new value into the data base, from which the SNOMAN code takes its inputs.

A.2 The Kolmogorov-Smirnov Test

The basic process of the online monitor is to compare two data distributions and determine whether they come from same underlying p.d.f.. Furthermore, it should be able to calculate the significant level of the difference between two distributions. Thus we could easily set a alarm threshold, above which the computer will report and update the corresponding parameter in the data base. There are many methods to fulfill this task. The simplest and the most widely used method is the Chi-Square test which calculates the χ^2

value defined as:

$$\chi^2 = \sum_i \frac{D_{1i} - D_{2i}}{D_{1i} + D_{2i}} \tag{A.1}$$

where D_{1i} and D_{2i} are numbers of events in the i^{th} bin of two data distributions respectively. The test assumes the number of events in each bin follows the Gaussian probability distribution function with the standard $\sqrt{N}$ error. However, the Chi-Square test requires first that two sets of data are binned into two histogrammes and number of events in each bin should be large (e.g. N $>$ 5 [117]) otherwise it follows the Poisson instead of the Gaussian distribution. As we want the on-line monitor to operate automatically and we do not know shapes and ranges of the data distributions to be compared in advance, it is difficult to define a binning method which is suitable for all possible data. Although there exist elegant algorithms to optimize the bin size for different data distribution [118], they may be so complex and slow that it prevents the code from comparing thousands of distributions quickly and efficiently.

We chose the Kolmogorov-Smirnov test [92] which is free of the binning process. First the data distribution is converted into a cumulative distribution function $S_n(x)$. For example, if there is a set of data x_i, as shown in figure A.1, the cumulative function is:

$$S_n(x) = \begin{cases} 0 & x < x_1 \\ i/N & x_i \leq x < x_{i+1} \quad (1 \leq i \leq N) \\ 1 & x \geq x_N \end{cases} \tag{A.2}$$

Where N is number of data (in this case N=10).

Different data distributions give different cumulative distribution function. There are many statistical methods to quantify the overall difference between two cumulative distribution functions, one of which is the Kolmogorov-Smirnov Test D method. D is defined as the maximal value of the absolute difference between two functions:

$$D = max \mid S_{N_1}(x) - S_{N_2}(x) \mid \; (-\infty < x < \infty) \tag{A.3}$$

where N_1 and N_2 are numbers of data points in two distributions respectively. The function that calculates the significance level of the difference can be written as:

$$Q_{ks}(l) = 2 * \sum_{i=1}^{\infty} (-1)^{i-1} * e^{-2i^2 l^2} \tag{A.4}$$

which is a monotonic function with the limiting values:

$$Q_{ks}(0) = 1 \;\; , \;\; Q_{ks}(\infty) = 0 \tag{A.5}$$

Figure A.1: **Cumulative Distribution Function with 10 data points.**

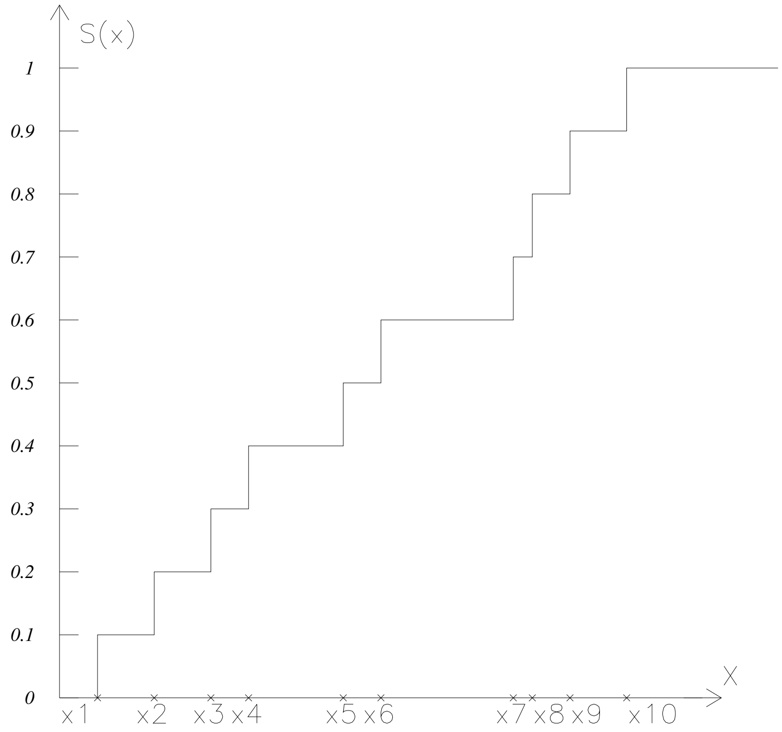

In this case, the significance level of an observed value of D (as disproof of the null hypothesis that the distributions are same) is given approximately by the formula:

$$Probability(D > observed) = Q_{ks}(\sqrt{\frac{N_1 N_2}{N_1 + N_2}}D) \tag{A.6}$$

This value is the quantitative representation of the probability that two data distributions come from the same underlying p.d.f.. For example, if D equals 0., two data distributions are identical; if D equals 1., there is no chance they come from the same p.d.f..

A.3 Results

There are not any real data at present. We are using this tool to compare outputs from different versions of the SNOMAN code. Unexpected difference are often caused by bugs in the code. By looking at causes of the difference, we may be able to correct bugs which otherwise are difficult to find.

Appendix B

Simulating the Radioactive Decays of ^{208}Tl and ^{214}Bi Nuclei

The radioactive decays of ^{208}Tl and ^{214}Bi nuclei are the dominant background in the SNO detector. As almost all of the assay techniques can only provide information about the uranium and thorium concentration levels in the detector, we rely heavily on Monte Carlo simulations to determine the effects of these backgrounds on the neutrino-induced signals. Thus the accuracy in simulating these two types of decays is critical in terms of understanding backgrounds in SNO.

Although the physics behind the β-γ decays of ^{208}Tl to ^{208}Pb and the β-γ decays of ^{214}Bi to ^{214}Po is well understood, the accurate simulations of these two types of decays involve considerable effort because of the complexity of the two decay schemes. The ^{208}Tl decay is relatively simple and has roughly 25 decay channels while the ^{214}Bi decay has roughly 100 channels. Before the 2_09 version of the SNOMAN code, only the top 16 ^{214}Bi decay channels, whose total branching ratio is 74.6%, were included in the simulation. It was expected that incompleteness in the simulation of these decays might have led to systematic errors in the background analyses.

I took the data about the decay schemes of these two nuclei from [119] and included all decay channels in the simulations. As the data contained in [119] may be out of date, the gamma spectra of the two types of decays generated by MC simulations have been compared with the spectra taken from the "nuclear decay data base" available by E_mail request from Lawrence Berkeley Lab[1] which contains the latest experimental data.

[1] E_mail address: " gamquest@Csa1.LBL.Gov".

Results of comparisons are shown in figure B.1 and figure B.2. The difference between the experimental data and the MC data is less than 2%, which is at the same order of the statistical error.

Including all decay channels in the simulations was necessary. This is shown by comparing figure B.2 and figure B.3, where the difference between the experimental data and the MC data is around 15%. Number of ^{214}Bi decay events falling within the cut window ($30 <$ nhits < 40) simulated by the older version of the code is 30% larger than that simulated by the new version of the code which includes all decay channels.

Figure B.1: **The gamma spectrum from ^{208}Tl decay.** The upper plot comes from the experimental data, the middle one is produced by the SNOMAN code and the lower one is the difference between the upper and the middle plot. Bin size is 0.05Mev which is much smaller than the energy resolution of the SNO detector.

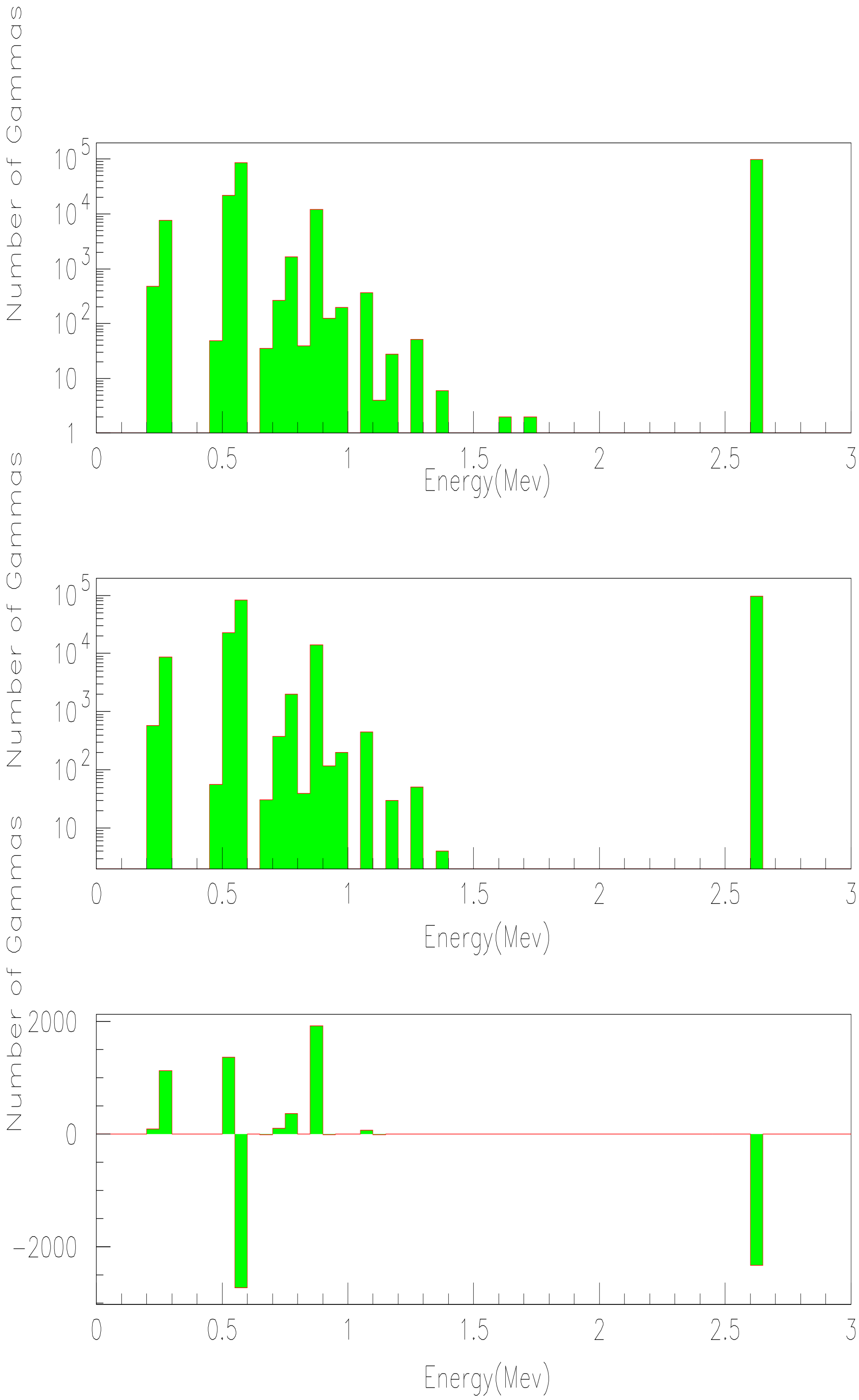

Figure B.2: **Gamma spectrum from ^{214}Bi decay.** The upper plot comes from the experimental data, the middle one is produced by the SNOMAN code and the lower one is the difference between the upper and the middle plot. Bin size is 0.05Mev which is much smaller than the energy resolution of the SNO detector.

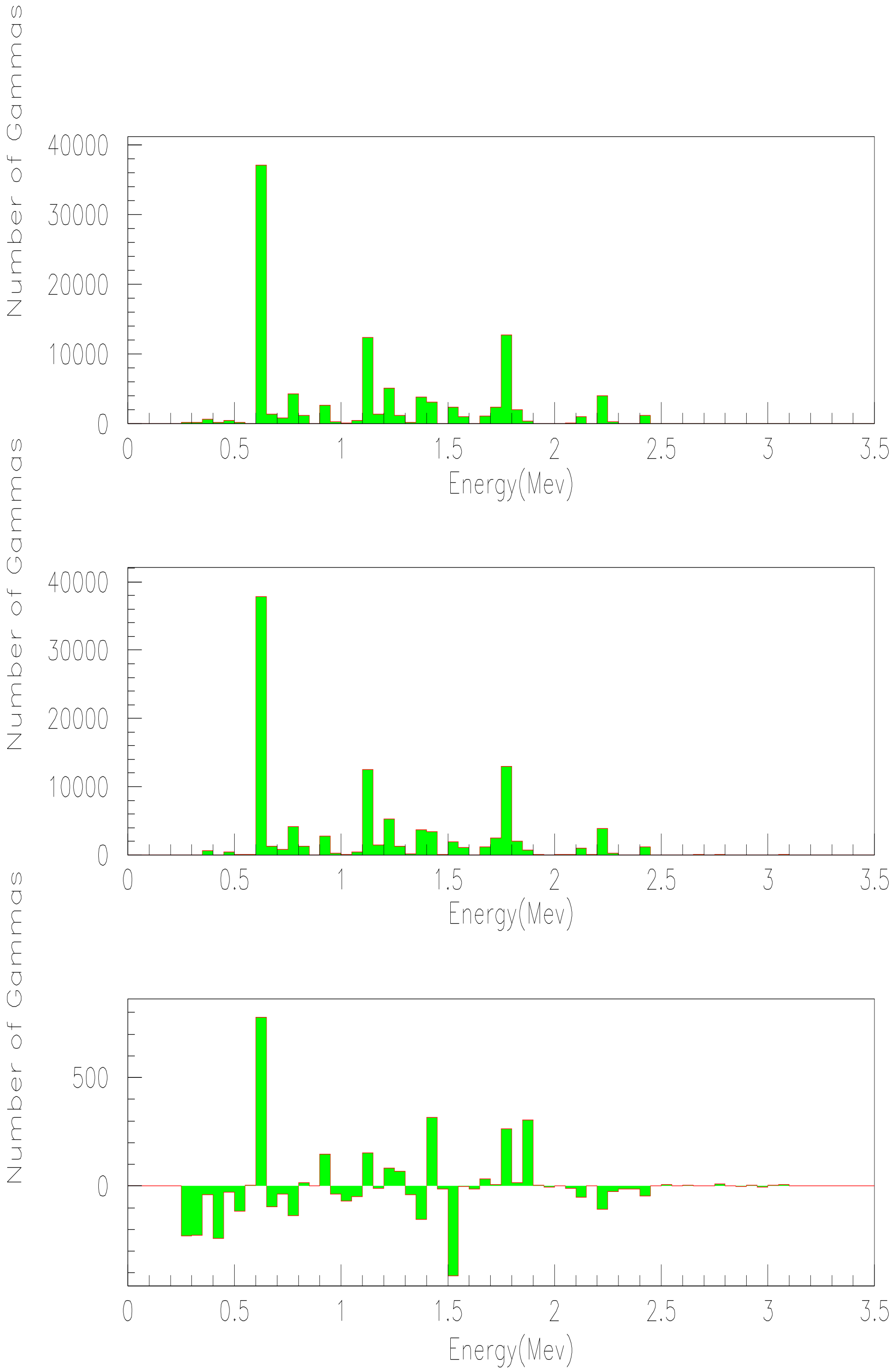

Figure B.3: **Gamma spectrum from ^{214}Bi decay simulated by the old version of the SNOMAN code.** The upper plot comes from the experimental data, the middle one is produced by the SNOMAN code and the lower one is the difference between the upper and the middle plot. Bin size is 0.05Mev which is much smaller than the energy resolution of the SNO detector.

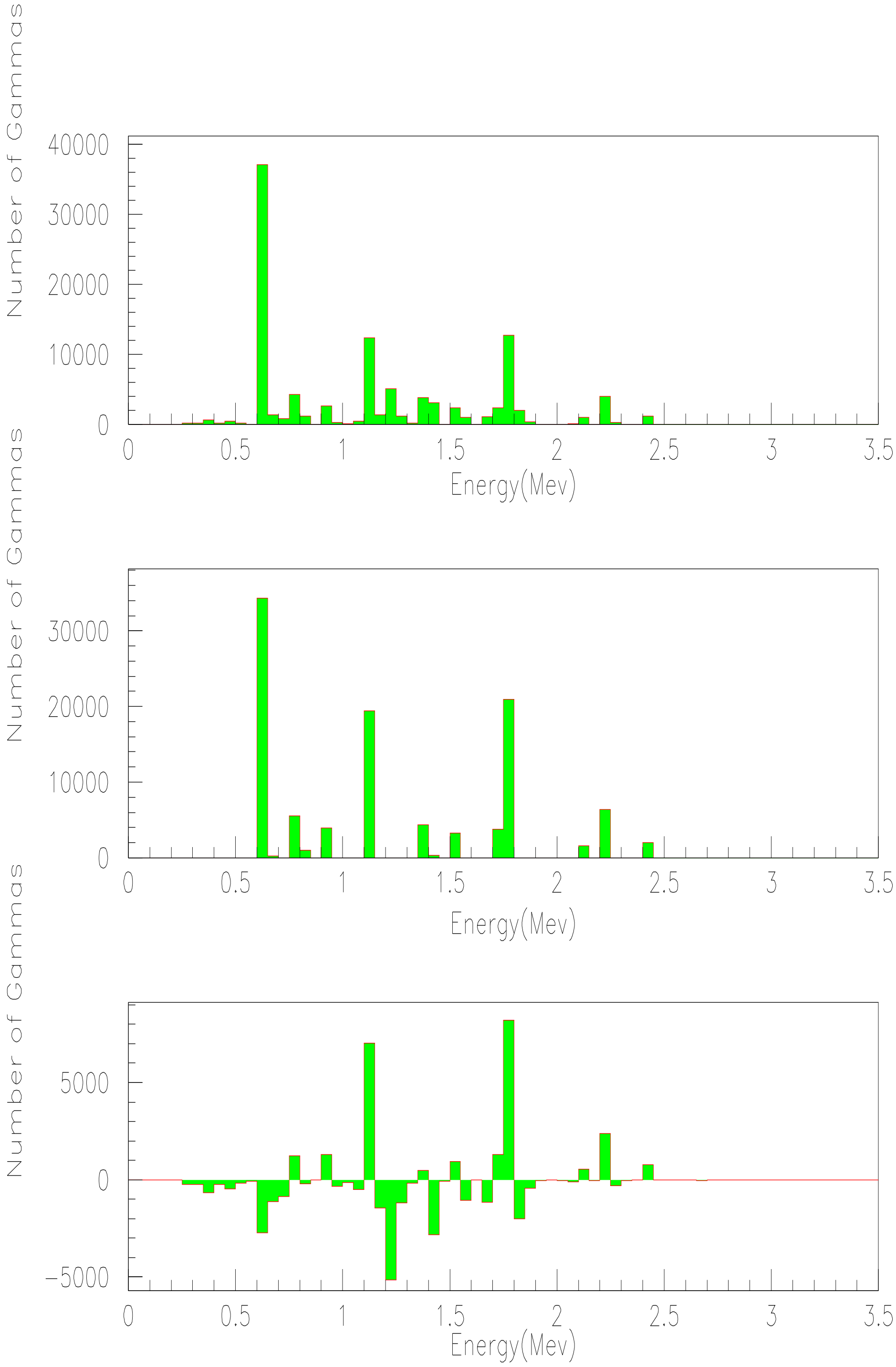

Bibliography

[1] H.A.Bethe. *Energy Production in Stars.* Physical Review, Vol.27, No.6, Pages 2220-2233,1992.

[2] J.N.Bahcall and M.H.Pinsonneault. *Solar Models with Helium and Heavy Element Diffusion.* Preprint, 1995.

[3] J.N.Bahcall and R.K.Ulrich. *Solar Models, Neutrino Experiment, and Helioseismology.* Reviews of Modern Physics,Vol.60,No.2,Pages 297-372,1988.

[4] N. Grevesse and A. Noels. *Origin and Evolution of the Elements.* Cambridge Univ. Press, Cambridge, 1993.

[5] M.Schwarzschild. *Structure and Evolution of the Stars.* Princeton University Press,1958.

[6] J.N.Bahcall. *Neutrino Astrophysics.* Cambridge University Press, 1989, Page 173.

[7] J.N. Bahcall et al.. *Review of Mordern Physics*, Vol. 54, page 767, 1982.

[8] J.N. Bahcall and A. Ulmer. *The Temperature Dependence of Solar Neutrino Fluxes.* February, 1996, Astrophysics Preprint Series, Princeton.

[9] R.B.Leighton, R.W.Noyse and G.W.Simon. Ap.J.135(1962) 474.

[10] J. Christensen-Dalsgaard, D. Gough and J. Toomre. *Seismology of the Sun.* Science, 6 september, 1985, Vol. 229, No. 4717.

[11] C. Frorhlich et al. *First Results from Virgo, the Experiment for helioseismology and Solar Irradiance Monitor on SOHO.* Solar Physics, Vol 170, Issue 1, Page 1-25, 1997.

[12] J. Christensen-Dalsgaard et al, 1991, Astrophys. J. Vol 378, Page 413.

[13] B.T.Cleveland et al. *Update on The Measurement of the Solar Neutrino Flux with the Homestake Chlorine Detector*. Nuclear Physics B (Proc. Suppl.), 38(1995) 47-53.

[14] J.N.Bahcall and R.Davis. *Essays in Nuclear Astrophysics*. Cambridge University Press, Page 243, 1982.

[15] K. Lande andP.S. Wildenhain. *The Homestake Solar Neutrino Detection Program: Chlorine and Iodine*. Proceedings of the 17th International Conference on Neutrino Physics and Astrophysics (Neutrino 96), 1996, Helsinki, Finland, World Scientific.

[16] J.N.Bahcall. *How many solar neutrino experiments are wrong ?* . Nuclear Physics B. (Proc. Suppl.), 38, 1995, Page 98-104.

[17] J.N.Bahcall. Review of Modern Physics, page 881, 50, 1978.

[18] K.S.Hirata et al. *Real-time, Directional Measurement of ^8B Solar Neutrinos in the Kamiokande* II *Detector*. Physics Review D, Vol. 44, No. 8, 15 October 1991

[19] J.N.Bahcall and M.Pinsonneault. *Standard Solar Models, With and Without Helium Diffusion, and the Solar Neutrino Problem*. Review of Modern Physics, Vol.64, No.4, October 1992.

[20] Yoichiro Suzuki. *Kamiokande Solar Neutrino Results*. Nuclear Physics B(Proc. Suppl.) 38, 1995, page 54-59.

[21] Yoichiro Suzuki. *Solar Neutrino Results from Kamiokande and Superkamiokande*. Proceedings of Neutrino 96, page 73-82.

[22] T.Stolarcyzk. *Thesis*. Universit e de Paris-Sud, 1990.

[23] J.N. Abdurashitov, et al. *Results From SAGE* II. Nuclear Physics B (Proc. Suppl.) 38, 1995 , Page 60-67.

[24] P.Anselmann, et al. *Update of GALLEX Solar Neutrino Results and Implication*. Nuclear Physics B (Proc. Suppl.) 38, 1995 , Page 68-76.

[25] D.Vignaud et al. *GALLEX solar neutrino observations: Results for GALLEX III*. Physics Letter B, Vol 388, Page 384, 1996.

[26] J.N. Abdurashitov, et al. PRL vol.77, 4708, 1996.

[27] A.Acker and S.Pakvasa. *Solar Neutrino Decay.* Physics Letters B, Vol.320, Pages 320-322, 1994

[28] Y.Suzuki. *The Superkamiokande Project.* Nuclear Physics B (proc. Suppl.), Vol. 35, Pages 273-275, 1994.

[29] Kenneth K. Yong. *First Results From the Super-kamiokande Experiment.* Preprint, Department of Physics, University of Washington, seattle, May 9, 1997.

[30] G.Nico etal. Proceedings of the XXVII International Conference on High Energy Physics, Glasgow, Scotland, 1994.

[31] Stephen Parke. *Status of the Solar Neutrino Puzzle.* Physics Review Letter, Vol. 74, No. 6, 6 February, 1995.

[32] W.A.Dziembowski et al. *A Seismic Model of the Sun's Interior.* Astrophysical Journal, Vol. 432, Page 417-426, 1994.

[33] O. Richard, S. Vauclair, C. Charbonnel and W.A. Dziembowski. *New Solar Models including Helioseismological constraints and Light-element Depletion.* Astronomy and Astrophysics, Vol. 312, Pages 1000-1011, August, 1996.

[34] N.Hata, S.Bludman and P.Langacker. *Astrophysical Solutions are Incompatible with the Solar Neutrino Data.* Physical Review D, Vol.49, No. 7, Pages 3622-3625, 1994.

[35] Andrew Cumming and W.C. Haxton. *^{3}He Transport in the Sun and the Solar Neutrino Problem.* Physical Review Letters, Vol. 77, No. 21, Page 4286, 18 November, 1996.

[36] B.Kayser. *On the Quantum Mechanics of Neutrino Oscillation.* Physical Review D, Vol. 24, No. 1, Pages 110-116, 1981.

[37] S.M.Bilenky and B.M. Pontecorvo. *Massive neutrino and Neutrino Oscillations.* Review of Modern Physics, Vol. 59, Page 671, 1987.

[38] J.N.Bahcall and S.C.Frautschi. *Physics Letter B.* 29, 263.

[39] L.Wolfenstein. *Neutrino Oscillations in Matter.* Physical Review D, VOl.27, Pages 2369-2374, 1978.

[40] S.P.Mikheyev and A.Yu.Smirnov. *Sov.J.Nucl.Phys*, **42**, 913, 1986.

[41] S.P.Mikheyev and A.Yu.Smirnov. *Sov.J.Nucl.Phys*, **64**, 4, 1986.

[42] T.K.Kuo. *Neutrino Oscillations in Matter*. Reviews of Mordern Physics, Vol. 61, No.4, Page 937, October, 1989.

[43] S.J.Parke. *Non-Adiabatic Level Crossing in Resonant Neutrino Oscillations*. Physical Review Letters, Vol. 57, Pages 1275-1278, 1986.

[44] N.Hata and P.Langacker. *Solar Model Uncertainties, MSW Analysis, and Future Solar Neutrino Experiments*. Physical Review D, Vol. 50, No. 2, Pages 632-660, 1994.

[45] A.Alimonti et al. *A New Solar Neutrino Detector*. Nuclear Physics B (Proc. Suppl.), Vol. 32, Pages 149-155, 1993.

[46] M.Giammarchi. Nuclear Physics B (Proc. Suppl.), Vol. 35, Page 433, 1994.

[47] G.T.Ewan, et al. *The Sudbury Neutrino Observatory - An Introduction*. Physics in Canada, Vol. 48, No. 2, 1992

[48] G.T.Ewan, et al. *Sudbury Neutrino Observatory*. SNO internal report, October, 1987.

[49] J.C.Zwinkels, W.F.Davidson and C.X.Dodd. *Optical Properties of UV Transmitting Acrylics for use in a Heavy Water Čerenkov Detector*. Applied Optics, Vol. 29, no. 22, pages 3240-3248, 1990.

[50] R.J.Boardman. *The Detection of Čerenkov Radiation from Neutrino Interactions*. Oxford Ph.D. thesis, Page 182, 1992.

[51] M.E.Moorhead. *Reflectors in čerenkov Detectors*. Oxford Ph.D Thesis, 1992.

[52] J.V.Jelley. *Čerenkov Radiation*. Pergamon Press, London, 1958.

[53] J.N.Bahcall and Eligio Lisi. *Test of electron flavor conservation with the Sudbury Neutrino Observatory*. Physical Review D, Vol. 54, No. 9, Page 5417, 1996.

[54] K.Kubodera and S.Nozawa. *Int. J. Mod. Phys.* E 3, 101, 1994.

[55] J.N.Bahcall and S.D.Ellis. *Nuclear Physics*. A114, 636, 1968.

[56] H.H.Chen. *Direct Approach to Resolve the Solar-Neutrino Problem.* Physical Review Letters, Vol. 55, Pages 1534-1536, 1985.

[57] S.Ying, W.C.Haxton and E.M.Henley. *Charged and Neutral Current Solar Neutrino Cross Sections for heavy water Čerenkov Detectors.* Physical Review C, Vol. 45, No. 4, Pages 1982-1987, 1992.

[58] M.E.Moorhead, Y.D.Chan et al. *^6Li Neutron Poison for SNO.* SNO-STR-95-056, 1995.

[59] S.J.Brice. *Monte Carlo and Analysis Techniques for the Sudbury Neutrino Observatory.* Oxford Ph.D. thesis, 1996.

[60] J.N. Bahcall. *Neutral-current reactions of solar and supernovaneutrinos on deuterium.* Phys. Rev. D 38, Page 1030, 1988.

[61] M.J.Lyon, D.wark et al. *Some Monte Carlo Studies of the Added Salt Option.* Sno internal report, 1996.

[62] D.Wark, private communication, 1996.

[63] R.G.H.Robertson et al. *Neutral-Current Detection in the Sudbury Neutrino Observatory (SNO).* Fin-94-ER-E-324, Los Alamos Laboratory, 1992.

[64] S.J.Brice. *An Overview of the Feedforward Neural Network Technique and its Application to SNO Event Classification.* SNO internal report, SNO-STR-95-037, 1995.

[65] M.Thorman. *Private Communication.* 1996.

[66] R.M.Bionta etal. Phys. Rev. Lett. Vol 51, Page 27, 1983.

[67] K.Arisaka. Ph.D. thesis, Department of Physics, University of Tokyo, 1985.

[68] R.C.Svoboda, Ph.D. Thesis, University of Hawaii, 1985.

[69] The SNO collaboration. *The Sudbury Neutrino Observatory Proposal.* SNO-STR-87-12, 1987.

[70] K.Hirata et al. Physics Review Letter, Vol. 58, Page 1490, 1987.

[71] E.W.Kolb et al. Physical Review D, Vol 35, Page 1906, 1987 .

[72] A. Burrows, D. Klein and R. Gandhi. *The Future of Supernova Neutrino Detection.* Physical Review D, Vol. 45, Page 3361, 1992.

[73] A. Burrows. Ap. J., Vol. 283, Page 848, 1984.

[74] R.Mayle et al. Ap. J., Vol. 318, Page 288,1987.

[75] D. Wark, N. West and M.D. Lay. *It's alive - The Birth of SNOMAN.* SNO internal report, SNO-STR-91-077, 1991.

[76] D. Wark et al. *The SNOMAN Users Manual.*

[77] D. Wark et al. *The SNOMAN Programmers Manual.*

[78] R. Brun and J. Zoll. *ZEBRA User Manual.* CERN program library entry Q100.

[79] M. Nakahata, reported at *the Workshop on Physics with Solar Neutrinos*, University of California, Santa Barbara.

[80] W.F. Davidson et al. *Background Measurements in the Creighton Mine.* SNO internal report, 1987.

[81] P. Skensved and B.C. Robertson. *Summary of Backgrounds in SNO.* SNO internal report, SNO-STR-94-13, April 21, 1994.

[82] W.R. Nelson, H. Hirayama and D.W.O. Rogers. *The EGS4 Code System.* SLAC report 265, 1985.

[83] R. Heaton, H. Lee and B.C. Robertson. *α-Particle Induced High Energy γ-Rays from Light Elements.* SNO internal report, July 13, 1992.

[84] A.P. Ferraris, 1992, D.Phil Thesis, Oxford.

[85] D.J. Hughes , Advisory Group *May 15,1952; Neutron Cross Section* (Printed in U.S.A.)

[86] R. K. Taplin. *The Use of Photomultipliers in SNO.* Ph.D Thesis, Oxford University, 1995.

[87] R. G. Gutman. *Membrane Filtration*, Adam Hilger, 1987. This is a mainly technical reference text.

[88] R. K. Taplin and M. E. Moorhead. *Beta-Alpha Coincidence Counters for the Sudbury Neutrino Observatory.* SNO internal report, March 24, 1997.

[89] Bill Frati and R.V. de Water. *Quad Fitter Introduction - Reconstruction and Pattern Recognition.* 1994, SNO-STR-94-030.

[90] M. Lay. *Calibration and PMT Backgrounds in SNO.* SNO internal report, February 9, 1996.

[91] Particle Data Group. *Particle Physics Booklet.* Page 179, 1996.

[92] W. Press, S. Teukolsky, W. Vetterling, and B. Flannery. em Numerical Recipes in Fortran. Cambridge University Press, 1992.

[93] D. S. Haslip. *An examination of the PMT $\beta\gamma$ Background in the SNO detector.* A thesis for master degree of science, Queen's university, Canada, April, 1996.

[94] M. Lay. *Creation and Detection of Čerenkov Light in the Sudbury Neutrino Observatory.* Ph.D. Thesis, University of Oxford, 1994.

[95] S. Kirkpatrick, C.D. Gelatt and M.P. Vecchi. *Optimization by Simulated Annealing.* SCIENCE, 13 May, 1983, Vol. 220, No. 4598.

[96] R. Karp, Math. Oper. Res., **2**, 209, 1977.

[97] Otten et al. *The Annealing Algorithm.* Boston, Kluwer, 1989.

[98] J.A. Nelder and R. Mead, 1965, Computer Journal, Vol. 7, pages 308-313.

[99] Bill Frati. *Quad Fitter Update.* 1994, SNO internal report.

[100] M.D. Thorman. *The Application of a Quad Fitter to SNO data.* 1994, SNO internal report.

[101] C.M. Ledevev and V.S. Shirley. *Table of Isotopes*, 1978, JOHN WILEY & SONS. INC.

[102] C.J. Jillings and T.J. Radcliffe. em Comparison of SNOMAN's Čerenkov Light Distribution to a Single-scattering Model. 1996, SNO-STR-96-32, SNO internal report.

[103] M.G. Bowler, X. Chen, N.A. Jelley and M. Thorman. *The distribution of Čerenkov Light and its effect on the separation of different classes of event by pattern recognition.* Nov. 28, 1996, SNO-STR-96-058, SNO internal report.

[104] John Hertz, Anders Krogh and Richard G. Palmer. *Introduction to the Theory of Neural Computation.* Addison Wesley, 1991.

[105] Bruce Denby, *Tutorial on Neural Network Application in High Energy Physics: 1992 perspective.* Proceedings of the Second International Workshop on Software Engineering, Artificial Intelligence, and Expert Systems for High Energy and Nuclear Physics, Pages 287-325, La Londe LesMaures, France, 1992.

[106] Carsten Peterson, *Pattern Recognition in Hih Energy Physics wit Neural Networks.* QCD at 200Tev, Pages 146-163, 1992.

[107] B. Denby et al. *Performance of the CDF Neural Network Electron Isolation Trigger.* Nuclear Instruments and Methods in Physics Research A, Vol. 356, Pages 485-492,1995.

[108] The DELPHI Collaboration. *Classification of the hadronic decays of the Z^0 into b and c quark pairs using a neural network.* Physics Letter B, 295, Pages 383-395, 1992.

[109] D. W. Dong and Y. Chan, *Neural Network for Recognizing Čerenkov Radiation Patterns*, LBL-33634.

[110] Andreas Zell et cl. *Stuttgart Neural Network Simulator.* Institute for Parallel and Distributed High Performance Systems, University of Stuttgart, Report No. 6/95.

[111] G. Cybenko. *Approximation by Superpositions of a Sigmoidal Function.* Mathematics of Control, Signals, and Systems, Vol. 2(4), Pages 303-314, 1989.

[112] S. Biller. Private communications.

[113] M. Goldberg, P.L. Mattern, K. Lengweiler and P.W. Levy. *Radiation Induced Coloring of Cerenkov Counter Glasses*, Nuclear Instruments and Methods, vol. 108, 119-123, 1973. 1978, JOHN WILEY & SONS. INC.

[114] R. Fittig, Ber, **12**, 1739, 1879.

[115] J.W.C. Crawford. *J. Soc. Chem. Ind.*, **68**, 201, 1949.

[116] B. Knox, private communication, 1997.

[117] Loius Lyons. *Statistics for Nuclear and Particle Physicists.* Cambridge University Press, 1986.

[118] W.T. Eadie, D. Drijard, F.E. James, M. Roos and B. Sadoulet. *Statistical Methods in Experimental Physics.* North-Holland Publishing Company, 1971.

[119] C.M. Lederer and V.S. Shirley. *Table of Isotopes.* 1978, John Wiley & Sons Inc.

[120] W. Frati. *Determination of Uranium and Thorium Contamination in the D_2O from the NPMT spectrum above 1.4 Mev.* SNO internal report, May 15, 1995.